

# NETS

2020



**CONFERENCE  
PROCEEDINGS**

**NUCLEAR and  
EMERGING  
TECHNOLOGIES for  
SPACE**

Knoxville, TN 2020, April 6th – 9th

## **Track 2: Nuclear Fission Power and Propulsion**

**Technical Track Chair: Paolo Venneri**

Author	Title
Abou-Jaoude, Abdalla	PARAMETRIC EVALUATION OF ALTERNATIVE NUCLEAR PROPULSION CORES USING CURVED FUEL
Angh, Caen	DEVELOPMENT OF ZIRCONIUM CARBIDE FOR INERT MATRIX FUELS
Cendro, Samantha	simulation and experimental validation of aN inductively HeATED Solid-core nuclear thermal rocket
Chaiken, Max	HEAT PIPE DEVELOPMENT FOR SPACE FISSION DEMONSTRATION MISSIONS
Colgan, Nathan	A HEAT EXCHANGER FOR HTGR WASTE HEAT REJECTION TO MARTIAN ATMOSPHERE
Duffin, Taylor	INTERFACE AND SUBSURFACE CERAMIC BEHAVIOR IN MOLYBDENUM CERMETS FOR NUCLEAR THERMAL PROPULSION
Floyd, Dan	PRE-IRRADIATION CHARACTERIZATION OF INSTRUMENT PERFORMANCE FOR NUCLEAR THERMAL ROCKETS: TEST PLAN
Gaffin, Neal	IRRADIATION TESTING OF MOLYBDENUM AND TUNGSTEN BASED CERMETS FOR USE IN NUCLEAR THERMAL PROPULSION
Hashkins, Justin	Toward an in-depth material model for Nuclear thermal propulsion fuel elements
Hirschhorn, Jacob	DEVELOPMENT OF A MULTISCALE MODEL FOR FUEL LOSS FROM NUCLEAR THERMAL PROPULSION
Howard, Richard	Design of the In-pile experiment Set (INSET) apparatus to support Nuclear Thermal Propulsion fuel and component testing.
Howe, Steve	SPRINTR: ADVANTAGES OF FLAT PLATE VERSUS PRISMATIC NTR FUELS
Hutchins, Emily	Activation analysis of subscale experimental testbed: towards simulating nuclear thermal propulsion prototypic conditions for material testing
Joyner, Russell	LEU NTP ENGINE SYSTEM FOR FLIGHT DEMONSTRATOR FOR A MARS CREW MISSION NTP
Kaffezaiz, Naiki	The Ultra-small Modular Reactor for Space Applications
Kajihara, Takanori	Neutronic Analysis of the Submersion-Subcritical Safe Space (S4) Reactor for Deploying LEU Fuel System Using Serpent
King, Jeffrey	SHIELDING ANALYSIS FOR A MODERATED LOW-ENRICHED URANIUM FUELED KILOPOWER REACTOR
Krecicki, Matt	QUANTIFICATION OF INTRA-ELEMENT POWER PEAKING IN LOW ENRICHED NUCLEAR THERMAL
Krecicki, Matt	NEUTRONIC FEASIBILITY OF A LOW ENRICHED FAST SPECTRUM NUCLEAR THERMAL PROPULSION
Lin, Ching-Sheng	DESIGN AND ANALYSIS OF A 250 MW PLATE-FUEL REACTOR FOR NUCLEAR THERMAL PROPULSION
Maydan, Jack	Combined Cycle Nuclear Power and Propulsion: Reduction in Engineering Complexity to Enable Human Mars Mission Architectures in the 2020s
Nikitaev, Dennis	A LABORATORY TEST TO EVALUATE SEEDED HYDROGEN IN A NUCLEAR THERMAL ROCKET ENGINE
O'Brien, Robert	THE SIRIUS-1 NUCLEAR THERMAL PROPULSION FUELS TRANSIENT TEST SERIES IN THE IDAHO NATIONAL LABORATORY TREAT REACTOR
Rader, Jordan	Dynamic Nuclear Thermal Rocket and Engine Modeling
Raftery, Alicia	FABRICATION OF UN-MO CERMET NUCLEAR FUEL USING ADVANCED MANUFACTURING TECHNIQUES
Rau, Adam	REDUCED ORDER NUCLEAR THERMAL ROCKET ENGINE MODEL
Shivprasad, A.P.	HYDROGEN ABSORPTION BEHAVIOR OF Y-10Ce
Sikorksi, David	REDUCED ORDER NUCLEAR THERMAL ROCKET ENGINE MODEL
Snead, Lance	PROCESSING TRISO-BEARING ULTRAHIGH TEMPERATURE CARBIDE FUELS FOR NUCLEAR THERMAL
Sprouster, David	MAGNESIUM OXIDE FOR COMPOSITE MODERATORS AND TRISO FUEL MATRICES
Steiner, Tyler	NUCLEAR THERMAL PROPULSION SUBSCALE EXPERIMENTAL TESTBED FOR MATERIAL INVESTIGATIONS USING THE OHIO STATE UNIVERSITY RESEARCH REACTOR
Unger, Aaron	DESIGN OF A RADIATION SHIELD FOR A LOW-ENRICHED URANIUM SPACE NUCLEAR REACTOR
Wang, Jim	initial comparison of reduced and higher order thermal hydraulic solvers for nuclear thermal propulsion fuel element design
Wood, Emily	Alternatives for electrical power production from a nuclear thermal propulsion engine

## PARAMETRIC EVALUATION OF ALTERNATIVE NUCLEAR PROPULSION CORES USING CURVED FUEL PLATES

Abdalla Abou-Jaoude<sup>1</sup>, and Gilles Youinou<sup>1</sup>

<sup>1</sup>Idaho National Laboratory, Idaho Falls, ID 83415  
 404-455-1657 | [abdalla.aboujaoude@inl.gov](mailto:abdalla.aboujaoude@inl.gov)

*Nuclear Thermal Propulsion (NTP) holds the potential of reducing travel times for deep space missions (e.g. to Mars). Previous reactor core designs considered by the Rover/NERVA program relied on highly enriched uranium (HEU) fuel contained within a hexagonal graphite matrix. An alternative layout is investigated in this paper. It consists of a circular assembly containing concentric curved plates of UN fuel. These fuel assemblies are placed within a beryllium block and reflector. Preliminary results indicate that many variations of this design are viable, with high power to mass ratio and outlet temperatures.*

### I. DESIGN SPECIFICATIONS

#### I.A. Introduction and Overview

The NTP core evaluated consists of circular fuel assemblies (FA) divided into three parts, each loaded with curved plates as highlighted in Figure 1. The total core power output is set at 250 MW. The outside diameter of each FA is fixed at 10.1 cm and the height at 80 cm. Assemblies are arranged in a hexagonal pattern. Each FA consists of:

- A UN fuel meat plate (0.8-3 mm thick)
- Mo/W cladding (0.50/0.25 mm thick)
- 3 Mo/W separators (0.50 mm thick)
- Hydrogen channel (0.75 mm thick)
- Between 8 to 16 fuel plates

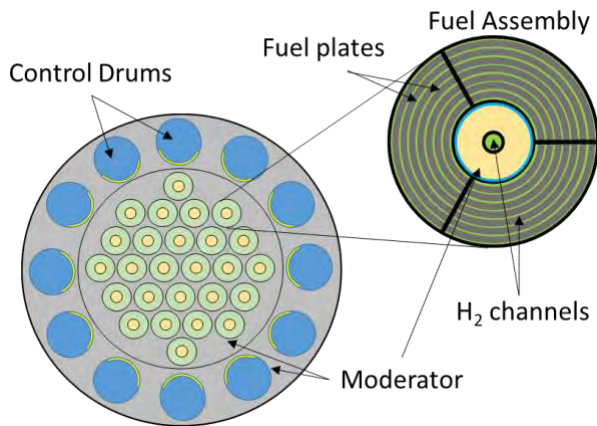


**Fig. 1.** Illustration of the curved plate fuel assembly and core layout for the proposed NTP.

The FA are surrounded by a Be block that will need to be cooled in a similar fashion to the Soviet RD-0140 design.<sup>1,2</sup> This is in turn surrounded by a Be reflector containing rotating drums with enriched B<sub>4</sub>C acting as a neutron poison. An axial Be reflector is placed above the fuel, while no lower reflector is used in light of the high outlet coolant temperatures.

MCNP6.1.0 was used to model the proposed NTP.<sup>3</sup> The fuel assembly geometries are modeled explicitly, including the separating structure. For all the criticality calculations, 10,000 virtual particles are used with 700 active cycles.

#### I.B. Sub-Design Specifications

Four main sub-designs are considered in this assessment. The main objective is to quantify key design trade-offs between them. They are labeled A to D and are summarized in Table I.

**TABLE I.** Design specifications for the four sub-designs.

	Design A	Design B	Design C	Design D
Fuel	UN	UN	UN	UN
Clad	Mo	W	W	184W
Moderator	Be	Be	Be	Be
Clad thick.	0.50 mm	0.25 mm	0.25 mm	0.25 mm
Fuel thick.	0.25 cm	0.25 cm	0.15 cm	0.09 cm
# plates	8	8	12	16
max(T <sub>clad</sub> )	2320 K	3000 K	3000 K	3000 K
max(T <sub>fuel</sub> )	3100 K	3100 K	3100 K	3100 K
Volume	16% H <sub>2</sub>	16% H <sub>2</sub>	24% H <sub>2</sub>	32% H <sub>2</sub>
Fractions	54% fuel 30% stru.	65% fuel 19% stru.	51% fuel 25% stru.	38% fuel 30% stru.

Additional design specifications will be defined in the following sections. This includes the FA pitch, the core radius, the minimum number of assemblies, the outlet temperature, flow rate, and the total core mass. These variables are strongly dependent on thermal and neutronic performances.

### II. PERFORMANCE EVALUATION

#### II.A. Thermal Hydraulic Performance

The driving factor for the thermal hydraulic performances inside the four designs are temperature

limits. The maximum allowable temperature for Mo and W, are respectively 2320 K and 3000 K. This corresponds to 80% of their melting temperatures. The added margin is due to a reduction of mechanical properties in W/Mo at temperatures approaching their melting temperature (the clad provides the structural integrity of the fuel). The maximum centerline temperature for UN is 3100 K (corresponds to its melting point).

The scoping study needs to compute an approximate maximum plate power for a given design in order to determine the maximum total power production in a given assembly. The inner clad temperature can be computed by Eq. 1. It is expressed as a function of the axial position  $z$ , the heat transfer coefficient  $h_{H2}$ , the heat flux  $q''$ , the bulk H<sub>2</sub> temperature  $T_{H2}$ , the clad thermal conductivity ( $k_c$ ) and thickness  $\delta_c$ .

$$T_{ci}(z) = q''(z) \left( \frac{1}{h_{H2}} + \frac{\delta_c}{k_c(z)} \right) + T_{H2}(z) \quad (1)$$

$$T_{CL}(z) = q''(z) \left( \frac{\delta_f^2}{2k_f} + \frac{\delta_g}{k_g} \right) + T_{ci}(z) \quad (2)$$

The fuel centerline temperature can be computed in a similar fashion in Eq. 2 using the fuel/gap thickness ( $\delta_f, \delta_g$ ) and thermal conductivity ( $k_f, k_g$ ). For a given outlet temperature and clad thickness (based on manufacturing limits) the maximum heat generation as function of fuel thickness can therefore be deduced. All limiting thermal parameters are highlighted in Table II. A peak-to-average FA ratio of 1.35 was used in the calculations to find an estimate for the minimum number of FA needed. The results show that the maximum power generated in a single assembly can range from 11 MW to 33 MW, leading to H<sub>2</sub> mass flow rates between 0.29 kg/s and 0.85 kg/s.

**TABLE II.** Assembly-level thermal limits for the four designs.

Design:	A	B	C	D
max(P <sub>FA</sub> )	11.0 MW	14.0 MW	23.2 MW	32.6 MW
Min(#FA)	31	24	15	10
FA $\dot{m}$	0.29 kg/s	0.36 kg/s	0.60 kg/s	0.85 kg/s
V <sub>out</sub>	0.7 km/s	0.9 km/s	1.0 km/s	1.0 km/s
av( $q''$ )	1.3	1.6	2.7	3.8
	kW/cm <sup>3</sup>	kW/cm <sup>3</sup>	kW/cm <sup>3</sup>	kW/cm <sup>3</sup>
T <sub>out</sub>	2100 K	2550 K	2550 K	2550 K

The thermal calculations above were conducted independently of neutronic simulations. These will be considered in later sections. The objective at this stage is to simply translate material limits into (thermal) performance limits that can help guide the parametric searches.

## II.B. Neutronic Performance

While the analysis of Section II.A determined the minimum number of assemblies, the final core layout is also affected by neutronic characteristics and the total fuel mass required to reach criticality. To provide sufficient margins, an eigenvalue above 1.02 is targeted for all cores with all control rod drums rotated out.

Figures 2&3 show a visualization of the MCNP6 models developed. The reflector and control drums are assumed to extend to the length of the core, with void above them. An axial reflector (orange) with 90% Be volume fraction is located above the core. It is modeled as a monolithic block at this stage in the analysis. All volume beneath the core is assumed to be occupied by the hydrogen exhaust. The main change between the various designs is the number of plates within each fuel assembly (as illustrated in Figure 4), the assembly pitch, and the overall core radius.

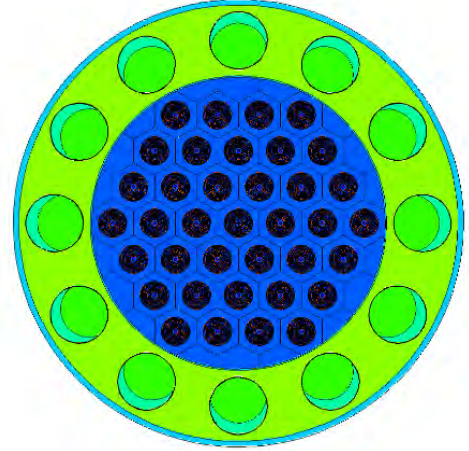


**Fig. 2.** MCNP6 visualization of the XY cross-section for Design A.

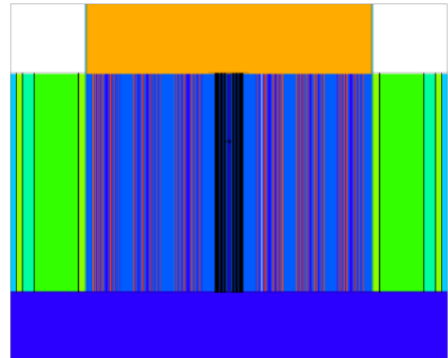


**Fig. 3.** MCNP6 visualization of the XZ cross-section for Design A. An axial reflector (orange) is modeled above the core while all volume below the core is assumed to be hydrogen (blue).

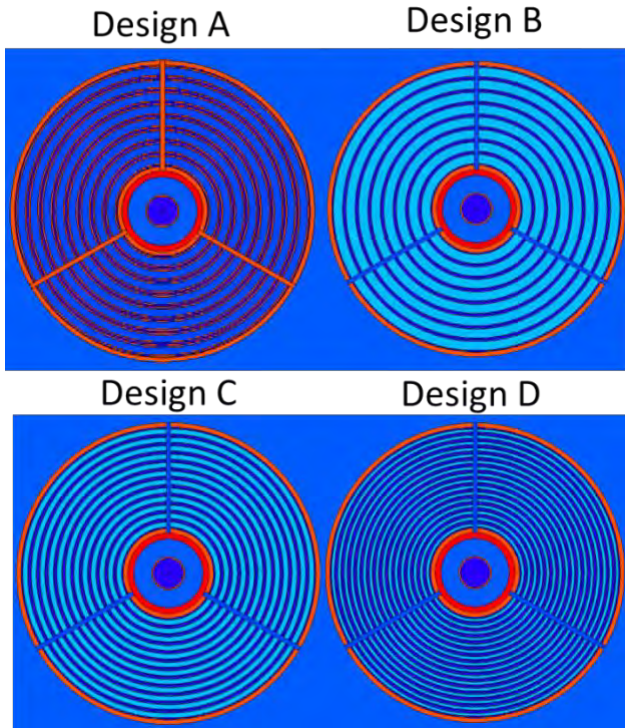


**Fig. 4.** MCNP6 visualization of the XY cross-sections for the different fuel assembly designs considered in the analysis. The three ‘separators’ in designs B, C, and D are made of W and are thinner (0.25 mm) than in design A.

The design space for the four variants is strongly dependent on the moderator/fuel ratio. This is driven by the fuel assembly pitch. Figure 5 plots the variation of the eigenvalue in Design A as a function of FA pitch. The curve peaks at a 23.5 cm pitch. After this point, parasitic absorptions compensate the added increases in fission cross-sections.

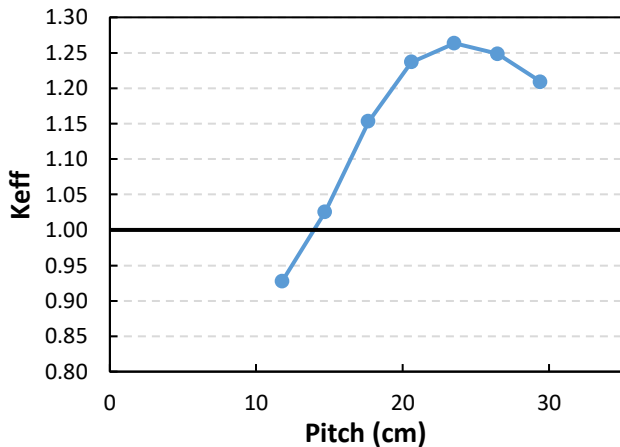


**Fig. 5.** Variation of the eigenvalue in Design A as a function of the FA pitch.

As observed in Design A, the pitch needed to reach an eigenvalue above 1.02 is around 14.7 cm. A similar iteration can be performed for all the other designs with the results summarized in Table III. The center assembly power in all four designs is below the estimated thermal hydraulic limits summarized in Table II.

**TABLE III.** Neutronic performance of the four designs and resulting core sizes and masses. The Monte Carlo standard deviation for the eigenvalue was 30 pcm.

Design:	A	B	C	D
# FA	37	37	19	10
FA pitch	12.71 cm	15.85 cm	20.60 cm	19.46 cm
Core diam.	103 cm	111 cm	103 cm	97.3 cm
Core+Refl diam.	158 cm	166 cm	158 cm	152 cm
Total mass	5.47 t	5.67 t	4.20 t	3.30 t
U mass	1.51 t	1.81 t	0.74 t	0.30 t
<sup>235</sup> U mass	299 kg	358 kg	146 kg	58 kg
max(P <sub>FA</sub> )	9.5 MW	10.1 MW	21.2 MW	31.9 MW
k <sub>eff</sub>	1.02533	1.02056	1.02337	1.02396

The maximum fuel assembly power in Table III was shown to always be below the thermal limits set in Table II. Fig. 6 plots the radial FA power distribution within Design C to illustrate the variation across the core. Orificing the flow rate at the inlet of each assembly (similarly to sodium fast reactor) can be relied upon in order to achieve a flat temperature distribution throughout the core. According to the diagram, four orifice zones would be needed in Design C.

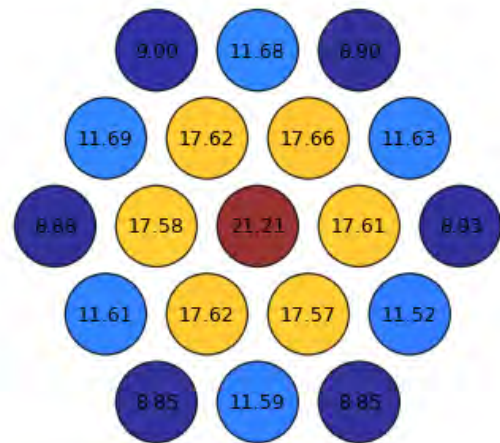


**Fig. 6.** Power generation in each fuel assembly (FA) of Design C in MW.

Design B is the least desirable option. It requires a higher pitch and core size relative to Design A in order to compensated for the higher absorption cross-section of W

(compared to Mo). Due to its reliance on Mo with a lower melting, the outlet temperature of Design A is limited. Design D requires the lowest core mass (3.3 tones) to reach the targeted eigenvalue. Its main drawback, however, is that it would require enriched W (0.5%  $^{182}\text{W}$  / 5.4%  $^{183}\text{W}$  / 93%  $^{184}\text{W}$  / 1.6%  $^{186}\text{W}$ ).<sup>4</sup> Sub-designs with natural W would exceed the mass of other designs. Lastly, Design C keeps the total mass at around 4.2 tons while relying on natural W. The total  $^{235}\text{U}$  loading in this model would be 146 kg.

When fuel elements have varying distances from the moderator, large gradients in power production can be observed between the elements.<sup>5</sup> This is mostly due to the short mean free path of thermal neutrons, leading them to generate more energy from fission preferentially in regions closer to the moderator. The regions further away from the moderating region will see a harder spectrum leading to lower fission cross-sections. This inter-assembly effect is considered beyond the scope of the current research and will be investigated in future work. However, a range of approaches are envisaged to potentially help alleviate this concern:

- Reducing the enrichment or plate thickness of the fuel plates closest to the moderating element.
- Reducing the fuel meat thickness at the outermost plate for a bottom axial portion.
- Doping axial portions of the outermost fuel plate with a neutron poison to dampen the peak power.

### III. CONCLUSIONS

Alternative nuclear thermal core configurations were investigated. They consist of curved fuel plates contained within circular fuel assemblies. They are arranged in a

hexagonal pattern inside a Be core block. Four variants of this configuration were analyzed, with different number of fuel plates per assemblies, various pitches, and material components. If enriched W is available, Design D can satisfy neutronic and thermal requirements with a total core mass as low as 3.3 t. Otherwise Design C is a suitable alternative that can use natural W and require a core mass of 4.2 t. Future work will investigate a hybrid configuration of Design C with Mo for the top region and W only used for the bottom of the core where temperatures exceed the Mo-limits.

### ACKNOWLEDGMENTS

The work at Idaho National Laboratory was supported by the U.S. Department of Energy, Office of Nuclear Energy, under DOE Idaho Operations Office Contract DE-AC07-05ID14517.

### REFERENCES

1. J. R. WETCH *et al.*, “Development of Nuclear Rocket Engines in the USSR”, *Proc. Conference on Advanced SEI Technologies*, Sept. 4-6 (1991).
2. V. ZAKIROV and V. PAVSHOOK, “Russian Nuclear Rocket Engine Design for Mars Exploration”, *Tsinghua Science and Technology*, **12**, 3, pp. 256-260 (2007).
3. J. T. GOORLEY *et al.*, *MCNP6 User’s Manual*, Los Alamos National Laboratory, IA-CP-13-00634 (2013).
4. S. A. Levin *et al.*, “The Separation of Tungsten-184”, *Proc. Space-Nuclear Conference*, Gatlinburg, TN, May 3 (1961).
5. A. Abou-Jaoude *et al.*, “Performance and safety evaluation of a mixed-spectrum reactor design”, *Annals of Nuclear Energy*, **126**, pp 33-42, (2019).

## DEVELOPMENT OF ZIRCONIUM CARBIDE FOR INERT MATRIX FUELS

Caen Ang<sup>1</sup>, Matthew Scott<sup>1</sup>, David Sprouster<sup>2</sup>, Ethan Deters<sup>1</sup>, Lance Snead<sup>2</sup>, and Yutai Kato<sup>1</sup>

<sup>1</sup>University of Tennessee, Department of Nuclear Engineering, 1412 Circle Dr, Knoxville, TN, 37996

<sup>2</sup>Stony Brook University, 314 Old Engineering Building, Stony Brook, NY, 11794

Primary Author Contact Information: [cang@utk.edu](mailto:cang@utk.edu)

### I. INTRODUCTION

The rapid development of high-temperature capable fuels is crucial for deployment of Nuclear Thermal Propulsion (NTP) systems. NTP uses a nuclear reactor to heat flowing hydrogen to >2000 K, providing a high-impulse propulsion roughly twice the capability of chemical rockets. However, both fuel forms operated by the US civilian fleet, and other fuels from historical approaches are incompatible with the current requirements of performance and operational safety. An alternative fuel form known as TRistructral ISOtropic (TRISO) can potentially satisfy these requirements. TRISO particles each contain a fissionable microsphere (e.g. UO<sub>2</sub>), triple-coated by pyrolytic carbon (PyC), SiC and PyC. The respective PyC and SiC “shells” provide each manufactured TRISO particle (~1 mm) with a fission product (FP) containment system and pressure vessel. Specifically, FP containment in irradiated TRISO particles up to ~1800°C(1, 2) has been demonstrated, representing a “materials-based” engineering control for operational safety. From 2011, consolidation of TRISO particles was conducted by random packing within a sintered SiC matrix. The SiC matrix effectively replaces the typical graphite found in HTGRs. The SiC acts a secondary FP barrier along with other diverse benefits to fuel performance. SiC is sintered with oxide additives(3). Using this type of approach, also referred to as Nano-Infiltration Transient Eutectic (NITE) SiC, consolidation occurs without damaging TRISO particles. Typically, low temperatures and applied pressures (~1850°C, 20 MPa) are needed to prevent TRISO damage. Such approaches are analogous to careful matrix consolidation to prevent damage to fibers in composite sintering. NITE SiC is one of the few SiC materials known to be radiation stable.(4) In addition, an approach for industrial feasibility of zero-rupture FCM fuel has been validated using stacked arrays of TRISO particles axially consolidated by Pulsed Electric Current Sintering (PECS) to form a fuel pellet.

Recently, hydrogen testing by Benensky et al(5) of the traditional NITE SiC material in hot hydrogen conditions at 2000K showed relatively high mass loss kinetics and leaching of the oxide grain boundary phase. It is unclear at present whether other variants of NITE SiC have the same limitations. Other carbides (such as ZrC) showed improved stability by an order of magnitude and beyond 2000K.

The study here focuses on the development of techniques to sinter ZrC as an inert matrix, toward a goal of synthesis conditions compatible with hosting particle fuels. The challenges with ZrC can be outlined by the known mass transport pathways for solid state sintering. These are respectively plastic flow, lattice diffusion and grain boundary diffusion. Consolidation studies on ZrC indicate a sintering mechanism dominated by lattice diffusion, and a high activation energy dependent on Zr self-diffusion.(6) Thermodynamically, the Zr affinity for oxygen plays a key role in promoting non-densifying surface diffusion and vapor transport, which reduces particle curvature without bringing particle centers together. As a result, a significant contribution of plastic flow is needed, based on intergranular glide at low pressures (~25 MPa) and a dislocation mechanism at high pressures (~100 MPa). However, such pressures are detrimental to TRISO particles. Therefore, introducing a grain boundary migration mechanism may be beneficial. This is typically conducted by dopants, which provide monolayer changes in grain boundary energy or increase the relative surface energy. For sintering, extension of the grain boundary requires a higher relative surface energy of powder. Secondly, the mobility of the new grain boundary must be higher to permit the process to occur. Preliminary results indicate that introduction of such a mechanism is possible. This permits improved sintering of ZrC at temperatures compatible with TRISO particles, but control of the microstructure may be challenging.

#### I.A. Overview of hydrogen testing of materials

Hydrogen testing was conducted at the Compact Fuel Element Environmental Test (CFEET) facility located at NASA George C. Marshall Space Flight Center. While experimental conditions are described elsewhere(5), the key conditions include a flow rate of 0.5 SLPM to maintain 1 atm H<sub>2</sub> pressure, and a heating rate of 400°C/min. After each test (typically 30 min) mass and dimensions were obtained. Fig. 1 shows the preliminary testing results for high purity materials (floating zone-refined or chemical vapor deposition).

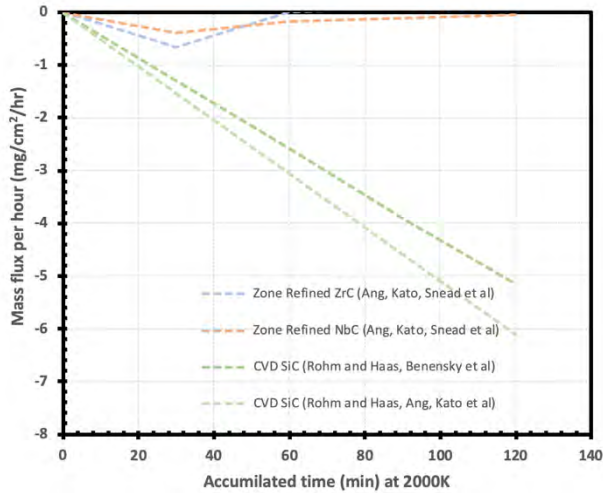


**Fig. 1.** High purity (>99.9%) SiC, ZrC, and NbC materials tested to an accumulated 120 min at 2000K.

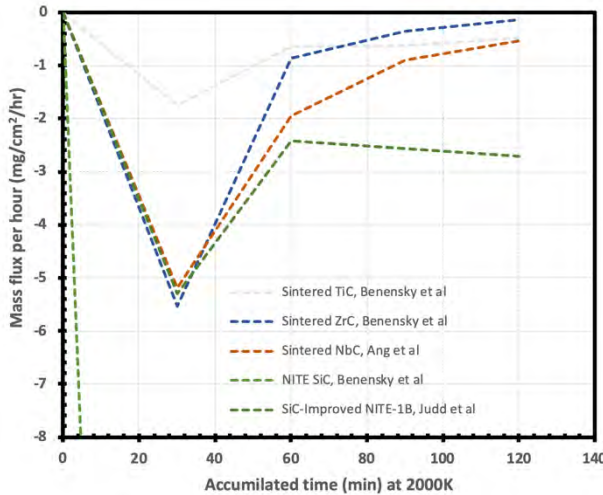
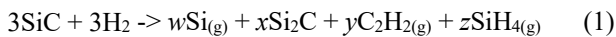


**Fig. 2.** Sintered SiC, TiC, ZrC, and NbC materials tested to an accumulated 120 min at 2000K. Data included from Benensky et al(5).

Fig. 1 shows the mass loss flux of high purity materials. The flux was calculated based on the exposed surface area. This assumes complete hydrogen permeation and mass loss between sample and holder. SiC clearly has a higher mass loss rate compared to NbC and ZrC. This is expected from Benensky et al(5), which shows the thermodynamic stability of Si species represented by (1);



where  $w$ ,  $x$ ,  $y$  and  $z$  are coefficients representative of the equilibrium molar fractions at  $T = 2000\text{K}$ . Irrespective of the values, all the species of containing Si are in gas phase, explaining why the mass flux rate is negative. Fig. 2 shows the mass loss flux of sintered materials. TiC,

NbC and ZrC appear to approach steady-state. The variant NITE-1B SiC has yet to be comprehensively analyzed. All sintered materials show higher initial mass losses. It is theorized this is due to the presence of impurities. Sintered materials begin from a powder process, are handled through several stages where contaminants can be introduced, such as milling media (other hard ceramic rods/balls) and solvents. These impurities may either segregate to the grain boundary, or form solid solutions in the final microstructure.

### I.B. Progress in advanced FCM concepts

Recently, miniature FCM pellets were developed and were qualified by X-ray Computed Tomography (XCT) and traditional metallography. XCT was conducted (ZEISS Xradia 520 Versa, Carl Zeiss X-ray Microscopy Inc., CA, USA) at 150 kV, at a voxel size of 0.002-0.010 mm for scan times from 4 to 6 hours. Imaging was generated using ZEISS ORS Dragonfly Pro. Fig. 3 shows a reconstruction of the capsule-size pellet, showing the distribution of  $\text{ZrO}_2$  kernels in each TRISO particle, which confirms their position in each plane.

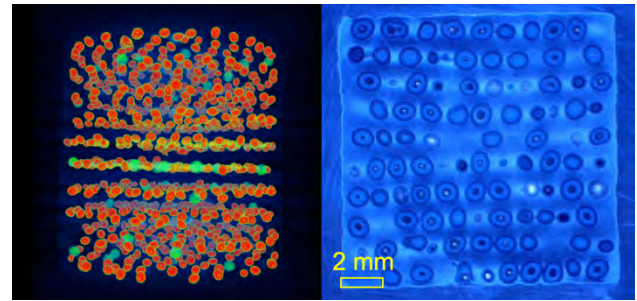


**Fig. 3.** XCT (left) and optical microscopy (right) of the current “zero-rupture” sintering of FCM fuels.

The designed interplanar spacing of TRISO kernels is based on the synthesis technique published by Ang et al using the “zero-rupture” approach.(7) The positions of surrogate fuel kernels are also confirmed by optical microscopy on mechanically cut cross-sections. The current fabrication method uses “green” ceramic powder disks hosting spherical particles. These are stacked to form a preform pellet and sintered under specific conditions designed to control the distribution of particles in-plane and between planes. This technique contrasts the prior “random packing” method where mechanical contact between particles occurred. Presumably, the statistical probability of rupture increased as a function of packing fraction. In the zero-rupture approach, mechanical contact between vertically adjacent particles becomes statistically impossible below a threshold packing fraction.(8, 9) The advent of zero-rupture FCM technology has a limitation due to impeded sintering. The

previous rupture problem was the result of convergence and re-arrangement of random packed particles. It is apparent that constraint caused by the planar arrangement now inhibits densification. Interparticle porosity can be observed by cavities of absent matrix. The optical microscopy shows bands of lighter contrast in each plane due to porous matrix. The matrix densities are typically 85%, but the theoretical value of ~95% is achievable when powder rheology and particle contact is optimized.

### I.C. Development of a Zirconium Carbide inert matrix

The development of a sintered ZrC replacement for the NITE SiC matrix is currently underway. ZrC powders (H.C. Starck, Grade B, AB134580, Lot 26011/18) were sintered to ~1875°C at up to 30 minutes under Pulsed Electric Current sintering mode (LABOX-675 (NJS Co. Ltd, Japan)) under an applied pressure of 10-30 MPa.

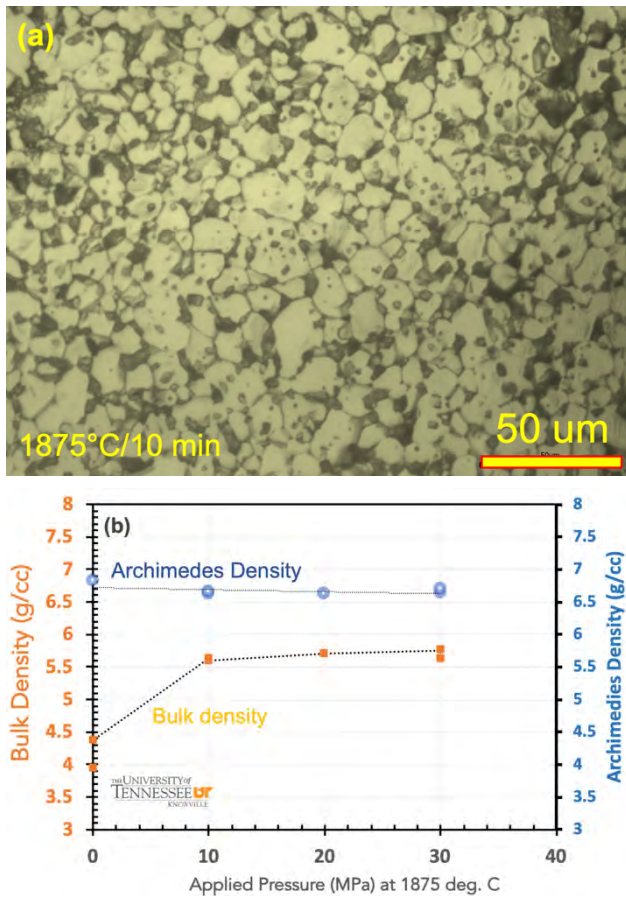


**Fig. 4.** (a) Sintered ZrC at 1875°C for 10 min and densities achieved at (b) increasing applied pressure.

Fig. 4(a) shows the microstructure sintered at 10 MPa and the densities achieved (Fig. 4(b)) as a function of increased pressure. The microstructure shows that ZrC has intergranular pores, with a few inside the grain

boundary, and a grain size ~5-10 μm. In cases where pores are intragranular, this indicates that the surface energy in the system is lower than the grain boundary energy, and thus insufficient energy is available to extend the grain boundary. Pore shapes are convex or flat, indicating shrinkage may not be favored. In general, the microstructure is representative of the final stage (>85% density). This indicates a limited contribution of grain boundary diffusion. Fig. 4(b) also shows that applied pressure does not significantly increase the density. This is surprising from the compiled data of Williams (1964), and Lee and Haggerty (1969), which indicated that the critical resolved shear stress (for 100, 111, 110) at 1825°C is about ~10-15 MPa. It is speculated that Hf contamination (~2%) may be increasing the critical shear stress higher. To improve sintering, powders were washed in concentrated acid to remove surface oxides. Several pores were determined to be residual graphite, which was removed via carbothermal reduction. However, the addition of a chemical reaction can add new consolidation processes where the microstructures are often difficult to control. Furthermore, the reaction must complete, else the oxides (such as ZrO<sub>2</sub>) further degrade the sinterability of the powder. The stability of a chemical system can be determined by the Gibbs free energy equation (2):

$$\Delta G = \Delta H - T\Delta S \quad (2)$$

where the negative value of free energy corresponds to a favorable reaction. Assuming ZrO<sub>2</sub> is the last remaining phase hindering consolidation, the free energy for carbothermal reduction of ZrO<sub>2</sub> in the presence of excess carbon can be written in the form of (3):



The reaction(10) becomes favorable above ~1928K (1655°C). The change in free energy from the reaction can be written in the form (4):

$$\Delta G = -RT \ln (K_{eq}) \quad (4)$$

where  $K_{eq}$  is the equilibrium constant for the reaction,  $T$  is the absolute temperature and  $R$  is the ideal gas constant. For values of  $K_{eq}$  at ~2.3 ((3.99/RT + 2.05)kJ/mol) for  $p(\text{CO}) = 1$  and  $T = 1928\text{K}$  (1655°C), this is 13.4 kJ/mol.(11) This is a significant amount of energy when considering the magnitude of energies in surface area changes during sintering. However, the free energy may not necessarily be able to be used for sintering, since specific diffusion pathways are required. In a preliminary kinetic study, optimized powders were sintered above

1655°C ( $t = 0, 10$  and  $30$  min at  $1750$  and  $1825^\circ\text{C}$ ) to determine the differences associated with the rate of reaction and the rate of densification. Fig. 5 shows the optimized ZrC sintered at  $1750^\circ\text{C}$  for  $10$  min at  $10$  MPa applied pressure.

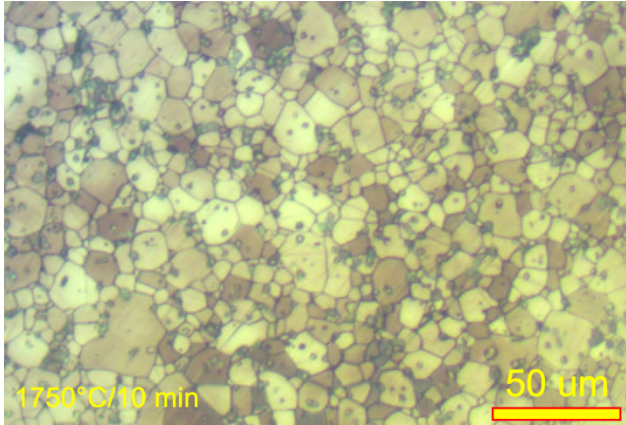


**Fig. 5.** Improved ZrC sintered at  $1750^\circ\text{C}$  for  $10$  min.

Fig. 5. shows a similar microstructure to Fig. 4(a), but at a lower temperature. There are several other distinctions. The pore shapes are relatively concave, which is favorable for shrinkage when the pore is at a grain boundary. The grain size is also larger  $\sim 10$   $\mu\text{m}$ , indicating increased grain boundary migration kinetics or decreased grain boundary energy. This is promising, because new mechanisms to manipulate the final stage of sintering are now available. Therefore, the chemical reaction has assisted in sintering. The density is above  $\sim 90\%$ , the higher coordination number ( $>10-14$ ) indicates sintering has progressed further, and the size of several grains is actually high, indicating inhomogeneous grain growth is occurring (i.e. the migration is now rapid). Further effort is underway to determine the relative rates of chemical reaction and densification, and implement mechanisms to control grain boundary migration and achieve full density.

## II. CONCLUSIONS

Nuclear Thermal Propulsion (NTP) systems may benefit from FCM fuels using TRISO embedded in a ceramic. While the technology of FCM has advanced to ordered arrangements of particles in a ceramic matrix, hot hydrogen at  $>2000$  K appears to demand new matrix materials. ZrC shows improved performance compared to SiC, but requires significant engineering to bring synthesis temperatures and pressures to compatibility with hosting TRISO. A possible pathway to sintering of ZrC appears to be the use of a partial reaction sintering process. Further work is needed to understand the relationship between density and grain growth.

## ACKNOWLEDGMENTS

Michael Koehler, William Scott Emert and John Dunlap (UTK) contributed to the experimental investigations. The authors acknowledge Paolo Venneri, Aaron Selby and Kelsey Souza (USNC-Space) for their contributions to the development of prototypes. The work presented in this paper was funded by Jacobs Technology Inc. Contract No. 80MSFC18C0011 supporting Versatile NTP and conducted on equipment donated by Ultra Safe Nuclear Corporation (Seattle, WA, USA).

## REFERENCES

1. Rohbeck N, Xiao P. Evaluation of the mechanical performance of silicon carbide in TRISO fuel at high temperatures. *Nucl Eng Des.* 2016;306:52-8.
2. Hayashi K, Fukuda K. Release behavior of metallic fission products from pyrocarbon-coated uranium-dioxide particles at extremely high temperatures. *J Nucl Sci Technol.* 1990;27(4):320-32.
3. Omori M, Takei H. Pressureless Sintering of SiC. *J Am Ceram Soc.* 1982;65(6):c92-c.
4. Snead LL, Nozawa T, Katoh Y, Byun T-S, Kondo S, Petti DA. Handbook of SiC properties for fuel performance modeling. *J Nucl Mater.* 2007;371(1-3):329-77.
5. Benensky K, Romnes, C., Eades, M., Venneri, P., Terrani, K., and Zinkle, S. Evaluation of Novel Refractory Carbide Matrix Fuels for Nuclear Thermal Propulsion, 2018 Nuclear and Emerging Technologies for Space. February 26 – March 1. Las Vegas, NV. Presentation and Proceedings. . 2018.
6. Gendre M, Maitre A, Trolliard G. A study of the densification mechanisms during spark plasma sintering of zirconium (oxy-) carbide powders. *Acta Mater.* 2010;58(7):2598-609.
7. Ang C, Snead L, Kato Y. A logical approach for zero-rupture Fully Ceramic Microencapsulated (FCM) fuels via pressure-assisted sintering route. *J Nucl Mater.* 2020:151987.
8. Ang C, Singh G, Snead L, Katoh Y. Preliminary study of sintering zero-rupture Fully Ceramic Microencapsulated (FCM) fuel. *Int J Appl Ceram Technol.* 2019;16:1699– 707.
9. Ang C, Snead L, Benensky K. Niobium carbide as a technology demonstrator of Ultra-High Temperature Ceramics for Fully Ceramic Microencapsulated (FCM) fuels. *International Journal of Ceramic Engineering & Science.* 2019;1:92–102.
10. Turkdogan ET. Physical chemistry of high temperature technology (Gibbs Free Energy Tables). 1980.
11. Samsonov GV, S. UY. NASA TT F-102 Technical Translation - Hard compounds of refractory metals. 1962.

## SIMULATION AND EXPERIMENTAL VALIDATION OF AN INDUCTIVELY HEATED SOLID-CORE NUCLEAR THERMAL ROCKET MODEL

Samantha Cendro<sup>1</sup>, Trey Cranney<sup>1</sup>, Spencer Powers<sup>1</sup>, Connor Powers<sup>1</sup>, Branden Kretschmer<sup>1</sup>, Diego Ochoa-Cota<sup>1</sup>, Micah Pratt<sup>1</sup>

<sup>1</sup>The Advanced Spacecraft Propulsion and Energy Laboratory, University of Southern California, Los Angeles, CA, 90007  
(714) 975-3230; [cendro@usc.edu](mailto:cendro@usc.edu)

*Nuclear thermal propulsion allows for thrust performance akin to liquid bi-propellant rockets along with efficiency close to ion propulsion drives. The objective of the Hyperion-I project is to model nuclear thermal propulsion and experimentally validate the numerical model. A coupled magnetic and computational fluid dynamic model for a single-channel test article was created using ANSYS Maxwell and ANSYS Fluent and subjected to experimental testing conditions. A test stand capable of meeting the testing requirements of a .00025 kg/s mass flow rate at 500 psi for 15 minutes was built. Four Omega K-type thermocouples and four Omega PX309 pressure transducers were utilized pre-regulator, post-regulator, pre-test-article, and post-test-article to acquire pressure and temperature data. The outlet flow temperature of 66.85 °C was validated with an experimental temperature of 66±2 °C. Future testing includes a multi-channel test core and a full-scale core for Phases II and III of the Hyperion-I project, respectively.*

### I. HYPERION-I CAMPAIGN INTRODUCTION

The University of Southern California's Advanced Spacecraft Propulsion and Energy (ASPEN) Laboratory's first project aims to model Nuclear Thermal Rocket Propulsion Engines (NTRE's) with its three-phase Hyperion-I engine campaign.

Liquid bipropellant rocket engines have become a staple across nearly every vehicle architecture due to their time-tested reliability. While they provide some of the highest thrust of any currently employed propulsion system, with the exception of solid boosters, specific impulses of the highest performing engines are capped near 450-460 seconds. Subsequently, required tank sizes and fuel weight severely limit the vehicle size and mission design. For smaller craft, ultra-efficient propulsion systems such as ion thrusters are frequently employed. These thrusters have specific impulses reaching well into the thousands of seconds – an order of magnitude higher than any liquid-propellant engine can achieve. However, this exceptional efficiency is met with an equally steep drop-off in thrust output, hindering the spacecraft's ability to perform corrective maneuvers and greatly increasing mission duration. By utilizing nuclear thermal propulsion, the high thrust of liquid propellant engines is achieved with the high efficiencies of various electric propulsion systems.

While heavy lift launch vehicles will most likely continue to utilize liquid propellant rocket engines in the foreseeable future due to their reliability, upper stages and spacecraft propulsion systems are the perfect applications of NTRE' as their thrust and efficiency performance allows them to compete with conventional chemical engines in terms of payload while offering the lowest total round-trip mission duration in a manned mission to Mars (Ref. 2.).

The overarching system of ASPEN's first engine, Hyperion-I, can be broken down into three main subsystems: the feed system, the reactor model, and the thrust chamber. The feed system utilizes inert nitrogen gas from standard commercial cylinders and regulates it to the flow and pressure requirements of the reactor subsystem, with multiple points of overpressure relief and flow isolation as well as ports for necessary temperature and pressure data acquisition. The reactor subsystem will consist of the metallic fuel element core heated by an off-the-shelf induction furnace as opposed to relying on nuclear fission as the source of heat. This is the same approach that the Nuclear Thermal Rocket Element Environmental Simulator (NTREES) facility at the NASA Marshall Space Flight Center currently takes to simulate fission-based nuclear thermal rocket engines without the risks and regulations inherent to fissile material (Ref. 1). The inductively heated element will be additively manufactured by utilizing USC's Center for Advanced Manufacturing (CAM). The working fluid will flow axially through the channels, heating up and accelerating as it progresses through the core much like the NERVA Program's design (Ref. 3). As Hyperion-I will not have an integrated power generation cycle to make it bimodal, the energized propellant will be directed into an exhaust plenum and then expanded through the nozzle as thrust.

With the Hyperion-I campaign, the ASPEN Laboratory aims to pioneer the coupled hardware and modeling research of NTRE's in a systematic approach consisting of three phases, ultimately testing its full engine design in Phase III (Figure 1).



**Fig. 1.** Core of the proposed Phase III Hyperion-I engine.

### I.A. Phase I Purpose and Goals

Phase I of the Hyperion-I campaign is meant to assess the functionality of the experimental design, including the feed system and inductive heating method. A standard 3/16" outer diameter stainless steel tube will integrate with the test stand instead of the full-scale core. Temperature and pressure data acquisition will still occur in the same locations as they will for the full engine test in order for ANSYS model predictions of  $\Delta T$  and exit temperature for of the test article to be compared to the experimental results. Any off-nominal behavior of the systems can then be remedied for Phases II and III.

## II. ANSYS MODELING

### II.A. Model Setup

The first model created was the electromagnetic model of the single channel test article within the induction coil. The test article solid volume was modeled in Siemens NX, imported into the ANSYS workspace, and subsequently meshed with 200,000 nodes. Then, the eddy current solver within the 3D Maxwell module of ANSYS was used to generate the electromagnetic simulation. After creating a 3D model of the induction coil directly within the Maxwell environment, induction currents were assigned as boundary conditions and an initial frequency through the coil was estimated from a prior heater checkout test. The test article geometry was then imported and then positioned with respect to the coil. Additional skin-depth-based meshing was applied to the test article based on its electrical properties for increased fidelity in heating behaviors, and a region in the shape of a rectangular prism was defined around the test article and coil in which the simulation would solve. Finally, the entire system was solved with plotted outputs of magnetic field vectors throughout the region and ohmic losses within the test article.

The next models created were steady-state and transient thermal models, using the corresponding modules in the ANSYS workspace. The steady state ohmic loss contour from the electromagnetic simulation was mapped to the geometry in the thermal model, and a standard convection coefficient based on ambient conditions and tube material was applied to the surface of the tube to ensure that convection with ambient air surrounding the article was considered. These models simply served to probe the limits of the "dry-heat" behavior, defined as heating the article without any coolant gas flowing through it.

The final model created was a computational fluid dynamics (CFD) model in ANSYS Fluent. Again, the steady state ohmic loss contour from the Maxwell

simulation was mapped to the solid body of the tube as a 3D volumetric heat source, and the working fluid (gaseous nitrogen) was assigned to the fluid volume of the test article. Similar to the approach taken in the thermal models, a standard convection coefficient was applied to the tube body, and the region around the tube was assigned to be standard atmosphere. Using predicted flow velocities and target mass flow rates obtained via internally developed compressible flow and nuclear thermal rocket engine sizing MATLAB scripts, a density-based solver was employed in Fluent; the pressure drop between the test article inlet and outlet was estimated in another MATLAB script using the Darcy-Weisbach method. Beyond these initial conditions and solver settings, default Fluent settings were used. While the primary metric of interest was the propellant outlet temperature profile, the temperature profile of the solid test article body was exported to the Maxwell module in a feedback configuration, enabling an iterative 2-way coupling between the electromagnetic and CFD models. These models were then re-run until both converged. The ANSYS Maxwell model setup is pictured in Figure 2.

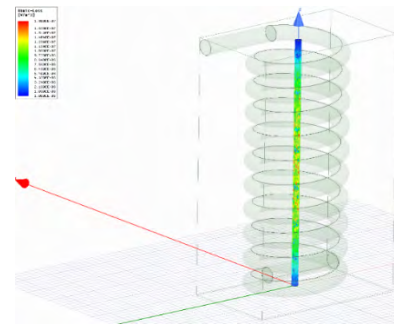


**Fig. 2.** ANSYS Maxwell model setup showing the test article and inductor coil with ohmic loss contour of single channel.

### II.B. Results

The primary result of interest was the average steady-state outlet gas temperature from the single channel article, as this is a value that is directly measured by a thermocouple inserted into the exhaust stream in the test stand setup. With an input gas temperature of 300 K (26.86 °C), the final models converged upon a steady-state average outlet gas temperature of 340 K (66.85 °C).

The next most important result was the maximum tube temperature achieved in the steady-state dry-heat thermal models, as it was imperative that the system remain safe if the coolant flow were somehow stopped while the heater remained operational. The steady-state thermal model showed a maximum dry-heat tube temperature of 400 K (126.85 °C).

### III. EXPERIMENTAL SETUP

#### III.A. Feed System

The feed system for Hyperion-I was designed to meet the requirements of full-scale testing. These requirements include supplying gaseous nitrogen for 15 mins at a flow rate of 0.05 kg/s and pressures of up to 1000 psi at the nozzle inlet. The feed system was also built to acquire temperature, pressure and thrust data to analyze the performance of the tests articles of each phase of the engine campaign. Lastly, the test stand was also built to safely relieve high pressures in order to keep certain components and personnel safe.

For Hyperion-I Phase I testing of the single channel test article, the system was slightly modified to supply the required nitrogen flow rate of 0.00025 kg/s at a pressure of 500 psi. To acquire the desired gaseous flow a Tescom 44-1330 pressure regulator with a flow coefficient ( $C_v$ ) of 0.8 that can supply pressures of up to 1450 psi was used. To ensure that the correct flow rate was achieved, it was also necessary to attach an orifice, sized to choke the flow of nitrogen gas, at the end of the feed system. To size the area of an orifice that would allow this performance Eq. (1) was used for the choked flow of a compressible gas, where  $\dot{m}$  is the mass flow rate,  $C_d$  is the discharge coefficient for a sharpened edge orifice,  $A$  is the orifice inlet area,  $P_0$  is the upstream pressure,  $\rho$  is the density of nitrogen at 500 psi and  $\gamma$  is the specific heat ratio of nitrogen.

$$\dot{m} = C_d A \sqrt{\gamma \rho_0 P_0 \left(\frac{2}{\gamma+1}\right)^{\frac{\gamma+1}{\gamma-1}}} \quad (1)$$

From Eq (1), an orifice with a diameter of 0.0254 cm (0.01 in) was calculated, and an orifice of that size was procured from O'keefe Controls Co. that can withstand pressure up to 4000 psi. Lastly, to ensure that nitrogen would be supplied to the test article for at least 15 minutes, two size 300CF K nitrogen bottles were attached to the feed system.

Before Phase I testing began, a leak and proof test of the feed-system was performed to qualify it for hot flow operation. During the leak test, visual inspection for leaks was performed and the leak rate was recorded at incremental pressure stages of 200 psi, 400 psi, and 600 psi. The leak rate was measured after the stage passed visual inspection. In order for the stage to pass the leak rate requirement, the leak rate had to be below 3 psi per minute. The feed system was proofed at a pressure 1.5 times the Maximum Expected Operating Pressure (MEOP) for Phase I testing ( $1.5 * \text{MEOP} = 750$  psi). The feed system passed the leak and proof test to ensure safe data acquisition during the hot flow.

#### III.B. Data Acquisition

The system that was used for data acquisition was designed specifically for use in the Hyperion-I engine

campaign. This system was created to operate with three primary sensor types.

For temperature measurements, four Omega K-type thermocouples were used. These K-type thermocouples were plunged into the flow of nitrogen at the following locations: before the regulator, after the regulator, before the test article, and after the test article. The voltage signals from these thermocouples were amplified using an AD8495 breakout board. This breakout board provided a 5 V analog output signal with a range of -250°C to +410°C. This range is more than the maximum gas outlet temperature predicted for all Phases of the Hyperion-I campaign.

For pressure measurements, four Omega PX309 pressure transducers were utilized. These pressure transducers have an operational range of 0 psig to 3000 psig: a maximum operational pressure much higher than any pressure that could be present in the feed system. These sensors feature a built in 5 V amplifier circuit which outputs a 0-5 V analog signal. These pressure transducers were placed at the following locations: before the regulator, after the regulator, before the test article, and after the test article

The third type of sensor that the system is built to interface with is an Omega Subminiature Compression Load Cell with a 0 - 10 Newton range that outputs a 0 - 5 V analog signal. This load cell will be used for Hyperion-I Phases II and III in order to gather thrust values of the midscale core and full core, respectively. For Hyperion-I Phase I this sensor was not installed on the test stand as thrust was not a measurement required for model evaluation.

These three sets of sensors integrate into a central data acquisition system. The main data acquisition system primarily consists of a NI USB-6211 inside of a custom chassis. The data acquisition system has a resolution of 16 bits and runs at around 1000 Hz per channel. This system also has the capacity to control feed system solenoid actuation.

### IV. RESULTS & DISCUSSION

During the Hyperion-I Phase I hot flow test, a significant amount of information pertaining to the characterization of the system was obtained. By analyzing the thermocouple and pressure transducer data at different points on the test stand, it was possible to determine both the change in pressure between the inlet and outlet of the single channel as well as the change in temperature of the nitrogen as it passed through the single channel test article.

As mentioned in the experimental setup, the first hot flow test of the system was run at an inlet pressure of 500 psig and an induction heater current level between 306 to 310 Amps. At the start of the test, a visible increase of temperature in the single channel test article was observed. This increase in temperature was determined by the

presence of steam forming on the test article clamps and was verified visually through the use of a thermal camera.

After 15 minutes of continuous heating, it was determined that the temperature and pressure of the system had reached steady-state. During this heating time there was substantial amount of electromagnetic interference from the induction coil that is seen in the pressure and temperature measurements. This led to a notable offset in the values measured during the heating process. The full transient for the pressure of the test can be seen below in Figure 3.

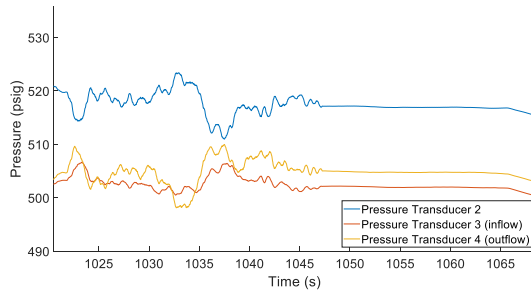


**Fig. 3.** Transient pressure at various stages along the test stand versus time. Pressure Transducers 3 and 4 represent the inlet and outlet of the test article, respectively. Note that Pressure Transducer 1 is not shown as it is the pressure of the nitrogen supply and non-critical to the hot flow test.

The temperature transient of the test was also extremely affected by the noise experienced by the pressure transducers. This led to a noticeable offset during the heating process. A moving average of the temperature values during this high noise transient was taken, and the values were then resampled to further limit noise for better analysis. Despite the large thermocouple offset, a clear asymptotic behavior was observed. The full temperature transient measured can be seen in Figure 4.

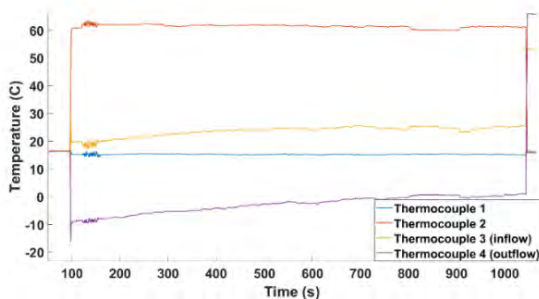


**Fig. 4.** Steady state temperature at various stages along the test stand versus time. Note that the steady state temperature does not contain the offsets seen during heating.

The hot flow test was allowed to run for a total of 15 minutes before the heating of the test article was shut off. Immediately after the heater was shut off the steady state temperature and pressure values were collected. These are the values calculated by the ANSYS model and

therefore hold the most importance for the test. Below in Figure 5 the steady state pressure of the system can be seen.

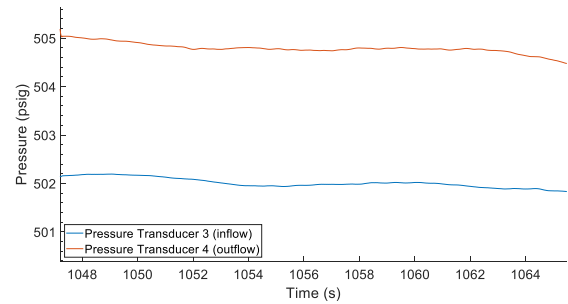


**Fig. 5.** Steady state pressure at the inlet (Pressure Transducer 3) and outlet (Pressure Transducer 2) of the test article. Note Pressure Transducers 1 and 2 were excluded from the figure as they are used primarily for adjusting inlet pressure.

As can be seen in Figure 5 the inlet pressure into the single channel test article was  $502 \pm 1$  psig and the outlet pressure was  $505 \pm 1$  psig, resulting in a  $\Delta P$  equal to  $3 \pm 2$  psig. This slight pressure gain across the test article can likely be attributed to loss of resolution due to non-ideal calibration. This value is best viewed as currently unresolved.

The most important measurement taken at steady state was the temperature of the gas at the inlet and outlet of the single channel test article. In Figure 6 these steady state temperature values can be seen.

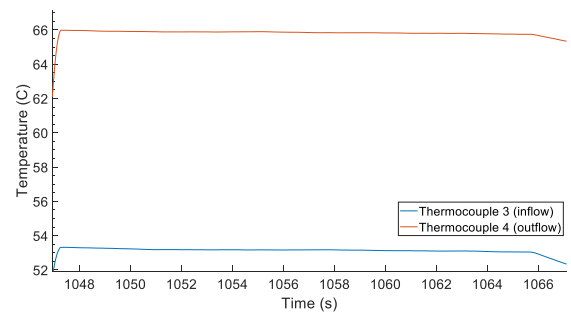


**Fig. 6.** Steady state temperature at the inlet (Thermocouple 3) and outlet (Thermocouple 4) of the test article. Note that temperatures from Thermocouples 1 and 2 were excluded from the figure as they are used to measure gas temperature before and after the pressure regulator.

As can be seen from Figure 6, at steady state the inlet temperature of the gas was measured to be  $53 \pm 2$  °C and the outlet temperature was measured to be  $66 \pm 2$  °C. This means that the  $\Delta T$  value measure was  $13 \pm 4$  °C.

The outlet temperature seen from the hot flow test is equal to the  $66.85$  °C outlet temperature predicted by the ANSYS model of the test article. This shows that the model was setup up properly and has correctly modeled the outlet conditions of the gas flow.

The measured  $\Delta T$  across the single channel test article was not equal to the predicted  $\Delta T$  of 26.86 °C from the ANSYS model. This disparity between the measured  $\Delta T$  and the modeled  $\Delta T$  is most likely caused by equipment design. Due to the shaping of the induction coil there was an unexpected coupling between the fitting for Thermocouple 3, which resulted in heating of the metal component. This heating caused an erroneous temperature measurement in which the thermocouple measured the temperature of the metal instead of the desired temperature of the gas flow. As measured gas inlet temperature of  $53 \pm 2$  °C. Through the use of a thermal camera, it was found that at steady state the fitting in question had a temperature of  $54 \pm 4$  °C. This is a strong indicator that the heating of the metal fitting is what resulted in an erroneous  $\Delta T$  value.

Due to this error, the  $\Delta T$  value from the hot flow test cannot be compared to the  $\Delta T$  value seen in the ANSYS model. This error will be corrected in subsequent testing by re-designing the induction heating coil in a manner that removes heating of the inlet fitting.

## V. CONCLUSION

The initial testing of Hyperion-I Phase I was proven to be a partial success. The hardware design and operation of the induction furnace to heat the single channel article worked nominally and the resulting gas exit temperature matched the ANSYS model predictions.

However, due to an error in equipment design, the value of  $\Delta T$  of the system cannot be compared against the  $\Delta T$  predicted by the ANSYS model. This means that more testing on the Hyperion-I single channel test article must be conducted to find this  $\Delta T$  value.

Despite this small setback, overall Phase I testing is close to completion. It has been shown that the hardware created to accomplish the test campaign generally functions as expected. It has also been shown that the equipment created has the capacity to gather meaningful data about the properties of the gas flow. Through small modification to pre-existing hardware it will soon be possible to finish Phase I testing and move forward with Phase II and Phase III of testing.

### V.A. Hyperion-I Phase II

Phase II of the Hyperion-I campaign is partially underway upon the results of Phase I. No major design changes to the test stand are needed except for the previously accounted for addition of the load cell to measure thrust and  $I_{sp}$ .

The goal of Phase II is to perform a scaled-down version of full core testing with a midscale test article containing 7 channels. The test article was additively manufactured at USC's Center for Advanced Manufacturing out of DMLS MS1 Maraging Steel and post-machined at the on-campus machine shop. End caps

that attach to the core and interface with the feed system have already been designed and manufactured.

Upon testing the article, the exit temperature and  $\Delta T$  parameters shall be compared to the ANSYS predictions, and additional parameters such as thrust and  $I_{sp}$  will be obtained in order to prepare for full core testing in Phase III of the Hyperion-I campaign.

## ACKNOWLEDGMENTS

First and foremost, the ASPEN Laboratory would like to thank its advisors: Dr. Charles Radovich, Dr. Paul Giuliano, and Dr. Matthew Gilpin from the University of Southern California for their continuous guidance throughout the lab's foundation and growth. Their expertise and support have allowed the team to progress the Hyperion-I campaign from concept to physical hardware implementation. Furthermore, without the dedication and hard work of ASPEN's general members, rapid progress and Phase I completion would not have been possible - it truly takes an entire team of passionate people wanting to contribute to the success of Hyperion-I.

The University of Southern California's Viterbi School of Engineering has been a tremendous help to ASPEN with its initial approval of team's foundation and for its continuous financial support of the team's endeavors.

The team would also like to thank Northrup Grumman for their sponsorship of the lab's activities and for being its first corporate sponsor.

## REFERENCES

1. W. J. EMRICH Jr., "Nuclear Thermal Rocket Element Environmental Simulator (NTREES)," NASA – Marshall Space Flight Center, M.S. ER24, Huntsville, Alabama 35812 (2008).
2. R. J. LITCHFORD, "Human Exploration of the Solar System by 2100," Planned and Future Missions, Huntsville, AL USA, 4-6 April 2017, NASA Space Technology Mission Directorate (2017).
3. W.H. ROBBINS and H.B. FINGER, "An Historical Perspective of the NERVA Nuclear Rocket Engine Technology Program," AIAA-91-3451, NASA Contractor Report 187154 (1991).

## GLOSSARY

T	temperature
P	pressure
$C_v$	flow coefficient
$C_d$	discharge coefficient
A	orifice inlet area
$P_o$	upstream pressure
$\rho$	density
$\gamma$	specific heat ratio

## HEAT PIPE DEVELOPMENT FOR SPACE FISSION DEMONSTRATION MISSIONS

Max Chaiken<sup>1</sup>, Marc Gibson<sup>1</sup>, and Jim Sanzi<sup>2</sup>

<sup>1</sup>NASA Glenn Research Center, 21000 Brookpark Road, Cleveland, Ohio, 44030

<sup>2</sup>Vantage Partners, LLC, 3000 Aerospace Parkway, Brook Park, Ohio, 44142

Primary Author Contact Information: 216-433-8177, [max.f.chaiken@nasa.gov](mailto:max.f.chaiken@nasa.gov)

*NASA is currently formulating a flight mission that will demonstrate a 10 kWe nuclear electric fission power system for use on the lunar surface, with extensibility to Mars. While preliminary mission concepts leverage the successful Kilopower Reactor Using Stirling Technology ground prototype demonstration of a 1 kWe reactor, there are significant engineering challenges associated with adapting that prototype reactor for flight. One of these challenges is to modify the high temperature sodium heat pipes for use in space operation. Ongoing technical work at the NASA Glenn Research Center seeks to address several key areas of heat pipe development, focusing on fluid return under reduced or microgravity conditions and improved interfaces for both the reactor and the power conversion ends of the heat pipe.*

### I. INTRODUCTION

Following the successful demonstration of the Kilopower Reactor Using Stirling Technology (KRUSTY) ground prototype reactor in March 2018, NASA has continued formulating a flight mission to demonstrate a nuclear fission capability for use on the lunar surface.<sup>1,2</sup> With a target launch date towards the end of the 2020's, the preliminary mission concept is to land a 10 kW electric power (kWe) fission reactor system near the south pole of the Moon and operate continuously for one year, with additional operation out to ten years for life testing. While detailed design concepts are still a work in progress, with NASA and Department of Energy (DoE) in discussions regarding nuclear core characteristics, the baseline design remains similar to the uranium molybdenum (U-Mo) metal alloy core KRUSTY reactor. An integral part of that design is the high temperature sodium heat pipes that serve as the heat transfer mechanism between the core and the Stirling engine power conversion system. Heat pipes are a passive means of heat transfer based on a two-phase evaporation-condensation cycle, using no moving parts. They are therefore a highly attractive option for long term space missions that rely on robust systems. However, though the KRUSTY test demonstrated the effectiveness of using heat pipes in a reactor system, there remains several key areas of development for this high temperature heat pipe technology before they can be used for flight missions. These areas are divided into four parts: fluid return under

reduced gravity conditions, heat pipe to power conversion interface, heat pipe to reactor core interface, and long-life performance. The Kilopower technical team at GRC has continued to pursue these four heat pipe maturation objectives while the lunar flight mission is being developed.

### II. HEAT PIPE TECHNICAL MATURATION

Over the course of 2019, NASA GRC engineers have performed several tests, supported external work, and developed internal test facilities to foster technical maturation of high temperature heat pipes.

#### II.A. Fluid Return under Reduced Gravity

The basic operation of a heat pipe involves a two-phase fluid cycle between the heat input end (the evaporator) and the heat output end (the condenser) of the heat pipe. As the name implies, the evaporator is where the working fluid is evaporated by the incoming heat from the reactor to produce the vapor pressure that transfers the heated vapor through the pipe. It follows then that the condenser is the point where this heated vapor collects and transfers its heat, returning to liquid form. The issue then lies in how that condensed liquid is returned to the evaporator to complete the cycle. On earth this cycle can be achieved simply through the force of gravity working on the fluid. In microgravity this effect is absent and the heat pipe operation must rely on a secondary force to draw the fluid back to the evaporator. This can be achieved through capillary forces using an internal wick or artery system. Various wick designs exist, mostly using metal meshes or sintered metal powders. Thin capillary tubing can be used to provide the return force and separate the returning liquid from the vapor pressure. Some examples are shown in Figure 1. Wickless heat pipes can also be achieved



**Fig. 1.** Examples of capillary tubing and metal screen artery

by designing grooved geometries in the heat pipe to provide capillary forces on corners.

Work is ongoing to see which wick design works the best for the high temperature sodium heat pipes, with the primary figure of merit being the maximum power throughput of a heat pipe design. Several heat pipe designs are planned to be tested using existing test facilities at GRC. In addition, Figure 2 shows a new vacuum test facility that has been designed with the ability to rotate to provide various angles to simulate the reduced gravity on the moon, Mars or in micro-gravity (running the heat pipe in a horizontal position). Despite the imperfections of this method, it is a reasonable way to determine the effectiveness of each wick design in reduced gravity environments.

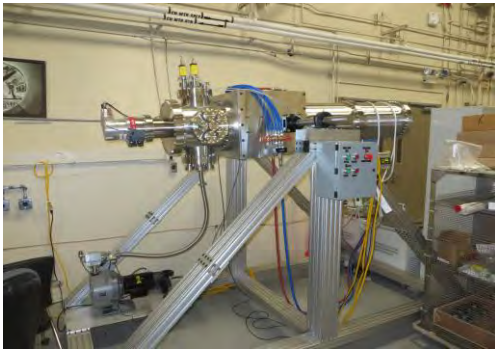


**Fig. 2.** Rotating heat pipe test rig at GRC

## II.B. Heat Pipe to Power Conversion Interface

Just as important as the two-phase cycle in the heat pipe are the interfaces to the heat input and output. Different interface solutions will likely be required based on the power conversion technology. For Stirling engines, there is an elegant solution that is likely to significantly increase the heat transfer efficiency of the heat pipe system. The linear Stirling cycle engine has a fairly compact form factor, with the heat acceptor and rejector being on opposite ends of basically cylindrical pressure vessel. The heat acceptor can therefore be fully integrated into the heat pipe, allowing the hot end of the engine to essentially be the condenser of the heat pipe. Figure 3 shows an example of this construction.



**Fig. 3.** Stirling hot end integrated into heat pipe condenser

The hot vapor will condense right onto the Stirling heat acceptor, reducing the drops in temperature through thermal interfaces to a bare minimum. Sunpower, Inc., the vendor that designed the Advanced Stirling Convertors (ASC) under the Advanced Stirling Radioisotope Generator program, is providing GRC with modified ASCs with direct heat pipe condenser interfaces. A new heat pipe condenser design developed by GRC, shown in Figure 4, was additively manufactured to mate with the ASC hot end.



**Fig. 4.** Additively manufactured heat pipe condenser

An ASC hot end and heat acceptor were connected to the additively manufactured heat pipe condenser at GRC and put through a series of break in tests, shown in Figure 5, to ensure that the heat pipe was operating nominally. Following this the whole assembly was shipped to Sunpower to integrate to the rest of the engine. Once assembled, these modified ASCs will undergo testing at GRC to determine the effectiveness of this interface design. This testing will consist of typical GRC Stirling engine tests, as well as additional testing in the rotating heat pipe test stand to determine the effectiveness of the heat pipe interface.

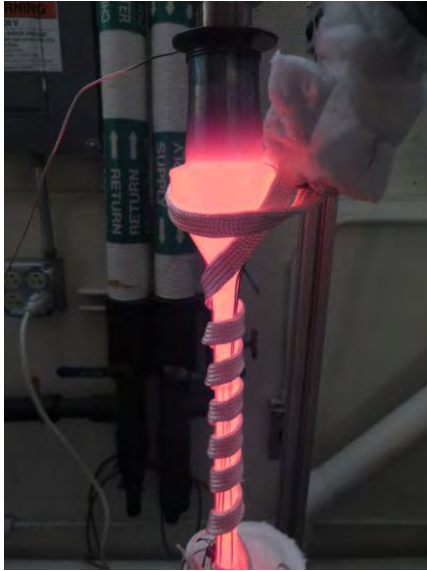


**Fig. 5.** Integrated hot end testing at GRC

### II.C. Heat Pipe to Reactor Core Interface

On the other end of the heat pipe, the evaporate needs to efficiently interface with the reactor core. This ensures both effective heat transfer, as well as robust continuous cooling of the reactor core for safety. For the KRUSTY test, the heat pipes were bonded into machined slots on the periphery of the U-Mo core with a Cu-Mo-Cu foil diffusion barrier between each pipe and the core. This was a simple solution that worked well at the lower thermal power (4 kW thermal for a 1 kWe system) of the demonstration. However, this method will likely not provide enough heat transfer surface for the increase to a 10 kWe lunar surface demonstration. The current proposed method for scaling to 10 kWe is to imbed the heat pipes throughout the reactor core. This provides increased heat transfer area per heat pipe as well as more space to include more heat pipes. Initial 10 kWe reactor designs included up to 24 heat pipes compared to the 8 used in KRUSTY. The challenge with this method is how to create a reliable thermal interface between the heat pipes and the core. Several methods have been proposed. One method is to provide a liquid sodium interface in the space between the pipes and the core. Work was performed at GRC to determine the viability of this option by testing the compatibility of the U-Mo alloy, using a depleted uranium sample shown in Figure 6, with liquid sodium.

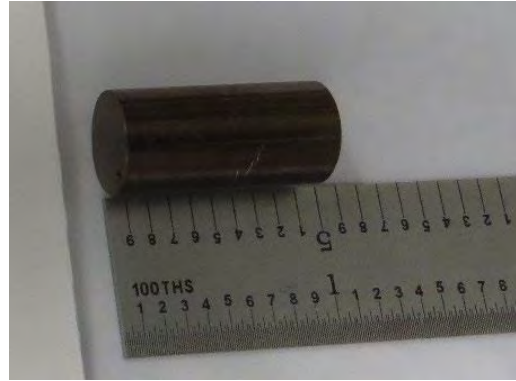


**Fig. 6.** Depleted uranium sample used in sodium compatibility testing

There was no significant mass exchange between the uranium and sodium observed under a scanning electron microscope after 2000 hours of testing at 850°C, supporting the potential viability of this thermal interface method. Another method was explored through an SBIR with the Peregrine Falcon Corporation, focusing on Liquid Interface Diffusion (LID) bonding. This process forms a solid interface between the heat pipes and the core, providing both a thermal and structural bond. Tooling was developed to demonstrate this bonding method between individual heat pipes and a copper surrogate for the uranium core.

### II.D. Longevity Testing

Robustness, reliability, and longevity are key characteristics for space hardware. Long term life testing is planned for the heat pipe designs developed at GRC in order to determine if they are suitable for multi-year missions in a space environment. This life testing will be performed in the rotating vacuum test chambers in order to simulate the mission conditions as closely as possible during the test. With the addition of a modified ASC operating off the heat pipe condenser, this testing will provide an excellent chance to determine the reliability of a complete power conversion string in a space-like environment. Startup transient testing will also take place, including startup at low temperatures to examine the freeze-thaw dynamics of high temperature sodium heat pipes. This testing will be performed using a liquid nitrogen cryojacket that fits into the rotating vacuum rigs.

## III. CONCLUSIONS

The technical team at GRC has continued to pursue technology maturation and hardware development while the next steps towards a space nuclear electric fission demonstration mission are being formulated. Continuing the development of high temperature sodium heat pipes is an important part of preparing for an eventual flight mission. The expertise in heat pipe fabrication and testing developed at GRC through the course of the KRUSTY test program is being put to good use to design the next

generation of heat pipes that may be used in a lunar fission power system. GRC has also relied on the support of several important partners such as Sunpower, Inc. and the Peregrine Falcon Company to ensure that the heat pipe technology not only performs well on its own, but also integrates smoothly into the full reactor system.

#### **ACKNOWLEDGMENTS**

We would like to acknowledge the work of Sunpower, Inc. and the Peregrine Falcon Corporation in exploring the interface designs for the power conversion and core sides of the heat pipes. We would also like to acknowledge Omar Mireles, Omar Rodriguez, and Tom Godfroy from Marshal Space Flight Center for their support in materials testing and additive manufacturing.

#### **REFERENCES**

1. M. A. GIBSON, S. R. OLESON, D. I. POSTON, P. R. McCLURE, "NASA's Kilopower Reactor Development and the Path to Higher Power Missions," *NASA Technical Reports Server* (2017).
2. M. GIBSON, D. POSTON, P. MCCLURE, T. GODFROY, M. BRIGGS, J. SANZI, "The Kilopower Reactor Using Stirling Technology (KRUSTY) Nuclear Ground Test Results and Lessons Learned" *AIAA Propulsion and Energy Forum*, Cincinnati, OH, July 9 - 11, International Energy Conversion Engineering Conference (2018).

## A HEAT EXCHANGER FOR HTGR WASTE HEAT REJECTION TO THE MARTIAN ATMOSPHERE

Nathan Colgan<sup>1</sup>, Gregory Nellis<sup>1</sup>, and Mark Anderson<sup>1</sup>

<sup>1</sup>UW-Madison, 1500 Engineering Dr, Madison, WI, 54706

Primary Author Contact Information: 610-608-0556, [ncolgan@wisc.edu](mailto:ncolgan@wisc.edu)

*A numerical model of a finned tube heat exchanger is developed to examine the feasibility of rejecting waste heat from a supercritical CO<sub>2</sub> (sCO<sub>2</sub>) closed Brayton cycle reactor (HTGR) to the Martian atmosphere convectively. The model is developed using heat transfer and pressure drop correlations for the relevant geometries in the low-Reynolds-number regime associated with the thin Martian atmosphere. The performance is obtained using an effectiveness-NTU method of heat exchanger characterization. The performance of the heat exchanger is compared to a radiator-based system that has been used in a previous optimization study. For the same heat rejection performance, the heat exchanger is 90% less massive; however, the hot side pressure drop is 1.17 kPa, and the required fan power reduces the total thermal efficiency of the system by 0.6%. The heat rejection system is sufficiently compact to fit within a typical rocket fairing and the cold side pressure rise required is attainable in the thin air.*

### Nomenclature

$c$	coefficient
$D_{fan}$	Fan Diameter, m
$D_o$	Tube outer diameter, m
$h$	heat transfer coefficient, W/m <sup>2</sup> K
$k$	Thermal conductivity, W/mK
$n$	Fan speed, rev/s
$Nu$	Nusselt number
$\Delta p_c$	Cold side pressure drop, kPa
$\Delta p_f$	Fin pressure drop, kPa
$\Delta p_{t,row}$	Cold side pressure drop per tube row from tube bank, kPa
$Pr$	Prandtl number
$Q$	Flow rate, m <sup>3</sup> /s
$Re$	Reynolds number
$u_c$	Free-stream cold side velocity, m/s
$u_m$	Maximum cold side velocity, m/s
$\dot{V}$	Volumetric flow rate, m <sup>3</sup> /s
$\delta$	Specific fan diameter
$\sigma$	Specific fan speed
$\rho$	Density, kg/m <sup>3</sup>
$\omega$	Fan rotational frequency, rad/s

### I. INTRODUCTION

A compact and reliable power source is required for future long-term crewed Mars surface missions. Current robotic missions rely on solar power or radioisotope thermal generators (RTGs) to produce power. However, RTGs require significant quantities of Pu<sup>239</sup> and are not affordably scalable to 40 kWe, the power requirement of NASA's reference Mars mission<sup>1</sup>. Solar power requires either constant insolation or some form of energy storage. Solar irradiance also decreases with the square of distance so missions farther from the Sun require more massive arrays, and dust storms on Mars can decrease available solar power by up to 85% for as long as 2 months<sup>1</sup>. Nuclear fission is an attractive power source for these missions as it offers high power density at the required power and does not rely on local insolation. The sCO<sub>2</sub> Brayton cycle used to provide direct gas cooling of a reactor offers high thermal efficiency, power density, and sufficient fuel loading for up to 10 years of power production, as shown by Sondelski<sup>2</sup>. A considerable challenge to using fission power in space applications is waste heat rejection. As even the most efficient Brayton cycles have thermal efficiencies around 40-50%, for a reactor large enough to sustain a prolonged crewed mission, 10's to 100's of kW of heat need to be transferred to the environment to maintain steady operation. In a vacuum, a radiator is the only viable option for this as there is no means to transfer heat convectively. The use of a radiator presents two challenges: heat transfer through radiation is relatively inefficient so a large radiator area is required which leads to a large penalty associated with system mass. Also, radiative heat transfer increases with temperature to the fourth power which leads to a relatively high cycle heat rejection temperature that reduces cycle thermal efficiency. For example, Sondelski<sup>2</sup> performed a mass optimization on a sCO<sub>2</sub> reactor system generating 40 kWe and found that the radiator accounted for the majority of the total system mass, 570 kg out of 782 kg, and pushed the compressor inlet temperature away from the vapor dome. This resulted in a substantial reduction in the fluid density entering the compressor, which is the primary benefit of using supercritical power cycles. As a result, the cycle efficiency was only 27%. The radiator also produced a pressure drop of 90.9 kPa.

A convective heat exchanger could potentially perform much better than a radiator for environments with

suitable conditions. While vacuum environments such as deep space or the lunar surface necessitate radiators, a Mars surface reactor could potentially take advantage of the Martian atmosphere as an ultimate heat sink. The Martian atmosphere is 95% CO<sub>2</sub> with the balance being mostly Nitrogen and Argon, an average surface pressure of 610 Pa and an average surface temperature of -60°C, although peak daytime temperatures can reach 20°C near the equator<sup>3</sup>. To determine if these conditions are suitable as an ultimate heat sink for a sCO<sub>2</sub> Brayton cycle-cooled reactor, a numerical model of a heat exchanger is developed in order to estimate the relationship between mass, pressure drop, conductance, and fan power required of a heat exchanger transferring power cycle waste heat to the Martian atmosphere. As a starting point, the optimum cycle parameters found by Sondelski are used so that a meaningful comparison can be made between a convective heat exchanger and an optimally designed radiator for the same system. A schematic of the recuperated Brayton cycle is shown in Figure 1. A *T-s* diagram of this cycle is shown in Figure 2. Heat rejection occurs between points 6 and 1. A power system optimized using a heat exchanger would likely lead to different optimal cycle parameters that would weigh high outlet temperatures less strongly and therefore, perhaps, provide higher efficiency. The conditions used for this initial comparison are listed in Table 1.

**TABLE I.** Conditions used for initial analysis.

Parameter	Value
Hot Side Inlet Temperature	500 K
Hot Side Outlet Temperature	414 K
Hot Side Mas Flow Rate	1.14 kg/s
Hot Side Pressure	9 MPa
Cold Side Inlet Temperature	218 K
Cold Side Pressure	610 Pa

## II. MODELLING

The initial heat exchanger design considered is a forced convection crossflow finned tube heat exchanger. A fan blows cold Martian air, modelled as pure CO<sub>2</sub>, at Martian atmospheric pressure across a bank of fins and tubes containing the reactor coolant. The tubes are staggered, with a pitch to diameter ratio of 2 and are made of 316 stainless steel with a wall thickness that is sized in order to contain 1.5 times the primary loop pressure. A diagram of a finned tube heat exchanger is shown in Figure 3. The fins are made of copper and are 0.1 mm thick. All hot side fluid properties are evaluated at the median hot side temperature and all cold side fluid properties are evaluated at the median cold side temperature.

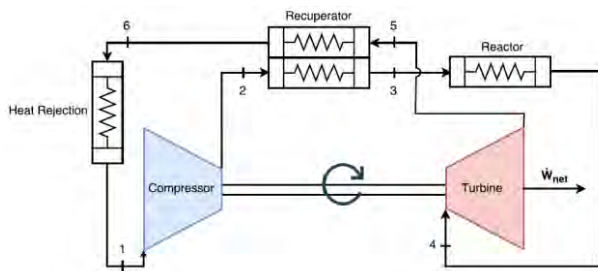


**Fig. 1.** Schematic of a recuperated Brayton Cycle

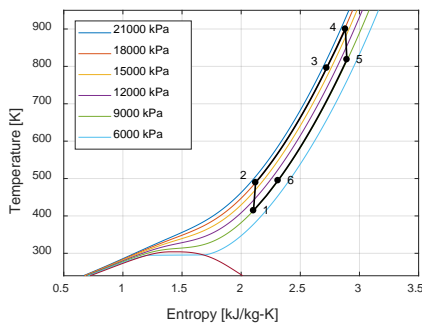


**Fig. 2.** T-S diagram of the optimal cycle found by Sondelski<sup>2</sup>

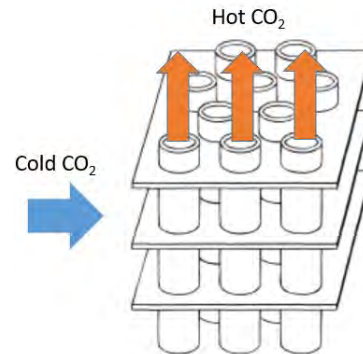


**Fig. 3.** Diagram of finned tube heat exchanger

The hot side pressure loss and heat transfer coefficient are determined using the non-dimensional pipe flow correlations proposed by Li, Seem, and Li<sup>4</sup> for friction factor and by Gnielinski<sup>5</sup> for the Nusselt number. The header loss has not yet been incorporated into the model. The low pressure side gas is very low density so the flow is laminar in all relevant conditions, with Reynolds numbers typically below 100. No correlations for flow through a fin and tube heat exchanger were found in the literature for these conditions. The heat transfer considering the tube bank and the fins are determined separately and then area-averaged to obtain the average heat transfer coefficient of the heat exchanger. For Reynolds numbers below 300, the Nusselt number for the tube bank-alone is given by the following relation from ESDU<sup>7</sup>.

$$\overline{Nu} = 1.309 Re_d^{.36} Pr^{.34} \left( \frac{Pr_w}{Pr} \right)^{.26} k_1 \quad (1)$$

where  $k_1$  is a correction term for tube banks with few tube rows. The Reynolds number is defined as

$$Re_d = \frac{\rho u_m D_o}{\mu} \quad (2)$$

and the Nusselt number is

$$Nu = \frac{h D_o}{k} \quad (3)$$

The fin-alone heat transfer coefficient is found using the rectangular duct correlation of Kakac et al.<sup>7</sup> The total pressure rise is found by adding the pressure rise associated with the tube bundle-alone and from the fins also considered alone, as first proposed by Rich<sup>8</sup>, i.e.

$$\Delta p_c = \Delta p_f + \Delta p_t \quad (4)$$

The tube bundle pressure rise is found using the *Heat Exchanger Design Handbook* (1983) (Ref. 9) correlation for Euler number

$$Eu = k_2 \sum_{i=0}^4 \frac{c_i}{Re_d^i} \quad (5)$$

where  $k_2$  is a correction term for tube banks with few tube rows and the Euler number is defined as

$$Eu = \frac{\Delta p_{t,row}}{.5 \rho u_m^2} \quad (6)$$

Values for the constants  $c_i$  for a staggered bank of pitch to diameter ratio 2 and Reynolds number less than 100 are given in Table 2.

**TABLE II.** Constants for Eq. (5).

Constant	Value
$c_0$	.713
$c_1$	44.8
$c_2$	-126
$c_3$	-582
$c_4$	0

The fin pressure loss is also calculated using the Kakac et al. correlation, corrected using the form provided by Shah and London<sup>10</sup> for the developing region.

To validate this superposition approach for determining overall heat transfer coefficient and pressure rise, the resulting average heat transfer coefficient and total pressure rise were compared to those found using the compact heat exchanger correlation given by Kays and London<sup>11</sup>, which is only valid for Reynolds numbers (based on hydraulic diameter) above 300; as a result, the

comparison can only be performed at Reynolds numbers that are much higher than those expected for the heat exchanger. The ratio between the heat transfer coefficient and pressure drop values obtained using the existing correlations to those obtained using the superposition approach are shown in Figure 4. The predictions are within about 30% across the range of hydraulic diameter Reynolds numbers. In general, the superposition approach appears to overpredict pressure drop and heat transfer coefficient at low Reynolds numbers. Figure 5 shows that the pressure rises associated with the fins and with the tubes are of similar magnitude at low Reynolds number.

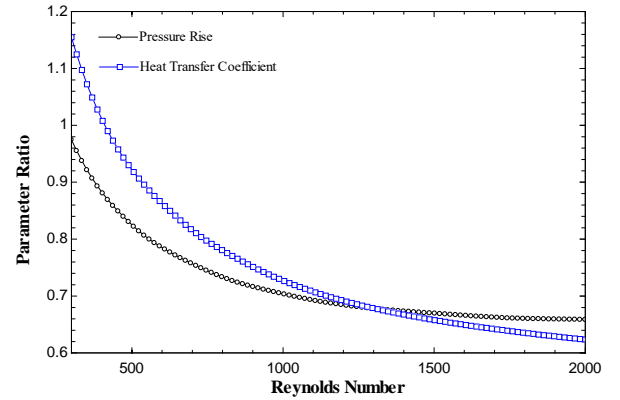


**Fig. 4.** Comparison of heat transfer coefficient and pressure rise using the proposed method

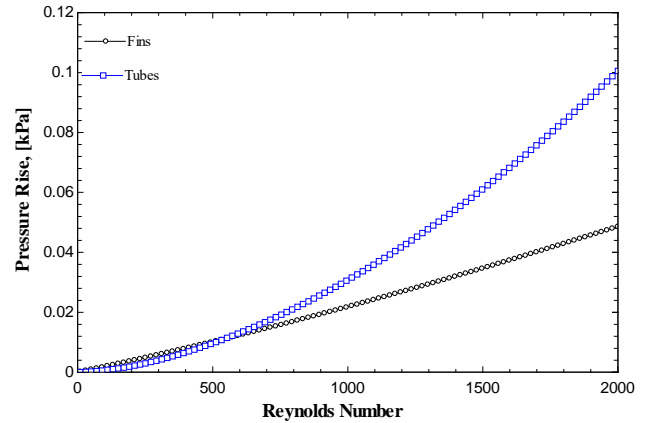


**Fig. 5.** Pressure rise associated with the fins and tubes as functions of Reynolds number. The ratio of fin to tube surface area is approximately 12 to 1 for the geometry used in this comparison.

To determine the effectiveness of the heat exchanger, the effectiveness-NTU method is used. The conductance is found by calculating the total resistance from the hot fluid to the tubes, through the walls of the tubes, and from the tubes and fins to the cold fluid. Initially, there is assumed to be no contact resistance between tubes and fins and no fouling resistance, although the presence of

dust may increase fouling resistance and reduce heat transfer. The fin efficiency is found by approximating each tube as having an annular fin with an outer radius such that the total area of the fictitious fins equals the true fin area, as shown in Nellis and Klein<sup>12</sup>. This technique sets the required heat transfer coefficient of the heat exchanger in order to satisfy the prescribed inlet and outlet conditions. From this value, the required airflow velocity is determined using the above correlations. The airflow velocity then determines the pressure drop. These equations are all solved simultaneously using an equation solver.

The power required to drive the air through the heat exchanger and the mass of the associated fans must also be estimated. The fan efficiency is calculated using the method described in Eppel et al.<sup>13</sup> for low speed axial fans based on an analytical derivation using the Cordier diagrams. The efficiency is given as

$$\eta = 1 - \frac{1}{4\delta^2} \left( \frac{4}{\delta^2} + \frac{1}{\sigma^2} \right) \quad (7)$$

where  $\delta$ , the specific diameter, is

$$\delta = \frac{D_{fan} \left( \frac{\Delta p}{\rho} \right)^{.25}}{\left( \frac{8}{\pi^2} \right)^{.25} Q^{.5}} \quad (8)$$

and  $\sigma$ , the specific speed, is

$$\sigma = \frac{(2\pi^2)^{.25} n Q^{.5}}{\left( \frac{\Delta p}{\rho} \right)^{.75}} \quad (9)$$

For this study, the fan diameter is assumed to be equal to the height of the heat exchanger and the system is modelled with only a single fan, but in practice it may be more efficient to have a number of smaller fans driving the airflow. No studies of fan efficiency found in the literature were found at Mars-like conditions so it is difficult to say with certainty that the fan efficiency and pressure rise calculated in this study are attainable; however, the efficiency, flow coefficient, head coefficient, and chord Reynolds number are all within the ranges listed in the *ESDU A Guide to Fan Selection and Performance*<sup>14</sup> for rotor-stator or contra-rotating fans, where the flow coefficient is

$$\phi = \frac{1}{\sigma\delta^3} \quad (10)$$

And the head coefficient is

$$\psi = \frac{1}{2\sigma^2\delta^2} \quad (11)$$

To estimate the mass of the fans, a rotor-stator fan is used. The blades of the rotor and the stator are assumed to be constructed of 1 mm Aluminum sheet and have a solidity factor of 1, and the motors are estimated to mass 5.75 kg/kW, based on commercially available motors of similar power. From the efficiency, the power is calculated as

$$P_{fan} = \frac{\Delta p_c u_c A_{fr}}{\eta_{fan}} \quad (12)$$

### III. RESULTS

The model is initially run using the input parameters listed in Table 1 to provide a comparison to the radiator system used by Sondelski<sup>2</sup>. The geometric parameters, the number of rows and columns of tubes, their lengths and diameters, and the fin pitch, will eventually be varied to minimize the heat exchanger mass, fan power draw, and hot side pressure drop. However, the set of baseline values summarized in Table 3 are used to test the model. The resulting heat exchanger parameters are shown in Table 4. This heat exchanger mass is 11.8% of the radiator mass, the power required to run the fan results in a 0.6% reduction in cycle efficiency, and the hot side pressure drop is negligible. It also is compact enough to fit within a typical rocket fairing and the cold side pressure rise is attainable in the thin Martian atmosphere.

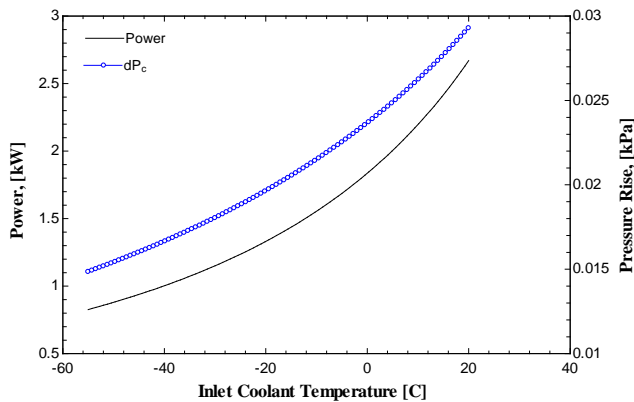
**TABLE III.** Baseline parameters

Parameter	Value
Number of rows	400
Number of columns	4
Length	2 m
Tube OD	3 mm
Fin pitch	5.5 mm
Fan Speed	66 rad/s

As shown in Figure 6, while the fan power and pressure rise are sensitive to inlet temperature, they are not unreasonably high even at the highest daytime Martian air temperatures.

**TABLE IV.** Results with baseline parameters

Parameter	Value
Mass	67.32 kg
Required Fan power	813 W
Height	2.4 m
Depth	2.4 cm
Hot side pressure drop	1.17 kPa
Cold Side pressure drop	0.015 kPa
Cold Side outlet temperature	195.6 °C
Cold side velocity	9.60 m/s
Fan efficiency	0.84
Flow Coefficient	0.1285
Head Coefficient	0.2519
Cold Side Heat Transfer Coefficient	21.99 W/m <sup>2</sup> K

**Fig. 6.** Fan power and pressure rise vs inlet air temperature

#### IV. CONCLUSION AND FUTURE WORK

Overall, the heat exchanger performs much better than a radiator for rejecting waste heat to the Martian environment. It is much less massive and causes less pressure drop in the primary loop than the radiator. Also, the power required to force the gas associated with the Martian environment through the device does not greatly reduce the cycle efficiency. The near term next steps in the project involve optimizing the heat exchanger geometry to minimize system mass and integrating the model with the existing system optimization model developed by Sondelski et al. to see how the different heat rejection system changes the optimal cycle. Long term steps could include CFD modelling of the airflow through the heat exchanger and experimental validation of the low-Reynolds-number heat transfer and pressure drop correlations in a simulated Martian environment. Correlations derived from the experimental data could then be used to refine the model.

#### REFERENCES

1. NASA-SP-2009-566, Human Exploration of Mars Design Reference Architecture (DRA) 5.0, National Aeronautics and Space Administration, Washington, D.C. (2009).
2. B. SONDELSKI, Mass Optimization of a Supercritical CO<sub>2</sub> Brayton Cycle with a Direct Cooled Nuclear Reactor for Space Surface Power. Master's Thesis, University of Wisconsin, Madison, (2019)
3. R.M. HABERLE, "Solar System/Sun, Atmospheres, Evolution of Atmospheres | Planetary Atmospheres: Mars", Encyclopedia of Atmospheric Sciences, 2015
4. P. LI, J.E. SEEM, and Y. LI, "A New Explicit Equation for Accurate Friction Factor Calculation of Smooth Tubes", International Journal of Refrigeration (2011)
5. V. GNIELINSKI, Int. Chem. Eng., Vol. 16, p. 359, (1976)
6. Engineering Sciences Data Unit, Convective Heat Transfer During Crossflow of Fluids Over Plain Tube Banks, ESDU Data Item No. 7303J, London, November (1973)
7. S. KAKAÇ, R.K. SHAH, and W. AUNG, "Handbook of Single-Phase Convective Heat Transfer", Wiley-Interscience, 1987.
8. D.G. RICH, "The Effect Of Fin Spacing On The Heat Transfer And Friction Performance Of Multirow, Smooth Plate Fin Tube Heat Exchanger", ASHRAE Trans., 79, 137-145. (1973)
9. *Heat Exchanger Design Handbook* (1983) Vol. 1, Hemisphere, New York, (1983)
10. R.K SHAH and A.L. LONDON, "Laminar Flow Forced Convection in Ducts", Academic Press, 1978
11. W.M KAYS and A.L. LONDON, *Compact heat exchangers*, 3rd ed., McGraw Hill, New York, 1984.
12. G.F. NELLIS and S.A. KLEIN, *Heat Transfer*, Cambridge University Press, (2009)
13. P.H. EPPLE, F. DURST, and A. DELGADO, *A Theoretical Derivation of the Cordier Diagram for Turbomachines*, Proc. IMechE Vol. 225, (2010)
14. ESDU. A guide to fan selection and performance. Data Item 79037. London, GB: Engineering Sciences Data Unit, Apr. 1980.

## INTERFACE AND SUBSURFACE CERAMIC BEHAVIOR IN MOLYBDENUM CERMETS FOR NUCLEAR THERMAL PROPULSION

Taylor G. Duffin<sup>1</sup>, Kelsa M. Benensky<sup>2</sup>, and Steven J. Zinkle<sup>1</sup>

<sup>1</sup>Department of Nuclear Engineering, University of Tennessee, Knoxville, TN, 37996

<sup>2</sup>Advanced Projects Group, Analytical Mechanics Associates Inc., Denver, CO, 80211

Primary Author Contact Information: [tduffin2@vols.utk.edu](mailto:tduffin2@vols.utk.edu)

*Nuclear thermal propulsion has both high thrust and high specific impulse and is a leading technology for a crewed Mars mission. Molybdenum cermets are an alternative to tungsten cermets that can reduce core mass and add ductility. The Mo matrix appears robust in a Mo-YSZ cermet after testing in hydrogen at 2500 K with thermal cycling. The subsurface Mo-YSZ interface also appears strong despite indications of debonding at the surface. Striations that appear parallel on the surface in the YSZ fuel surrogate extend below the surface.*

### I. INTRODUCTION

Nuclear thermal propulsion is an in-space propulsion technology capable of both high thrust (110 kN-1100kN) and high specific impulse (850-900 s).<sup>1</sup> This efficiency is roughly double that of the best chemical rockets. This efficiency boost is particularly impactful for crewed missions beyond low-earth orbit (LEO) and NTP is a leading propulsion technology for a crewed mission to Mars.<sup>2</sup> NTP benefits include reduced travel times, additional abort capability and fewer heavy launch vehicles to enable the mission.<sup>3</sup> The fuel in the nuclear reactor core needs to withstand temperatures above 2500 K in hot hydrogen and thermal cycling. Ceramic-metallic fuels (cermets) can meet these requirements using a ceramic nuclear fuel (UO<sub>2</sub> or UN) in a refractory metal matrix. While tungsten (W) is the traditional metal studied for NTP cermet designs due to its high melting temperature, molybdenum (Mo) cermets have additional benefits including lower mass, more ductility and do not need to be enriched to enable a low-enriched uranium (LEU) core design.<sup>4</sup>

### II. EXPERIMENTAL

Mo-cermets were produced using a powder blending method originally designed for W-cermets.<sup>5</sup> Yttria-stabilized zirconia (YSZ) particles are used as a surrogate for UO<sub>2</sub> fuel. Small 5-7 $\mu$ m Mo powder was mixed with 212-250  $\mu$ m diameter YSZ spheres along with a polyethylene binder. These were consolidated in a spark plasma sintering furnace at 1400°C for 5 min. Mo-YSZ cermets with 40, 50, 60 and 70 vol% ceramic loadings were produced. Sample preparation included grinding with SiC papers to remove the Mo-carbide reaction layer and polishing to a 1  $\mu$ m finish. The sample preparation is more thoroughly detailed in other work.<sup>6,7</sup>

Sample testing used the Compact Fuel Element Environmental Test (CFEET) facility at NASA Marshall Space Flight Center. The hydrogen flow rate for all tests was 500 standard cubic centimeters per minute with the chamber pressure at 1 atm. Samples were heated to test temperatures of 2000, 2250 and 2500 K and held at temperature for a total of 80 min either at steady-state or with four thermal cycles. The thermally cycled samples were held at temperature for 20 min and then cooled to room temperature between cycles (~480 K/min peak cooling rate) with a total test temperature after four thermal cycles of 80 min. Mass loss data and surface observations of these samples have been reported elsewhere.<sup>6,8,9</sup>

### III. ANALYSIS

Analysis of the Mo matrix has shown a predominantly unchanged microstructure following the hot hydrogen testing.<sup>9</sup> The Mo grain boundaries on the surface became more prominent, however no matrix cracking or significant erosion has been observed for any test condition. This demonstrates the robust material behavior of the Mo matrix and supports further study of Mo cermets with UO<sub>2</sub> or UN for NTP.

Following high temperature testing in hydrogen, the YSZ grains experienced grain boundary erosion as well which can be seen in Figures 1 and 2. Many grains of the YSZ also exhibited a distinct striation behavior, as demonstrated in Figure 1. These laminations are predominantly parallel within a single grain and change direction in neighboring grains as viewed from the surface. The striations are visible under optical microscopy after even a single 20 min thermal cycle as shown in Figure 2. Some striations change direction near edges in a single grain. Striations are also visible in a scanning electron microscope (SEM) for both backscattered electron images (BSE) and secondary electron images (SE) in some regions. These striations did not appear in the 2000 K tests but did appear in both the 2250 and 2500 K tests. The 2000 K tests did not have a well-polished surface which many have obscured the effect. Alternatively, the striation mechanism may be temperature dependent with a threshold between 2000-2250 K. These striations may be caused by buckling due to uneven thermal expansion in the long crystal direction of the YSZ tetragonal structure.

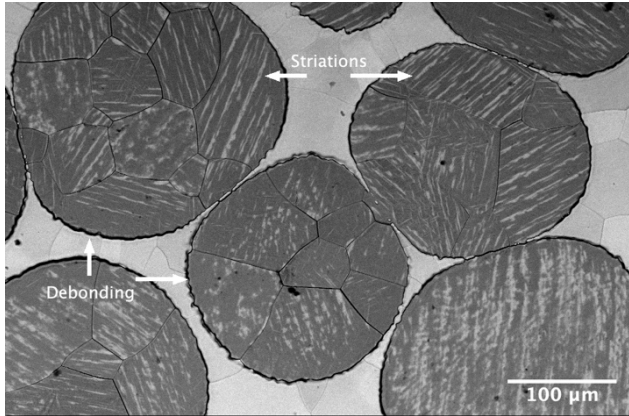


**Fig. 1.** BSE image of Mo-YSZ cermet showing apparent debonding and laminated features in YSZ particles developed after four thermal cycles at 2500 K.

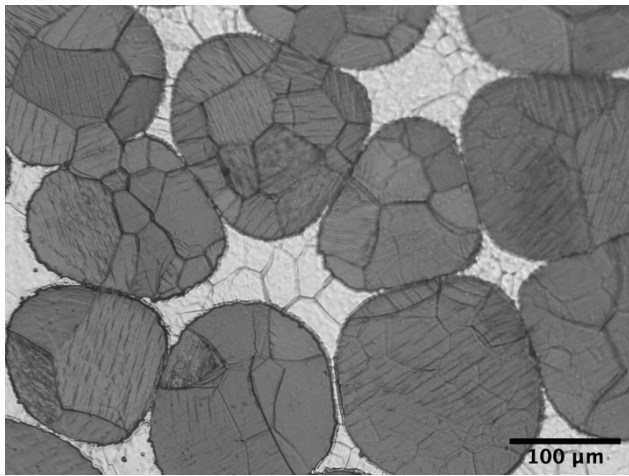


**Fig. 2.** Optical image of Mo-YSZ cermet showing striations on the surface of the YSZ after a single thermal cycle of 20 min at 2500 K.

At the surface, many YSZ particles have shown some apparent debonding from the Mo matrix as shown in Figure 1. The YSZ is often at a slightly lower vertical height than the Mo matrix following high temperature testing, whereas prior to testing they are polished to the same level and is likely caused by the large difference in the thermal expansion coefficients for Mo and YSZ. This behavior motivates exploring the Mo-YSZ interface below the surface.

A Zeiss Auriga Focused Ion Beam (FIB) was used to create a thin slice of the Mo-cermet thermally cycled four times at 2500 K. The dimensions of this lift-out section before additional thinning were approximately 15x10x2 μm. A SEM image is displayed in Figure 3 taken during the thinning process. This sample was taken from a region with apparent debonding at the surface; significantly, the lift-out section shows that the debonding does not continue along the interface and is exclusively a near surface effect. The sample showed structural integrity through this extraction process demonstrating that the

sintered bond at the interface remained strong even after thermal cycling and exposure to hydrogen. This is significant as the sample was taken from the hydrogen exposed surface of the material and not an interior position. This slice was then thinned with the FIB to a thickness of ~100 nm which was then imaged with a Zeiss Libra200 transmission electron microscope (TEM). Figure 4 shows a TEM image along the interface between the Mo and YSZ. The TEM analysis along the full length of the interface region does not show evidence of cracking or secondary phase formation anywhere along the boundary.

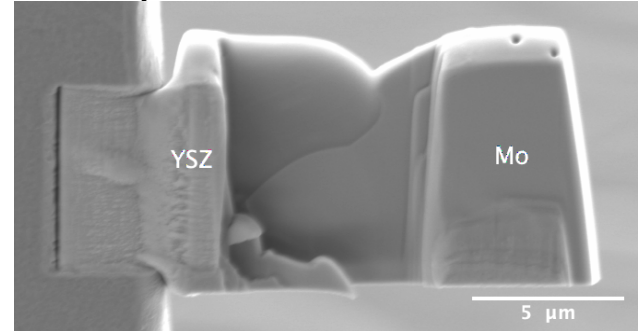


**Fig. 3.** SE image of Mo-YSZ cermet tested with thermal cycling at 2500 K in hydrogen. This slice is cut with a focused ion beam.

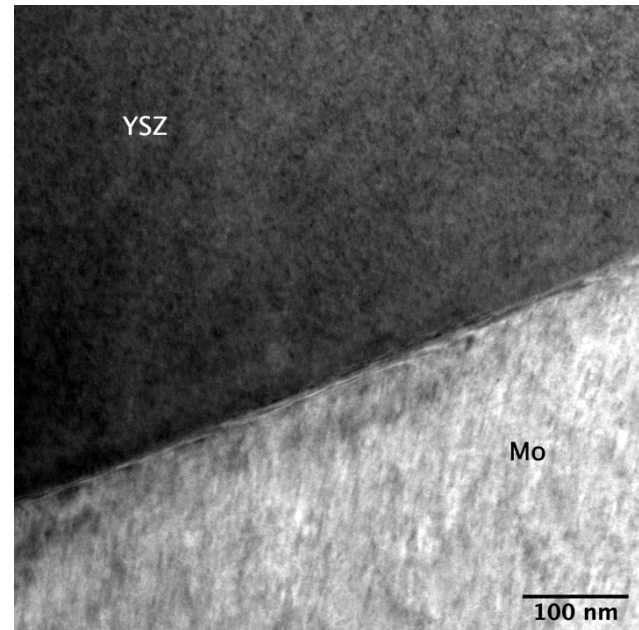


**Fig. 4.** Mo-ZrO<sub>2</sub> cermet interface as observed by the TEM in bright field mode.

A second sample was prepared from the same material and images collected from the FIB are displayed in Figures 5 and 6. Some striations are visible in the YSZ in the SE image in Figure 5. Even more intricate patterns are shown using the in-lens SE detector shown in Figure 6. The image in Figure 6 was taken after the sample had been thinned considerably, to an appropriate thickness for

TEM i.e. ~100-150 nm. The contrast shown in the Mo section of this figure is due to only the central section being thinned to this thickness, whereas the darker vertical band region is thicker. Figure 7 shows the YSZ portion of this sample under TEM. These patterns in the YSZ may be the subsurface examples of the striations along the ceramic surface. However, it is notable they are not parallel below the surface.

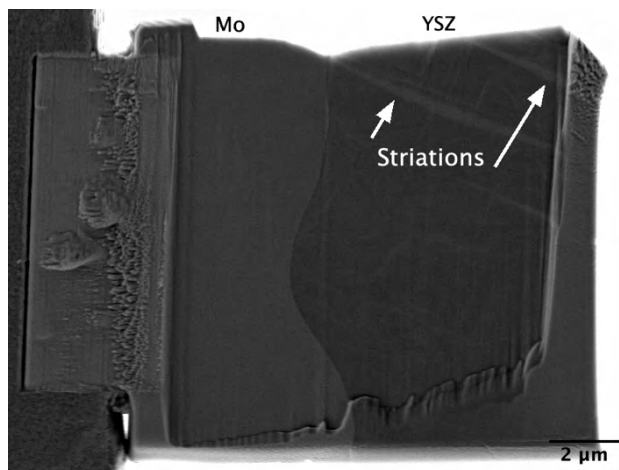


**Fig. 5.** SE image of Mo-YSZ cermet cut with a FIB. Some striations visible in the subsurface zirconia.

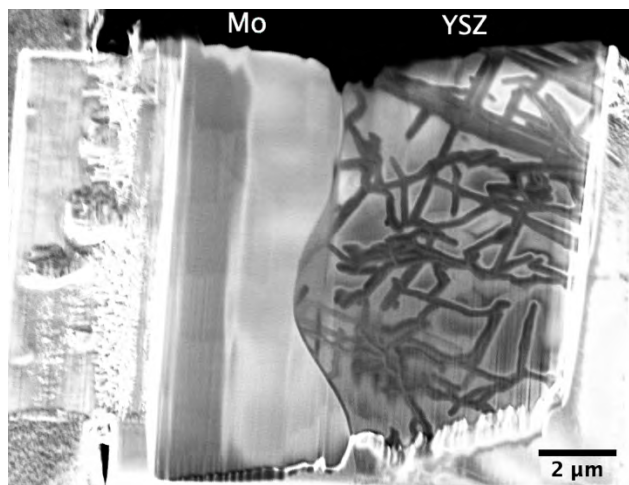


**Fig. 6.** SE image viewed with the in-lens detector to show more contrast of Mo-YSZ cermet. This is a subsurface example of the previously seen striations on the surface.

An alternative explanation for the intricate subsurface behavior is the optical observation of discolored spots on the YSZ surface as shown in Figure 8. These spots have brown and gray discoloration under optical microscopy. This spot-type behavior appears white in the BSE image in Figure 9, just like the parallel striations. There is some evidence from surface Raman spectroscopy that the spots may be due to reduction of the YSZ during the hydrogen exposure.

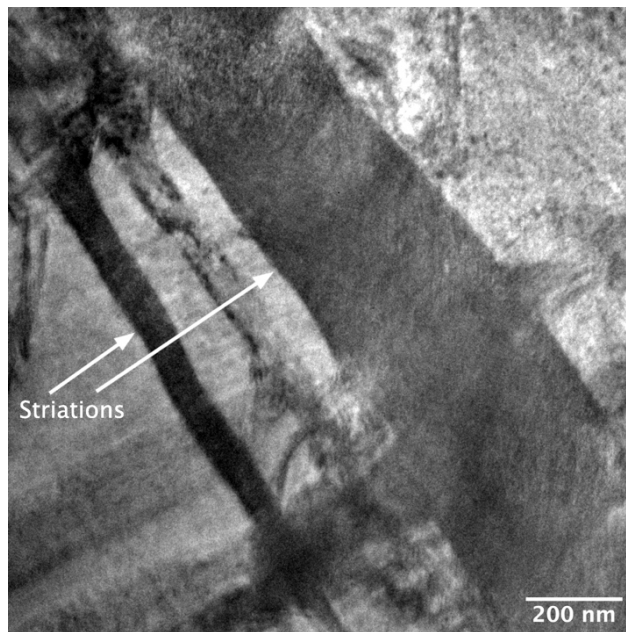


**Fig. 7.** Bright field TEM image of YSZ section highlighting the subsurface striations.

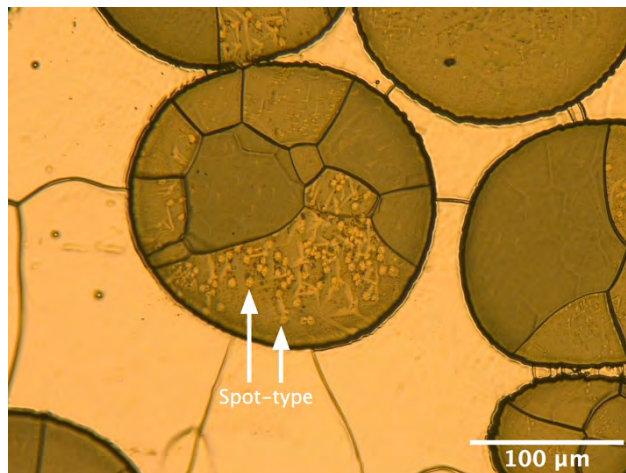


**Fig. 8.** Optical image of Mo-YSZ cermet that shows the spot-type behavior in the YSZ. Tested with four thermal cycles at 2500 K.

Pomfret et. al. performed Raman spectroscopy on YSZ samples exposed to a 5% H<sub>2</sub> atmosphere at 1000° C in 6 hr cycles.<sup>10</sup> They observed reduced Raman intensity by 50% based on hydrogen pickup in a reversible process. However they did not observe a shift in Raman peaks, which they interpreted as “no change in the chemical composition of the bulk crystal structure.”<sup>10</sup> They also synthesized YSZ with varying yttria concentrations between 8-15% and observed that as yttria content increases that the Raman signal shifts to lower frequencies; “the characteristic Raman peak associated with the cubic-phase phonon structure shifts from 617 to 598 cm<sup>-1</sup>.”<sup>10</sup>

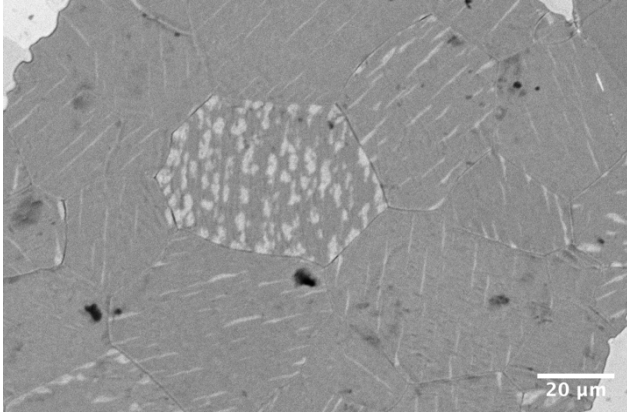


**Fig. 9.** BSE image of Mo-YSZ cermet that shows both spot-type behavior in the central grain and striation-type behavior in the surrounding grains. Sample tested at steady-state at 2250 K.

A Raman spectrometer was used to observe both the spot-type areas and striation-type regions of the Mo-YSZ cermets. The striations did not show a substantial difference from the spectra of the surrounding area. This could be due to their small size as compared to the laser spot size of  $\sim 2\mu\text{m}$ , or to minimal chemical and structural differences. However, the observation of the spot-type areas as shown in Figure 10 showed both a significant reduction in Raman intensity as well as peak broadening and shifts. The intensity reduction could be caused by a variety of factors, such as surface roughness, or could indicate reduction of the  $\text{ZrO}_2$ . The cubic-phase phonon peak from Pomfret ( $617\text{ cm}^{-1}$ ) appears as  $645\text{ cm}^{-1}$  for the dark tetragonal regions of these samples. It is notable that this peak is down shifted to  $\sim 590\text{ cm}^{-1}$  in the light-spot regions shown in Figure 10. This may indicate a loss of  $\text{ZrO}_2$  relative to  $\text{Y}_2\text{O}_3$  in the spot regions. However, not all of the spectra collected from spot regions show the peak shift away from  $645\text{ cm}^{-1}$ . Other spectra maintain this peak while shifting those near  $500\text{ cm}^{-1}$  as shown in Figure 11. This effect is not purely due to laser wavelength as most spot regions show the shifts from Figure 10 using both 532 and 473 nm wavelengths.

While some evidence of reduction is observed in the YSZ fuel surrogate, the rate of reduction must be relatively slow at these test temperatures as there has been no evidence of melted Zr or Y metal. It is expected that the reduction of the YSZ would be highly mitigated with a Mo overcoat preventing direct exposure of the ceramic to the hydrogen as is proposed for a NTP fuel system.

#### IV. CONCLUSIONS

In summary, this study investigated the microstructure of Mo-YSZ cermets after hot hydrogen thermal cycling at 2000 – 2500 K. The Mo matrix is robust with no matrix cracking or significant erosion observed. The ceramic surrogate (YSZ) exhibited striation

and spot-type behavior visible after a single thermal cycle at high temperatures ( $> 2000\text{ K}$ ). There is some evidence from reduced Raman intensity and a shift in several peaks that the spot-type behavior may be linked to reduction of the ceramic by the  $\text{H}_2$ . Below the surface these behaviors are forming intricate patterns. FIB lift outs and thinning were successfully performed along the Mo-YSZ interface which appears well bonded in the TEM with no cracking or secondary phase formation. These results are encouraging for the use of Mo cermets for nuclear thermal propulsion and support additional testing with  $\text{UO}_2/\text{UN}$  fuel.

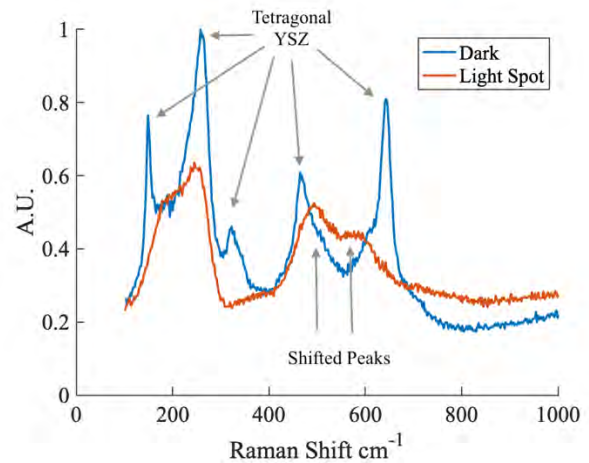


**Fig 10.** Blue: Spectra of typical dark region, very good match to expected tetragonal YSZ. Red: Light-colored spot region. Peaks shifting towards 500 and  $590\text{ cm}^{-1}$  may indicate increased yttria content relative to zirconia content. Reduction in intensity may be indicative of hydrogen pickup. Taken with a 532 nm laser.

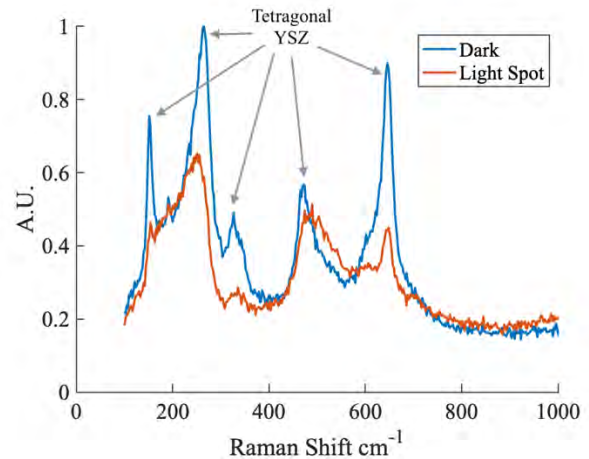


**Fig 11.** Blue: Spectra of typical dark region, matching expected tetragonal YSZ. Red: Light-colored spot region. Reduction of intensity still present, but all peaks are present and remain unshifted. Taken with a 473 nm laser.

## ACKNOWLEDGMENTS

This work was performed under a contract with Oak Ridge National Lab for the NASA Nuclear Thermal Propulsion Project. SEM, FIB and TEM were performed at the Joint Institute for Advanced Materials (JIAM) at the University of Tennessee, Knoxville.

## REFERENCES

1. S. K. BOROWSKI, D. MCCURDY, and T. PACKARD, "Nuclear Thermal Propulsion (NTP): A Proven, Growth Technology for 'Fast Transit' Human Missions to Mars," in AIAA SPACE 2013 Conference and Exposition, p. 5354 (2013).
2. B. G. DRAKE, "Human Exploration of Mars Design Reference Architecture 5.0," NASA/SP-2009-566, National Aeronautics and Space Administration (2009).
3. C. R. JOYNER et al., "Enabling Multiple Abort Strategies Using the NTP Approach for Human Mars Missions," 12 September 2017, American Institute of Aeronautics and Astronautics; <https://doi.org/10.2514/6.2017-5273>.
4. W. DEASON, M. EADES, and V. PATEL, "Use of Molybdenum Cermet to Decrease Mass and Increase Thermal Performance of Nuclear Thermal Rockets," in 2018 Nuclear and Emerging Technologies for Space, Las Vegas, NV (2018).
5. D. S. TUCKER et al., "High density, uniformly distributed W/UO<sub>2</sub> for use in Nuclear Thermal Propulsion," *Journal of Nuclear Materials* **486**, 246 (2017); <https://doi.org/10.1016/j.jnucmat.2017.01.033>.
6. T. G. DUFFIN et al., "Production and Hot Hydrogen Testing of Subscale Molybdenum Cermets for Nuclear Thermal Propulsion," in 2018 Joint Propulsion Conference, American Institute of Aeronautics and Astronautics, Cincinnati, Ohio (2018); <https://doi.org/10.2514/6.2018-4672>.
7. J. ZILLINGER et al., "INVESTIGATION OF PRODUCTION PARAMETER EFFECTS ON SPARK PLASMA SINTERED MOLYBDENUM CERMET WAFERS FOR NUCLEAR THERMAL PROPULSION APPLICATIONS," 2019 Nuclear and Emerging Technologies for Space (2019).
8. T. G. DUFFIN et al., "Hot Hydrogen Testing and Microstructural Characterization of Molybdenum Cermets for Nuclear Thermal Propulsion," Nuclear and Emerging Technologies for Space Conference 2019 (2019).
9. T. G. DUFFIN, S. J. ZINKLE, and K. M. BENENSKY, "Material Characterization of Subscale Molybdenum Cermets for Nuclear Thermal Propulsion," in 2019 Joint Propulsion Conference, American Institute of Aeronautics and Astronautics, Indianapolis, IN (2019).
10. M. B. POMFRET et al., "Structural and Compositional Characterization of Ytria-Stabilized Zirconia:

Evidence of Surface-Stabilized, Low-Valence Metal Species," *Analytical Chemistry* **77** 6, 1791 (2005); <https://doi.org/10.1021/ac048600u>.

## **PRE-IRRADIATION CHARACTERIZATION OF INSTRUMENT PERFORMANCE FOR NUCLEAR THERMAL ROCKETS: TEST PLAN**

Dan C. Floyd<sup>1</sup>, N. Dianne Bull Ezell<sup>2</sup>, and Richard Wood<sup>1</sup>

<sup>1</sup>University of Tennessee, Knoxville, TN, 37996-1410

<sup>2</sup>Oak Ridge National Laboratory, Oak Ridge, TN, 37831

Primary Author Contact Information: [dfloyd7@vols.utk.edu](mailto:dfloyd7@vols.utk.edu)

*The development of nuclear rocket technology can provide several benefits over current chemical rockets. However, these benefits are accompanied by several issues associated with the environment. Temperature extremes and the presence of radiation causes complications in instrument selection. Additionally, maintenance activities are not possible during the operation of the rocket. Because of this, detailing the effects of radiation on instruments can improve the system. To this end, there is a future plan for the irradiation of a set of instruments. However, the instruments require performance characterization before radiation exposure. A simple flow path can be implemented to determine the performance of various instruments. This report discusses the representative instrumentation along with the development and design of a simple flow path. Concerning the instrumentation: details regarding their manufacturer and datasheet information initial performance characteristics. Necessary information concerning the flow loop along with ambient conditions will also be provided.*

### **I. INTRODUCTION**

Nuclear thermal rockets (NTRs) produce harsh environments that can degrade sensor performance. Instruments implemented within these environments are exposed to various levels of irradiation that degrade the performance of the instrument. Due to the safety constraints that are placed on NTRs, the performance of specific sensors and transducers is incredibly important for continued operation. Before changes in sensor performance due to radiation can be characterized, the standard performance of the instrument must be fully investigated. For this purpose, a simple gaseous flow path is developed to test various instruments.

As current NTR efforts are in the definition and preliminary design phase, characterizing the performance of representative instruments will aid in developmental efforts. The current state of NTR efforts causes the specific requirements of the system to be uncertain. However, instrumentation requirements may be similar to those in previous NTR developmental efforts. Specifically, those made during Project Rover and the Nuclear Engine for Rocket Vehicle Application

(NERVA) program. These investigations are informative on sensor selection and the important measurements for the system.

Historical NTR investigations culminated in the testing of a flight-style engine test known as the Experimental Engine or XE-Prime. During these tests, the temperature of the exit gas and the chamber pressure were implemented in control of the NTR. Because of this, these measurements are extremely important for the operation of the rocket. Temperature is also important due to its role in measuring various coolant temperatures throughout the rocket<sup>1</sup>. Another critical measurement is the flow rate of the reactor's coolant. As the coolant in NTRs also provides the rocket's thrust, ensuring there has been no degradation in flow is incredibly important. Another measurement of interest is the vibrational forces impacting various components.

Representative instruments are taken from instruments that have been implemented for aerospace applications. Instruments implementing similar measurement technologies that were applied in previous NTR tests also prove to be useful. One temperature measurement technology that was previously implemented were resistance temperature detectors (RTD). These devices were applied for low temperature hydrogen coolant measurements and could measure temperatures up approximately 100°C (Ref. 1). This allows for a platinum RTD to function as a representative sensor for these measurements.

The representative instruments for other measurements are determined using similar information. During Project Rover, bonded strain gauge pressure transducers were investigated for measuring nozzle chamber pressure. This allows for bonded strain gauge instruments implemented for aerospace applications to function effectively. Similar statements concerning historical application are made concerning tri-axial piezoelectric accelerometers for vibration measurements. Flow measurements during XE-Prime were acquired using venturi tubes in a limited number of locations. These measurements could be expanded upon using current technological developments such as digital meters that can measure flow, pressure, and temperature of the fluid of interest.

## II. Representative Sensors

The representative instruments monitoring temperature, pressure, flow, and vibration were selected for characterization. A collaborator provided these instruments and similar models have been used during previous space missions. In comparison to the instruments implemented within the XE-Prime, the representative instruments have a relatively limited operational temperature range. Additionally, the majority of the instrumentation has smaller measurement ranges than the historical counterpart. This can best be seen in the measurement range of the temperature sensors.

The representative temperature sensors are RTDs with measurement ranges of  $-18^{\circ}\text{C}$  to  $93^{\circ}\text{C}$ . While the upper range is relatively similar to XE-Prime instruments, the lower range is much higher than cryogenic hydrogen. Even though cryogenic temperatures are not within the measurement range, these instruments were previously investigated for application in liquid rockets. As such, the RTDs are prime candidates for investigation. The provided sensors are bridge in head RTDs designed to meet the requirements for rocket testing. These requirements include high accuracy, reliability, and safety. These requirements lead to the instruments having an accuracy of  $\pm 0.25\%$  full-scale<sup>2</sup>. Additional information regarding the sensor is known but may no longer be accurate due to aging. Sensor testing will allow for verification of the sensor's performance and any changes from the known data.

Another significant instrument is those that monitor pressure. The provided pressure sensors all implement bonded strain gauge technology. This technology measured various pressures during previous NTR tests such as the XE-Prime<sup>1</sup>. The specific instruments under investigation have been implemented in previous rocket engine tests. The measurement range of each instrument differs greatly with the ranges of the instruments covering: 0 psig to 100 psig, 0 psia to 200 psia, 0 psig to 5000 psig, and 0 psig to 6000 psig. Additionally, some of the performance characteristics are similar across the units. Like the previously mentioned temperature sensors, some of these instruments are approaching ages of 3 decades.

For flow measurements, a multi-parameter digital mass flow meter is used as the representative instrument. As the measurement of flow was not a concern during historical NTR tests, the usage of a multi-parameter instrument may be beneficial. The implemented instrument measures the volumetric mass flow of a gaseous medium. As it is a multi-parameter instrument, the temperature and the pressure of the process can also be measured. The measurement range of this particular instrument is 0 liters per minute to 30 liters per minute (LPM). The instrument available for test has been

calibrated within the last few years and may still be within calibration.

The final set of representative instruments are 2 piezoelectric, triaxial accelerometers. Similar instruments were previously implemented for vibration measurements during the XE-Prime tests. The current sensors have a measurement range of  $\pm 500\text{gpk}$ . These accelerometers are capable of operating within a temperature range of  $-54^{\circ}\text{C}$  to  $121^{\circ}\text{C}$ . These ranges are similar to instruments implemented within the XE-Prime, though the operational temperature range is more limited.

## III. Sensor Test Plan

The majority of the instruments can be tested using a simple flow path. The pressure and flowmeter instruments can be easily tested while under flow conditions. This is accomplished through the use of several different components that allow for flowrate and pressure variability. Both the accelerometers and the temperature sensors can be tested using different apparatuses.

Due to the purpose of characterizing instrument performance, calibrated instruments are required for the verification of the instruments. As the calibration curves for the test instruments are not known, the calibrated instruments can provide the necessary information about the process. By verifying the output of the instruments, a new curve can be developed for each of the instruments. However, the disadvantage of this is the available accuracy of the instruments. The calibrated instruments have measurement accuracies that are generally within 1% full span. Because of this, the accuracy of the older instruments may be larger than desired.

The flow path is constructed of 304 stainless steel tubing. The gaseous media available for use in the flow path is compressed air at 90 psi. A simple illustration of the test stand is available in Figure 1.

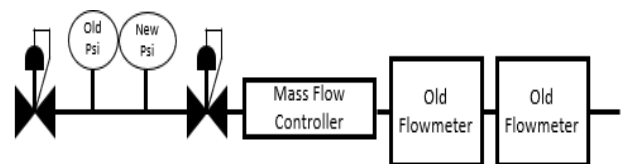


**Figure 1:** Simple illustration of the instrument test stand.

Beyond the basic tubing material and the pressure supply, several components are required to test the instruments. The first component past the source is a pressure regulator. This component allows for the pressure within the tube to be varied over a desired input range. The next two components of the flow path are the pressure sensors. Another pressure regulator is installed

after the pressure sensors to further control the pressure that is provided to the mass flow controller. This component can then vary the flow through the tubing to test the flow meter performance.

The expected pressure output from the pressure regulators ranges from 5 psi to 90 psi. In comparison to the range of the pressure sensors, the available range for testing is considerably limited. This limitation is more apparent concerning the sensors that are capable of measuring up to 5000 psi and 6000 psi. The available pressure supply prevents the performance of the upper range of the pressure sensors being investigated. However, characterizing these instruments over the available range can provide necessary information concerning their performance. The characterization of performance in this range will allow for performance changes due to irradiation to be investigated.

Additional testing concerning the pressure sensors is related to the response time of the instruments. Currently, there are several different methods to conduct response time testing of pressure sensors. One method uses a pressure ramp input. The pressure supplied to sensor is increased at a steady rate. The output of the tested sensor is then compared to a reference sensor's output. With a high-speed reference sensor, the reference sensor's output is a close approximation of the actual pressure ramp. By comparing the response of the reference and test sensor, the resultant lag between the two is the response time<sup>3,4</sup>. However, this method requires a high-speed reference sensor that the current instrument may not qualify as.

The response time of the sensor can also be investigated using noise analysis tests. While effective, the noise analysis technique requires a large amount of operational data. This technique functions by analyzing the noise on the DC output of the sensor. The noise is then isolated from the DC signal to allow for both frequency and time domain analysis<sup>3</sup>. Either of these techniques would be appropriate for the determination of response time testing. The selection of these techniques will be dependent on the available information from the flow path.

The included mass flow controller will allow for a variable flow for testing of the flowmeters. This device will allow for air flow covering the range of 1 LPM to 40 LPM. This covers the full range of the instruments available for testing in addition to providing information regarding the performance slightly beyond the instrument's range. Characterization of the instrument's full measurement range will allow for future tests to indicate any changes over this entire range. In addition to this, the measurement of the flowmeter's response time may be important. As the flowmeter under test is digital, the response of the instrument may be affected by irradiation. The determination of the flowmeter's

response time may be found using the ramp input method. This is similar to the method described for the pressure sensors where a flow ramp is used to determine response time. This measurement will be dependent on the changes in the flow caused by the mass flow controller.

The temperature sensors are tested using either a heater or a furnace. As the known range of the temperature sensor is limited to a maximum 93°C, the entire temperature range is easily covered. However, testing the sensors within the flow path requires additional components. With the chosen pipe diameter of ¼" temperature sensors cannot be fully immersed within the flow. The implementation of a hollow container attached to the flow path will allow for the sensor to be fully immersed in the flow. An electrical heater is then applied to increase the temperature of the air within the container. A simple schematic of this test setup is demonstrated in Figure 2. Conducting tests using a furnace and the container will provide information concerning the sensors standard performance and any effects that occur from flow.

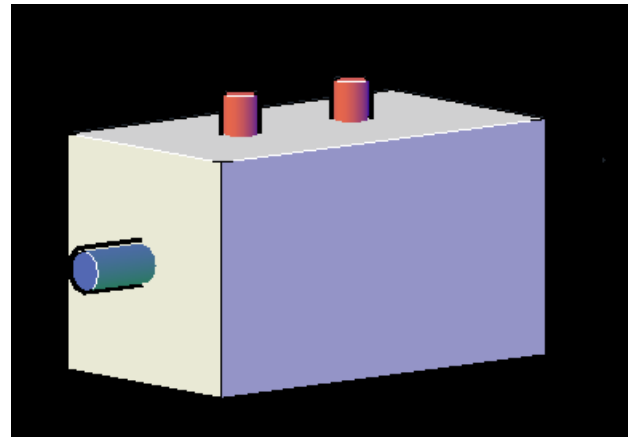


**Figure 2:** Heater flow test schematic with red cylinders indicating the RTDs and the blue indicating flow. (Not to scale)

The accelerometers are tested using a shaker table to determine performance characteristics. These platforms provide an input force that have frequency ranges between 2Hz to 7kHz. Each accelerometer is tested over the available input range of the available shaker table. Furthermore, testing the instruments at different frequencies improves the information regarding the sensor's current performance.

#### IV. CONCLUSIONS

This report describes the test plan for the characterization of instruments prior to irradiation. The inability to conduct maintenance during NTR flight requires performance changes due to irradiation to be characterized. This will improve knowledge concerning sensor irradiation and add in the selection of sensor

technology for NTR systems. Comparing the performance of the sensors pre and post irradiation allows for a quantification of the effects. This then allows for the development of algorithms or construction techniques that can account for these affects.

Future work for this project is related to collecting the information regarding sensor performance. With the characterization of performance before irradiation completed, the instruments are then irradiated in a test reactor. These tests will also include a simple hydrogen flow loop to investigate possible activation effects. Further tests will implement sensor technologies that can withstand high temperatures with hydrogen flow. This investigation can then be leveraged for the benefit of NTR instrument system design.

#### REFERENCES

1. XE-Prime Engine Final Report Vol.1 Engine and Facilities Description, Aerojet General RN-S-0510, (1969).
2. Chandon, H. C. *Temperature measurement systems*. No. TID/SNA-1410. Aerojet Liquid Rocket Co., Sacramento, Calif.(USA), 1964.
3. Hashemian, H. M., et al. *Long term performance and aging characteristics of nuclear plant pressure transmitters*. No. NUREG/CR--5851. Nuclear Regulatory Commission, 1993.
4. Hashemian, H. M. *Effect of Aging on Response Time of Nuclear Plant Pressure Sensors. Analysis and Measurement Services Corporation*. NUREG/CR-5383.

## IRRADIATION TESTING OF MOLYBDENUM AND TUNGSTEN BASED CERMETS FOR USE IN NUCLEAR THERMAL PROPULSION

Neal Gaffin<sup>1</sup>, Kelsa Benensky<sup>2</sup>, and Steven Zinkle<sup>1</sup>

<sup>1</sup>University of Tennessee, 1412 Circle Dr., Knoxville, TN, 37996

<sup>2</sup>Advanced Projects Group, Analytical Mechanics Associates Inc., Denver, CO, 80211

Primary Author Contact Information: (702) 734-3355 and [ngaffin@vols.utk.edu](mailto:ngaffin@vols.utk.edu)

*Nuclear thermal propulsion (NTP) is a leading candidate for crewed space propulsion missions to Mars due to its capability for high in-space thrust and specific impulse. While NTP was tested extensively during the nuclear engine for rocket vehicle application (NERVA)/Rover program (1955 – 1972), the manufacture and test infrastructure of historic NTP programs has been lost. The development of a robust fuel form capable of enduring the demanding operating conditions of modern NTP engine designs is necessary to enable successful NTP implementation. One aspect of fuel performance that must be understood is behavior under irradiation. In this study, irradiation behavior of ceramic metallic (cermet) fuels was investigated. Ion irradiation was used as a surrogate to neutron irradiation for preliminary experiments to characterize the irradiation hardening and embrittlement in molybdenum (Mo) and tungsten (W) based cermet surrogates. Samples were irradiated at both room temperature and 1075 K to doses between 0.001 and 0.008 dpa. Hardness was measured using nanoindentation and found that in conditions relevant to NTP, Mo and W based cermets could experience 20 and 30% increase in hardening, respectively.*

### I. INTRODUCTION

Nuclear thermal propulsion (NTP) is a leading in-space propulsion candidate for crewed interplanetary missions, including missions to Mars.<sup>1,2</sup> NTP has a high specific impulse (Isp), 875 – 950+ s, at comparable thrust ( $10^1$  –  $10^2$  klbf) levels to in-space liquid engines. Moreover, the combination of high thrust and Isp allows for large mission abort windows, increases cargo capacity, and decreases total launch mass. Mission times would also be shortened for missions beyond low earth orbit (LEO), thereby greatly decreasing astronauts' exposure to cosmic radiation, microgravity, and prolonged confinement. NTP is a tested and proven technology with 20+ full-scale NTP systems designed, built, and tested with high levels of success during the nuclear engine for rocket vehicle application (NERVA)/Rover program (1955 – 1972).<sup>1</sup>

#### I.A. NTP Operating Conditions

NTP generates heat via fission. Cryogenic hydrogen ( $H_2$ ) is then pumped into the reactor, heated, and expanded out a nozzle to generate thrust. NTP fuel materials will

need to endure an incredibly harsh environment, including exposure to radiation, contact with hot flowing  $H_2$ , temperatures as high as 3000 K, and large thermal gradients. Several full-scale reactors tested during the NERVA/Rover Program utilizing HEU graphite-matrix fuels experienced some mass loss of the fuel element.<sup>3</sup> Before any NTP system can be designed and built, the fuel element needs to be tested to ensure survivability.

#### I.B. Cermet Fuels for NTP

Ceramic-metallic (cermet) materials have been proposed as a promising fuel for future NTP systems.<sup>1</sup> Cermets consist of ceramic fuel particles, namely uranium dioxide ( $UO_2$ ) or uranium nitride (UN), suspended in a refractory metal matrix. Cermets have good potential as the NTP fuel element due to their fission product retention, resistance to thermal shock, hydrogen compatibility, corrosion resistance, high thermal conductivity, and high strength.<sup>4,5</sup> Molybdenum (Mo) and tungsten (W) are the two leading refractory metal candidates due to their high melting points, good heat transfer properties, hydrogen compatibility, and availability.<sup>6,7</sup>

The mechanical properties of cermets are primarily dependent upon the structural refractory metal matrix. Zirconia ( $ZrO_2$ ) was selected as a surrogate for  $UO_2$  to facilitate experimentation. The manufacturing of these cermets has been optimized through the process of spark plasma sintering (SPS) and have been tested at high temperatures with hot flowing hydrogen.<sup>6,8</sup> However, the effects of irradiation on cermets has not been studied extensively. The results discussed in this summary are the preliminary investigation into the effect of the NTP radiation environment on the mechanical properties of a cermet-based fuel core.

#### I.C. Irradiation Hardening and Embrittlement

In an NTP system, materials will experience gamma and neutron irradiation, as well as transmutation, fission product generation and attenuation, nuclear decay, and other irradiation degradation mechanisms. Radiation affects material properties differently based on the dose, type of irradiation, and temperature. In crystalline materials, dose is approximated using displacements per atom (dpa), which represents the number of instances each atom of a material is knocked out of its crystal lattice to a

new lattice sight.<sup>9</sup> Due to the irradiation conditions associated with NTP, irradiation hardening and embrittlement will likely be the primary irradiation degradation mechanisms for a cermet NTP fuel core.<sup>10</sup>

Irradiation hardening and embrittlement occurs below around 0.3 the absolute melting temperature ( $T_M$ ), and at doses starting as low as  $1 \times 10^{-6}$  dpa.<sup>11,12</sup> Irradiation hardening produces an increase in the strength and hardness accompanied with a dramatic loss in ductility. Irradiated materials also experience a decrease in fracture toughness and an increase in potential for brittle fracture.<sup>12</sup>

A comprehensive literature review was conducted on pure Mo and W and on some Mo and W alloys to determine if irradiation hardening and embrittlement would likely be a problem for a Mo or W NTP cermet fuel core.<sup>10</sup> This review provides a high level summary of the impact of irradiation effects relevant to NTP conditions. The review found that both Mo and W will experience hardening up to at least 1075 K, a temperature where some parts of the NTP fuel core will never exceed even at full power.<sup>13</sup> Measurable hardening was found to occur as low as  $7.2 \times 10^{-5}$  dpa, much lower than the total cumulative dose expected for an NTP system of around 0.01 dpa.<sup>10</sup>

## II. ION BEAM EXPERIMENT

### II.A. Materials Preparation

Eight different materials were selected and prepared in preparation for the ion irradiation experiment. Half were Mo-based and the other half were W-based. For each base metal (Mo and W), the materials chosen for irradiation included pure stock metal, spark-plasma-sintered (SPS) metal, and cermets with both 50-volume percent (vol%) and 60-vol%  $ZrO_2$  particles. The pure stock materials were both reported at 99.95% purity and acted as control materials. All of the Mo based SPS materials were sintered at 1400 °C and 50 MPa for 5 minutes. All of the W based SPS materials were sintered at 1700 °C and 50 MPa for 10 minutes. The pure SPS Mo and W were tested to determine whether the cermet particles would have an effect on the irradiation hardening of the metal matrix.

All samples were cut into 1 mm thick plates with faces 5 by 15 mm. The pure stock and SPS materials were cut to the desired sample dimension using electron discharge machining (EDM) with a copper wire. Extensive care was used when polishing to remove all copper discharge from the sample. The cermet samples with  $ZrO_2$  particles could not be machined using EDM due to differences in electrical conductivity between the ceramic particle and the metal matrix, so traditional mechanical cutting and grinding were used. All materials were polished using standard metallographic procedure, finishing with 1  $\mu$ m polycrystalline diamond.

The samples were then mounted onto four specialized holders using carbon tape for the room temperature

irradiations and high temperature vacuum-compatible silver paste for the 1075 K irradiations. Thermocouples were attached to the surface of the samples to monitor the high temperature irradiations as seen in Figure 1. Solid scintillators were attached to align the ion beam with the sample irradiation area. The samples were also masked using niobium foil to provide a definitive line between ion and non-ion irradiation regions.

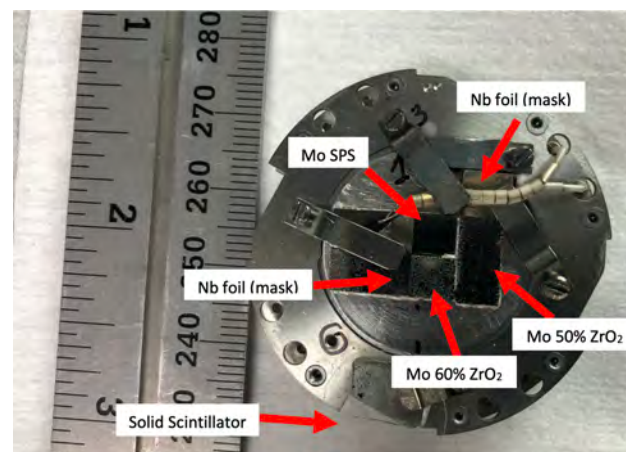


**Fig. 1.** Mo and Mo cermet samples mounted on the high temperature test holder with niobium foil masking and attached thermocouple.

### II.B. Nickel Ion Irradiation

The samples were irradiated at the Ion Beam Materials Laboratory (IBML) at the University of Tennessee-Knoxville. The beam was rastered to cover a total area of 10 x 10 mm (encasing either 3 samples for the 1075 K irradiation or 4 samples for the room temperature irradiation). 21 MeV  $Ni^{7+}$  ions were selected for this experiment in order to provide a high ion penetration depth of around 3  $\mu$ m. This high penetration depth was selected to provide a deep uniform damage region for future hydrogen corrosion experiments.

The damage and Ni implantation profiles were approximated using the quick Kinchin Pease simulation from the SRIM software.<sup>14</sup> Figure 2 summarizes the Ni implantation and damage profiles in both Mo and W. The area shaded in blue represents the area used for the analysis after nanoindentation, and represents 100 nm to 2.7  $\mu$ m in Mo and to 2.5  $\mu$ m in W.

Since the metal matrix determines the majority of the mechanical properties, the damage rate was determined in pure Mo and W. The samples were irradiated to fluence of  $1 \times 10^{13}$  ion/cm<sup>2</sup>, corresponding to a dose of between 0.001 and 0.008 dpa in Mo and between 0.001 and 0.007 dpa in W. This experiment was meant to be a preliminary study to determine qualitatively whether irradiation hardening would be of concern for a cermet NTP system, so the targeted maximum dose was on the same order of

magnitude as the expected maximum dose for a crewed NTP mission to Mars. For each material and dpa condition, samples were irradiated at both room temperature and 1075 K. This temperature range was selected to include as wide a range as possible, given the capabilities of IBML, to determine the cutoff temperature for irradiation hardening in Mo and W based cermet.

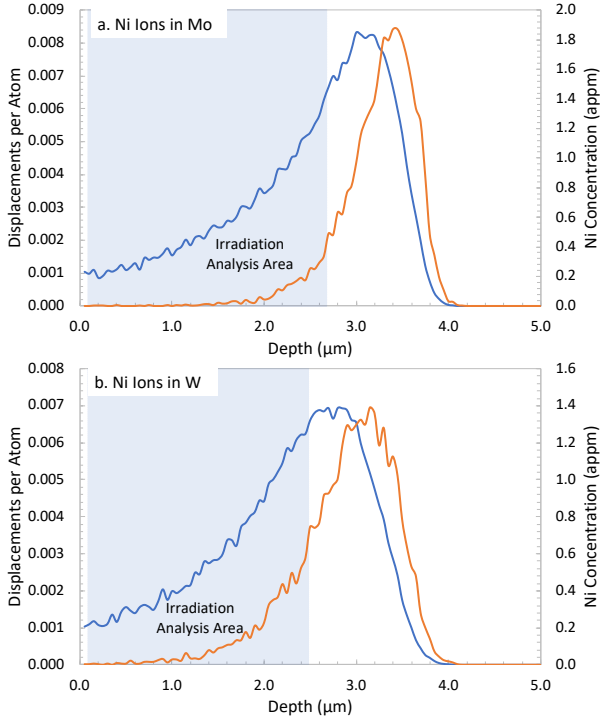


**Fig. 2.** Damage (blue curve) and Ni implantation (orange curve) profiles calculated in SRIM for 21 MeV Ni ions in **a.** Mo and in **b.** W.

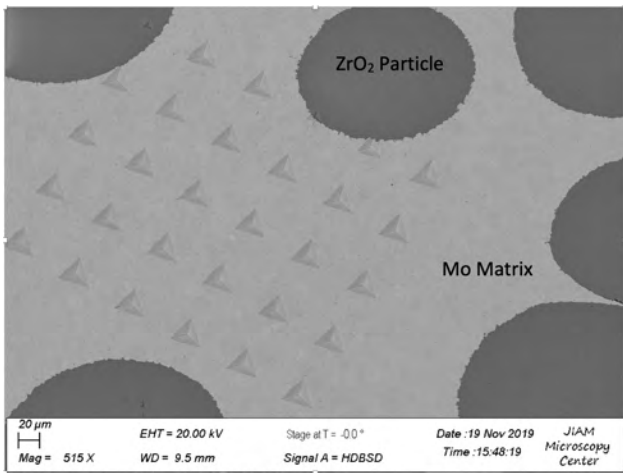


**Fig. 3.** SEM micrograph of the nanoindentation array of a Mo 50-vol% cermet.

### II.C. Nanoindentation

Nanoindentation was performed using the KLA iMicro™ nanoindenter at KLA Nanoindenter Group in Knoxville, TN. Samples were indented using the continuous stiffness method (110 Hz oscillation) and a constant strain rate of 0.2 s<sup>-1</sup> using a Berkovich diamond tip. Samples were indented to a load of 1 Newton corresponding to indentation depths around 3.4 and 4.2 μm in the W and Mo samples, respectively. Around 30 indentations were performed in each sample region as seen in Figure 3.

Nanoindentation measures the hardness of the material for a given depth, which correlates to the strength of the material. To overcome indentation size effects, especially for the irradiated samples where shorter depths are important, the Nix-Gao method was used to determine a bulk hardness value from the data.<sup>15</sup> Using Eq. (1) derived by Nix and Gao, the bulk hardness values,  $H_0$ , for both the unirradiated samples and the irradiation region (averaged over the area shown in Figure 2) of the ion irradiated samples were determined.<sup>16</sup>

$$\left(\frac{H}{H_0}\right)^2 = 1 + \frac{h^*}{h} \quad (1)$$

$H$  is the hardness at any given point,  $h$  is the indent depth,  $h^*$  is the characteristic length, and  $H_0$  is the bulk hardness value. Significant research has been conducted to determine hardness using nanoindentation for thin coatings. The ion irradiation region can be considered as a thin coating, since its hardness differs from the bulk material with a relatively sharp cutoff.<sup>17</sup> These experiments found that the indentation is sensitive to regions up to 5 to 10 times the indent depth. The first 100 nm were ignored to avoid near-surface effects. For the irradiation samples, the maximum indent depth was selected as one fifth the maximum damage depth, or 572 nm for W, 630 nm for Mo, and 938 nm in ZrO<sub>2</sub>. The analyzed region is shown in Figure 2. For the unirradiated samples, the entire range except for the first 100 nm, was used. For the cermet samples, some data from several indents were ignored due to the indenter interacting with a hidden cermet particles. In all cases, the Nix-Gao method was applied to determine the bulk hardness in the analyzed region.

### III. RESULTS

The results of the Nix-Gao analysis are presented in Table I for the Mo experimental results and in Table II for the W experimental results. Due to the relatively low ion fluences, only a small amount of hardening was expected. The two-tailed student's T-test was used with two samples of unequal variances to determine the probability that the hardening was statistically significant. The analysis for all of the Mo and W hardness tests found there was a probability of 99% or greater that statistically significant hardening occurred.

**TABLE I.** Mo materials hardness data with the bulk hardness,  $H_0$ , the change in hardness,  $\Delta H$ , and with RT and HT meaning room and high temperature respectively.

Sample	$H_0$ (GPa)	$H_0$ (GPa)	$\Delta H$ (GPa)
	Unirradiated	Ion irradiated	
RT Stock	$3.44 \pm 0.08$	$3.78 \pm 0.22$	0.34
RT SPS	$2.78 \pm 0.14$	$3.26 \pm 0.38$	0.48
RT 50 vol%	$2.47 \pm 0.14$	$2.87 \pm 0.47$	0.40
RT 60 vol%	$2.26 \pm 0.23$	$2.87 \pm 0.36$	0.62
HT SPS	$2.93 \pm 0.13$	$3.46 \pm 0.30$	0.52
HT 50 vol%	$2.65 \pm 0.12$	$2.99 \pm 0.34$	0.34
HT 60 vol%	$2.44 \pm 0.14$	$2.79 \pm 0.48$	0.35

**TABLE II.** W materials hardness data with the bulk hardness,  $H_0$ , the change in hardness,  $\Delta H$ , and with RT and HT meaning room and high temperature respectively.

Sample	$H_0$ (GPa)	$H_0$ (GPa)	$\Delta H$ (GPa)
	Unirradiated	Ion irradiated	
RT Stock	$5.22 \pm 0.24$	$5.73 \pm 0.60$	0.51
RT SPS	$5.47 \pm 0.64$	$5.56 \pm 0.77$	2.08
RT 50 vol%	$3.80 \pm 0.36$	$5.11 \pm 0.43$	1.31
RT 60 vol%	$3.50 \pm 0.40$	$4.31 \pm 0.60$	0.81
HT SPS	$3.56 \pm 0.99$	$6.00 \pm 0.97$	2.44
HT 50 vol%	$3.53 \pm 0.53$	$4.52 \pm 1.31$	0.98
HT 60 vol%	$3.18 \pm 0.60$	$4.43 \pm 0.89$	1.25

In addition to the previously described statistical analysis, another analysis found no statistically significant difference between the room temperature and 1075 K ion beam irradiations. This may be due to the low damage doses used in this experiment. A higher ion fluence would likely produce a more statistically significant hardening difference at various temperatures as seen in experiments performed on pure Mo and W.<sup>10</sup> Another analysis discovered that the matrix hardening differences between the 50 and 60-vol% cermetes were insignificant as well. Because of this, all the cermet matrix data was combined as presented in Table III. W-based cermetes experienced more hardening than the Mo-based cermetes, by around a factor of two, suggesting that Mo-based cermetes have a higher resistance to irradiation hardening.

**TABLE III.** Combined cermet hardness results.

Sample	$H_0$ (GPa)	$H_0$ (GPa)	$\Delta H$ (GPa)
	Unirradiated	Ion irradiated	
RT Mo Cermet	$2.37 \pm 0.21$	$2.87 \pm 0.43$	0.50
HT Mo Cermet	$2.54 \pm 0.17$	$2.93 \pm 0.40$	0.39
RT W Cermet	$3.66 \pm 0.40$	$4.75 \pm 0.65$	1.09
HT W Cermet	$3.36 \pm 0.59$	$4.48 \pm 1.15$	1.12

Hardness can be correlated to the macroscopic property of yield strength using Tabor's relationship,

where the Tabor factor for body-centered-cubic materials is 3, according to Eq. (2).

$$\Delta H \approx 3\Delta\sigma \quad (2)$$

$\Delta H$  is the change in hardness and  $\Delta\sigma$  is the change in yield strength. Based off of this experiment, for a crewed mission to Mars, Mo based cermetes would expect an increase in yield strength of around 0.15 GPa and W based cermetes could expect an increase of around 0.40 GPa. These values are relatively modest but also are accompanied by decreases in ductility and fracture toughness.

The hardness of the  $ZrO_2$  particles was also determined using similar methods. The statistical analysis found that no significant hardening occurred in the ceramic particles at either irradiation temperature.

#### IV. CONCLUSIONS

This experiment used ion irradiation to simulate the irradiation hardening behavior expected in Mo and W based surrogate fuel cermetes for an NTP mission to Mars. Even at the low fluences associated with NTP, all materials, including the pure metals and cermetes, experienced statistically significant hardening in the metal matrix. All of the Mo and W samples saw a statistically significant hardening increase at both room temperature and at 1075 K, with the W samples experiencing a greater magnitude and percentage of hardening than the Mo samples. The Mo cermetes experienced around a 20% increase in hardening, while the W cermetes experienced a 30% increase in hardening. In this study, volume loading and irradiation temperature did not have a significant effect on hardening behavior.

Irradiation hardening of Mo and W based cermetes will need to be considered in the design of an NTP fuel core, since the hardening was significant enough to cause a degradation of material properties. However, the magnitude of the hardening is likely small enough that this hardening and corresponding decline in ductility and fracture toughness can be accounted for in the design of a cermet-based reactor.

Before any definitive conclusions can be reached, more experiments are needed to determine both the temperature and dose dependence on irradiation hardening of cermetes. Also, combining hot hydrogen testing with ion irradiation is necessary to determine what effect irradiation hardening will have on the hydrogen corrosion resistance of the materials. Finally, even though ion irradiation is useful and can provide insight into irradiation hardening and embrittlement, it only affects microscopic properties of the materials and cannot fully simulate the effect of irradiation on the bulk mechanical properties. Neutron irradiation experiments are needed not only to validate the ion irradiation results, but to also provide macroscopic irradiation hardness data.

## ACKNOWLEDGMENTS

This work is funded in part by NASA Marshall Space Flight Center's Center Innovation Fund (CIF) and the NASA NTP Project. Funding was provided through the ORNL subcontract under the NASA/DOE-NE funding. Samples were manufactured by KB at NASA Marshall Space Flight Center. The ion irradiations were performed at the Ion Beam Materials Laboratory at the University of Tennessee-Knoxville with the help of Miguel Crespillo. Nanoindentation was performed at KLA Nanoindenter Group in Knoxville, TN with the help of Jennifer Hay and Briar Faulkner. Additional aid was given by Richard Howard and other members of the Reactor and Nuclear Systems Division at Oak Ridge National Laboratory.

## REFERENCES

1. S. K. Borowski et. al., "A Proven Growth Technology for Human NEO/Mars Exploration Missions," *IEEE Aerospace Conference*, Big Sky, MT, 2012, p. 1-20, IEEE (2012).
2. S. K. Borowski et. al., "Nuclear Thermal Propulsion (NTP): A Proven Growth Technology for 'Fast Transit' Human Missions to Mars," *AIAA Space Conference and Exhibition*, San Diego, CA, 2013, p. 1-22, AIAA (2013).
3. J. Finseth, "Rover Nuclear Rocket Engine Program: Overview of Rover Engine Tests," Final Report, (N—92-15117). Sverdrup Technology, Inc, Huntsville, AL, (1991).
4. M. Stewart, B.G. Schnitzler, "A Comparison of Materials Issues for Cermet and Graphite-Based NTP Fuels," *49th AIAA/ASME/SAE/ASEE Joint Propulsion Conference*, San Jose, CA, 2013, p. 1-13, AIAA, (2013).
5. R. Hickman et. al., "Fabrication of High Temperature Cermet Materials for Nuclear Thermal Propulsion," *43<sup>rd</sup> JANAF Propulsion*, Nashville, TN, 2012, p. 1-5, NASA (2012).
6. R. Hickman et. al., "Fabrication and Testing of CERMET Fuel Materials for Nuclear Thermal Propulsion," *48<sup>th</sup> AIAA/ASME/SAE/ASEE Joint Propulsion Conference & Exhibit*, Atlanta, GA, 2012, p. 1-18, AIAA/ASME/SAE/ASEE (2012).
7. C. Haertling and R.J. Hanrahan Jr, "Literature Review of Thermal and Radiation Performance Parameters for High-Temperature, Uranium Dioxide Fueled Cermet Materials," *Journal of Nuclear Materials*, **366**, 317-335 (2007). DOI:10.1016/j.jnucmat.2007.03.024
8. T.G. Duffin et. al., "Production and Hot Hydrogen Testing of Subscale Molybdenum Cermets for Nuclear Thermal Propulsion," *Joint Propulsion Conference*, Cincinnati, OH, July 9, 2018, p. 1-8, AIAA (2018).
9. S.J. Zinkle, "1.03-Radiation-Induced Effects on Microstructure," *Comprehensive Nuclear Materials*, p. 65-98, R.J.M. Konings, Ed., Elsevier, Waltham, Ma (2012).
10. N. Gaffin et. al., "Review of Irradiation Hardening and Embrittlement Effects in Refractory Metals Relevant to Nuclear Thermal Propulsion," *Nuclear Emerging Technologies in Space*, Richland, WA, 2019, p. 1-6 ANS (2019).
11. S.J. Zinkle and F.W. Wiffen, "Radiation Effects in Refractory Alloys," *Space Technology and Applications International Forum*, American Institute of Physics, p. 733-740 (2004).
12. K.J. Leonard, "4.06 – Radiation Effects in Refractory Metals and Alloys," *Comprehensive Nuclear Materials*, p. 99-122, R.J.M. Konings, Ed., Elsevier, Oxford (2012).
13. M. Stewart, "Fuel Element to Moderator Element Heat Transfer Analysis," *Nuclear Emerging Technologies in Space*, Richland, WA, 2019, p. 1-3 ANS (2019).
14. J.F. Ziegler and J.P. Biersack, "The Stopping Power and Range of Ions in Matter," *Treatise on Heavy Ion Science*, p. 93-129, Springer (1985).
15. Y. Huang et. al., "A Model of Size Effects in Nano-indentation," *Journal of Mechanics and Physics of Solids*, **54**, p. 1668-1686 (2006). DOI:10.1016/j.jmps.2006.02.002
16. W.D. Nix and H. Gao, "Indentation Size Effects in Crystalline Materials: A Law for Strain Gradient Plasticity," *Journal of Mechanics and Physics of Solids*, **46**, p. 411-425 (1998). DOI:10.1016/j.jmps.1998.5096
17. D. Armstrong et. al., "Hardening of Self Ion Implanted Tungsten and Tungsten 5-wt% Rhenium," *Journal of Nuclear Materials*, **432**, p. 428-436 (2013). DOI:10.1016/j.jnucmat.2012.07.044

## TOWARD AN IN-DEPTH MATERIAL MODEL FOR NUCLEAR THERMAL PROPULSION FUEL ELEMENTS

Justin Haskins<sup>1</sup>, Lauren Abbott<sup>2</sup>, William C. Tucker<sup>2</sup>, Piyas Chowdhury<sup>2</sup>, and Charles W. Bauschlicher<sup>1</sup>

<sup>1</sup>Thermal Protection Materials Branch, NASA Ames Research Center, Moffett Field, CA, 94035, USA

<sup>2</sup>AMA, Inc., Thermal Protection Materials Branch, NASA Ames Research Center, Moffett Field, CA, 94035, USA

Primary Author Contact Information: [justin.b.haskins@nasa.gov](mailto:justin.b.haskins@nasa.gov) (650)604-4856

*The development and qualification of nuclear thermal propulsion (NTP) fuel element technologies would be aided by an in-depth model of material response and failure modes at operation conditions. Integrated computational materials engineering techniques have the potential to provide such a model, as demonstrated here through three case studies. The first case focuses on the erosion of a ZrC coating material in hot hydrogen. Ab initio techniques are used to calculate erosion rates at NTP operating conditions; erosion rates are found to agree well with available heritage data. The second focuses on the stability of UN fuels at high temperature and in the presence of hydrogen. Phase diagram techniques reveal potential instabilities and decomposition pathways at high hydrogen concentrations. The third focuses on using microstructure information to predict high temperature mechanical response and failure of tungsten, used in cermet materials. Combined finite element and discrete dislocation dynamics techniques provide mechanical properties in agreement with experimental methods. The integration of these techniques for an all-encompassing material model is discussed.*

### I. INTRODUCTION

NTP offers benefits over conventional chemical propulsion, such as a higher specific impulse ( $I_{sp} \sim 900$  s, a factor of  $\sim 2$  better), a higher thrust to mass ratio, better tolerance to payload mass growth and architecture, and lower initial mass in low-Earth orbit, and is aligned with the STMD (Space Technology Mission Directorate) Strategic Thrust of Advanced Propulsion. These benefits could lead to a reduction in heavy lift launch count, cost, and risk<sup>1,2</sup> and have led to NTP being considered for faster transit for manned missions to Mars and beyond as well as for commercial missions to the Moon.<sup>3</sup>

The canonical version of an NTP rocket has a solid fuel element that is composed of a matrix material containing uranium ceramic fuel particles and has longitudinal channels running through the fuel element that allow thermal energy generated from nuclear reactions to directly heat the  $H_2$  propellant, which is exhausted for propulsion. The earliest exploration of NTP was carried out by project Rover and the nuclear engine for rocket vehicle application (NERVA) from 1955 to 1972.<sup>4,5</sup> These efforts were deemed successful based on numerous rocket ground tests, but they were ultimately

cancelled due to budget challenges. Mission concepts and feasibility studies<sup>1,3</sup> focused on realizing this technology have arisen periodically over the half century since. Unfortunately, none of these studies progressed to the point of full scale ground testing in NTP thermal and fission environments like the original efforts. This trend, however, appears likely to change with the current NASA NTP project at MSFC (Marshall Space Flight Center), which has made significant advances in NTP reliability that open up the possibility of ground testing in the near future.

The project Rover/NERVA rocket ground tests provided a unique wealth of information related to the performance of fuel elements with graphite matrix material in extreme thermal and fission environments. Two major factors that reduced the useful lifetime of the graphite fuel elements were identified from these tests but not fully resolved. The first is instability in the propellant channel coatings during operation due to thermal expansion mismatch, which causes cracking and accelerates coating corrosion.<sup>5</sup> The second is the migration of fuel and fission products that results in damage to the matrix material.<sup>5</sup> In parallel with the project Rover/NERVA efforts, Argonne National Lab (ANL)<sup>6</sup> and General Electric (GE)<sup>7</sup> worked on fuel elements that used ceramic-metal (cermet) matrix materials. They identified similar challenges with respect to fuel and fission product migration and damage, although this material architecture was not involved in ground tests. Thus, improved coatings are required for both the  $H_2$  channels and U-ceramic particles to mitigate the identified fuel matrix degradation mechanisms and ensure the success of NTP. Although strides in these directions have been made recently (notably by the MSFC NTP project)<sup>8-10</sup> more extensive development, and eventually testing at representative conditions, is needed.

Many of the material issues faced by heritage NTP efforts could have been more quickly identified and remedied by in-depth material modeling available today, which also would have reduced the costly trail-and-error development that required experimental fabrication and testing in hot hydrogen. Namely, integrated computational materials engineering techniques, which span the atomistic scale (e.g., ab initio and molecular dynamics) to the microscale (e.g., finite element and mechanical models), can provide diagnostics such as corrosion of coatings due to  $H_2$  reactions and vaporization,

intercalation and mobility of hydrogen or fission species into coatings, proclivity of fuel materials to creep and hydrogen embrittlement effects, and the mechanical response and fracture in fuel materials. These techniques are demonstrated for three NTP relevant test cases: (1) erosion of coatings in hot hydrogen, (2) the phase stability of uranium nitride fuel in a tungsten matrix that is exposed to different levels of hydrogen, and (3) the mechanical properties and failure of tungsten.

## II. METHODS

### II.A. Ab Initio Computations and Simulations

Ab initio computations are used to understand the chemical reactions of coating materials with hot hydrogen to inform erosion. Such computations were performed with the Vienna Ab Initio Simulation Package (VASP). VASP is a plane-wave electronic structure code that solves the Kohn-Sham equations to inform material energetics and, through molecular dynamics, basic thermodynamic properties.

### II.B. Microscale Mechanical Modeling

To evaluate the mechanical response and failure initiation of such microstructures, DAMASK, Dusseldorf Advanced Material Simulation Kit, is employed. DAMASK is a highly modular freeware code for modeling materials structure/property relationships with different types of mechanistic constitutive laws and numerical solvers. It is designed to accurately correlate microscopic phenomena (e.g. plastic deformation, phase transformation, hydrogen embrittlement, microcracking, irradiation damage) with macro-scale responses. For the present work, DAMASK is employed to study the microscopic damage evolution in tungsten under the operating conditions of NTP.

## III. RESULTS

### III.A. Coating Erosion in Hydrogen

One objective related to the development of carbon composite fuels for NTP is to identify hydrogen propellant channel coatings that are resistant to erosion. The coating must be of sufficient thickness to withstand erosion from hot hydrogen and protect the underlying carbon composite fuel. Thus, understanding the loss of coating material at given operation conditions (time, temperature, pressure) is critical. The primary mechanism for coating loss will be attributed to chemical reactions with atomic hydrogen and the subsequent formation of gaseous refractory products. To examine this phenomenon, the free energies of the various solid materials under consideration for coating materials must be obtained, along with the free energies of possible gaseous, hydrogenated refractory molecules. The free energies can be used to evaluate equilibrium constants for reactions that will inform the loss of coating material, given that equilibrium is met. Because accurate experimental databases of the thermodynamics for the various solid coatings and gaseous products do not exist at the temperatures of interest, ab initio computations are performed to obtain free energies.

An experimental comparison of the accuracy of the approach used in the present work can be made with data obtained from the Nuclear Engine Rocket for Vehicle Application (NERVA) project. NERVA fabricated and tested NTP rockets and required hydrogen channel coatings that would operate at 2800 K. The original tests recorded detailed erosion data for hydrogen channels that were coated in ZrC. The data obtained from ab initio calculations for ZrC (see Fig. 1a) are used to provide recession comparisons to the NTP coating experiments (Fig. 1b). The recession was measured along the length of

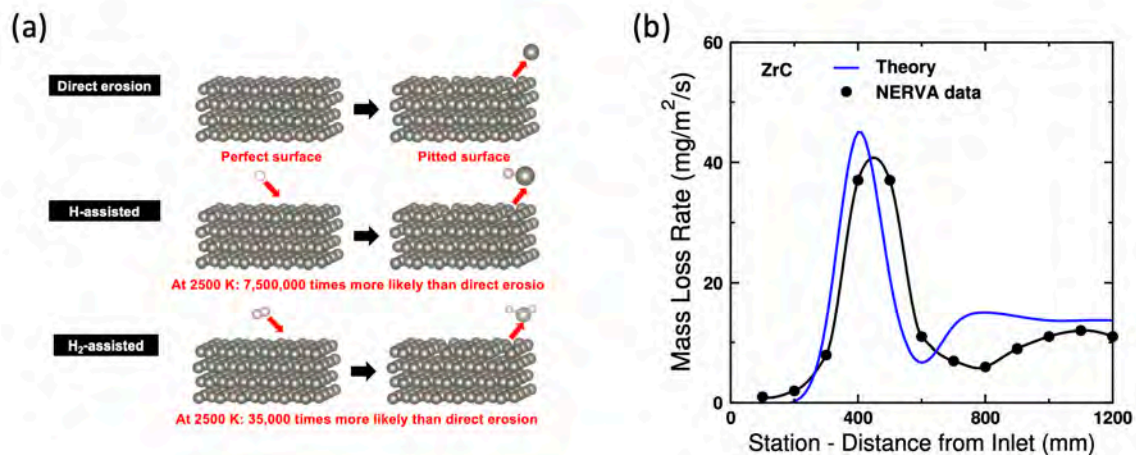


**Fig. 1.** (a) Atomistic modeling of coating surface erosion from hydrogen reaction. (b) Comparison of hydrogen erosion of ZrC coatings to heritage experimental data obtained from the Nuclear Engine Rocket for Vehicle Application (NERVA) project.

the coating channel (labeled as station) and exhibited a maximum in the mid-range region of the channel. (Mass loss from carbon erosion through cracks was also incorporated into this plot to describe this maximum, but requires a more in-depth discussion beyond the scope of the present document.) Overall, the computational recession estimates compare favorably along the coating channel to the experiments from the NERVA project and suggest a predictive capability.

### III.B. Fuel Stability in the Presence of Hydrogen

The stability of uranium fuels in high temperature fuel elements exposed to different levels of hydrogen is of critical importance, as decomposition could lead to fuel element failure. Here, the stability of UN fuels in a W matrix, akin to a cermet fuel element, is examined as a function of hydrogen concentration using ab initio calculations and phase diagram techniques.

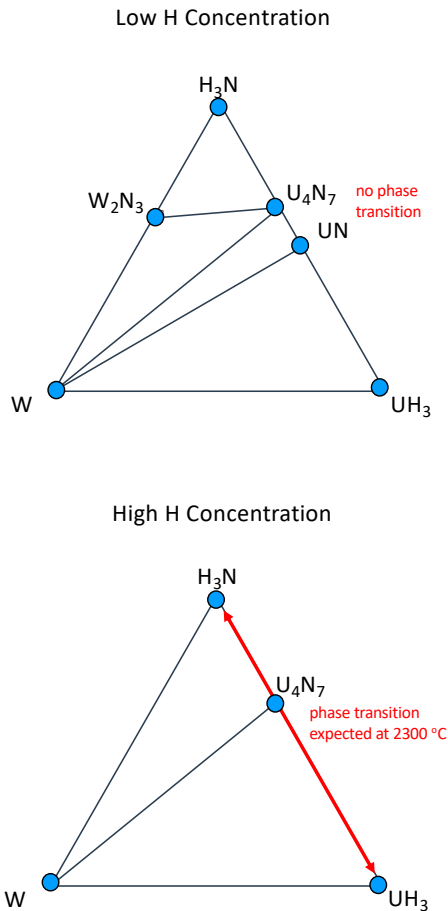


**Fig. 2.** Ternary phase diagram of UN fuel in the presence of W and at different concentrations of hydrogen.

A low hydrogen concentration (representing minimal hydrogen diffusion into the cermet and -3.7 eV chemical

potential) case and a high concentration (larger quantities in the cermet and -3.3 eV chemical potential) case are examined (Fig. 2). At low concentrations, the UN fuel is stable and would require 1.4 eV (10000 K) to decompose into  $U_4N_7$  and  $UH_3$  compounds. At high concentrations, UN can completely destabilize to these compounds, and the remaining  $U_4N_7$  can decompose further at 2300 °C.

### III.C. Material Thermal-Mechanical Stability

The base of many cermet fuel materials is tungsten; thus, tungsten is used here as a benchmark case against which to test microstructure and mechanical modeling capabilities. In Fig. 3, a tungsten polycrystalline microstructure with randomly oriented grains is created using DAMASK with Voronoi tessellation algorithm. The average grain diameter is chosen to be 20 microns, which is typical for engineering materials. The representative volume element (RVE) is then subjected to uniaxial tension at a strain-rate of  $10^{-3} \text{ s}^{-1}$ , which is within the standard range of performing laboratory tensile testing per ASTM standards. Note that both the material structure and mechanical conditions are reflective of realistic empirical conditions.

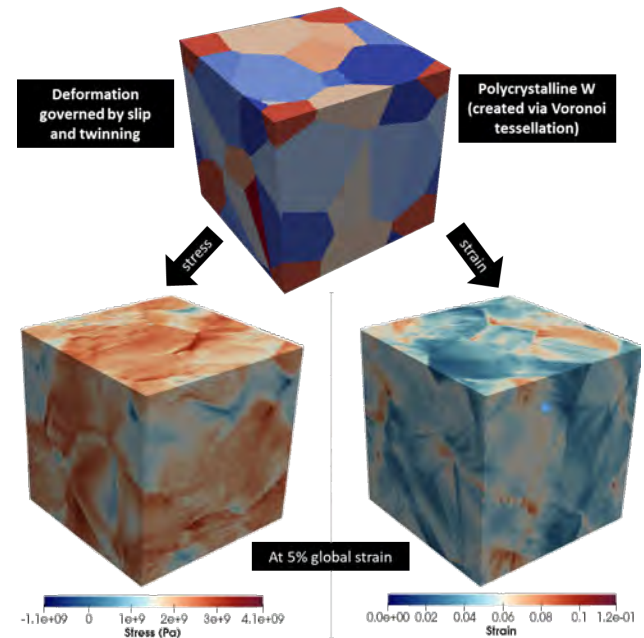


**Fig. 3.** Model of tungsten coating material microstructure mechanical response. Notice contours of stress and strain distributions where highly localized strain at grain boundaries constitute crack damage initiation sites.

In the current case, the evolution of stress and strain concentration at the microstructural level is studied. The high stress concentration sites are identified as being the grain boundaries, which is consistent with earlier experimental observation in the literature reporting initiation of damage at these sites. The unique feature

about the current modeling approach with DAMASK is that the microscopic stress contour is computed as a direct outcome of discrete dislocation and twinning based crystal plasticity informed by inherent physics of plastic deformation evolution. The modeled stress-strain properties obtained through this approach (Fig. 4) closely approximate that obtained from experiments on polycrystalline material.

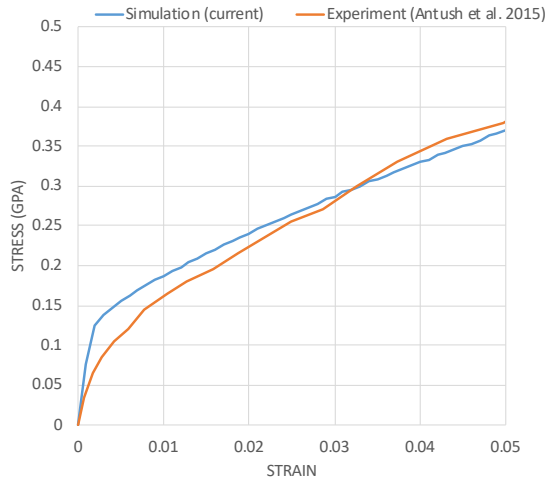


**Fig. 4.** Mechanical behavior of tungsten from DAMASK simulations of discrete dislocation dynamics and experiment.

## V. CONCLUSIONS

Three applications of integrated computational materials engineering techniques to problems related to nuclear thermal propulsion fuel element materials were presented. The applications focused on the interaction of fuel elements with hydrogen, erosion and phase destabilization, and the mechanical performance and damage of fuel element matrix materials. The promise of these techniques is to provide predictions of fuel element performance and failure modes. Work is on-going to integrate these techniques into a unified model of fuel elements, which would greatly aid the qualification of materials for NTP.

## ACKNOWLEDGMENTS

The authors thank the NASA Ames' Center Innovation Fund for sponsoring this work.

## REFERENCES

1. S. K. BOROWSKI, D. R. MCCURDY, T. W. PACKARD, "7-Launch' NTR Space Transportation System for NASA's Mars Design Reference Architecture (DRA) 5.0," *Proceedings of the 45<sup>th</sup> AIAA/ASME/SAE/ASEE Joint Propulsion Conference & Exhibit*, Denver, CO, AIAA-2009-5308, AIAA (2009).
2. M. G. HOUTS, D. P. MITCHELL, T. KIM, W. J. EMRICH, R. R. HICKMAN, H. P. GERRISH, G. DOUGHTY, A. BELVIN, S. CLEMENT, S. K. BOROWSKI, J. SCOTT, K. P. POWER, "NASA's Nuclear Thermal Propulsion Project," *Proceedings of the AIAA Space Conference and Exhibition*, Pasadena, CA, AIAA 2015-4523, AIAA (2015).
3. S. K. BOROWSKI, R. R. CORBAN, M. L. MCGUIRE, E. G. BEKE, "Nuclear Thermal Rocket/Vehicle Design Options for Future NASA Missions to the Moon and Mars," *Proceedings of the AIAA Space Programs and Technologies Conference and Exhibit*, Huntsville, AL, AIAA (1993).
4. J. M. NAPIER (ED.), "NERVA Fuel Element Development Program. Summary Report, July 1966-June 1972. Extrusion Studies," *Oak Ridge Y-12 Plant Report* (1972).
5. D. R. KOENIG, "Experience Gained from the Space Nuclear Rocket Program (Rover)," *Los Alamos National Laboratory Report*, LA-10062-H (1986).
6. W. D. WILKINSON (ED.), "Nuclear Rocket Program Metallurgy Division Progress Report for Quarter Ending Dec. 31 1964," *Argonne National Laboratory Report*, ANL-7031 (1965).
7. J. F. COLLINS, D. L. NEWSOM "710 High Temperature Gas Reactor Program Summary Report," *General Electric Company Report*, GEMP-659 (1968).
8. M. E. M. STEWART "A Historical Review of Cermet Fuel Development and the Engine Performance Implications," NASA Technical Report, GRC-E-DAA-TN21122 (2015).
9. M. W. BARNES, D. S. TUCKER, K. M. BENENSKY "Demonstration of Subscale Cermet Fuel Specimen Fabrication Approach using Spark Plasma Sintering and Diffusion Bonding," A Historical Review of Cermet Fuel Development and the Engine Performance Implications," *Proceedings of ANS NETS*, NASA Technical Report, M17-6413 (2018).
10. D. S. TUCKER, "CERMETS for Use in Nuclear Thermal Propulsion," in *Advances in Composite Materials Development*, IntechOpen (2019).

## DEVELOPMENT OF A MULTISCALE MODEL FOR FUEL LOSS FROM NUCLEAR THERMAL PROPULSION CERMETS

Jacob Hirschhorn<sup>1</sup>, Marina Sessim<sup>1</sup>, Jhonathan Rosales<sup>2</sup>, Marvin Barnes<sup>2</sup>, and Michael Tonks<sup>1</sup>

<sup>1</sup>Department of Materials Science and Engineering, University of Florida, Gainesville, FL 32611

<sup>2</sup>Marshall Space Flight Center, National Aeronautics and Space Administration, Huntsville, AL 35808

Contact Information for Michael Tonks: 352-846-3779 and [michael.tonks@ufl.edu](mailto:michael.tonks@ufl.edu)

*Nuclear thermal propulsion is a promising technology for deep space exploration missions, but fuel qualification will require mitigation of fuel loss. In the current work, we introduce a mechanistic, multiscale model for fuel loss. The model will be used to supplement experimental studies by investigating the relationships between fuel microstructure and performance and identifying beneficial design features. These findings will narrow the design space, reducing cost and expediting qualification.*

### I. INTRODUCTION

The Nuclear Thermal Propulsion (NTP) Program was created by the National Aeronautics and Space Administration (NASA) in 2015. NTP involves using a nuclear reactor to superheat hydrogen gas for spacecraft propulsion, and the goal of the NTP Program is to assess the viability and affordability of such an approach. NTP systems provide the high specific-impulse necessary for extended spaceflight, making them a promising technology for missions to Mars and beyond.

NTP fuel concepts date back to the 1960s and typically take the form of CERamic METal composites (CERMETS), consisting of ceramic fuel particles embedded within a refractory metal matrix. Due to their high operating temperatures (~2,500°C), refractory metals have been down selected for the fuel matrix, external fuel cladding, and cooling channel formation. Much of the early work was conducted using W-UO<sub>2</sub> composites, but W-UN and W/Mo-UN composites are now also being considered. These new combinations allow for use of lower enrichment fuels while maintaining a good balance between melting temperature, thermal conductivity, and mechanical toughness.

CERMETS must remain stable when subjected to extremely harsh environmental conditions to ensure that the fuel performs safely and effectively throughout its life. The presence of flowing hydrogen, irradiation, and high temperature contribute to a phenomenon known as fuel loss, in which repeated thermal cycling results in loss CERMET integrity and fissile material over time. NTP CERMET qualification will ultimately require selection of a CERMET design that optimizes desirable thermomechanical properties and minimizes fuel loss.

A variety of experimental studies have been conducted to characterize CERMET fuel loss behaviors, and several influential chemical reactions and mechanical behaviors have been identified. These behaviors are shown in Fig. 1 along with a schematic representation of the three stages of fuel loss from a W-UO<sub>2</sub> CERMET thermally cycled in hydrogen<sup>1</sup>. A number of fuel loss mitigation strategies such as refractory metal particle coatings and fuel element claddings have been successfully applied to mitigate fuel loss. However, there is still no robust theory for the behavior, and many of the experimental facilities necessary for further study have been lost.

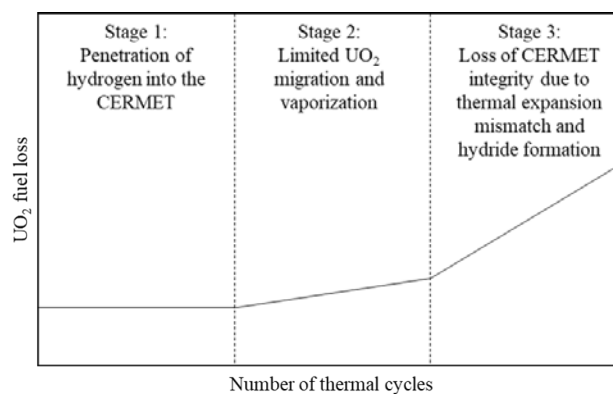


**Fig. 1.** Schematic representation of the three stages of fuel loss from a W-UO<sub>2</sub> CERMET thermally cycled in hydrogen and the influential physical behaviors involved in each stage (modified from Ref. 1).

This combination of technical challenges and logistical constraints leaves a vast design space to be explored. The cost of such an undertaking using experiments alone would be prohibitively high, but similar obstacles in the nuclear power industry have been overcome with the help of mechanistic, multiscale models. The purpose of the current work is to develop a model for the three stages of fuel loss from NTP CERMETS. The model will be used to characterize the relationships between CERMET microstructural features and performance and to identify the most influential physical processes and material properties for further study. These findings will narrow the design space,

reducing the expense of design optimization and expediting qualification.

## II. FUEL LOSS MODEL DEVELOPMENT

The fuel loss model is being developed within the Multiphysics Object-Oriented Simulation Environment<sup>2</sup> (MOOSE), a fully-implicit finite element framework maintained by Idaho National Laboratory. MOOSE-based fuel performance codes like Marmot and Bison have been used to model the thermal performance of W-UO<sub>2</sub> CERMETS in the past as shown in Fig. 2, making them ideal for use in fuel loss modeling. Existing physics modules and meshes are being used wherever possible to expedite model development and testing. Models are being developed and validated using the more widely-available W-UO<sub>2</sub> material properties, but W-UN and W/Mo-UN material properties are being incorporated as they become available.

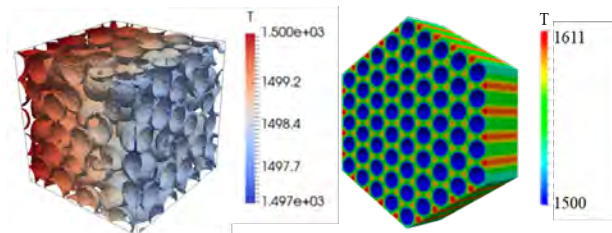


**Fig. 2.** Mesoscale homogenization simulation conducted using Marmot to calculate the effective thermal conductivity of a W-UO<sub>2</sub> CERMET (left), and macroscale simulation conducted using Bison to evaluate the bulk thermal performance of the CERMET (right). Temperatures are given in Kelvin.

A successful CERMET should remain stable and exhibit minimal fuel loss over tens of thermal cycles. A standard thermal cycle consisting of a one-minute heat up from room temperature to 2,500°C followed by a one-minute cooldown back to room temperature was established to simulate prototypic operating conditions. Behavioral models were then assembled to represent the influential physics involved in each of the three stages of fuel loss. Finally, the models were populated with temperature-dependent material properties from the literature, including interdiffusion coefficients, chemical reaction systems, and mechanical properties.

Modeling the mechanical behaviors responsible for the third stage of fuel loss is the most challenging task. This is because the range of temperatures encountered during the thermal cycle is wide enough to encompass both the matrix and particle phases' brittle and ductile regimes. These phases transition between the two regimes at different times during the thermal cycle due to their differing transition temperatures, producing complex

deformation and stress states throughout the CERMET. These transition behaviors and their strong temperature dependencies are illustrated by the W and UO<sub>2</sub> yield and failure stresses<sup>3,4</sup> shown in Fig. 3.

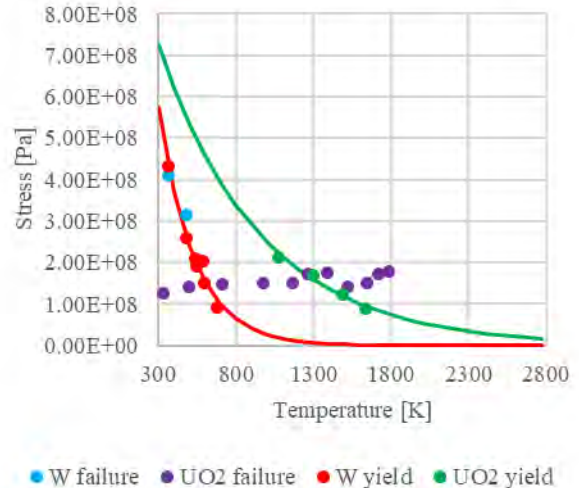


**Fig. 3.** Yield and failure stresses for W and UO<sub>2</sub> over the range of temperatures encountered during heat up and cooldown<sup>3,4</sup>. The matrix and particle phases both transition between brittle and ductile regimes during the thermal cycle, producing complex deformation and stress states throughout the CERMET.

The yield stresses shown in Fig. 3 were combined with thermal expansion coefficients and elastic moduli to capture the mechanical behavior of the CERMET throughout the thermal cycle. Finally, hardening behaviors and material properties were incorporated to account for the accumulation of defects over multiple thermal cycles. Each model component was verified using a series of 2D and 3D tests on the separate materials before using the combined model to simulate the interactions of the two within the CERMET.

## III. RESULTS AND DISCUSSION

Two sets of preliminary simulation results are presented and discussed in this section. The first set involves simulations conducted to examine the diffusive and chemical reaction behaviors that dominate the first two stages of fuel loss. The second set consists of simulations performed to investigate the mechanical behaviors believed to be responsible for accelerated fuel loss in the third stage.

The change in composition of a single UO<sub>2</sub> fuel particle embedded in W over twenty thermal cycles in hydrogen is shown in Fig. 4. UO<sub>2</sub> content changes over time as thermal cycling causes it alternate between its stoichiometric and oxygen-deficient states. Excess

oxygen tends to diffuse away from the oxygen-deficient  $\text{UO}_2$  due to its higher interdiffusivity. Spatial segregation of the two species results in a net loss of  $\text{UO}_2$  and a net gain of free U metal, which can react with hydrogen at low temperature to form  $\text{UH}_3$  hydrides.

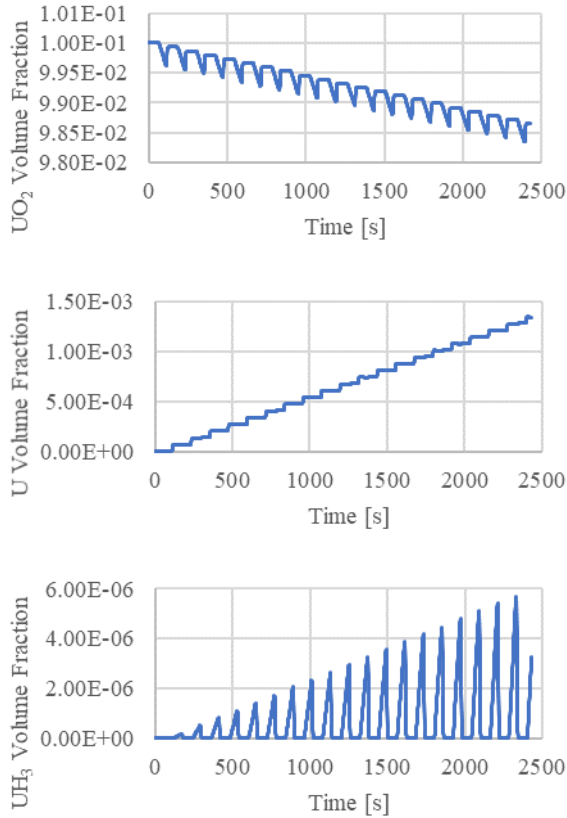


**Fig. 4.** Change in composition of a single  $\text{UO}_2$  fuel particle embedded in W over twenty thermal cycles in hydrogen. The results exhibit the trends expected during the first two stages of fuel loss: net loss of  $\text{UO}_2$  and net gain of free U metal and  $\text{UH}_3$  hydrides.

Each of these trends is reflected in the model predictions shown in Fig. 4. However, the magnitude of composition changes predicted by the model are smaller than those observed in experiments on bulk samples. This observation suggests CERMET fuel loss involves a significant mechanical component.

The results of a simulation conducted to investigate the role of mechanical interactions between CERMET phases are shown in Fig. 5. Tungsten and  $\text{UO}_2$  have thermal expansion coefficients<sup>4</sup> of approximately  $6.15 \times 10^{-6}$  and  $1.55 \times 10^{-5}$  per  $^\circ\text{C}$  at  $1250^\circ\text{C}$ , respectively. The results show that this thermal expansion mismatch produces stresses the matrix both around and between fuel particles. This behavior has the potential to disrupt the

particle-matrix interface, which could increase the available surface area for chemical reactions. These mechanical interactions could also weaken the matrix itself, enhancing the transport of diffusing species throughout the CERMET. Both of these behaviors would tend to accelerate fuel loss.

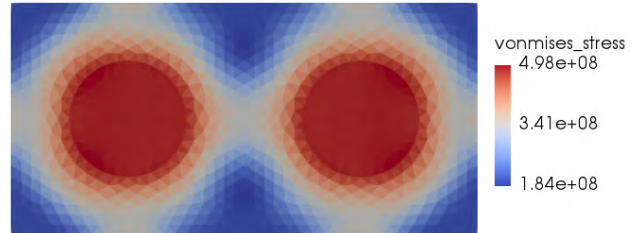


**Fig. 5.** Stresses resulting from thermal expansion mismatch between CERMET phases at room temperature. These interactions have the potential to disrupt the particle-matrix interface and the matrix itself, accelerating fuel loss. Stresses are given in Pascals.

Similar mechanical behaviors have been observed experimentally in the microstructures of CERMETs thermally cycled in hydrogen, as shown in Fig. 6. The micrograph shows that an interconnected network of cracks forms in the CERMET in response to thermal cycling. The cracks are concentrated in the brittle particle phase, the particle-matrix interface, and the portions of the matrix between particles, behaviors that are consistent with the stress states predicted by the model.

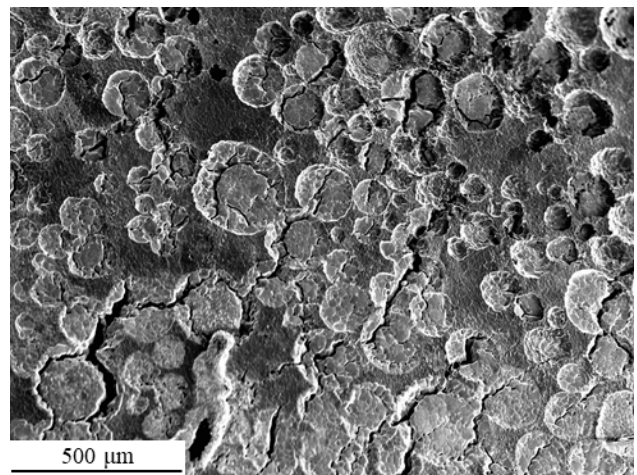


**Fig. 6.** Scanning electron microscope image of an experimental Mo- $\text{UO}_2$  CERMET taken after thermal cycling in flowing hydrogen. The micrograph shows that the particle phase, the particle-matrix interface, and the portions of the matrix between particles are particularly susceptible to damage. These observations are consistent with the stress states predicted by the model.

The stresses within the simulated microstructure shown in Fig. 5 vary over each thermal cycle and are sometimes sufficient to induce plasticity and hardening. Changes in the predicted principle and von Mises stresses at the center of the matrix over three thermal cycles are shown in Fig. 7. The stresses are highest at low temperature – conditions that would tend to induce brittle failure. The results show that stresses in the matrix tend to increase with the number of thermal cycles, making failure more likely. In the future, simulations like these will be conducted to determine how variations in different microstructural features impact bulk CERMET performance.

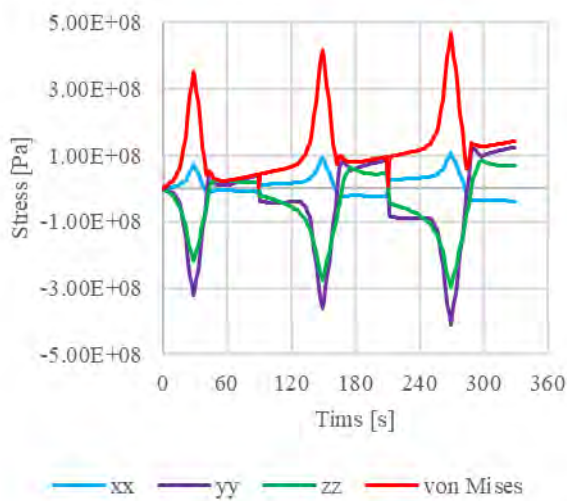


**Fig. 7.** Changes in the predicted principle and von Mises stresses at the center of the microstructure shown in Fig. 5 over three thermal cycles. Stresses tend to increase with the number of thermal cycles due to plasticity and hardening, making failure more likely.

#### IV. CONCLUSIONS

NTP technology has the potential to revolutionize extended spaceflight, but CERMET qualification will require design optimization and mitigation of fuel loss. Mechanistic, multiscale models like the one introduced in the current work can be used to investigate poorly-understood behaviors and identify promising design features more quickly and affordably than experiments alone. The results presented in the current work show that the model can begin to capture the physical behaviors that govern fuel loss. The model will be used to investigate how CERMET microstructural features impact performance and to determine the most influential physical processes and material properties. These findings will narrow the design space, helping to manage cost and expediting qualification.

#### ACKNOWLEDGMENTS

This work was funded by the National Aeronautics and Space Administration’s Nuclear Thermal Propulsion Program under grant number 80NSSC19K0754 from the Marshall Space Flight Center.

#### REFERENCES

1. C. HAERTLING and R. J. HANRAHAN, “Literature Review of Thermal and Radiation Performance Parameters for High-Temperature, Uranium Dioxide Fueled Cermet Materials,” *Journal of Nuclear Materials*, **366**, 3 (2007). DOI: 10.1016/j.jnucmat.2007.03.024
2. D. GASTON, C. NEWMAN, G. HANSEN, and L. DAMIEN, “MOOSE: A Parallel Computational Framework for Coupled Systems of Nonlinear Equations,” *Nuclear Engineering and Design*, **239**, 10 (2009). DOI: 10.1016/j.nucengdes.2009.05.021
3. P. RAFFO, “Yielding and Fracture in Tungsten and Tungsten-Rhenium Alloys,” *National Aeronautics and Space Administration Technical Report*, NASA TN D-4567 (1968).
4. M. O. MARLOWE and A. I. KAZNOFF, “Development of Low Thermal Expansion Tungsten-UO<sub>2</sub> Cermet Fuel,” *General Electric Company Technical Report*, NASA CR-72711 GESP-9014 (1970).

## DESIGN OF THE IN-PILE EXPERIMENT SET (INSET) APPARATUS TO SUPPORT NUCLEAR THERMAL PROPULSION FUEL AND COMPONENT TESTING

Richard Howard, PhD

*Oak Ridge National Laboratory  
One Bethel Valley Rd., Oak Ridge, TN 37831*

865-576-4867, [howardrh@ornl.gov](mailto:howardrh@ornl.gov)

*There is renewed interest in space travel, and domestic support for research and development activities to enable crewed missions to the moon and beyond is currently very strong. Nuclear thermal propulsion (NTP) is considered the most mature and viable nuclear propulsion technology available, but NTP fuel remains an Achilles heel of the system because it must withstand extreme conditions: temperatures ranging from cryogenic to an excess of 2,500 K, corrosive and erosive hydrogen working fluid, and power densities on the order of 5 MW/l.*

*To prove that NTP is fit for manned missions, fuels and reactor components must be tested and qualified. Moreover, test facilities must be cost effective and rapidly deployable so that the qualification effort does not financially cripple the development effort. This work describes the In-pile Experiment Set (INSET) apparatus design. This apparatus is intended to employ sub-scale fuel and component specimens to facilitate in-pile radiological tests to support the NTP effort.*

### I. INTRODUCTION AND BACKGROUND

The topic of exploring the solar system is exciting, and it is evolving into more serious plans and technology development to support crewed missions. To support these missions, propulsion technologies that provide sufficient thrust and specific impulse (a measure of propulsion efficiency) must be developed so that mission times are long enough to allow crews to perform sufficient exploration while minimizing personnel exposure to the adverse conditions of space. Current proven propulsion technologies such as chemical rockets provide adequate thrust, but the specific impulse is around 450 s and does not allow for optimal mission times. Other advanced technologies such as electronic propulsion and light sails have specific impulses on the order of 1,000–5,000 s but currently do not provide sufficient thrust for crewed missions.

The current frontrunner for improving performance for crewed spaceflight is nuclear thermal propulsion (NTP), which involves using nuclear fission to heat a working fluid, in this case hydrogen, and accelerate it

through a nozzle to produce thrust. NTP is not a new technology; it was pioneered during the 1950s–1970s under Project Rover/NERVA [1]. During that time, much work was performed to demonstrate and test NTP engines, and the outcomes were encouraging. However, the work required employing tens of full-scale reactor tests, some of which were even deliberately destroyed in fiery explosions, with a price tag on the order of \$10B (inflation adjusted). After Project Rover/NERVA was cancelled, advances in NTP slowed or stopped all together. Much of what was known was lost over time, making it imperative to undertake a large-scale development effort to establish and modernize NTP for current use. Despite current public and political excitement about space travel, obtaining funding and tolerance for nuclear testing similar to that provided during previous decades is unlikely. Therefore, a more cost-effective, rapidly deployable platform for qualifying fuels and components is needed to successfully develop an infrastructure for NTP engine development. The work described herein details the In-pile Experiment Set (INSET) apparatus, which is designed to meet this need.

### II. TESTING STRATEGY AND DESIGN OUTLINE

A testing strategy to efficiently qualify NTP fuels and components is necessary to understand the requirements of the affiliate experiment designs and facilities needed to carry out qualification work. Benensky and Qualls [2] outlined a fuel qualification plan that identified several deficient NTP areas to be addressed to ensure development of a qualified NTP fuel. In response to this plan, a strategy was proposed to develop and evolve out-of-pile testing to in-pile testing by using general experiment designs and research reactors. [2]. This strategy includes three phases; a simplified graphical representation is seen in Fig 1.

The out-of-pile testing observed in Phase 1 of the strategy includes demonstrating that an experiment facility can reliably provide NTP conditions to candidate specimens and then gather data on specimens to understand performance. This initial testing stage allows

researchers to decide whether to optimize a promising candidate or downselect those that perform poorly.

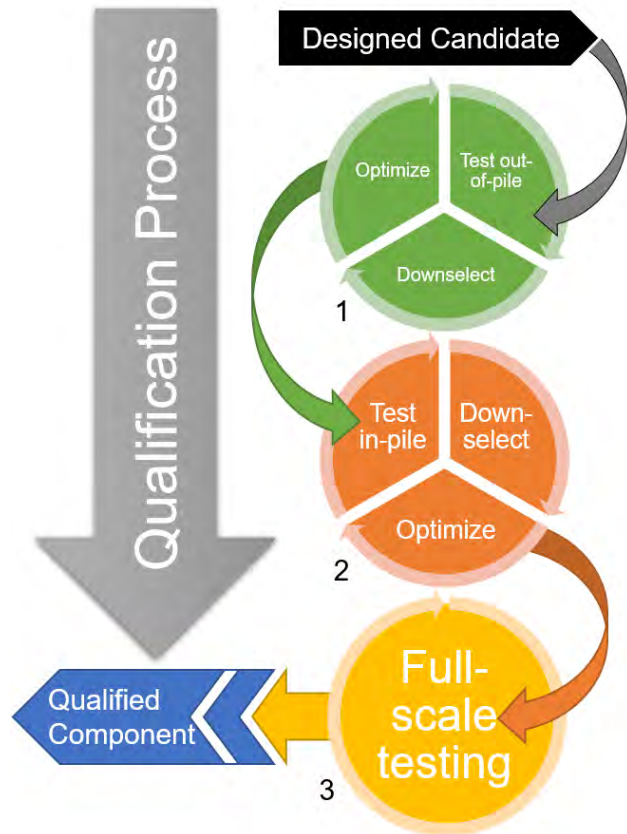


Fig 1. NTP qualification strategy.

Several out-of-pile experiment facilities are available, including the Compact Fuel Element Environmental Test (CFEET) facility [3], the Nuclear Thermal Rocket Element Environmental Simulator (NTREES) [4], and the Out-of-Pile Experiment Set (OUTSET) [5]. While CFEET and NTREES are stand-alone facilities explicitly for testing fuels and fuel surrogates, OUTSET was designed and deployed to demonstrate a direct current (DC), electrically heated capsule that could be scaled and modified for reactor, or it can be used for in-pile testing. The remainder of this paper focuses on the analogous In-pile Experiment set, or INSET.

### II.A In-Pile Experiment Set (INSET) design details

INSET was designed to provide all the functionality of OUTSET. The INSET design requirements were developed as described in R. Howard’s doctoral dissertation [6] and are listed below:

1. appropriate materials selection,
2. flexibility to accept various instrumentation techniques and electrical power delivery,
3. capability to provide and maintain a well-controlled atmosphere,

4. provision of thermal cycling,
  5. temperature control and thermal management, and
  6. establishment of a standard specimen geometry.
- Howard’s work [5], [6] provides a detailed overview of OUTSET and out-of-pile performance. A computer-aided design (CAD) model of the experiment is shown in Fig 2.

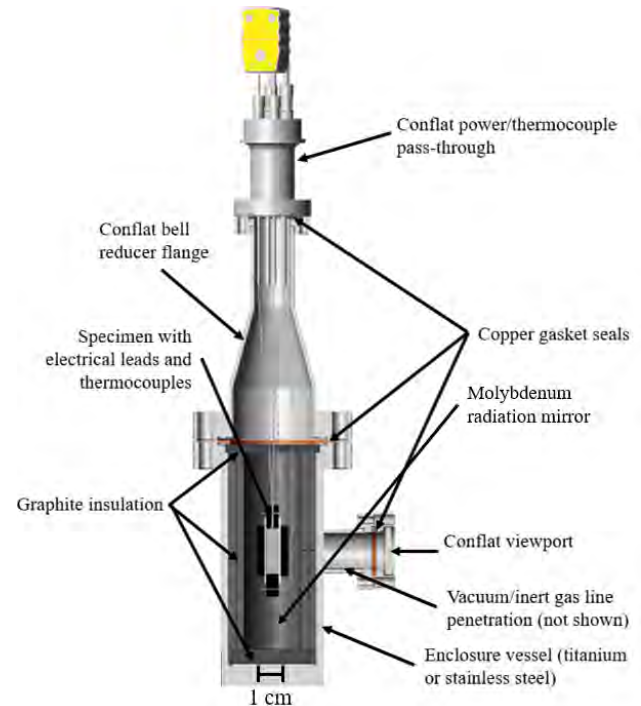


Fig 2. CAD rendering of OUTSET.

Fundamentally, the INSET design philosophy and operating processes are identical to OUTSET. However, INSET is intended to be used in-pile, and OUTSET is to be used for out-of-pile testing. The first iteration of OUTSET was to produce a proof of concept prototype that would evolve into an in-pile experiment. Future iterations will likely have complimentary INSET and OUTSET instances so that design modifications can be demonstrated in the lower risk out-of-pile environment.

Both formats use Conflat® flanges and components to establish the experiment container, the commercially available DC electrical power and thermocouple passthroughs to deliver power and instrumentation, the high-temperature resistant graphite felt insulation, and reflective foils to establish NTP temperatures in the heated region. Moreover, both experiments are operated under vacuum conditions, and the heated region, which contains the heating element and specimens, are common to both designs. Lastly, the experiments are both instrumented with type C (W-Re) and type K (Ni,Cr) thermocouples to verify heated region and containment temperatures, respectively.

The INSET design deviates from the OUTSET design in three primary areas:

1. The INSET containment size is larger;
2. The INSET material selection was optimized to minimize neutron activation; and
3. INSET power limits may be larger than those in the OUTSET platform.

INSET containment was enlarged for several reasons. Primarily, the assembly of OUTSET was tedious, requiring the use of fine tools to mate parts together and to connect instrumentation and power wires. A larger container provides a more ergonomic interface for researchers assembling the experiment. Also, a larger containment volume provides additional space for accommodating a larger heated region or specimens. As the purpose for INSET is to test fuels and components for NTP, its larger experiment plenum provides a more versatile interface for unqualified instrument candidates and other infrastructure that may not yet be identified. See Fig 3 for a comparison of OUTSET and INSET containments.

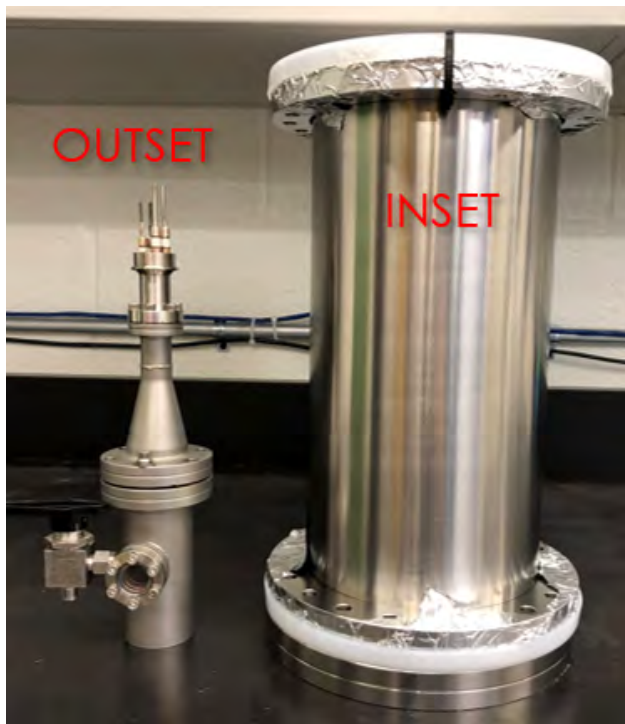


Fig 3. Size comparison of the 120 cm<sup>3</sup> internal volume OUTSET (left) and the 6,000 cm<sup>3</sup> internal volume INSET (right).

The OUTSET experiment containment was fabricated from 304L stainless steel, an alloy notorious for producing <sup>60</sup>Co as a neutron activation product that emits high-energy gamma rays, which can be problematic and costly to shield during shipping and handling. For

INSET, Al-6061 alloy was selected to replace the 304L stainless steel, because the Al alloy produces less activation products, making it more manageable during post-irradiation shipping and handling. Neutronic analyses were performed to verify that the material change was beneficial and are documented elsewhere [7].

The OUTSET design was power limited because the power passthrough used was rated for a maximum of 15 amps-DC. Howard's work [6] showed that to reach higher heated region temperatures, a 15 A source was not feasible. Therefore, a 30 A power passthrough and larger gauge electrodes were incorporated into the INSET design. INSET's increased containment size made incorporating the larger passthrough and electrodes easier to deploy. A CAD rendering of INSET is shown in Fig 4.

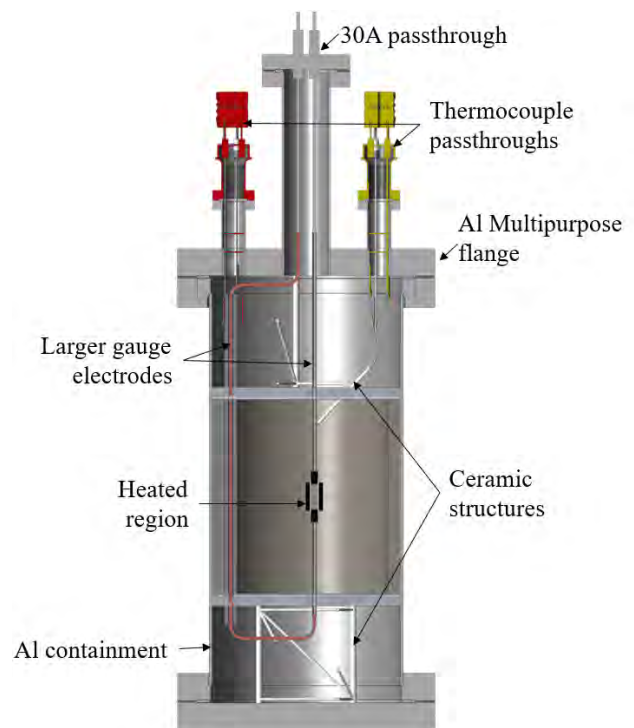


Fig 4. CAD rendering of INSET.

Other design changes that were not included in the earlier list are as follows:

- incorporation of a multipurpose flange to provide more penetration points for instrumentation and gas communication,
- Al alloy Conflat® metal gaskets compatible with the flanges and reduced activation,
- zirconia “paper” to provide an electrical barrier between the larger electrode and the containment wall, and
- ceramic structures to support internal insulation and wiring.

### III. ONGOING AND FUTURE WORK

The INSET design is currently being tested, and its thermal performance is being characterized. A scale stainless steel OUTSET version (out-of-pile) prototype was fabricated for this purpose. Many modifications incorporated into INSET have been shown to improve functionality. For example, power levels as high as 1 kW have been safely delivered, whereas earlier powers were limited to ~350 W. However, the experiment platform's design should be considered as evolving, and improvements are expected to be incorporated to further simplify assembly and reliability.

To date, INSET has successfully undergone its first irradiation experiment to test NTP fuel surrogates at the Ohio State University Research Reactor. This work is fully detailed in other submissions to the Nuclear & Emerging Technologies for Space (NETS 2020) conference proceedings [7], [8]. OUTSET and INSET were developed to provide the NTP research community with a viable experimental platform that is rapidly deployable and relatively inexpensive to use. The outcomes of this initial irradiation and experiment demonstration are considered to be a successful beginning to providing a new experimental capability to the NTP community.

### ACKNOWLEDGMENTS

This work was funded by the National Aeronautics and Space Administration through the US Department of Energy office of Nuclear Energy.

The author also acknowledges Dr. Thomas J. Harrison and Dr. Dianne Ezell of the Oak Ridge National Laboratory, along with Mr. Tyler Steiner and Ms. Emily Hutchins of the University of Tennessee, Knoxville, for their support of this work. Also, we acknowledge the Ohio State University Nuclear Reactor Laboratory for providing us with the opportunity to use their facility.

### REFERENCES

1. S. K. BOROWSKI, D. R. MCCURDY, and T. W. PACKARD, "Nuclear Thermal Rocket (NTR) Propulsion: A Proven Game-Changing Technology for Future Human Exploration Missions," Global Space Exploration Conference (GLEXP-2012.09.4.6x12341), Washington, DC (2012).
2. R. H. HOWARD, T. J. HARRISON, and J. D. RADER, "*Technology Implementation Plan: Irradiation Testing and Qualification for Nuclear Thermal Propulsion Fuel*," Oak Ridge National Laboratory, ORNL/TM-2017/376, Oak Ridge (2017).
3. K. BENENSKY, M. BARNES, D. BRADLEY, C. ROMNES and R. HICKMAN, "Operational Characterization and Testing of NASA MSFC's Compact Fuel Element Environmental Test (CFEET)," Nuclear and Emerging Technologies for Space, Richland, WA (2018).
4. W. J. EMRICH, "Initial Operation and Shakedown of the Nuclear Thermal Rocket Element Environmental Simulator (NTREES)," AIAA/ASME/SAE/ASEE Joint Propulsion Conference, Cleveland, OH (2014).
5. R. H. HOWARD and A. E. RUGGLES, "Design and Out-of-Pile Testing of a Novel Irradiation Experiment Vehicle to Support Qualification of Nuclear Thermal Propulsion Components," *Nuclear Engineering and Design* **361** (2020).
6. R. HOWARD, *A High Temperature Out-Of-Pile Experiment for Testing Nuclear Thermal Propulsion Surrogate Fuels*, Doctoral Dissertation: The University of Tennessee, Knoxville (2019).
7. E. HUTCHINS et al., "Activation Analysis of Subscale Experimental Testbed: Towards Simulating Nuclear Thermal Propulsion Prototyping Conditions for Material Testing," Nuclear & Emerging Technologies for Space, Knoxville, TN (2020).
8. T. STEINER et al., "Nuclear Thermal Propulsion Subscale Experimental Testbed for Material Investigations Using the Ohio State University Research Reactor," *Nuclear & Emerging Technologies for Space*, Knoxville, TN (2020).

## SPRINTR: ADVANTAGES OF FLAT PLATE VERSUS PRISMATIC NTR FUELS

Dr. Steve Howe<sup>1</sup>, Dr. Troy Howe<sup>1</sup>

<sup>1</sup>Howe Industries LLC, 1435 E. University Drive Ste C-108, Tempe, Arizona, 85281

Primary Author Contact Information: [Steve@howeindustries.net](mailto:Steve@howeindustries.net), 480-967-5660

As the US migrates from space exploration into space development, an infrastructure must be put in place that can transport tons of equipment and personnel rapidly and cost effectively. Nuclear fission is currently at the forefront in high energy density systems, boasting over 10,000,000 times more energy per pound than comparable amounts of gasoline, natural gas, coal, or even rocket fuel. Nuclear power opens up an entire new world of space development, allowing for fast transit times, longer missions, reliable power sources, and greatly reduced costs. Howe Industries LLC has conceived a new concept for a flat plate nuclear rocket fuel form which emits clean exhaust, has high Isp, has a high thrust to weight, and is affordable. The SPRINTR will utilize High Assay Low Enriched Uranium (HALEU), produce a thrust of over 100,000 N, and have an Isp over 900 s.



Figure 2: Concept of the SPRINTR nuclear thermal rocket.

### I. SPRINTR Concept

The Scored Plate Reactor for an Innovative Nuclear Thermal Rocket, or SPRINTR [1], concept relies on using flat plate fuel geometry instead of the long, thin, prismatic fuel elements usually used. The plate material can be tungsten cermet based or adapted to other fuel forms such as graphite or carbides as desired. Efforts into flow channel optimization have revealed that the temperature profile of the SPRINTR core can be leveled by altering the flow characteristics at every point in the core, drastically reducing temperature peaking issues. The ability to readily control the shape, depth, and length of the flow channels on the surface of the plate enables the cooling rate to match the power profile. No other NTR design has had this capability. Thus, the potential exists for the entire volume of the core to be near the same temperature and allows



Figure 1: A graphite based SPRINTR fuel plate.

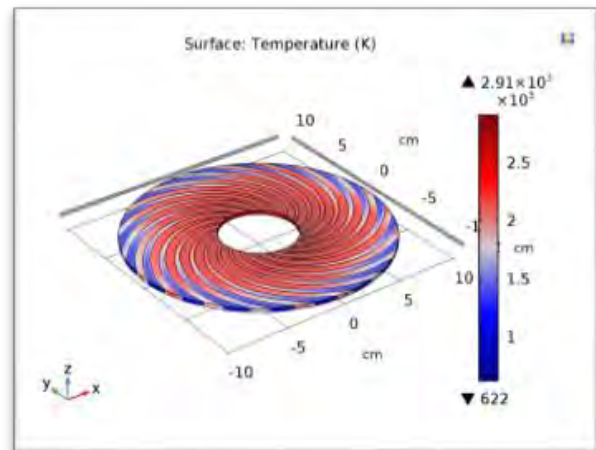


Figure 3: Thermal analysis results of a SPRINTR fuel plate. The solid fuel matrix maintains a favorable temperature distribution while simultaneously heating the propellant to very high temperatures.

maximum Isp to be produced. With the new push for humanity to explore space with nuclear power [2], the SPRINTR nuclear rocket is ideal to provide the necessary performance and reliability.

## II. Coating the Plates

The fuel rods of the past had a number of issues that needed to be addressed before nuclear thermal propulsion could be achieved. One of these issues for graphite-based fuels was the presence of mid-band corrosion [3]. During operation, hot hydrogen would react with the graphite in the fuel and erode away the material. To prevent this, a layer of ZrC was applied to protect the graphite.

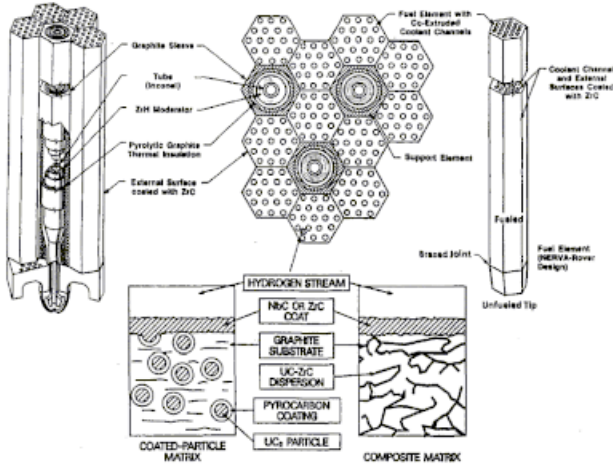


Figure 4: Previous iterations of NTR designs had long prismatic fuel forms made of graphite.

However, given the long, thin nature of the flow channels, often this coating would be difficult to apply uniformly. Any faults in the application would allow hydrogen to penetrate and damage the fuel [4-7].

The SPRINTR fuel plates address this issue by exposing the flow channels and allowing the ZrC coating to be applied effectively every time over the entire surface of the plate. The coated plates are then stacked together to make the core. This ensures there will be no faults in the coating, and no fission products released into the exhaust.

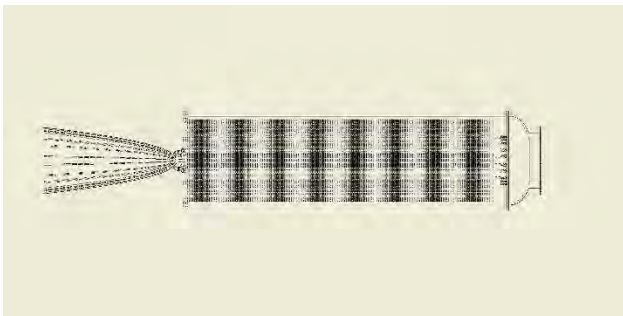


Figure 5: Assembly of fuel plates stacked together to create an engine core.

To achieve this, the plates can be treated with a plasma spray, CVD coating, or reactive melt infiltration (RMI). The RMI method would allow for a zirconium metal layer to be deposited and baked at high temperature.

The carbon from the fuel plate would diffuse into the coating to form ZrC. This method has the added benefit of allowing the subcore to be welded together while the metal coating is present, then baked to form ZrC after being assembled.

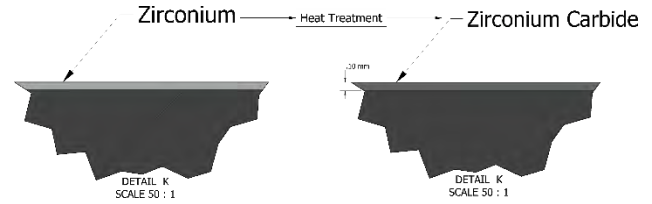


Figure 6: Visualization of the zirconium metal layer on the fuel plate transforming to ZrC through heat treatment.

## III. Subcore Concept



Figure 7: A single SPRINTR subcore.

One very attractive aspect of the SPRINTR design is that it can utilize an outside-in flow direction. The full core is comprised of a number of individual stacks called subcores. There are numerous benefits to the subcore design, including:

- 1) The mounting of the subcores can be done with low temperature materials, as the sides will remain cool.
- 2) Low temperature moderator (LiH) can be used between the subcores to minimize mass.
- 3) Cores are modular and can be removed to refuel or detach for other uses.

## IV. Controls and Flow

Controlling the criticality of the system can be achieved by placing control drums between the subcores. These would have neutron absorbing boron on one side, and neutron moderator on the other. When they are rotated, they either absorb neutrons to reduce criticality or moderate neutrons to increase it. By being directly in the path of the neutrons, the controls are extremely effective.

The subcore design also allows for the ship to be directly through throttling of the propellant. Each subcore is fed independently through electric pumps. If the flow rate of the pump is increased, the mass flow through that subcore will increase, and increase thrust. Therefore, the ship can make adjustments to its trajectory simply by temporarily modifying the flow rate through subcores.

The flow of the propellant is extremely simple and unidirectional. The propellant enters at the top of the subcore and passes down along the outside of the fuel

plates. From there it passes through the flow channels in the plates, heats up, and provides thrust. However, a small portion of the hydrogen propellant enters the double walled nozzle. The inside of the nozzle is porous and allows for transpiration cooling. Thus, the design avoids the need to divert portions of the flow, pre-cool the nozzle, cool tie tubes, or otherwise add complications to the flow path.

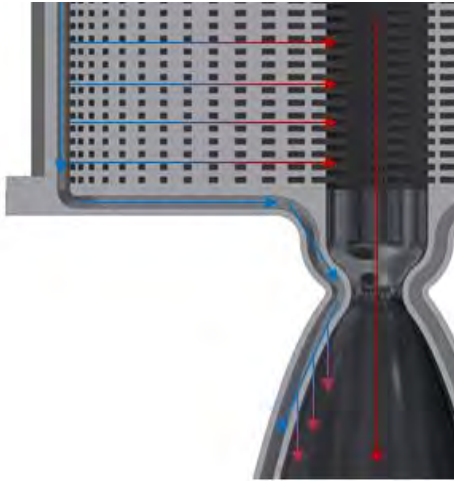


Figure 8: Direction of propellant flow through the subcore.

### V. Bi-Modal Operation

Because the subcores are modular, they do not all need to be exactly the same design. It is possible to have one of the subcores reduced in size and equipped with a closed loop power cycle. This would prevent it from providing thrust but would generate electrical power during operation. This would also allow the system to operate at the destination



Figure 9: Assembly of subcores in the full core. The central subcore is reduced in size and equipped to provide electrical power.

Having a bimodal option reduces the need for a secondary power generation system to be onboard the craft. Additionally, the modular cores can be taken off the ship and used for ground based power if desired. Future designs may include excess subcores to “seed” power stations on outer planets which can then breed more fuel for more SPRINTR rockets.

### VII. Performance

The SPRINTR is able to achieve the high performance of the previously tested NTR designs [8,9] without sacrificing Isp, thrust, or safety.

With the effective and verifiable coating method there is no risk for fission products to escape to the flow stream. This allows for the use of graphite-based fuels, such as were used in the NERVA program. Without this coating capability, the material must be a high temperature refractory metal that does not react with the propellant [10-12]. Although such options exist, they are currently not financially viable solutions.

The Isp of the SPRINTR can reach over 900s, thanks to the use of the high performance graphite matrix. The heating profile of the plates has a higher power generation on the outside edges, due to the interaction with other subcores. This is ideal for heating the low temperature propellant at its coldest point. As it flows inward, the propellant approaches the maximum fuel plate temperature and exits at over 2800K.

The SPRINTR rocket delivers a high thrust of over 10,000 N in current designs and can be modified based on subcore size and number of subcores needed. High thrust missions, such as building lunar bases, may require a dozen or more subcores, while deep space probes may prefer only four subcores to minimize mass.

### VIII. Missions

A functioning nuclear thermal rocket will open the door to many new missions which are necessary for the exploration and expansion of humanity into space. For near earth purposes, an NTR can provide rapid response in orbit to defend assets, deploy satellites, or monitor sensitive areas. Having a fleet of NTR equipped spacecraft will allow for immediate action capabilities in the near future.

Taking humans to the moon and constructing a lunar base will require metric tons of equipment and materials. Achieving this with chemical rockets will require numerous launches and very large budgets. An NTR mission to the moon would be able to take 3x the payload, and drastically reduce costs. Furthermore, ice deposits on the moon could be used to re-fuel the NTR hydrogen tanks and save even more money in the space fairing economy.

Transit to Mars using chemical rockets will require hitting very precise launch windows which only

appear every few months. This means astronauts will be in space for very long periods of time and will be exposed to lethal doses of galactic cosmic rays. The NTR allows for alternative trajectories to be used which can decrease overall mission times and ensure the Martian explorers return safely to Earth.

The future space fairing infrastructure will be dependent on nuclear technologies, as nearly everything required for nuclear space travel is available in-situ. Uranium or thorium can be mined from the moon and used to breed more fuel. The modular subcores can deposit power stations on distant worlds and return later as more fuel is created. Water can be electrolyzed by those power stations to create life giving oxygen and hydrogen propellant. And without the steep gravity well of earth, those hydrogen refueling stations on other worlds will be major assets to space explorers.

## IX. Summary

The SPRINTR design solves the issue of mid band corrosion, which allows for a high-performance graphite fuel matrix to be used. The NTR technology will provide propulsion and power to many missions in the near future and will be necessary for mankind's expansion into space. The technology is currently under development by Howe Industries and will pave the way to future space missions using advanced concepts and nuclear power.

## ACKNOWLEDGMENTS

Thank you to NASA's SBIR program for funding the Phase I effort for SPRINTR design. We would also like to thank USNC for their assistance with the SPRINTR design.

## REFERENCES

1. S. Howe and T. Howe, "Fuel Element for an Affordable NTR Phase I Final Report", Contract Number: NNX17CM30P, submitted to NASA MSFC, 2017.
2. <https://www.whitehouse.gov/presidential-actions/presidential-memorandum-launch-spacecraft-containing-space-nuclear-systems/>
3. Daniel Koenig. "Experience Gained from the Space Nuclear Rocket Program (Rover)." Los Alamos National Laboratory. May 1986.
4. Jordan, H.S., "Effluent Effects Evaluation, Pewee 1 SER", Los Alamos Scientific Laboratory report, H8-NTS-1346, October, 1968.
5. Boker, P.C., Kirk, W.L. and R.J. Bohl, "The Behavior of Fission Products During Nuclear Rocket Tests", Los Alamos National laboratory report LA-UR-90-3544, 1990.
6. R.J. Hanrahan Jr., R.L. Smith III, J. Morgan, "Review of the historical capabilities and testing of composite and cermet fuels in Los Alamos. ". LA-UR-02-7186. Los

Alamos National Laboratories, Los Alamos, New Mexico, 2002.

7. D.A. Seifert, R.L. Stuart, P.K. Conn, H.W. McLaughlin, G.J. Luersen. "Fission product behavior within two W-UO<sub>2</sub> cermet fuel elements irradiated in a temperature gradient.", Nuclear Space Programs Space Systems, General Electric, Cincinnati, Ohio, 1968.
8. R.A. Haslett, "Space Nuclear Thermal Propulsion", program final report, pl-tr-95-1064, May 1995.
9. Paolo F. Venneri and Yonghee Kim, "A feasibility study on low enriched uranium fuel for nuclear thermal rockets e II: Rocket and reactor performance", Progress in Nuclear Energy, April 2015.
10. Wesley R. Deason, Michael J. Eades, Peter J. Husemeyer, and Vishal K. Patel, "Exploring the Design Space of CERMET LEU ZrH<sub>1.8</sub> Moderated Nuclear Thermal Propulsion Systems", Nuclear and Emerging Technologies for Space (NETS) conference proceedings, 2015
11. Knight, B.W., McInteer, B.B., Potter, R.M., Robinson, E.S., "A METAL DUMBO ROCKET REACTOR", Los Alamos Scientific Laboratory report LA-2091, January, 1957.
12. R.C. O'Brien, R.M. Ambrosi, N.P. Bannister, S.D. Howe, H.V. Atkinson, "Spark Plasma Sintering of simulated radioisotope materials within tungsten cermets", Journal of Nuclear Materials, 393, 2009, p.108-

## ACTIVATION ANALYSIS OF SUBSCALE EXPERIMENTAL TESTBED: TOWARDS SIMULATING NUCLEAR THERMAL PROPULSION PROTOTYPIC CONDITIONS FOR MATERIAL TESTING

Emily N. Hutchins<sup>1,2</sup>, Richard H. Howard<sup>2</sup>, N. Dianne Bull Ezell<sup>2</sup>, Tyler R. Steiner<sup>1,2</sup>, and C. Miller McSwain<sup>1</sup>

<sup>1</sup>University of Tennessee, Knoxville, Department of Nuclear Engineering, Knoxville, TN, 37996

<sup>2</sup>Reactor and Nuclear Systems Division, Oak Ridge National Laboratory, Oak Ridge, TN, 37830

Primary Author Contact Information: [ehutchi8@vols.utk.edu](mailto:ehutchi8@vols.utk.edu)

*As human space exploration continues to progress, we must change our technologies to ensure safer, faster, and more reliable space travel. One facet of this advancement can be done with Nuclear Thermal Propulsion (NTP), which utilizes the heat from Uranium fission to heat flowing hydrogen propellant, generating thrust. As of today, there is still much work to be done to get NTP from research laboratories to Mars and beyond. Oak Ridge National Laboratory (ORNL) is continuing the effort by creating an experiment capable of replicating the thermal conditions and, in concert with the Ohio State University's Research Reactor (OSURR) facility, radiological conditions expected with NTP. Prior to the first irradiation, a neutron activation analysis was performed to determine the proper handling and shipping timeline. This summary discusses this analysis, with the intention of validating the computational model with experimental data that will be collected in late February 2020.*

### I. INTRODUCTION TO THE EXPERIMENT

Nuclear Thermal Propulsion is rooted in the 1950's, during the Space Race between the United States and the Soviet Union. The general concept of NTP is that uranium fission will heat a propellant, assumed at this time to be hydrogen, and the heated propellant will be expanded through a rocket nozzle, generating thrust.<sup>1</sup> For the missions NTP would prove useful, this rocketry must be capable of withstanding a 950 second specific impulse, thermal conditions up to 3000 K, and a core neutron fluence of about  $10^{17}$  neutrons/cm<sup>2</sup> (Ref. 2, 3). Under such extreme conditions, completing full-scale tests to find the best materials, fuel, instrumentation, and controls is unrealistic and costly. Oak Ridge National Laboratory is one of a handful of facilities to create an experiment capable of simulating one or more of the aforementioned prototypic conditions of an NTP rocket.

The subscale testbed, referred to as In-Pile Experiment Set Apparatus (INSET), was designed at ORNL. INSET was built for both easy reactor irradiation and electrical heating of subscale candidate material samples up to NTP prototypic temperatures, which allows for faster, cheaper, and more customizable testing of the samples desired. Figure 1 to the right shows the fully

assembled testbed prior to the first irradiation at the OSURR facility.

There is a thorough depiction of INSET's design in the NETS 2020 conference proceedings by ORNL's Dr. Richard Howard, titled: *Design of the In-pile experiment Set (INSET) apparatus to support Nuclear Thermal Propulsion fuel and component testing.*



**Fig. 1.** INSET fully assembled prior to irradiation at OSURR.

In a joint effort between ORNL and OSU, the experiment shown in Figure 1 was irradiated in November 2019 at OSU's Research Reactor facility. The OSURR was chosen for this irradiation because of the ease of access and flux capability.

INSET was irradiated in the 9.5 inch inner-diameter (ID) moveable dry tube for a total of 5 hours at 225 kilowatts, which corresponds to a flux of roughly  $10^{16}$  n/cm<sup>2</sup> (Ref. 4). In the last 15-minute period of the irradiation, the temperature in the specimen region was raised to about 455 degrees Celsius. The NETS 2020 conference proceedings by the University of Tennessee, Knoxville's Tyler Steiner, titled: *Nuclear Thermal*

*Propulsion Subscale Experimental Testbed for Material Investigations Using the Ohio State University Research Reactor*, presents the irradiation in detail.

## II. METHOD FOR ACTIVATION ANALYSIS

### I.A. Computational Models

In the interest of material selection for the experiment and safety for handling and shipping, a neutron activation analysis was performed on a computational model of INSET using the Monte Carlo N-Particle (MCNP) and Oak Ridge Isotope Generation (ORIGEN) codes. MCNP provides a neutron flux spectrum by a tally on a user-defined surface.<sup>5</sup> SCALE can calculate the activation of nuclides from a user-defined spectrum, made easier by the COUPLE module. The SCALE input can also be customized to specify the reactor power level, elemental composition of the experiment, and time for both reactor power and decay.<sup>6</sup>

The dimensions and material compositions of INSET's parts were used to make a realistic MCNP model. The specimens modeled in INSET were provided by Neal Gaffin, a doctoral student at the University of Tennessee, Knoxville. Figure 2 below shows the experiment modeled in MCNP, where each color corresponds to a specific material.

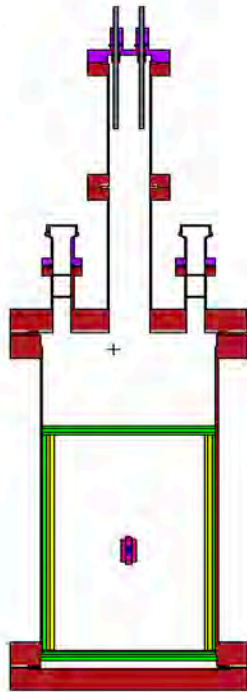


**Fig. 2.** MCNP Model of INSET.

The most notable materials in this model are the aluminum and stainless steel. The body and ConFlat (CF)

flange of INSET was constructed from aluminum-6061, shown in Figure 2 as red, for its low activation under a neutron fluence. Conversely, the surfaces shaded purple in Figure 1 correspond to the greatest activation concern of INSET: stainless steel. These steel parts make up the power and thermocouple CF flange passthroughs, which are incredibly difficult and expensive to find in a less activated materials. Table I below shows a complete list of elements and the amount, in grams, present in the entire experiment based on calculating the volume for each component.

**TABLE I.** INSET Elemental Composition

Element	Mass (g)
Silicon	106.2
Carbon	81.3
Molybdenum	52.9
Zirconium	79.9
Oxygen	48.2
Aluminum	6153.2
Titanium	8.8
Copper	146.3
Magnesium	56.9
Iron	398.9
Chromium	133.3
Zinc	12.7
Nickel	63.9
Manganese	15.5
Tungsten	4.9
Rhenium	5.4
Phosphorus	0.3
Nitrogen	0.28
Hydrogen	0.1
Sulfur	0.2

An existing MCNP model of the OSURR was provided by Neil Taylor, a current doctoral candidate at the Ohio State University. INSET was added to the reactor model to most accurately depict the experiment placement and the reactor's source term. Figure 3 shows the MCNP model of INSET within the OSURR dry tube. Note that the stainless steel is kept out of the path of

greatest neutron fluence in an effort to reduce its activation. The OSURR MCNP model containing INSET was run to tally the fluence on the outside surface of the aluminum body and the outside of the specimen region.

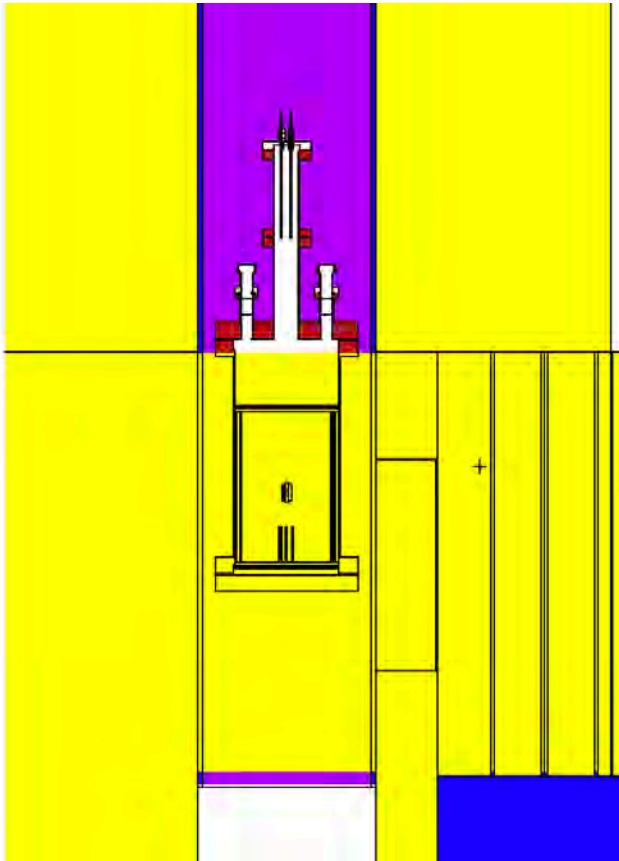


**Fig. 3.** MCNP model of INSET in the OSURR dry tube (reactor core to the right of INSET’s lower half).

After the MCNP model was run, the neutron flux spectrum, mass information in Table I, reactor power level, reactor power time, and decay time were used with the COUPLE module as inputs for the SCALE code. The flux values were taken from the tally on the body of INSET, where the flux is the highest. This means even the stainless steel received the same flux as the other materials, when, in reality, the most-activating materials, such as stainless steel, will be kept further away from the irradiation field.

The activation analysis results in a dataset that shows the activity, in Curies, of each isotope produced by the irradiation for the 72-day time period that was specified. The activities of isotopes undergoing gamma decay are converted to dose, in units of millirem per hour at 1 meter (mrem/Hr @ 1 m). The doses calculated are used to determine the time at which INSET is safe to be handled or shipped.

### I.B. Experimental Data Collection

After irradiation, the experiment was shipped from the OSURR to ORNL’s Low Activation Materials Development and Analysis (LAMDA) facility. It will involve the gamma spectroscopy of the tungsten-rhenium thermocouple wires leading into the specimen region of INSET. This work will be conducted in late February 2020.

### III. Results

The computational activation analysis shows that the safe to handle dose, 100 mrem/Hr @ 1 m, occurs between days 2 and 3 post-irradiation, and the experiment reaches the dose for the Department of Transportation’s Yellow II shipping category, 1 mrem/Hr @ 1 m, at 55 days.<sup>7</sup> It also shows the level of radiation at which only the long-lived isotopes are still decaying. Figure 4 shows that there is a large amount of short-lived gamma ray activity that, within 3 days of irradiation, has gone below the safe-to-handle level.

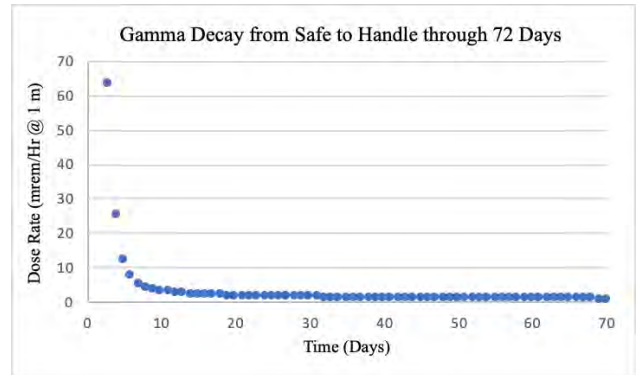


**Fig. 4.** Plot of the gamma decay from 3-72 days after irradiation.

Table II shows the timeline for after irradiation at the OSURR developed from the MCNP and SCALE results.

**TABLE II.** Timeline for INSET Handling and Shipping

Time from Irradiation Start	Time	Status	Dose Rate (mrem/Hr @ 1 meter)
0	8:00 AM	First Day of Experiment (Reactor ON)	0
5 Hours	1:00 PM	End of Irradiation (Reactor OFF)	267E+05
2 Days	3:00 PM	End of Day, 2 Days After Irradiation Ended (Reactor OFF)	134.08
3 Days	8:00 AM	Morning, 3 Days After Irradiation Began (Reactor OFF)	63.26
55 Days	8:00 AM	Safe to Ship	1.00

To date, the only dose data recorded of INSET was before shipping it to LAMDA, at 57 days post-irradiation. The highest contact and 1-meter dose rates were 7 mrem/Hr and 0.5 mrem/Hr @ 1 m, respectively. At roughly half of the aforementioned value, the dose rate from the computational activation analysis is 0.98 mrem/Hr @ 1 m, which may be caused by model shortcomings or the use of conservative flux values on the most activating materials in the experiment.

The remaining results of this work will be comparing the computational and experimental data, as described in the previous section. The activity of the isotopes in the tungsten-rhenium thermocouple wire specimens will be compared to the activity of the corresponding isotopes from SCALE, at matching times of decay.

The Post-Irradiation Examination (PIE) will be conducted in late February 2020, which will complete the objective of the work described in this summary.

#### IV. Future Work

The MCNP model will need to be reconstructed. There has been a magnitude of changes made to INSET since the first irradiation that have to be captured for the simplicity of future in-pile tests. It is expected that once a final model is made, future activation analyses can be performed by simply adding the appropriate sample geometry and material and then executing the code.

#### ACKNOWLEDGMENTS

This work is funded by the National Aeronautics and Space Administration through Oak Ridge National Laboratory Subcontract Number 4000169281. We would like to acknowledge Oak Ridge National Laboratory's Dr. Thomas J. Harrison for the procurement of this funding, in addition to his guidance as this project has developed.

We would like to acknowledge the Ohio State University's Nuclear Reactor Laboratory for their support and flexibility in getting this experiment in the reactor. In addition, we acknowledge the assistance in the irradiation process from reactor staff Andrew Kauffman and Kevin Herminghuysen.

We acknowledge Neal Gaffin for providing the samples that were used as the first specimens to undergo irradiation in INSET.

Emily Hutchins acknowledges the assistance from Neil Taylor, a current PhD Candidate at the Ohio State University. His insight on the neutron activation analysis process and knowledge of the existing MCNP model of the OSURR was crucial in the work presented in this summary.

Emily Hutchins acknowledges Dr. Brandon Wilson, who assisted her in checking each activation analysis for errors.

Emily Hutchins would also like to thank her advisor, Dr. Lawrence Heilbronn, for his mentoring and support with both the computational and experimental aspects of this work.

#### REFERENCES

1. Gunn, Stanley V. (1989) "Development of Nuclear Rocket Engine Technology," *AIAA/ASME/SAE/ASEE 25<sup>th</sup> Joint Propulsion Conference*. Monterey, CA, 10-12 July. Washington, D.C.: American Institute of Aeronautics and Astronautics, pp. 1-17.
2. S. Borowki, D. McCurdy and T. Packard, "Nuclear Thermal Propulsion (NTP): A Proven Growth Technology for Human NEO / Mars Exploration Missions," *IEEE Aerospace Conference*, pp. 1-20, 2012.
3. M. King and M. Houts, "Sensor Needs for Nuclear Thermal Propulsion," in *IEEE Wireless for Space and Extreme Environments*, 2018.
4. "Nuclear Reactor Laboratory," Ohio State University College of Engineering, 2019. [Online]. Available: <https://reactor.osu.edu/>.
5. J. K. Shultis and R. E. Faw, "An MCNP Primer," Manhattan: Department of Mechanical and Nuclear Engineering, v. 1, 2004.
6. B. T. Rearden and M. A. Jessee, "SCALE Code System," ORNL/TM-2005/39, version 6.2. 1.
7. "Understanding Shipping Labels and Placards for Radioactive Materials." Understanding Shipping Labels and Placards for Radioactive Materials - Radiation Emergency Medical Management, [www.remm.nlm.gov/transportation\\_hazard\\_id.htm](http://www.remm.nlm.gov/transportation_hazard_id.htm).

## LEU NTP ENGINE SYSTEM FOR FLIGHT DEMONSTRATOR FOR A MARS CREW MISSION NTP

C. Russell Joyner II<sup>1</sup>, Wesley Deason<sup>2</sup>, Michael Eades<sup>2</sup>, David Hanks<sup>4</sup>, Tyler Jennings<sup>1</sup>, Timothy Kokan<sup>3</sup>, Daniel J. H. Levack<sup>4</sup>, Brian J. Muzek<sup>3</sup>, and Christopher B. Reynolds<sup>3</sup>

<sup>1</sup>Aerojet Rocketdyne, West Palm Beach, Florida 33410, USA,

<sup>2</sup>Ultra-Safe Nuclear Corporation -Technologies, Seattle, Washington 98199, USA,

<sup>3</sup>Aerojet Rocketdyne, Huntsville, Alabama 35806, USA,

<sup>4</sup>Aerojet Rocketdyne, Canoga Park, California 91309, USA,

561-882-5349; [claudio.joyner-ii@rocket.com](mailto:claudio.joyner-ii@rocket.com)

*The development work accomplished over past few years as part of the NASA STMD GCD LEU Nuclear Thermal Propulsion (NTP) program, is moving towards the full development and launch of a nuclear space system demonstrator. This demonstrator development activity would use a nuclear fuel material that is capable of high temperature (e.g., peak temperatures between 2,800 to 3,000-deg K) operation to achieve specific impulse (Isp) at or above 900 seconds. This flight demonstrator NTP would likely use hydrogen propellant as the coolant, use either a Ceramic-Metallic (Cermet) or Carbide based fuel in the reactor core, and employ as much off-the-shelf liquid rocket hardware as determined possible to save cost during the development. The flight demonstrator nuclear fuel, components, cryo-fluid management (CFM) systems, control systems, and stage integration approaches will have direct lineage to the full-scale development (FSD) NTP system that crewed Mars NTP missions would employ. It is envisioned that the flight demonstrator could be sized between 7,000-lbf and 15,000-lbf and use a fuel assembly similar to that of the larger Mars crew NTP, in the 25,000-lbf class.*

*The future of human exploration missions to Mars is dependent on solutions to the technology challenges identified by the United States Government agencies and industry. Many key architecture technology solutions are needed in propulsion, power, cryo-fluid systems, crew transport vehicle life-support systems, planetary lander designs, surface habitat and life-support systems, and other sub-systems so that the human crew can depart from Earth orbit, travel to other planets and return back to Earth with the lowest risk to crew and the mission.*

*Nuclear propulsion methods, proven by the work performed during the Rover and Nuclear Engine for Rocket Vehicle Applications (NERVA) programs with more than 20 reactors and engine system tests, have demonstrated that nuclear propulsion is feasible.*

*When used in a high-thrust, high-Isp propulsion system, NTP can produce fast crew Mars mission transits (within 120 to 220 days each way), mission trajectories that can be altered to create 1-year return abort capability, accomplish both long-stay and short stay missions with a common propulsion and stage design, and develop a fully reusable space transportation infrastructure.*

*Nuclear space systems can provide the power for surface and other crew systems and could evolve over the next several decades so they can be integrated with electric thrusters to create Nuclear Electric Propulsion (NEP).*

*Aerojet Rocketdyne (AR) has stayed engaged for several decades in working nuclear space systems and has worked with NASA recently to perform an extensive study on using Low Enriched Uranium (LEU) NTP engine systems for a Mars campaign involving crewed missions from the 2030s through the 2050's.*

*AR has used a consistent set of NASA ground rules and has assessed NTP as the high-thrust propulsion option to transport the crew and provide more mission capability than chemical or other propulsion systems. These ground rules have been recently updated in 2019 to include the characteristics for examining short-stay or Opposition-class Mars missions.*

*AR study activity in 2019 has focused on showing that a flight demonstrator NTP design can be defined that reduces the technical risk for larger thrust NTP designs. This work will continue in 2020 and will examine the impact on the demonstrator stage concept and implications to the stages that will be needed to perform Mars crew missions.*

*This paper provides an update on the work to define a NTP flight demonstrator and the results of the on-going engine system and mission trade studies.*

## I. INTRODUCTION

AR has been working with NASA, Ultra-Safe Nuclear Corporation - Technologies (USNC-Tech), BWX Technologies (BWXT), and Analytical Mechanics Associates (AMA) to examine NTP mission approaches, NTP reactor configurations, NTP engine systems concepts, and spacecraft design challenges. Past studies have looked at discrete LEU NTP designs to compare LEU to High Enriched Uranium (HEU) core designs for NTP. Earlier efforts identified LEU NTP design characteristics for further examination to improve the LEU core designs based on CERMET fuel operating in the thermal spectrum via neutron moderation. Those designs were moderated using materials in a structural assembly (tie-tubes) similar to the Nuclear Engine for Rocket Vehicle Applications (NERVA) design.<sup>1,2</sup>

In 2019, AR continued NTP engine systems work and performed additional architecture trades based on LEU NTP designs matured to use a Uranium Nitride kernel in one of two fuel forms (i.e., Cermet or a Packed Particle in a refractory material matrix). Much of the work performed in 2019 on the LEU NTP fuel and overall engine system is being updated for new fuel and core designs to permit eventual higher temperature fuel operation and provide a path to lower mass NTP systems. These updates to the LEU NTP are the foundation for the roadmap being developed to determine a “linked” pathway or roadmap between a fuel/core designed and manufactured for a flight demonstrator and the FSD 25,000-lbf thrust crew vehicle NTP.

Updated architecture trades in 2019 included looking at the NTP designs for crew Mars missions with shorter stay times (e.g., 50 days in Mars vicinity). More on this area of analysis will be discussed in Section IV.

## II. LEU NTP CORE AND ENGINE SYSTEM DEFINITION FOR FULL SCALE MARS MISSION NTP

AR, USNC-Tech, and BWXT in 2019 went through a design iteration to refine the LEU NTP fuel details and core layout and increase the detail in the engine mechanical assembly. These efforts identified core designs with lower mass and provided a wider range of analysis to capture more detail in the engine thermodynamic design. LEU core configurations were optimized for maximum specific impulse (Isp) and minimum core reactor mass while being designed to assure that the core could achieve criticality for continuous operation.

AR is leading the overall engine system integration of the external components. BWX technologies is the lead for defining the pressure vessel/reactor assembly (a.k.a., PVARA), manufacturing approaches of the fuel, and the mechanical design of the internal reactor assembly.

In designing the components that make up a LEU NTP system, the mission architecture and vehicle design set many of the operating conditions (e.g., operating burn times of 200 to > 1,000 seconds).

The LEU NTP engine system is comprised of a reactor subsystem, a turbomachinery component system, regeneratively cooled nozzle and chamber section, four control valves (moderator element, fuel element, regeneratively cooling flow, and turbine flow bypass), at least two blocker or check valves (main turbine back flow prevention, main pump back flow prevention), propellant shut-off valve, radiatively-cooled nozzle and extension device, engine control unit, and an external shield/vehicle mount plate.

The engine operates using an expander or topping cycle where the hydrogen flow leaves the tank supply duct and is controlled by the shut-off valve to supply hydrogen to the turbopump machinery inlet. The hydrogen, at ~37 deg Rankine and ~20 to 35 psia pressure, enters the pump inlet (inducer) and is pumped to the required pressure (i.e., 2,500 to 3,000 psia) and proceeds to a flow split where some hydrogen goes to be heated as it cools the nozzle and chamber (regen-cooling) as well as the radial reflector that surrounds the reactor core. Another part of the hydrogen flow goes to cool the moderator elements within the reactor core. Both of these flows recombine on exiting the pressure vessel and reactor assembly (e.g., PVARA) and are then directed to the turbine(s) of the turbomachinery subsystem. The flow can be split and used to drive a boost pump (used to reduce pump system inlet pressures from the tank and reduce sensitivity to two-phase flow) or go directly to the main turbine. The flow through the turbomachinery is controlled (and thus its speed and pressure) using the turbine bypass valve. Some flow goes through this valve and some goes to the turbine of the main turbopump to drive the turbomachinery. The warm hydrogen gas exits the turbomachinery subsystem and is directed to the fuel element control valve (used to control flows for reactor start and shutdown) and then proceeds to enter the reactor subsystem. The warm hydrogen then flows through the internal shield (if needed) and the

axial reflector at the forward end of the reactor core. The flow then proceeds through all the fuel elements where it is heated by the thermal energy deposited into the coolant flow by nuclear fission. The flow is heated as it proceeds through a series of channels in each fuel element and exits the reactor aft end at temperatures greater than 4,600 deg. Rankine. The hot hydrogen at nearly 1,000 psia is choked (i.e., Mach 1 conditions) at the throat or nozzle entrance and then is accelerated by the pressure differential due to the low pressure (space vacuum conditions) at the nozzle exit. The hot hydrogen exits at velocities at or greater than 28,000 feet per second.

The turbopump requirements are based on the mission architecture operating duration and the engine operation for multiple burns, some that can last up to 15 minutes continuous. Also the turbopump (boost pump element) can serve to support the pressurization and feed some propellant for cooldown operation.

The propulsion system will be started and re-started many times over the life of the engine system. Also there will be long periods when the engine system is shut-down. During the mission the shutdown could be as long as 600 days. This wide variation of operating requirements put a premium on weight, performance, and reliability and the turbomachinery trades attempt to address these requirements.

The LEU NTP design that evolved in 2019 featured a moderated design that is comprised of hexagonal fuel elements and moderator elements arranged in a near 1:1 ratio within the reactor core. The thermodynamic cycle is based on an expander or topping methodology to provide the drive gas for powering the turbine or turbines to get the pump discharge pressure that can meet a design chamber pressure of 1,000 psia. The hydrogen propellant is used to cool the moderator, nozzle, and chamber. The flow then is passed to the turbine of the turbopump.

The design approach and assumptions discussed previously showed a turbopump that can meet the performance requirements for an “expander or topping” cycle but do not necessarily support a wide range of operation during the mission. The scaled 2-stage centrifugal pump and 1-stage turbine provides good performance and reduced complexity for the cycle but it does not provide sufficient NPSP margin for any propellant flow phase change at the inlet due to nuclear heating.

AR determined, after trades with three types of boost-pumps, to use a non-integrated gas-driven turbine approach for the boost pump. The horsepower requirements for the boost pump to deliver 28 lbm/sec of flow to the main pump was calculated to be between 50 to 100 psia.

Figure 1 presents the LEU NTP engine system cycle for the non-integrated boost and main turbopump with the bleed flow from the moderator element to provide gas to drive the boost pump.

The LEU NTP long start and the complexity impact on engine system reliability lead the LEU NTP engine design team to recommend a decoupled (gas driven) boost pump. Using the decoupled boost and main turbopump permits the start to be controlled more smoothly using the minor flow split of gas from the moderator elements that feed the main pump turbine. Also the decoupled gas driven boost pump has potential to be used to support pumping the cool down hydrogen flow to the reactor post-shutdown.

LEU NTP engine cycle optimization and turbomachinery integration are continuing as this paper is prepared. Additional details for the valves and control assumptions are being added as the control system is refined and as material specifics for the turbomachinery and valves are included in the design. The reactor design analysis cycles DAC-3 and DAC-4 in 2019 analyzed two fuel form types in the hexagonal shape: packaged particle and ceramic metallic (Cermet), both comprised of a Uranium Nitride, Molybdenum, and Tungsten matrix.

The schematic shown in Figure 1 illustrates the type of NTP flow path that the current thermodynamic analysis is being based on using the AR NTP cycle model.

As reported in the papers presented at NETS 2018 and 2019, the AR NTP cycle model captures the effects of the power density distribution and heat transfer variations for any LEU NTP reactor core FE and ME design approach.<sup>3,4</sup>

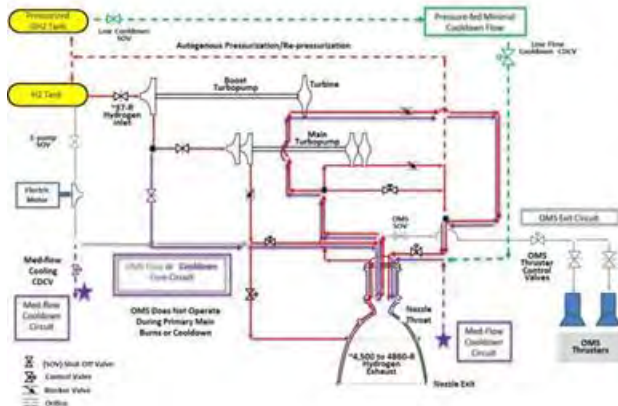


**Fig. 1.** A Schematic of a LEU NTP Engine System – 25,000-lbf Thrust Class.

The NTP is capable of 900+ seconds of Isp with a nozzle similar in size to the AR RL10B-2. AR, working with fuel and core design specialists, is evolving the analysis of the NTP flight demonstrator so it has alignment with the design needs of a larger 25,000-lbf NTP.

Figure 2 shows the 25,000-lbf NTP as compared to the RL10B-2 with the larger 400:1 area ratio nozzle. It is important to understand the crew Mars mission performance needs of the larger 25,000-lbf thrust NTP design in order to define a robust pathway for the technology risk reduction the NTP flight demonstrator will provide.

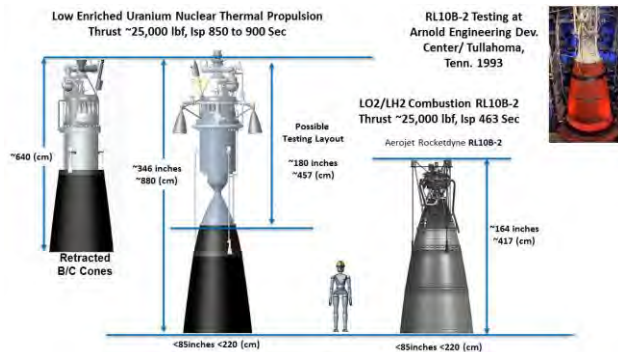


**Fig. 2.** Example LEU NTP Engine System Configuration with Integrated Boost and Main Turbopumps and Orbital Maneuvering Thrusters.

### III. LEU NTP FLIGHT DEMONSTRATOR CONCEPT

In 2019, AR started examining various approaches for flight demonstrator size NTP systems

that would have lineage to a NTP-based Mars architecture based on the human Mars mission.

Mission concepts were considered that provided information on NTP operational verification, demonstration of integrated cryogenic systems versus non-cryogenic systems, NTP integration with a cryogenic stage similar to the Mars vehicle, packaging capability for launch on a commercial launch systems, and many other attributes.

Other non-cryogenic systems that were more space-storable like ammonia were examined for mission performance and engine cycle capability. An ammonia NTP delivers about 430 seconds of Isp at a maximum reactor exit temperature similar to the 4,800-deg R discussed earlier. When considering the mass of the reactor system and this Isp performance, the spacecraft capability would not have a higher performance capability than a storable liquid rocket stage. The ammonia performance could be useful for a demonstration but was not considered useful for other missions of NASA (e.g., deep space kick stage) or commercial interest (e.g., Geostationary transfer stage or high inclination delta-velocity (delta-V) maneuvers).

The best NTP and stage approach appears to be one that achieves the following goals:

1. Demonstrates NTP operability over several main engine burns (startup / main stage / shutdown cycles);
2. Provides significant  $\Delta V$  capability on the order of several kilometers per second ;
3. Provides risk reduction on the NTP and stage cryogenic fluid management (CFM) systems;
4. Launches on existing commercial launch vehicles.

Aerojet Rocketdyne is looking at a NTP flight demonstrator (FD) mission concept that could address the four points above. The mission would use a commercial launch vehicle with a payload capability of 15 to 30 metric tons to a nuclear safe orbit (e.g., 1,300 km). The NTP FD mission would perform the first burn to raise the apoapse of the insertion orbit to 13,000 km. After a 2 to 3 hour coast, a second burn would circularize the orbit at 13,000 km, inclined at 10-deg. This type of NTP demonstrator mission would provide the needed data on NTP operability for start, shut-down, and cooldown after burns that last 8 to 10 minutes. This level of operability (two starts and shutdowns) and the burn times are typical of part of the missions an

NTP stage would perform as a Lunar tug or on a Mars crew mission.

Additional details on NTP flight demonstration mission and vehicle options can be found in a companion paper at NETS 2020 entitled “LEU NTP Flight Demonstration Vehicle and Applications to Operational Missions”.

#### **IV. LEU NTP CREWED MARS SHORT-STAY MISSION TRADES**

NASA has been studying other crewed Mars mission approaches in 2019 and it will continue in 2020. One of these is an examination of space transportation systems that can achieve short-stay or Opposition-class missions.

The NTP FD fuel/core design has a strong impact on the near-term and future NTP crew Mars mission capability. Defining the NTP propulsion performance requirements to close on the crewed Mars missions, both long-stay and short-stay, is critical to defining a NTP development roadmap.

In order to satisfy the requirements of a Mars opposition mission, a study was performed to determine the optimal NTP Mars Transfer Vehicle (MTV) architecture, while also taking advantage of previous work completed for Mars conjunction missions. Trades were performed on NTP main engine Isp, number of NTP engines, NTP MTV assembly/aggregation orbit, Mars aggregation orbit, MTV stage/drop tank diameter, and stage/drop tank launch vehicle. From these trades, four NTP MTV configurations were developed, each sized to fulfill a requirement of landing a crew on the Martian surface by the end of 2036. Each configuration uses a combination of SLS delivered NTP stages and either SLS or commercially delivered drop tanks. By utilizing the drop tank approach, the mass ratio of the NTP MTV can be maximized over the entire Mars opposition mission. The propellant mass fraction of the entire vehicle stack can be increased at the start of the mission, while also reducing the dry mass that is carried throughout the mission.

The Mars short-stay mission study showed that the higher delta-velocity requirements drive the burns times up by a factor of 2 versus long-stay Conjunction-class missions. The 25,000-lbf thrust NTP was still adequate to perform the harder Opposition-class missions, but some required 4 versus 3 NTP engine systems.

In summary, if the Mars mission is a long-stay, Conjunction-class type then 3 to 4 - 15,000-lbf NTP engines could be used and cumulative operating time

is less than 2 hours. If the Mars mission is a short-stay, Opposition-class type then 3 to 4 - 25,000-lbf NTP engine systems are needed to minimize cumulative operating time to less than 3 hours. During the NERVA/Rover program, those reactor cores and engine systems demonstrated burn times from minutes to hours with cumulative burn times between 2 to 3 hours.

The NTP flight demonstration mission needs to show single burn times on the order of several minutes in order to translate the demonstrated operation and control to the Mars mission NTP systems.

Further details on the Aerojet Rocketdyne Mars Opposition-class mission study will be presented in upcoming papers at several other conferences (i.e., American Institute of Astronautics and Aeronautics Propulsion and Energy 2020).

#### **V. LEU NTP CORE AND ENGINE SYSTEM DEFINITION FOR FLIGHT DEMONSTRATOR**

NASA has been tasked to define a flight demonstrator mission and NTP demonstrator concept by congress and have it ready to flight before 2026. AR working with several reactor design organizations has created several NTP flight demonstrator engine approaches that cover a range of thrust size from 7,000-to-15,000 lbf thrust using liquid hydrogen propellant as the coolant.

The NTP demonstrator concepts are based on a nuclear material and geometry fuel design that has direct use in a larger FSD NTP for crewed Mars missions, Mars uncrewed cargo, and lunar tug applications. The mission definition discussed in the NETS 2020 paper entitled “LEU NTP Flight Demonstration Vehicle and Applications to Operational Missions” was used to examine the impact of various NTP demonstrator thrust sizes from 7,000-to-15,000-lbf.

The NTP demonstrator in the 7,000-lbf class would be based on using as much possible off-the-shelf designed liquid rocket hardware (e.g., valves, LH2 turbopump, and additively manufactured (AM) chamber and nozzle per current LOX/LH2 RL10 manufacturing). This approach has the potential to reduce the cost of the ancillary propellant feed hardware for the NTP flight demonstrator. Larger thrust (e.g., 10,000 to 15,000 lbf thrust) NTP demonstrator approaches would likely use scaled designs for the valves and turbopump per the higher LH2 flowrates in the order of 10-to-17 lbf/sec. The scaled additively manufactured components may

impose some increases in hardware cost if the size exceeds current AM build machine sizes.

Figure 3 shows the relationship between the lower thrust NTP flight demonstrator engine system and the larger size Mars mission 25,000-lbf NTP.

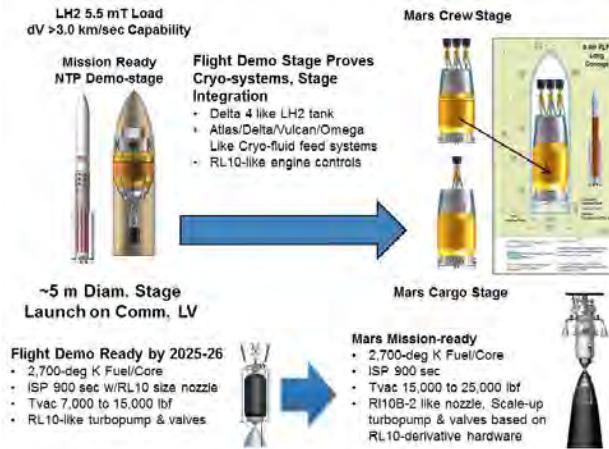


**Fig. 3.** NTP Demonstrator Fuel-Core-NTP Design Relationship to Full-size NTP Roadmap

It is expected that a tiered testing approach would be the most affordable path to achieving NTP development milestones that permits a full-size NTP engine prototype and that can be transitioned to production for a Mars mission application.

The tiered testing would start with lower complexity materials testing to prove the fuel elements and material for a moderator system, then evolves over a several more tests of components and fuel assemblies (with increasing complexity) to some reactor-level and control system ground tests. The size of the ground tests would be designed to provide enough risk reduction to permit building and flying the flight demonstrator.

The road-map in Figure 3 aligns the flight demonstrator, based on off the shelf proven liquid rocket engine hardware, to a higher thrust NTP for later crew NTP vehicle for Mars.

The following figures provide more insight into the various NTP demonstrator design options AR is examining for possible use by NASA in a future flight test. Figure 4 illustrates one probable flight demonstrator reactor core design based on either a CERMET (e.g., Uranium Nitride and Tungsten-Molybdenum) or Uranium Carbide type low-enriched fuel. The circular fuel assemblies (fuel elements) are positioned within a moderator material (e.g., Beryllium or Zirconium Hydride) that then make up the reactor core within a pressure vessel. The smaller

7,200-lbf thrust NTP would be comprised of 90-120 fuel assemblies while the larger 15,000-lbf NTP would have a slightly larger diameter and use 150 to 200 fuel element assemblies. The fuel assemblies in the outer radius could be configured to take hydrogen from the bottom of the core and heat it to provide turbine drive gas. Then the turbine discharge hydrogen gas flow at 300 to 400-deg Kelvin would be returned to the fuel assemblies to cool the other fuel elements and get further heated to temperatures near 5,000-deg Kelvin and exit the NTP via a nozzle.

Generic Circular NTP Fuel Element Assemblies within a Moderator Block Core Control Drums Shown are Notional and Do Not Represent A Final Approach

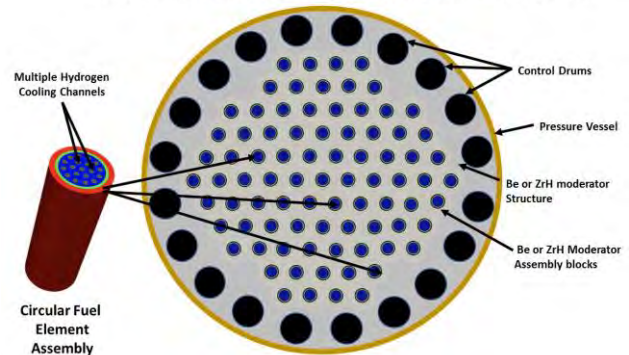


**Fig. 4.** Example LEU NTP Demonstrator Fuel and Core Design for 7,200-lbf or 15,000-lbf Thrust NTP

Figure 5 shows a CAD representation AR has created for the 15,000-lbf NTP demonstrator. This design has a fixed radiation-cooled nozzle section. The full length of the NTP is approximately 6.5 meters as shown.

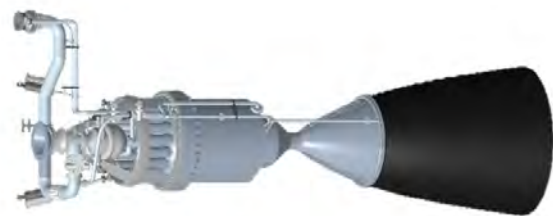


**Fig. 5.** Example LEU NTP Demonstrator 15,000-lbf Thrust NTP

The lower thrust NTP could make use of legacy AR RL10 hardware designs and some evolved RL10 approaches such as the single-shaft fuel turbopump versus the geared turbopump. The flow-rate for the 7,200-lbf thrust design is the same as the hydrogen fuel flow for the RL10 that has over 2 million seconds of testing and flight operation. The control valves and the new additive manufactured chamber-

nozzle approach being used for the RL10C has direct application for the 7,200-lbf NTP engine system. Figure 6 shows the general cycle design and some of the design operating parameters.

The higher thrust 15,000-lbf NTP would most likely employ designs derived from earlier AR rocket designs such as the RL60 and MB-XX. (e.g., valves, fuel turbopump, and nozzle designs). The flow-rate for the 15,000-lbf thrust design is the same as the hydrogen fuel flow for the RL60 and MB-XX designs that were both tested in various forms before development ended on those engines. Figure 7 provides a cycle design layout for a 15,000-lbf thrust NTP demonstrator.

These LEU NTP demonstrator engine systems are estimated to have very competitive mass and could be used as propulsion for planetary missions or as a reusable lunar tug. The 7,200 -lbf LEU NTP demonstrator is estimated to have a mass of approximately 3,000 to 4,000 kg depending on the fuel type (e.g., Carbide or CERMET). The 15,000-lbf LEU NTP demonstrator could have a mass between 3,500 to 4,500 kg. These masses would be further optimized for the best performance system when applied to the larger 25,000-lbf Mars crew mission NTP engine system to achieves masses between 5,000 to 5,500 kg.

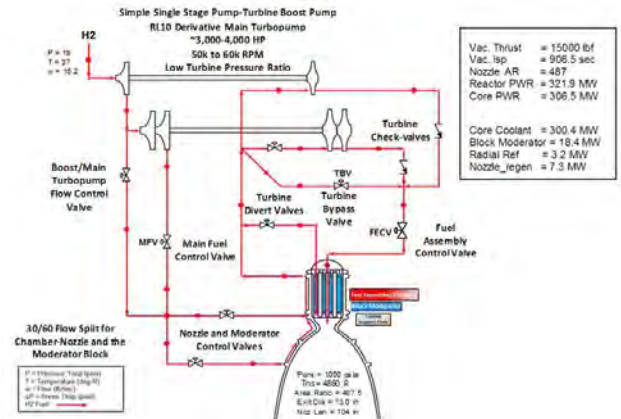


Fig. 7. NTP Engine Cycle Diagram for 15,000-lbf Thrust Demonstrator

## VI. CONCLUSIONS

Analysis has shown the LEU NTP approach is technically feasible based on work from 2016 through 2019. Significant conceptual design evaluations have been completed to define an approach for a LEU NTP flight demonstrator between 7,000-to-15,000 lbf thrust that has high Isp potential, and can have low mass.

A mission concept and NTP approach that will test NTP operability, using a fuel assembly with lineage to the full-scale Mars NTP flight system, can be defined to meet the intent of the Congressional mandate to develop a NTP flight demonstration. Aerojet Rocketdyne is determined to provide the leadership to make this NTP system a reality.

## ACKNOWLEDGEMENTS

The authors would like acknowledge the support of the USNC-Tech, BWXT, NASA Marshall Space Flight Center and Glenn Research Center, NASA Space Technology Mission Directorate (STMD) Game Changing Development (GCD) and the Department of Energy engineers that continue working NTP for Mars crewed missions and other missions that can benefit from NTP.

The primary author of the paper would like to also acknowledge the guidance of Dr. Stanley K. Borowski, who retired recently from NASA Glenn research Center. He has over several decades always been available for discussions on nuclear systems, and has been a strong advocate of advanced propulsion technologies.

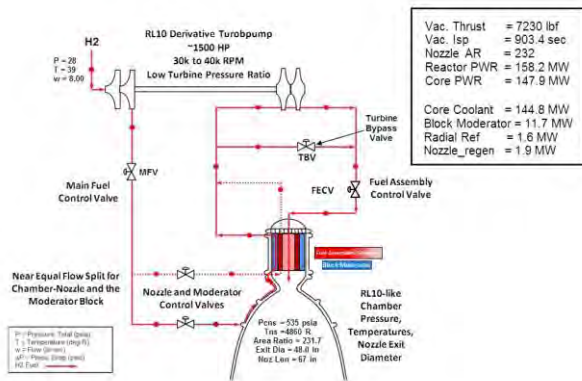


Fig. 6. NTP Engine Cycle Diagram for 7,200-lbf Thrust Demonstrator

## REFERENCES

1. Koenig, D., *Experience Gained From the Space Nuclear Rocket Program (ROVER)*, LA-10062-H, Los Alamos National Laboratory, Los Alamos, New Mexico (1986).
2. Dewar, J. A., *To the End of the Solar System-The Story of the Nuclear Rocket*, The University Press of Kentucky, Lexington, Kentucky (2004).
3. Joyner II, C. R., Jennings, T., Levack, D. J. H., “An Examination of the Engine Cycle Trends for a HEU and LEU NTP”, ANS Proceedings of Nuclear and Emerging Technologies for Space, Huntsville, Alabama, February 22-25 (2015)
4. Joyner II, C. R., Eades, M., Horton, J., Jennings, T., Kokan, T., Levack, D. J. H., Long, M., Widman, F., “Update on Approaches for LEU NTP Engine Systems and Exploration Implications”, ANS Proceedings of Nuclear and Emerging Technologies for Space, Las Vegas, Nevada, February 26-March 1 (2018)

## THE ULTRA-SMALL MODULAR REACTOR FOR SPACE APPLICATIONS

Naiki Kaffezaïs, Matt Krecicki, and Dan Kotlyar

<sup>1</sup>Georgia Institute of Technology  
770 State St NW, Atlanta, GA 30313

Primary Author Contact Information: (770)891-7120, [naiki.kaffezaïs@gmail.com](mailto:naiki.kaffezaïs@gmail.com)

This paper presents an introduction to the Ultra-Small Modular Reactor (USMR) design and its potential application for nuclear electric propulsion. Here, the USMR is presented as an alternative to the Krusty space reactor system, along with the results of a space application specific design study. By utilizing direct heat conversion through thermophotovoltaic panels (TPV), the USMR is able to operate at higher-efficiencies and with greater system-wide, mass power densities than other space reactors that are based on the Brayton cycle heat-pipe design.

### I. INTRODUCTION

#### I.A. Nuclear Electric Propulsion

One of the most well-known nuclear electric propulsion concepts was the Prometheus spacecraft for the Jupiter Icy Moons Orbiter (JIMO) mission. The electric ion thrusters were designed by Jet Propulsion Laboratory (JPL) and the nuclear system was designed by Knolls Atomic Power Lab (KAPL) during the early 2000's<sup>1</sup>. Figure 1 shows some of the considered and publicly available reactor cores for the mission profile. These concepts include a heat-pipe Brayton cycle design, which is still currently investigated under the Kilopower Space Nuclear Fission Power Reactor, a.k.a. Krusty.<sup>2</sup> A direct gas reactor was selected for the JIMO mission because the system met performance requirements, minimized development challenges and was the most readily tested system. A common feature of all considered reactor types was the coolant fluid power conversion system<sup>1</sup>.

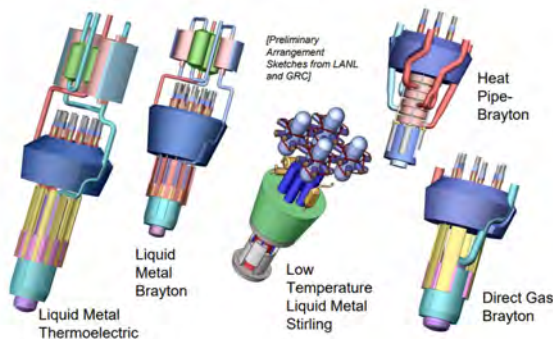


Fig. 1. Various proposed designs for the JIMO reactor<sup>1</sup>.

A significant amount of technical progress was made during the design and development of the JIMO reactor system. However, at the end of development campaign the reactor design team concluded that “Further improvements in power and energy density beyond the capabilities of a gas reactor system can only be achieved through widespread use of refractory metals in liquid metal systems, which will require greater development, particularly for materials compatibility and lifetime integrity.” One of the other major concerns of the program was reactor dynamics and stability during extended operation with intermitted earth communication to monitor reactor operation. One of the key metrics for any space reactor system is the total mass of the system. A one-megawatt thermal (200 kWe) JIMO reactor module was estimated to have a mass of approximately 11,000 Kg. The reactor mass is approximately a quarter of the entire power plant system. This trend shows that the power conversion system was bottleneck for low mass JIMO systems<sup>1</sup>.

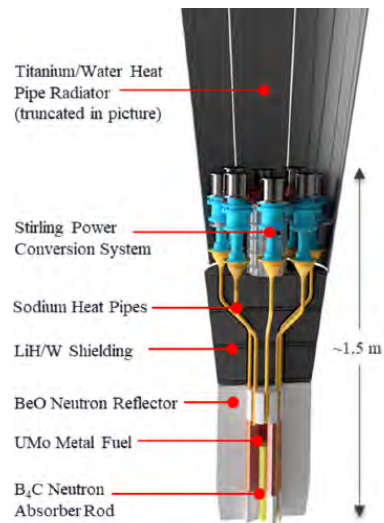


Fig. 2. Schematic of the Krusty reactor system.

After the cancellation of the Prometheus project, work continued on the Krusty concept at LANL lead by David Poston. The most promising of Krusty designs rely on HEU U-Mo fuel. However, recent policy goals have directed space nuclear research towards the use of LEU

fuel systems. This policy shift has resulted in the design and analysis for several LEU Krusty concepts which are much larger and heavier systems. The key limiting factor of the Krusty concept is the material limitations of the U-Mo fuel system. The material phase-stability of U-Mo prevents the core from operating at higher temperatures where its heat-pipe stirling power conversion system is the most efficient. The highest power LEU Krusty configuration has a rated electric power of 10 kWe and a mass of 1863 kilograms. After several transient experiments Krusty has been proven to be an extremely stable and controllable reactor.

An ideal nuclear electric propulsion system would have the stability and compactness of the Krusty core and power output of a JIMO system. In order to achieve this goal a significant technological advancement would be required on the power conversion system.

### I.B. The USMR Design

A new avenue for technological advancement of nuclear electric propulsion dominance may exist in the Ultra Small Modular Reactor (USMR). The USMR is a small-modular reactor design under development by a multi-disciplinary team at Georgia Institute of Technology.<sup>4</sup> The design is ground-breaking in that it eschews the standard model of using a Rankine (or Brayton) cycle to cool the core and generate electricity. In the USMR design, electricity is produced by coupling a small reactor core, wrapped in a tungsten photon emitter, with thermophotovoltaic (TPV) cells. By operating the core at high temperatures, greater than 1300 °C at the outer boundary, electricity production efficiencies of over 50% are possible using modern TPV technology with back surface reflectors to recycle sub-bandgap photons.<sup>5</sup> The move to direct conversion of heat to electricity allows for a significant reduction in the mass of the system by removing the need for working fluids and heat pipes.

The USMR design is composed of 5 concentric hexagonal rings: an inner graphite moderator, a 19.75% enriched uranium nitride fuel block, an outer graphite moderator, a beryllium reflector and a tungsten emitter, as illustrated in Figure 3. The system is primarily controlled through boron control drums, turned inwards for startup and outwards for shutdown. Additional emergency shutdown control is provided by a bank of secondary control rods. However, the high temperature materials and simple design allows for high tolerance to transients and promises walk-away safety. Though originally examined for terrestrial applications, the USMR system can be optimized for high power and compactness that can bridge the gap between the JIMO and Krusty systems.

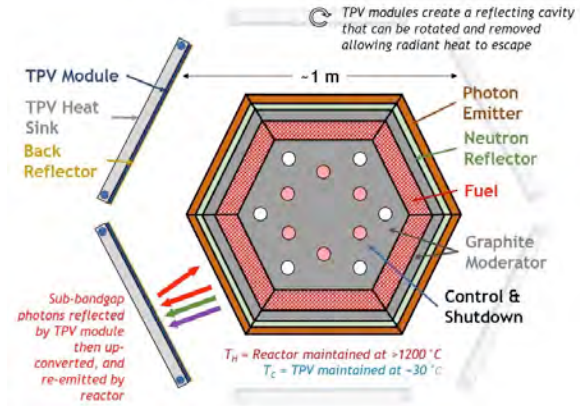


Fig. 3. Schematic of the USMR system.

## II. METHODOLOGY

### II.A. USMR Design Space Study

In order to broadly analyze the USMR design, a thermal and neutron physics solver was developed.<sup>4</sup> This tool utilized an in-house developed, finite method, 1D heat transfer solver based on the equivalent circuit approximation for the calculation of steady state temperature profiles. The Monte Carlo neutronics code SERPENT 2 was utilized to develop neutron flux and power profiles, as well as to conduct burnout analysis.<sup>6</sup> From an initial description of the USMR dimensions, materials and temperature limits (1300°C at the outer wall with a 300°C margin to thermal failure across the system), the temperature profile, maximum power output and system lifetimes were found utilizing the iterative process that is described in Figure 4. For the purpose of optimizing for space, the core mass was calculated from material volume and mass, and an additional 10% was added to cover the mass of the TPV panels which is dependent on the selection of photovoltaic materials and distance away from the core, which has not been fully studied.

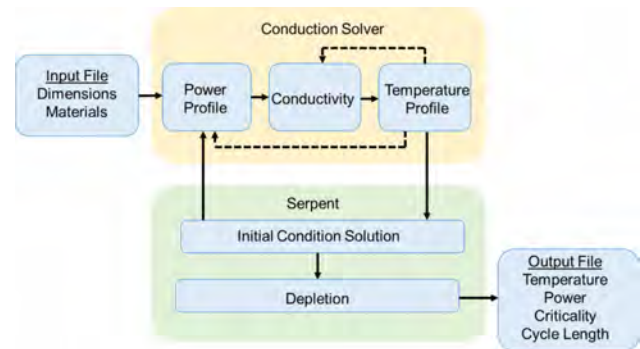


Fig. 4. Illustration of computational sequence.

In order to rapidly explore design selections, a simplified description of the USMR geometry was utilized. In the transition to a 1D model, it was assumed that an equivalent volume, cylindrical system could be utilized instead of the hexagonal system with little loss of general design trends. A cylindrical system might also prove to be a better design choice when examining heat stresses and manufacturing in future studies. Further, it was assumed that the USMR units would be long enough such that the axial variation would be negligible in comparison to the radial. For purposes of calculating the system lifetime from the fuel cycle depletion analysis, a 3% axial neutron leakage is assumed for a 1 m tall core with 25 cm beryllium axial reflectors.

### II.B. Key Performance Criteria

To compete with the other nuclear electric propulsion systems, the USMR design presented in this study was optimized to have the maximum mass power density. However, in order to conduct a direct evaluation of the USMR design, the optimized system is compared to the KRUSTY LEU 10 kWe device. Therefore, the USMR design must fall within the limitations of mass and volume of the KRUSTY. This limits the optimal USMR system, including spacing for the TPV, to a radius less than 230 cm, an axial length of 150 cm, and a system mass less than 5000 kg. Further, the USMR optimal design should have, at minimum, a comparable system lifetime of 15 years.

### III. RESULTS

In order to present the design tradeoffs of the key dimensions, namely the moderator and fuel regions, Figures 5 and 6 are presented below. These figures represent a focused portion of the design space, centered on the optimal USMR design for space applications and show the trends in the mass power density and system lifetime, respectively. These figures highlight the major opportunity cost presented by the USMR system in that improving the thermal performance and power output comes at the price of neutronic performance and reactor lifespan. Therefore, the optimum power density is constrained to the surface with the minimum acceptable system lifetime.

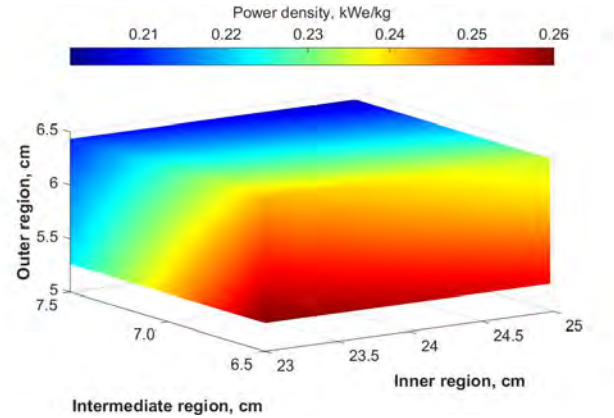


Fig. 5. The mass power density of the USMR design as a function of moderator and fuel dimensions.

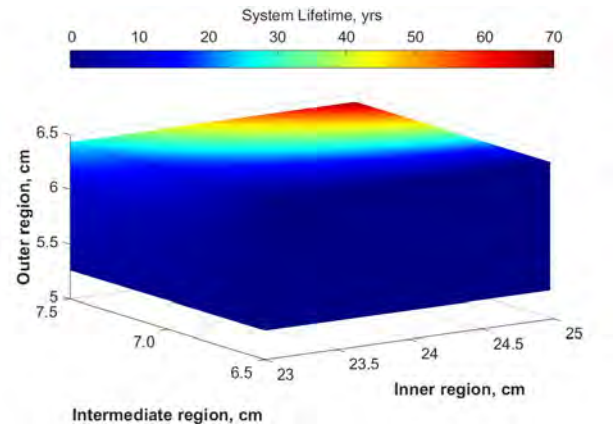
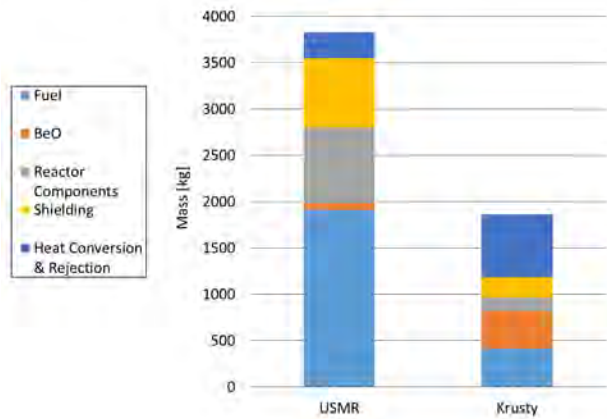


Fig. 6. The system lifetime of the USMR design as a function of moderator and fuel dimensions.

Using the criteria previously described, Table 1 contains the dimensions of a USMR core that is optimized for nuclear electric propulsion and other space applications by maximizing the mass power density. Figure 7 presents the component mass breakdown of 1 meter long optimized USMR core with axial shielding as compared to the Krusty core. Table II and Figure 8 present the comparison of the USMR design's performance to the Krusty LEU design. As can be seen, the thermal mass power density of the USMR design is a magnitude greater than that of Krusty core, and the additional boost from the high efficiency means that in the same envelope, the USMR system is able to provide 35 times the electric output.

**TABLE I.** Parameters of the optimal USMR design for space applications

USMR Parameter	Value
Inner Moderator Thickness, cm	25
UN Fuel Thickness, cm	7.4
Outer Moderator Thickness, cm	5.85
Beryllium Reflector Thickness, cm	1
Tungsten Emitter Thickness, cm	0.5
Core outer surface temperature, °C	1300
Temperature Safety Margin, °C	300



**Fig. 7.** Breakdown of system mass into components.

**TABLE II.** Comparison of the USMR to Krusty

Parameter	USMR	Krusty	Units
Fuel Type	UN	U-Mo	n/a
Efficiency	>50	20	%
Fuel Enrichment	19.75	19.75	wt% U-235
Core Diameter	39.75	29	cm
Core Height	100	~75	cm
System Lifetime	15.2	15	yrs
Mass Power Density	0.23	0.03	kWt/kg
Electric Output	355	10	kWe
System Mass	3831	1863	kg

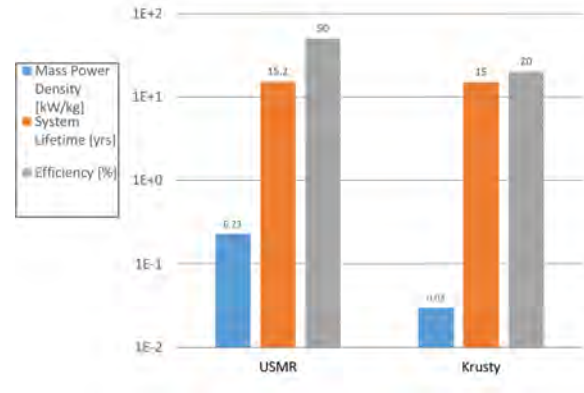


**Fig. 8.** Comparison of USMR to Krusty in key performance parameters.

#### IV. CONCLUSIONS

Though the USMR is still in its design infancy for terrestrial power sources, the results of early optimizations on the design suggest that it could be an important step in the future of space reactors. There are still open questions about the survivability of the TPVs in the mixed neutron gamma fields and the effects of thermal stresses in a large system, which might prove to be a limiter to the system lifespan. However, there is significant worth in continuing this ongoing design project. Having a LEU fueled reactor that can produce 100's kWe rather than 10's will be vital for long-term colonization of extraterrestrial bodies.

#### REFERENCES

1. KNOLLS ATOMIC POWER LABORATORY. SPP-SEC-0039. Documentation of Naval Reactors Papers and Presentations for the Space Technology and Applications International Forum (2006).
2. D. POSTON, et Al. "Kilopower Reactor for Potential Space Exploration Missions." Los Alamos National Laboratory, NETS (2019)
3. P. MCCLURE, et. Al., "Comparison of LEU and HEU Fuel for the Kilopower Reactor," Los Alamos National Lab, LA-UR-18-29623 (2018)
4. N. KAFFEZAKIS, et. Al., "High Temperature Ultra-Small Modular Reactor: Pre-Conceptual Design," *Annals of Nuclear Energy* (2020)
5. H. SEYF and A. HENRY, "Thermophotovoltaics: a potential pathway to high efficiency concentrated solar power," *Energy & Environment* (2016)
6. J. LEPPÄNEN, et Al. "The Serpent Monte Carlo code: Status, development and application in 2013," *Ann. Nucl. Energy* (2015)

## NEUTRONIC ANALYSIS OF THE SUBMERSION-SUBCRITICAL SAFE SPACE (S<sup>4</sup>) REACTOR USING REDUCED ENRICHMENT URANIUM FUEL

Takanori Kajihara<sup>1</sup>, Chaitee Godbole<sup>2</sup>, and Jared Magnusson<sup>3</sup>

<sup>1</sup>Department of Nuclear Engineering, Texas A&M University, College Station, TX, 77845,

<sup>2</sup>Department of Nuclear Engineering, North Carolina State University, Burlington Engineering Lab, NC, 27695,  
[cgodbol@ncsu.edu](mailto:cgodbol@ncsu.edu)

<sup>3</sup>Department of Mechanical and Aerospace Engineering, University of California – Los Angeles, Los Angeles, CA, 90095,  
[jmagnusson@ucla.edu](mailto:jmagnusson@ucla.edu)

Primary Author Contact Information: (979)-450-3666, [kajihara@tamu.edu](mailto:kajihara@tamu.edu)

*There is a resurgent interest in using space reactors for various space missions. This work models the S<sup>4</sup> (submersion-subcritical safe space) reactor for deploying LEU fuel using Serpent 2. The S<sup>4</sup> reactor is a fast spectrum gas-cooled reactor that ensures subcriticality in case of accident scenarios where the reactor gets submerged in seawater. Increased pressure to curb highly enriched uranium fuel (HEU) in reactor designs has heightened interest in low enriched uranium (LEU). To accomplish this, the S<sup>4</sup> reactor was scaled to multiple sizes: one at twice the diameter and three times the length, another at twice the diameter and length. For the original reactor size, 82 % enrichment possessed a  $k_{eff}$  of 1.017 after seven years of operation. For the S<sup>4</sup> reactor scaled to 2X the diameter and 3X the length, initial  $k_{eff}$  only attained 0.81 in the case of 20 % enrichment fuel. A 34 % <sup>235</sup>U concentration was estimated to be the lowest enrichment that allowed for criticality after seven years at a more feasible 2X scaling of this reactor design.*

### I. INTRODUCTION

There is a resurgent interest in using space reactors for various space missions on lunar surfaces as well as for in situ calculations to be done on Mars. When space reactors are launched, they remain noncritical and contain almost no radioactive material until at safe trajectory they are brought to startup<sup>1</sup>. A major concern that arises for space reactors is regarding their criticality in the case of submersion accidents. When a reactor is submerged in seawater or wet sand during an accident, the neutron spectrum is thermalized<sup>2</sup>, and the effective neutron fission cross-section increases, making the reactor critical. To prevent the reactor from being critical during accident scenarios, neutron-absorbing materials are added to ensure the reactor remains subcritical. In the S<sup>4</sup> reactor, this is achieved by the utilization of B<sub>4</sub>C, whose boron-10 has a significantly large cross-section of neutrons. The S<sup>4</sup> reactor also possesses sufficient excess reactivity at the beginning of the mission to operate at full power for seven to fifteen years without refueling<sup>1</sup>. In this study, seven years is considered the minimum operational time for reported Serpent calculations.

Historically, space reactors used HEU for fuel because it can easily realize a small and lighter reactor, which is essential to decrease launch costs. However, recent U.S. government policy emphasizes the risk of proliferation and increases security costs of HEU usage. Also, the launch costs are gradually decreasing thanks to the movement of commercial launch vehicles<sup>3</sup>. This paper investigates the feasibility of deploying the LEU fuel system for the S<sup>4</sup> reactor by scaling.

### II. REACTOR AND POWER SYSTEM DESIGN AND SPECIFICATION

#### II.A. Power System Specification

For power levels above 10 kW, Brayton power cycles provide a mass advantage over Stirling power conversion systems<sup>4</sup>. For this reason and the absence of high-speed pistons, the S<sup>4</sup> reactor utilizes three closed Brayton conversion units, each giving an output of 31.2 kW<sub>e</sub> for a net power output of 93.6 kW<sub>e</sub> (Ref. 5). The design's nominal thermal output is 471 kW<sub>th</sub>, and the total generated thermal output for the three sectors of the reactor is 437 kW<sub>th</sub> (Ref. 5). The net system efficiency is 21.4 % (Ref. 5) after accounting for the losses and efficiency of the power conversion, turbomachinery, and electrical systems.

#### II.B. S<sup>4</sup> Reactor Design and Specifications

The reactor system uses a binary mixture of He-28 atom% Xe gas, having a molecular weight of 40 mole/gram (Ref. 2). This reactor has a hexagonal Mo-14Re (molybdenum with 14 wt% rhenium) solid core block with cavities loaded with uranium mononitride (UN) fuel stacks surrounded by circular coolant channels<sup>2</sup>. Each fuel cavity has a 5 cm long fission gas plenum with a compression spring, a Mo-14Re spacer as well as caps at both ends.

The hexagonal solid core is surrounded by a hexagonal annulus for the coolant to flow into the reactor. The outlet flow is through the coolant channels that are placed inside the Mo-14Re core block. The axial and radial beryllium oxide (BeO) reflectors are clad in 0.2 mm thick Mechanically Alloyed Oxide Dispersion Strengthened (MA-ODS) 956 steel<sup>2</sup>. Six beryllium oxide/boron carbide (BeO/B<sub>4</sub>C) control drums inside the radial reflector are

clad with 0.2 mm thick MA-ODS 956 steel<sup>2</sup>. These control drums contain 0.5 mm thick B<sub>4</sub>C sectors in a 120° arc around the outer edge<sup>2</sup>. These radial panels are enriched in boron-10 and face inward in the shutdown configuration, rotate outward to bring the reactor to critical start-up, and face fully outward at the end of cycle<sup>2</sup>.

### II.B.1. Design Modification

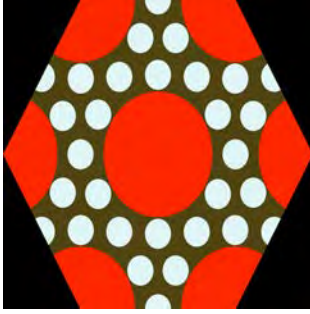


**Fig. 1.** Modified design of the S<sup>4</sup>'s coolant channels<sup>2</sup>. Fuel(red), coolant(white), black(core block).

To reduce the maximum temperature of fuel rods from more than 1900 K to 1302 K, King and El-Genk made various alterations to the fuel and coolant geometry, as shown in Figure 1. This configuration allowed for more effective cooling of the channels but also increased the relative pressure drop across the reactor by a significant but still acceptable amount<sup>2,5</sup>. Their model divided the reactor core into three sectors that are hydraulically decoupled but thermally coupled. However, these thermohydraulic modifications weakened the neutronics performance so that approximately 95 % of uranium enrichment is required. It led us to revisit the neutronics analysis of the S<sup>4</sup> reactor to reduce the enrichment as much as possible.

## III. SERPENT CALCULATION SETTINGS

The S<sup>4</sup> reactors (original size and scaled) were modeled in Serpent 2. High fidelity to the design was preserved by including reflectors, cladding, control drums, and insulation of the fuel block (see Figures 2 and 3). Sector inlets, outlets, and hydraulic boundaries were not modeled as they were anticipated to be insignificant to criticality and burnup calculations. Otherwise, slight variation to coolant was made, as the high enrichment reactor models used 30 atom% Xe in the coolant. The core temperature is estimated from the thermal-hydraulic analysis in the previous research<sup>2</sup>. Neutron population, active cycle, and inactive cycle were set 450,000, 2,000, and 300, respectively. ENDF/B-VII.1 is adopted as the nuclear data libraries, and thermal scattering libraries associated with Beryllium oxide are ENDF/B-VII.0 with interpolation. Note that unresolved resonance probability table sampling was used. The depletion time step was set 14 days and simulated until seven years, which is the

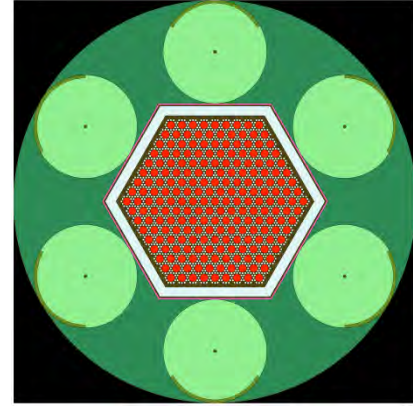


**Fig. 2.** Radial cross-section of the S<sup>4</sup> reactor modeled in Serpent. Hydraulic boundaries were deemed negligible for burnup calculations. Beryllium oxide drums(light green) are colored differently for clarity, though they are the same material as the rest of the reflector(dark green).

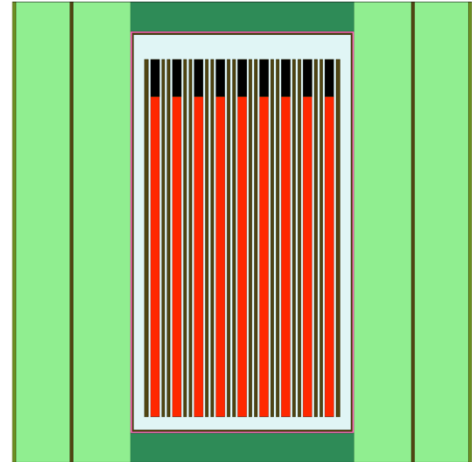


**Fig. 3.** Side cross-section of the S<sup>4</sup> reactor modeled in Serpent. Note the omission of the sector inlets and outlets.

minimum requirement for operation. Predictor corrector method was used for the depletion solution. Linear extrapolation on predictor and linear interpolation on corrector with 10 substeps were set.

Increasing pressure to HEU fuel in reactor designs has heightened interest in LEU ( $\leq 20\%$ ). To accomplish this, the S<sup>4</sup> reactor was scaled to multiple sizes: one at twice the diameter and three times the length, another at twice the diameter and length (see Figure 4). Though the reactor was scaled diametrically, fuel rod and coolant channel diameters were unchanged though their respective quantities doubled. The size of control drums surrounding the fuels is also directly scaled instead of increasing the number of drums of the same sizes.

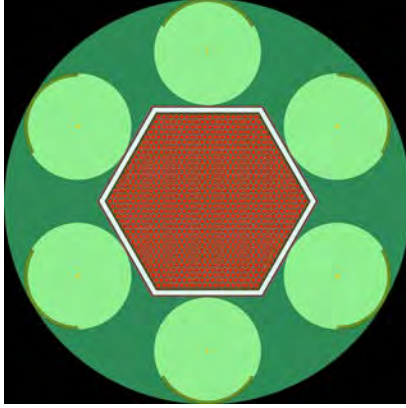


**Fig. 4.** Radial cross-section of S<sup>4</sup> reactor at twice the initial size. Coolant channels and fuel rods were the same diameters.

Enrichments up to 95 % were typical of fast space reactors, and 58.5 % was reasonably achievable, according to King and El-Genk<sup>1</sup>. However, their design did not account for changes associated with the thermo-hydraulic analysis performed the following year<sup>2</sup>. Thus, based on the reference parameters of the original design, 58.5 %, 82 %, and 95 % of enriched uranium nitride fuels were tested in Serpent.

#### IV. RESULTS

For the original reactor size, 58.5 % enrichment only attained a  $k_{eff}$  of approximately 0.74; therefore, enrichment had to be increased. The 82 % enrichment possessed a  $k_{eff}$  of 1.017 after seven years of operation and was selected as possible minimum enrichment for the original reactor size. Figure 5 shows the evolution of the multiplication factor during burnup. The reactor core keeps excess reactivity at the end of cycle (EOC) with  $2\sigma$  of uncertainty.

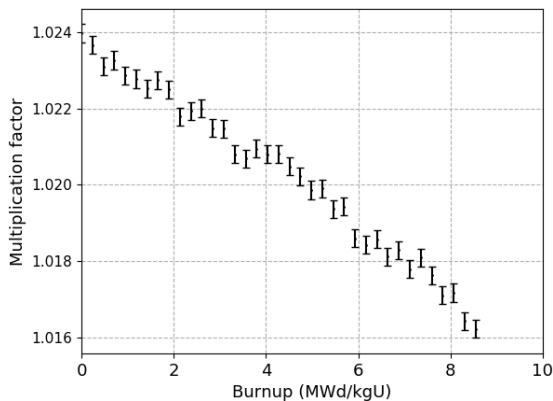


**Fig. 5.** Neutron multiplication factor of the S<sup>4</sup> reactor as a function of burnup in the case of 82 % enrichment of original reactor size.

Table I shows the neutron multiplication factor at the beginning of cycle (BOC) and after seven years, depending on the enrichment.

**TABLE I.** Neutron multiplication factor of each enrichment in the original size operation.

Uranium Enrichment (%)	$k_{eff}$ (BOC)	$k_{eff}$ (7 years)
58.5	0.867360	0.858616
82.0	1.02397	1.01695
95.0	1.09594	1.08905

For the S<sup>4</sup> reactor scaled to 2X the diameter and 3X the length,  $k_{eff}$  at the BOC only attained 0.81 in the case of 20 % enrichment fuel. Even a substantial size of the core is not sufficient to deploy the LEU for the current S<sup>4</sup> design. A 34 % of <sup>235</sup>U concentration was estimated to be the lowest enrichment that allowed for criticality after seven years at a more feasible 2X scaling of this reactor design compared with the 95 % of enrichment for the original design. The uranium enrichment decreased significantly, but proliferation concerns remain unacceptable.

The core dry mass (sans coolant) was estimated for the original size and scaled sizes, as shown in Table II. Note that the 2X scaled reactor core requires 8.9 times more mass compared to the original size.

**TABLE II.** The mas of core depending on scaling size.

Scaling	Mass (kg)
Original size	280.57
2X diameter & 2X length	2470.83
2X diameter & 3X length	5876.93

#### V. CONCLUSION AND FUTURE WORK

Due to necessary thermal-hydraulic design updates by King and El-Genk, the S<sup>4</sup> reactor core was retested in Serpent and requires 95 % enrichment of UN fuel to achieve an adequate neutron multiplication factor. Our scaling of the core to 2X the diameter and 3X the length decreased enrichment requirements to 34 %. The reactor holds great promise, but preliminary analyses, as shown, do not yet meet the 20 % LEU standard.

The thermal-hydraulics analysis of the S<sup>4</sup> core was not performed in this paper, and re-evaluation of the larger core's maximum temperature and pressure drop will be necessary. Furthermore, subcriticality capabilities in the case of submersion need to be confirmed in the scaled core.

From this paper, it is clear that a simple scaling is not enough to deploy LEU for an S<sup>4</sup> reactor. Additional revisions for the core design parameters are required to advance the design of the S<sup>4</sup> reactor using LEU.

## ACKNOWLEDGMENTS

We would like to thank Dr. Jeffrey C. King for providing us with the MCNP input files and thereby allowing us to cross-check with our implemented code. We also thank Dr. Herring from CSNR for his support of this research. This research made use of the resources of the High Performance Computing Center at Idaho National Laboratory, which is supported by the Office of Nuclear Energy of the U.S. Department of Energy and the Nuclear Science User Facilities under Contract No. DE-AC07-05ID14517.

## REFERENCES

1. J. C. KING and M. S. EL-GENK, "Submersion-subcritical safe space (S4) reactor," *Nuclear Engineering and Design*, **236**, 17 (2006).  
DOI:10.1016/j.nucengdes.2005.12.010
2. J. C. KING and M. S. EL-GENK, "Thermal-hydraulic analyses of the submersion-subcritical safe space (S<sup>4</sup>) reactor," *AIP Conf. Proc.*, Albuquerque, NM, February 11-15, Vol. 880, p. 261, AIP (2007).
3. D. I. POSTON and P. R. MCCLURE, "White paper – use of LEU for a space reactor," LA-UR-17-27226, LANL(Aug.2017).
4. L. S. MASON, "A comparison of Brayton and Stirling space nuclear power systems for power levels from 1 kilowatt to 10 megawatts," TM-2001-210593, NASA(Jan. 2001).
5. M. S. EL-GENK, "Space nuclear reactor power system concepts with static and dynamic energy conversion," *Energy Conversion and Management*, **49**, 3 (2008).  
DOI: 10.1016/j.enconman.2007.10.014

# SHIELDING ANALYSIS FOR A MODERATED LOW-ENRICHED URANIUM FUELED KILOPOWER REACTOR

Jeffrey C. King<sup>1</sup> and Leonardo de Holanda Mencarini<sup>2</sup>

<sup>1</sup> Nuclear Science and Engineering Program – Colorado School of Mines  
201 Hill Hall, 1500 Illinois Street, 80401, Golden, CO, United States of America  
kingjc@mines.edu

<sup>2</sup> Subdivisão de Dados Nucleares - Instituto de Estudos Avançados (IEAv)  
Trevo Coronel Aviador José Alberto Albano do Amarante, nº 1  
12228-001 São José dos Campos, SP, Brasil  
mencarini@ieav.cta.br

## Abstract

A Low Enriched Uranium (LEU)-fueled space reactor could avoid the security and proliferation concerns inherent with Highly Enriched Uranium (HEU)-fueled space nuclear reactors. Recent LEU-fueled space reactor designs include a moderator to reduce the size and mass of the reactor core. This paper considers shadow shield options for an unmoderated HEU-fueled space reactor and a moderated LEU-fueled space reactor. Both reactors are kilowatt-class reactors, producing 15 kWth of thermal power over a 5-year operational lifetime. Based on the shielding required to meet established dose limits (a neutron fluence of less than  $10^{14}$  n/cm<sup>2</sup> (>1 MeV equivalent in silicon) and a gamma ray dose of less than 1 Mrad in silicon), the moderated LEU-fueled space reactor will require a thicker shadow shield than the unmoderated HEU-fueled space reactor. The thinner reflector of the moderated LEU-fueled reactor results in more neutrons reaching the shadow shield at higher energies compared to the unmoderated HEU-fueled reactor. The presence of a significant reflector in most space reactor designs means that the core spectrum is relatively unimportant in terms of shadow shield design, as the reflector thickness has a much stronger impact on the neutrons and gamma rays reaching the shadow shield.

## 1. Introduction

Historic space nuclear reactor development has focused on Highly Enriched Uranium (HEU)-fueled reactors containing uranium enriched to over 93 wt% uranium-235, based on the assumption that Low Enriched Uranium (LEU)-fueled space nuclear reactor containing uranium enriched to less than 20 wt% uranium-235 would not be feasible (United Nations General Assembly, 1992). Recently, several non-nuclear weapon states and commercial entities have expressed interest in developing space nuclear reactor power systems. This has led to renewed concerns about proliferation, inspiring several recent projects to reconsider the feasibility of an LEU-fueled space reactor (Von Hippel, 2007; Nishiyama et al., 2009; Lee et al., 2015; Mencarini and King, 2018). One of these

studies (Mencarini and King, 2018) concluded that while an LEU-fueled system will be more massive than a comparable HEU-fueled system, the use of a moderator can reduce the mass of an LEU-fueled system, potentially making LEU-fueled space reactors viable (Mencarini and King, 2018). This study focused on only the neutronics aspects of the reactor and did not consider reactor heat transport nor the impact of the change of reactor spectrum on the design of the reactor's shadow shield.

This paper presents Monte Carlo models of the radiation shadow shields for a moderated 1 kW<sub>e</sub> LEU-fueled space nuclear reactor power system (Mencarini and King, 2018). The resulting model includes estimated reactor temperatures in an improved neutronics model that serves as the neutron and gamma source for the design of a corresponding reaction shadow shield. The paper also considers the design of a shadow shield for an equivalent HEU-fueled space nuclear reactor. A comparison of the two shield designs provides insight into the impact on shadow shield design as a result of changing from an unmoderated HEU-fueled reactor to a moderated LEU-fueled reactor.

## **2. Model Descriptions**

Based on the previous mass optimization study for a moderated LEU-fueled kilowatt-class space nuclear reactor (Mencarini and King, 2018), the present research assumes a disc-type core configuration consisting of 60 wt% zirconium hydride (ZrH<sub>1.5</sub>) and 40 wt% U-10Mo alloy (consisting of 90 wt% uranium enriched to 19.75 wt% uranium-235 and 10 wt% natural molybdenum). The chosen core configuration, shown in Figure 1, is 48.85 cm in length and 12.175 cm in diameter, surrounded by a 5 cm thick beryllium oxide reflector. The core consists of alternating stacked discs of U-10Mo (0.3 cm thick) and zirconium hydride (1.35 cm thick). A central control rod (4.4 cm in diameter and 24.82 cm in length) provides startup and shutdown control.

The reference unmoderated HEU-fueled reactor, based on the Kilowatt Reactor Using Stirling Technology (KRUSTY) (Poston, 2016), consists of a solid U-10Mo core, with an outer diameter of 11 cm and a length of 20 cm. The uranium in this reactor is enriched to 93 wt% uranium-235, alloyed with natural molybdenum. The beryllium oxide reflector is 11 cm thick in all directions.

The Monte Carlo N-Particle (MCNP) version 6 particle transport code (Pelowitz et al., 2014) provided the dose estimates presented in this paper. Both reactor models use the ENDF/B-VII.1 data libraries, adjusted, where

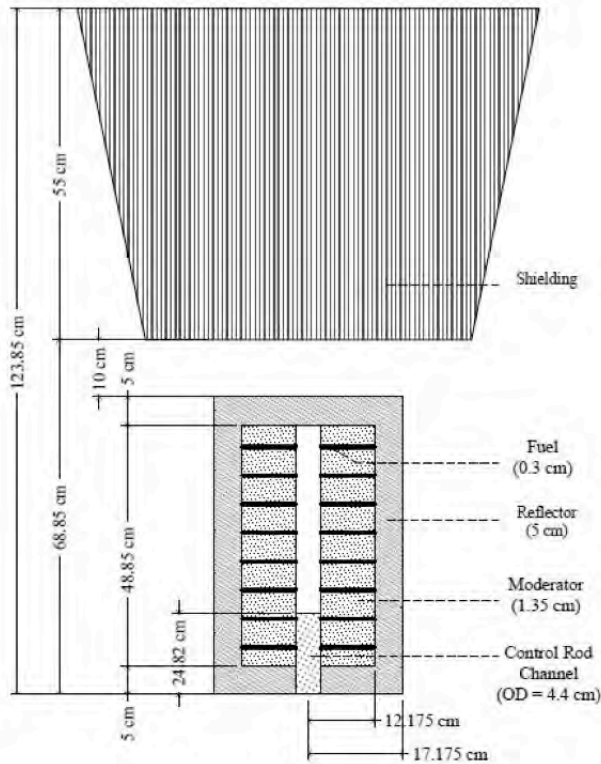


Figure 1. Axial view of the LEU-fueled reactor and shadow shield.

necessary, with the MAKXS utility program to provide Doppler-broadened cross sections at the appropriate temperatures. Both models account for the expected hot beginning-of-life (BOL) temperatures in the reactor by adjusting the material densities, cross-section libraries, and the free gas scattering temperatures for each region in the models.

The moderated LEU-fueled reactor model incorporates distributed temperatures based on a nodal, finite-difference heat transfer model of the reactor core and reflector, summarized in Table 1. The unmoderated HEU-fueled reactor model assumes a uniform core temperature of 1100 K, based on the results reported for KRUSTY (Poston, 2016). The disassociation temperature of lithium hydride limits the maximum temperature in the core to 930 K, which makes the average LEU-fueled reactor temperature significantly lower than that of the unmoderated HEU-fueled reactor model. While this difference in temperature will have a significant impact on the power conversion efficiency of the moderated LEU-fueled reactor, it should have a minimal impact on the amount and type of radiation reaching the shadow shield.

Table 1. Temperature predictions for the moderated LEU-fueled reactor.

Region	Temperature (K)	
	Lowest	Highest
Fuel disc	467.1	930.4
Moderator disc	463.3	921.7
Reflector	300.6	549.4

The shielding models presented in this chapter represent a truncated cone with a side angle of 22.1 degrees, positioned 10 cm from the outer surface of the reflector. The minor diameter in each model ensures that the entire reactor fits within the shadow cone. The shield thickness varies between 1 and 55 cm. The shield for both reactors consists of a monolithic shielding material with an assumed temperature of 300 K.

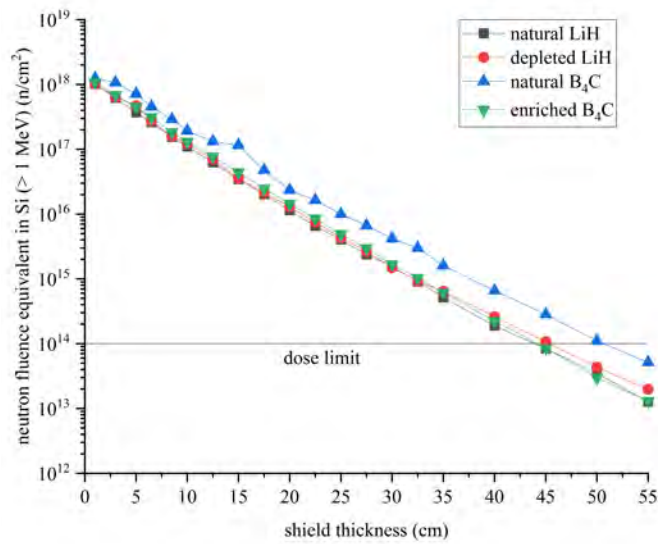
A combination of the SSW, SSR and WWG cards allow MCNP to produce accurate estimates of neutron and gamma fluences exiting the shadow shield. Then, conversion factors provided by energy response function (DE/DF) cards allow MCNP to convert the predicted particle fluences to a >1 MeV neutron fluence equivalent in silicon and a photon dose in silicon in rad units (DePriest, 2014). Each case presented in this paper included sufficient source particles to insure that the variances associated with the dose predictions in every case are less than 5%.

### 3. Shielding Results

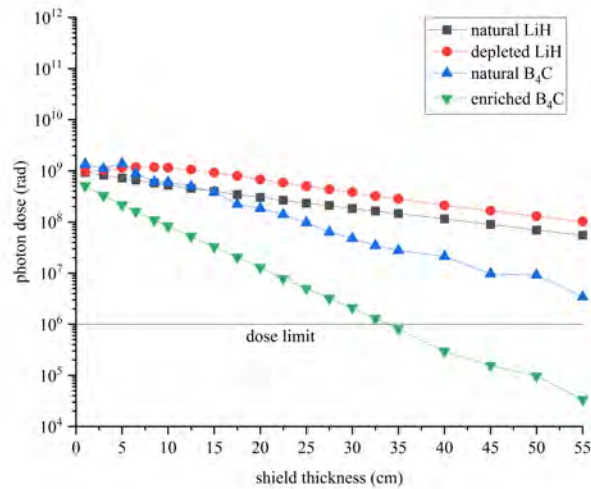
The neutron and gamma fluences at the minor surface of the shield for the unmoderated HEU-fueled core after 5 years of operation at 15 kW<sub>th</sub> (producing 1 kW<sub>e</sub> at a conversion efficiency of 6.67%) are 1.47×10<sup>21</sup> n/cm<sup>2</sup> and 2.24×10<sup>10</sup> gamma/cm<sup>2</sup> respectively. The corresponding values for the moderated LEU-fueled core are 1.33×10<sup>22</sup> n/cm<sup>2</sup> and 4.29×10<sup>10</sup> gamma/cm<sup>2</sup> for the neutron and gamma ray fluences, respectively. The neutron fluences result in neutron doses of 1.25×10<sup>18</sup> n/cm<sup>2</sup> (> 1 MeV equivalent in silicon) and 1.12×10<sup>18</sup> n/cm<sup>2</sup> (> 1 MeV equivalent in silicon), at the minor surfaces of the unmoderated HEU-fueled reactor and the moderated LEU-fueled reactor, respectively. The gamma ray fluences at the minor surfaces of the unmoderated HEU-fueled reactor and the moderated LEU-fueled reactor correspond to gamma ray doses of 1.43x10<sup>9</sup> rad and 1.71x10<sup>9</sup> rad, respectively.

### 3.1. Unmoderated HEU-fueled reactor results

Figure 2 shows the doses calculated at the major surface of the shadow shield as a function of the thickness of the shield for the unmoderated HEU-fueled reactor, using the four selected shielding materials (natural lithium hydride, depleted lithium hydride, natural boron carbide, and enriched boron carbide). Figure 2a presents the calculated neutron doses in terms of equivalent neutron fluence above 1 MeV in silicon and Figure 4b presents the calculated gamma ray doses in terms of rads in silicon. Figure 2a shows little difference between natural lithium hydride, depleted lithium hydride, and enriched boron carbide. A shield using natural lithium hydride or enriched



a) Calculated neutron doses.



b) Calculated gamma doses.

Figure 2. Calculated neutron and gamma doses from the unmoderated HEU-fueled reactor as a function of shield thickness.

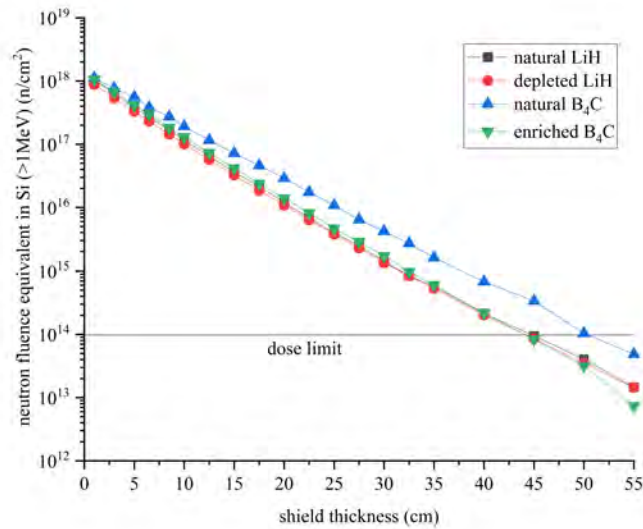
boron carbide would need to be 44 cm thick to meet the dose limit of  $1 \times 10^{14}$  n/cm<sup>2</sup> neutron fluence greater than 1 MeV in silicon. A depleted lithium hydride shield would need to be slightly thicker (46 cm) to meet the same dose limit. Natural boron carbide provides somewhat less effective neutron shielding than the other materials, requiring a greater than 50 cm thick shield to meet the dose limit (see Figure 2a).

With respect to gamma ray shielding for the unmoderated HEU-fueled reactor, enriched boron carbide is the only material that can meet the dose limit of  $1 \times 10^6$  rad within the chosen range of shield thicknesses. The 38 cm of enriched boron carbide shielding required to meet the gamma dose limit ( $10^6$  rad) is significantly less than the 44 cm of enriched boron carbide required to meet the neutron dose limit ( $1 \times 10^{14}$  n/cm<sup>2</sup> (>1 MeV) equivalent in silicon). This suggests that a layer of gamma absorbing material, such as tungsten, will be required in shadow shields for any kilowatt space nuclear reactor power system shield that does not use boron carbide. Looking closely Figure 2b, it is possible to see that the absorbed gamma ray dose at the major surface of the depleted lithium hydride shield increases until the shield is at least 10 cm thick. Similarly, the absorbed gamma ray dose at the major surface of the natural boron carbide shield does not decrease until the shield is more than 5 cm thick. That suggests that there is a significant contribution from gamma ray photons generated by the inelastic scattering of fast neutrons in these materials.

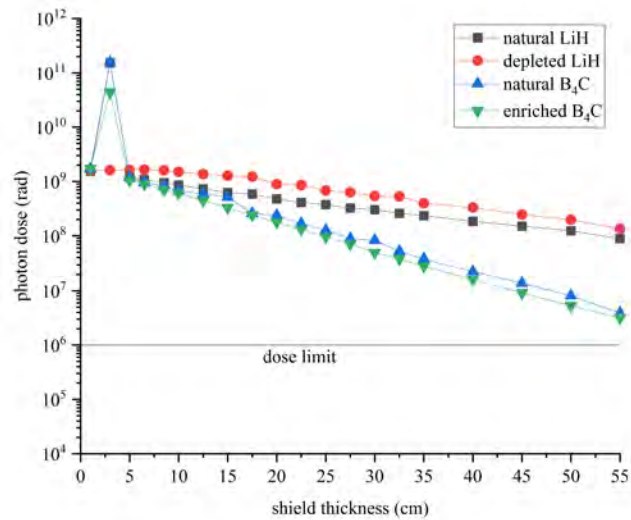
### 3.2. Moderated LEU-fueled reactor results

Figure 3a shows the calculated neutron dose at the major surface of the shadow shield as a function of the shield thickness for the moderated LEU-fueled reactor using natural lithium hydride, depleted lithium hydride, natural boron carbide, and enriched boron carbide as the shielding materials. Figure 3b shows the calculated gamma ray dose at same location using same shielding materials. In terms of neutron shielding, the shield for the moderated LEU-fueled reactor is comparable to the shield for the unmoderated HEU-fueled reactor. Natural lithium hydride, depleted lithium hydride, and enriched boron carbide would all require a shield thickness of at least 44 cm to meet the dose limit of  $1 \times 10^{14}$  n/cm<sup>2</sup> (>1 MeV) equivalent in silicon. Natural boron carbide is slightly less effective, requiring greater than 50 cm to meet the same dose limit. While the neutron shielding cases for the unmoderated HEU-fueled and the moderated LEU-fueled reactors are relatively similar, the gamma ray shielding cases for the moderated LEU-fueled reactor is significantly more challenging. Figure 3a shows all of the shielding materials will require greater than 55 cm of shielding material to meet the gamma ray dose limit ( $1 \times 10^6$  rad). Additionally, natural

lithium hydride, natural boron carbide, and enriched boron carbide all result in a significant increase (15-20x) in the gamma ray dose with a shield thickness less than 5 cm. This implies that there is a very strong contribution from gamma rays produced by the interaction of high-energy neutrons with the shielding material. The higher contribution from secondary gamma rays in the shield for the unmoderated LEU-fuel indicates that a strong gamma ray absorber such as tungsten will be required in the first few centimeters of the shield, making the shield for the moderated LEU-fueled reactor much more massive than the shield for the unmoderated HEU-fueled reactor. This is contrary to the assumption that a moderated LEU-fueled reactor would require less gamma ray shielding than an



a) Calculated neutron doses.



b) Calculated gamma doses.

Figure 3. Calculated neutron and gamma doses from the moderated LEU-fueled reactor as a function of shield thickness.

unmoderated HEU-fueled reactor and requires further consideration.

While the moderated LEU-fueled reactor requires a lower lifetime core fluence for the same power (by a factor of approximately two), the thicker reflector of the unmoderated HEU-fueled system results in a nearly six-fold reduction in the fluence emitted from the outside surface of the reflector, which reduces the neutron current reaching the shield. The thinner reflector of the moderated LEU-fueled reactor means that more neutrons reach the shield at higher energies compared to the unmoderated HEU-fueled reactor; thus, the presence of a significant reflector means that the core spectrum is relatively unimportant in terms of shield design, as the reflector thickness has a more significant impact than the presence of a moderator.

The higher energy of the neutrons leaving the reflector of the moderated LEU-fueled reactor will most likely require the shadow shield to incorporate a tungsten or depleted uranium layer near the minor surface of the shadow shield, increasing the mass of the shadow shield. The higher gamma ray fluence produced by the moderated LEU-fueled reactor will further contribute to a larger, more massive, shield for that reactor.

#### **4. Summary and Conclusions**

A moderated LEU-fueled reactor containing 60 wt% zirconium hydride ( $ZrH_{1.5}$ ) in an alternating disc geometry with 19.75 wt% enriched uranium alloyed with 10 wt% molybdenum (U-10Mo) could be a feasible alternative to an unmoderated HEU-fueled reactor with a monolithic block of 93 wt% enriched U-10Mo. However, the radiation shielding required by any space nuclear power system is frequently the most massive component of the power system. The present study considers the shield design for comparable unmoderated HEU-fueled and moderated LEU-fueled space nuclear power reactors operating at the same thermal power (15 kW<sub>th</sub>) and operating lifetime (5 years).

Considering both reactors, the shielding analyses show that the moderated LEU-fueled reactor will need a thicker shadow shield compared to the unmoderated HEU-fueled reactor. The thinner reflector of the moderated LEU-fueled reactor means that more neutrons reach the shield at higher energies compared to the unmoderated HEU-fueled reactor; thus, the presence of a significant reflector means that the core spectrum is relatively unimportant in terms of shield design, as the reflector thickness has a more significant impact than the presence of a moderator.

Based on the analyses presented in this paper, the design of the radiation shadow shield for a space nuclear is tightly coupled to the reflector thickness. The presence of a significantly high-worth reflector means that the core spectrum is somewhat de-emphasized in terms of shield design, as the reflector thickness has a more significant impact. Therefore, mass optimization of a space nuclear reactor needs to consider the coupled impacts of the core, the reflector, and the radiation shield.

## 5. References

- DePriest, K., R., "Impact of ASTM Standard E722 Update on Radiation Damage Metrics", SANDIA Report, SAND2014-5005, June, 2014.
- Lee, H. C., Lim H.S., Han T.Y., Čerba Š., "A neutronic feasibility study on a small LEU fueled reactor for space applications", *Annals of Nuclear Energy*, Volume 77, pp.35-46, 2015.
- Mencarini, L. H. and King, J. C., "Fuel Geometry Options for a Moderated Low-enriched Uranium Kilowatt-Class Space Nuclear Reactor.", *Nuclear Engineering and Design*, Vol. 340, pp 122-132, 2018.
- Nishiyama, T., Nagata, H., Nakashima, H., "Proposal of space reactor for nuclear electric propulsion system". *Proceedings of 2009 international congress on advances in nuclear power plants*, (p. 2572), Japan (2009).
- Pelowitz, D., Fallgren, A. J., McMath, G.E.; "MCNP6™ User's Manual code version 6.1.1beta", Los Alamos National Laboratory report LA-CP-14-00745, Rev. 0, 2014.
- Poston, D. I., "KRUSTY Design and Modeling", KRUSTY Program Review, LA-UR-16-28377, 2016-11-01.
- United Nations General Assembly, "Principles Relevant to the Use of Nuclear Power Sources in Outer Space", A/RES/47/68, 14 December 1992, <http://www.un.org/documents/ga/res/47/a47r068.htm> (accessed on 20 June 2017).
- Von Hippel, F., "Two policy issues: 1) Safety of RTG Earth Flybys 2) HEU vs. LEU space-reactor fuel", presented at American Nuclear Society Space Nuclear Conference, Boston, MA, 27 June 2007.

# NEUTRONIC FEASIBILITY OF A LOW ENRICHED FAST SPECTRUM NUCLEAR THERMAL PROPULSION ENGINE

Matt Krecicki, Dan Kotlyar

Georgia Institute of Technology, Atlanta, GA, 30318

Primary Author Contact Information: [mkrecicki@gatech.edu](mailto:mkrecicki@gatech.edu)

*This paper explores the feasibility of a fast spectrum nuclear thermal propulsion (NTP) low enriched uranium (LEU) engine. The analysis presented focuses on a uranium nitride cermet fuel form. The main objective is to compare the neutronic characteristics of an unmoderated and hence fast system against moderated systems. The results of this study show that unmoderated configurations have the potential to sustain a critical system with enough reactivity margin. In addition, the kinetic parameters of unmoderated LEU NTP systems are more favorable. Namely, the delayed neutron fraction and average number of neutrons produced per fission of unmoderated configurations are 5.2% and 7.1% greater, respectively. Finally, unmoderated configurations are the least sensitive to the amount of tungsten loaded into the fuel matrix and thus experience the lowest reactivity penalties.*

## I. INTRODUCTION

Recent LEU NTP core designs have focused on the use of moderator elements (ME) in conjunction with ceramic metallic (cermet) fuel elements (FE) to provide excess core reactivity. However, the use of moderator elements reduces the available flow area in the core, and requires the development of a stable higher temperature hydride material to moderate the neutrons. Moderated cores also suffer from increased power peaking factors (on the order of 1.9), especially near the FE-ME interfaces<sup>1,2</sup>. The latter requires to down rate the total core power, which in turn reduces the engine’s thrust. Such edge heating can also cause significant stress fields inside the FE and potentially lead to a mechanical failure. Removal of the ME could significantly reduce the complexity of NTP systems and improve the overall performance of these engines.

### I.A. Problem Description

The problem considers a standard KIWI-B4E<sup>3</sup> moderator element and fuel element design in an inverse Pewee configuration. Table I presents the fuel element and moderator element dimensions. Fig. 1 presents the 2D infinite lattice configuration. Periodic boundary conditions (BC) were applied to the unit cell problem, shown by the dotted purple line in Fig. 1.

The fuel type considered in this paper is a refractory cermet. The fuel kernel is uranium nitride (UN) with a molybdenum (Mo)-tungsten (W) alloy (Mo/W) matrix, similar to the fuel utilized in previously published NASA

studies.<sup>4,5</sup> No isotopic enrichment of Mo, Zr, or W is assumed. In this study the vol% of tungsten in the matrix material will be perturbed. Increasing the vol% of tungsten is matrix material advantageous for thermal hydraulic performance due to tungsten’s superior thermal conductivity, vapor pressure, and melting temperature.<sup>6,7</sup>

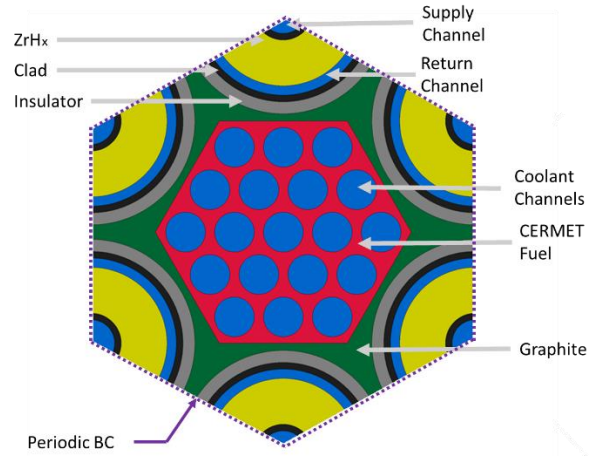


Fig. 1. Inverse pewee infinite lattice

TABLE I. Fuel and moderator element dimensions.

Element	Parameter	Value
FE	Coolant Channel Radius	0.1727 cm
FE	Cladding Thickness	0.0150 cm
ME	Supply Channel Radius	0.2000 cm
ME	Supply Channel Cladding Thickness	0.0570 cm
ME	ZrH <sub>2</sub> Thickness	0.3930 cm
ME	Return Channel Thickness	0.0800 cm
ME	Return Channel Cladding Thickness	0.0570 cm
ME & FE	Hexagonal Flat to Flat	1.9050 cm

The cermet fuel loading is fixed at 60 vol% UN, porosity of 7%, and a uranium enrichment of 19.75%. The cladding material is the same material as the matrix. The moderator element utilizes a zirconium hydride (ZrH<sub>2</sub>) to provide moderation. Table II details the materials used in each component of the fuel and moderator elements. The conversion factor from ME:FE ratio to H:U235 ratio is also

included in Table II, for example an ME:FE ratio of 3 would have an H:U235 ratio of 44.946.

**TABLE II.** Fuel and moderator element material descriptions.

Region	Material
Fuel Meat	Mo/W-UN Cermet
Fuel Cladding	Mo/W Alloy
Fuel Loading	60 vol%
Fuel Porosity	7%
Moderator Cladding	Zircaloy-4
Moderator Insulator	ZrC (50% dense)
Moderator Hydride	ZrH <sub>2</sub>
Moderator Sleeve	Graphite
H:U235 / ME:FE Conversion	14.982

The moderator-to-fuel (ME:FE) ratios were mimicked by changing the density of the ME composition. More specifically, the porosity factor was varied from zero to one. When the fraction is equal to zero the unit cell is only comprised of fuel element, and when the fraction is one the unit cell has an ME:FE ratio of 3:1. The design of the moderator element, and use of a graphite sleeve was based on previous publicly available designs<sup>3</sup>. While graphite can be considered a moderating material, the average logarithmic energy decrement per collision of graphite is 6.34 times lower than hydrogen. Additionally, the moderating power, based on thermal scattering cross sections<sup>8</sup>, of Hydrogen is approximately 33 times larger than graphite in the system considered. It can be assumed that the main moderating material in this configuration is the ZrH<sub>x</sub>. This simplified approach allows for continuous trends to be obtained, but neglects spatial effects of perturbing the ME:FE ratio. The difference is expected to be negligible but should be verified in the future.

## II. ANALYSIS AND RESULTS

The analyses presented in this paper were performed with the Monte-Carlo based Serpent code, with coupled neutron and gamma transport enabled<sup>9</sup>. The serpent code has been extensively verified, and is well suited for multi-physics calculations<sup>10</sup>. In this paper the ENDF/B-VII.0 evaluated data library was used.

### II.A. Infinite Multiplication Factor

The infinite multiplication factor was calculated for various ME:FE ratios ranging from 0 to 3 and for the matrix tungsten loading of 30 vol%. The relationship between  $k_{inf}$  and the ME:FE ratio is presented in Fig. 2. The multiplication factor initially decreases as ME:FE ratio increases, and then increases again with ME:FE ratios greater than 0.3. This behavior can be explained by examining the weighted one group macroscopic fission and absorption cross sections. These macroscopic cross sections are presented on a logarithmic scale as a function

of the ME:FE ratio in Fig. 3. The fission-to-absorption cross-section ratio is also presented in Fig. 3 using a linear scale. As the ME:FE increases so does the fission cross section, however the absorption cross section increases at a faster rate than the fission cross section until an ME:FE ratio of 0.3 is achieved. This effect becomes apparent via the ratio between the fission and absorption cross section.

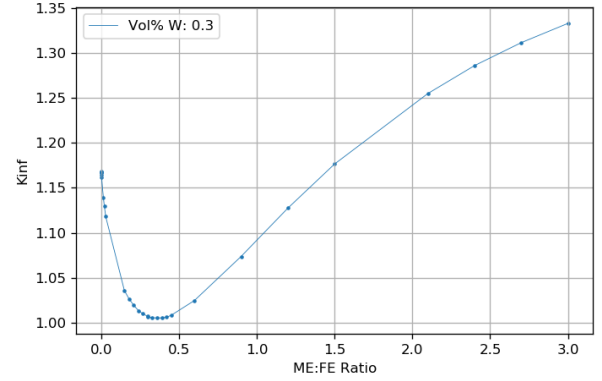


**Fig. 2.**  $k_{inf}$  vs ME:FE ratio

It is also important to note that the average number of neutrons produced per fission monotonically decreases from 2.505 (ME:FE=0) to 2.468 (ME:FE=3). This effect is minor but shows that fast systems produce 7.1% more neutrons per fission than thermal systems, as expected

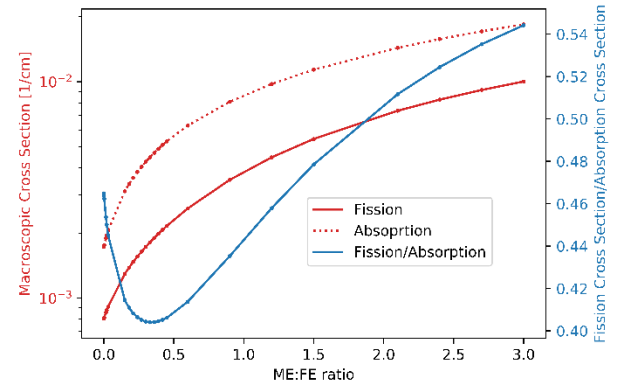


**Fig. 3.** Fission and absorption macroscopic cross sections vs ME:FE ratio

The primary contributors to the infinite multiplication factor are the reproduction and fuel utilization factors. The reproduction factor ( $\eta$ ) is defined in Eq. 1, and the fuel utilization factor ( $f$ ) is defined by Eq. 2.

$$\eta = \frac{\nu \Sigma_f^{fuel}}{\Sigma_f^{fuel} + \Sigma_{cap}^{fuel}} \quad (1)$$

$$f = \frac{\Sigma_f^{fuel} + \Sigma_{cap}^{fuel}}{\Sigma_{abs}^{all}} \quad (2)$$

The trends show that both the reproduction factor and fuel utilization factor reach a minimum at an ME:FE ratio of 0.3. The highest fuel utilization factor of 0.628 is achieved with an ME:FE ratio of 3, however the unmoderated case still achieves a fuel utilization factor of 0.545.

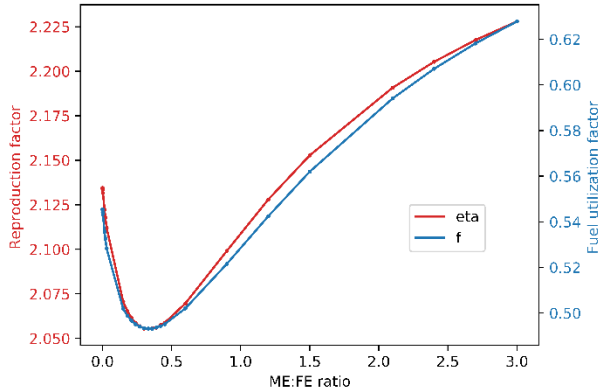


Fig. 4. Two factor formula vs ME:FE ratio

The total absorption cross section of the ME has a very minor role in the criticality of the system. At a maximum the moderator element absorption cross section only accounts for 2.03% of the total absorption cross section. The ME absorption cross section monotonically increases as the ME:FE ratio increases.

### II.B. Delay Neutron Fraction

Meulekamp's method results, were used to evaluate the delayed neutron fraction. Fig. 5 presents the total delayed neutron fraction, represented by the dashed red line, and the fourth group delayed neutron fraction, represented by the dashed blue line, as a function of the ME:FE ratio. As the ME:FE increases from 0 to 3 the delayed neutron fraction decreases by 5.2% from 0.00699 to 0.00664. The decrease in the delayed neutron factor is primarily due to the decrease in the fourth delayed group, whereas the other five groups remain fairly constant.

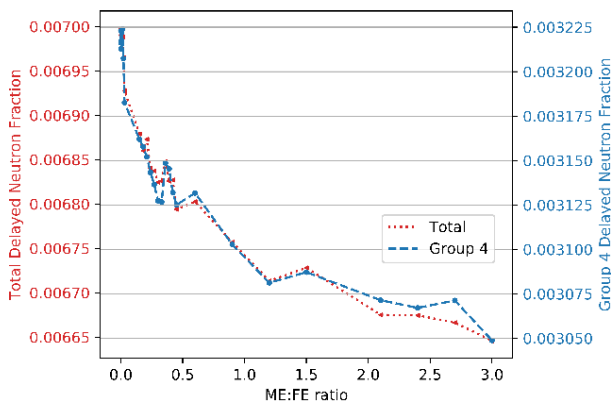


Fig. 5. Delayed neutron fraction vs ME:FE ratio

The degradation of the fourth group is caused by the increase in the U-235 to U-238 fission rate ratio. The total delayed neutron fraction of a fission in U-235 is 0.0065, while the total delayed neutron fraction in U-238 is 0.0148<sup>10</sup>. The ratio of fissions in U-235 to U-238 is presented in Fig. 6. The ratio increases by a factor of 10.6 as the ME:FE ratio increases from 0 to 3.

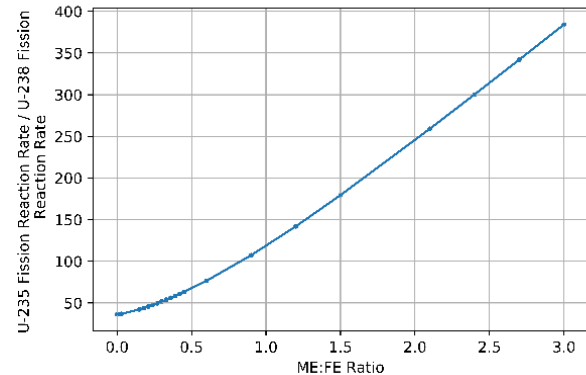


Fig. 6. Uranium fission ratio vs ME:FE ratio

### II.C. Neutron Spectrum and Macroscopic Cross Sections

As the ME:FE ratio increases, the neutron spectrum softens (*i.e.*, the thermal peak is amplified). This effect is presented in Fig. 7. The unmoderated case has a large peak in the fast energy range, while the completely moderated case displays the characteristic Maxwell-Boltzmann thermal neutron distribution. When the fuel is only partially moderated the neutron spectrum resides predominately in the epi-thermal energy range, which is also where the tungsten matrix isotopes have strong resonances.

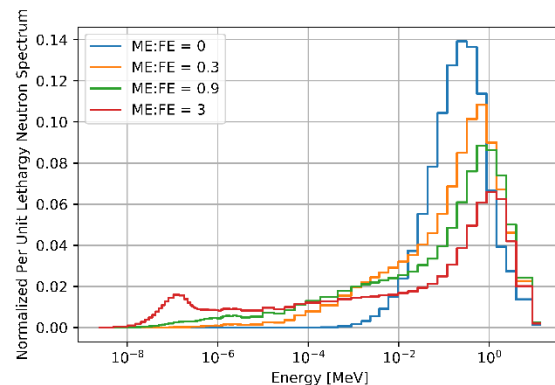


Fig. 7. Normalized neutron flux per unit lethargy vs energy

The macroscopic absorption and fission cross sections were binned into a three-group energy structure

detailed in Table III. The group structure energy bins are the default MCNP three group structure, additionally the epi-thermal energy range completely contains the resolved resonance region of the tungsten and molybdenum microscopic cross section, presented in Fig. 8 and Fig. 9 respectively.

**TABLE III.** Three group structure.

Group	Energy Range
Fast	$>100$ keV
Epi-Thermal	$0.625$ eV $< E < 100$ keV
Thermal	$<0.625$ eV

The three-group absorption cross sections for molybdenum and tungsten are plotted as a function of the ME:FE ratio in Fig. 10. The plot demonstrates that as the ME:FE ratio increases the total absorption cross section increases, however each element's fractional share of the total absorption cross section changes as the ME:FE ratio increases. In the unmoderated case the absorption cross section is fairly even split between tungsten and molybdenum.

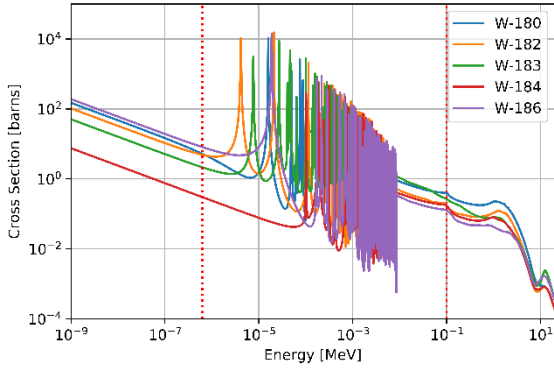


**Fig. 8.** Tungsten microscopic cross section vs energy

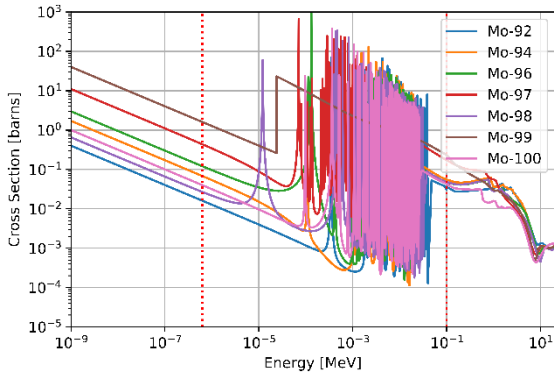


**Fig. 9.** Molybdenum microscopic cross section vs energy

As the ME:FE ratio increases the tungsten and molybdenum epi-thermal absorption cross section grows rapidly. In the fully moderated case the tungsten epi-thermal absorption cross section dominates the total absorption cross section.

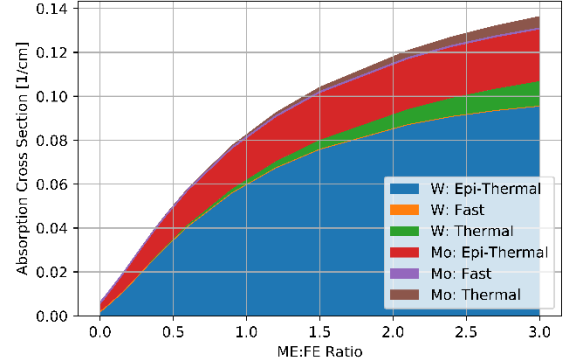


**Fig. 10.** Three group absorption cross section vs ME:FE ratio

Fig. 11 presents the three-group macroscopic fission cross section as a function of the ME:FE ratio. The red dashed vertical line shows where the ME:FE ratio is equal to 0.3. The thermal fission cross section begins to become significant with ME:FE ratios greater than 0.3. Before this point there is almost no fission gain in the thermal region. While the fast and epi-thermal fission cross section remain fairly constant.

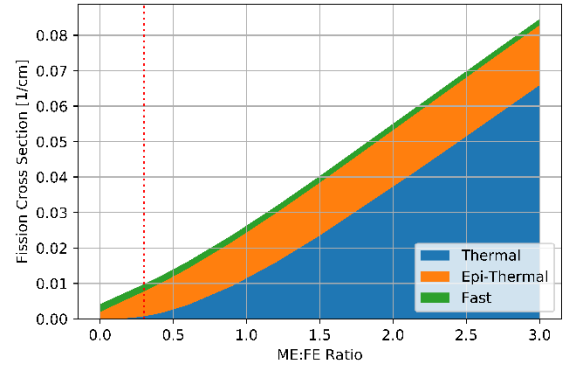


**Fig. 11.** Three group fission cross section vs ME:FE ratio

#### II.D. Tungsten Sensitivity Analysis

Increasing the volume fraction of tungsten in the cermet matrix material is extremely advantageous for thermal hydraulic performance. Therefore, it is crucial to understand how the tungsten loading affects the criticality of each configuration. Fig. 12 presents the dependence of  $k_{inf}$  on the ME:FE ratio and W loading. In general, as the tungsten loading increases  $k_{inf}$  decreases. This is due to the fact that tungsten has a much larger absorption cross section than molybdenum.

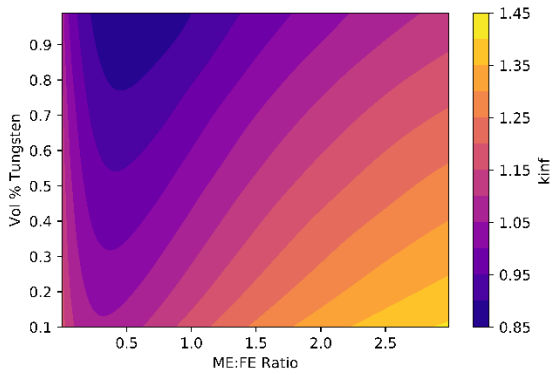


**Fig. 12.**  $k_{inf}$  vs ME:FE ratio for various tungsten loadings

However, not all ME:FE ratio configurations are equally sensitive to the amount of tungsten loading in the matrix. The sensitivity of several ME:FE ratios to vol% of tungsten loaded in the fuel matrix is presented in Fig. 13. Each of the ME:FE ratio trend is normalized to each ME:FE ratio's 10 vol% Tungsten infinite multiplication factor to calculate the change in reactivity. The most sensitive ME:FE ratio is 0.9, while the unmoderated configuration is the least sensitive to the tungsten loading.

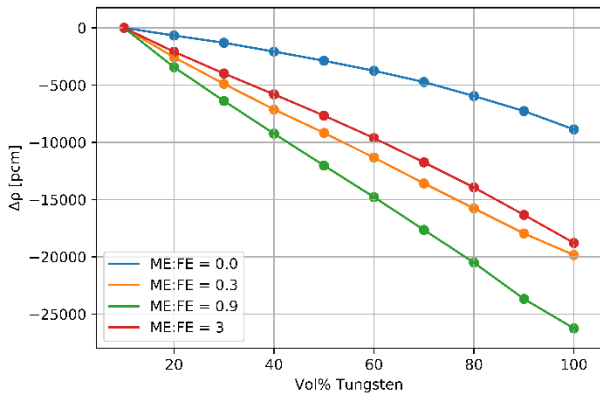


**Fig. 13.** Change in reactivity vs tungsten loading

The trends presented in Fig. 13 are assumed to be linear. Therefore, the tungsten sensitivities ( $\alpha$ ) of each ME:FE ratio is the slope of the lines presented in Fig. 13. Eq. 4 presents this relationship where  $\rho$  is the reactivity and  $v$  is the vol% of tungsten loaded in the matrix.

$$\alpha = \frac{\Delta\rho}{\Delta v} \quad (4)$$

Fig. 14 presents the tungsten sensitivity coefficient as a function of the ME:FE ratio. The trends presented in Fig. 13 are confirmed in Fig. 14. The tungsten sensitivity sharply increases as the ME:FE ratio increases from 0 to 0.6 before reaching a minimum at 0.9. After this point the sensitivity begins to decrease again.

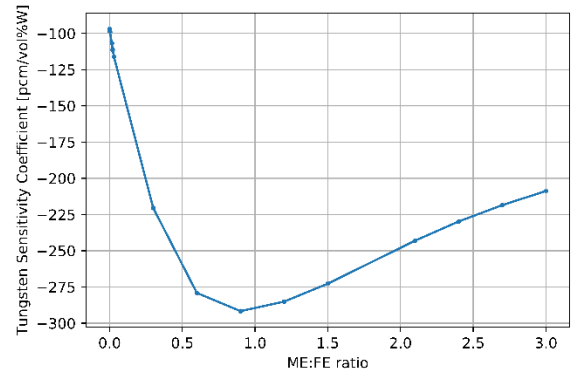


**Fig. 14.** Tungsten sensitivity coefficient vs ME:FE ratio

Fig. 14 demonstrates that unmoderated systems are approximately half as sensitive to the tungsten loading than fully moderated systems, and that partially moderated cores suffer from extreme neutronic penalties when additional tungsten is loaded into the matrix material. It is important to note that most NTP design studies seek to minimize the ME:FE ratio, typically resulting in designs with ME:FE ratios between 1 and 1.5. In this region the reactivity penalty from loading additional tungsten into the fuel matrix is still close to the maximum.

## IV. CONCLUSIONS

This paper has demonstrated that an unmoderated UN cermet-based fuel can provide significant excess reactivity. Unmoderated systems have a larger delayed neutron fractions due to the increased fraction of total fissions occurring in U-238. Additionally, unmoderated cores are the least sensitive to the tungsten loading in the fuel matrix material. This reduced sensitivity could provide significant thermal hydraulic advantages. Further studies into unmoderated LEU NTP cermet fuel-based systems should be performed.

## IV. FUTURE WORK

Future work will focus on the analysis of a full core Serpent model to determine three-dimensional leakage effects on the criticality of the system. Further investigation of the tungsten sensitivity coefficient will be perused.

## REFERENCES

1. Krecicki M., et Al. Quantification of Intra Element Peaking in Low Enriched Nuclear Thermal Propulsion Cores, BWX Technologies, NETS, 2020.
2. Stewart M., 2019. Thermal, Fluid, and Neutronic Analysis of an LEU Nuclear Thermal Propulsion Core. VPL at NASA Glenn Research Center. AIAA Propulsion and Energy 2019 Forum

3. Finseth J. L., 1991. Rover Nuclear Rocket Engine Program: Overview of Rover Engine Tests: Final Report. Tech, Rep. NASA-CR-184270
4. Houts et al., 2019. NASA's Nuclear Thermal Propulsion Project. <https://ntrs.nasa.gov/archive/nasa/casi.ntrs.nasa.gov/20170003378.pdf>
5. NASA, Space Technology Mission Directorate Game Changing Development Program, FY19 Annual Review
6. Lassner, E., Schubert, W.D., 2012. Tungsten: Properties, Chemistry, Technology of the Elements, Alloys, and Chemical Compounds.
7. Lewis, J.V., 1967. Estimating Thermal Conductivity of Cermet Fuel Materials for Nuclear Reactor Application. Lewis Research Center, Cleveland, Ohio Tech. Rep. NASA TN D-3898.
8. Hill J., 1961. Textbook of Reactor Physics An Introduction.
9. Leppänen, J., Pusa, M., Viitanen, T., Valtavirta, V., Kaltiaisenaho, T., 2015. The Serpent Monte Carlo code: Status, development and applications in 2013. *Ann. Nucl. Energy* 82, 142–150.
10. Leppänen, J., Mattila, R., Pusa, M., 2014. Validation of the Serpent-ARES code sequence using the MIT BEAVRS benchmark – initial core at HZP conditions. *Ann. Nucl. Energy* 69, 212–225.
11. Oka, Y., Suzuki, K., 2008. Nuclear Reactor Kinetics and Plant Control.

## QUANTIFICATION OF INTRA-ELEMENT POWER PEAKING IN LOW ENRICHED NUCLEAR THERMAL PROPULSION CORES

M. Krecicki<sup>1,2</sup>, R. Swanson<sup>1</sup>, J. Witter<sup>1</sup>

<sup>1</sup>BWX Technologies, Inc., Lynchburg, VA, 24501

<sup>2</sup>Georgia Institute of Technology, Atlanta, GA, 30318

Primary Author Contact Information: 407-415-3647, [makrecicki@bwxt.com](mailto:makrecicki@bwxt.com)

*NERVA-like Low Enriched Uranium (LEU) Nuclear Thermal Propulsion (NTP) cores have the unique design feature of requiring a heterogeneous layout of moderator and fuel elements to form the reactor core. Modern NTP designs require the use of highly absorbing materials as the fuel matrix material. This material choice and core configuration causes a higher density of fission events to occur at the fuel element and moderator element interface. The result is intra-element power peaking as high as 1.90 in some cases.*

### I. Introduction

LEU NTP cores have the unique feature of requiring a heterogeneous layout of moderator and fuel elements to form the reactor core. This layout causes pockets of thermal neutrons to be created in the moderator element. The fuel element matrix materials and uranium nitride fuel have significant neutron capture and fission cross sections. The thermal neutrons impinging on the fuel element cause fission at a higher rate in the outer edges of the fuel element. The neutron flux becomes depleted of thermal neutrons towards the center of the element. The harder spectrum increases the ratio of capture events, which release much less energy to fission events. The resulting intra-element peaking has detrimental impacts on the thermal hydraulic performance and increases the stress fields in the fuel elements. Understanding the driving phenomenon is critical to developing mitigation solutions.

### IA Problem Description

Cermet fuel has been the focus of NASA's Game Changing Development (GCD) NTP program. Updates from the GCD program have stated that "in the cooler regions of the engine (<2000 K) a Mo/UN ceramic metallic (Cermet) alloy is utilized, and in the hotter regions (>2000 K) a Mo/W metal alloy is used in conjunction with UN fuel."<sup>1,2</sup> Previous published work has focused on a Mo-30W alloy. A similar material will be used in this work.<sup>3</sup> The core is composed of hexagonal fuel and moderator elements presented in Fig. 1. The general axial core configuration is presented in Fig 2, which presents the axially segmented of Mo to Mo/W.<sup>1,4</sup> The upper fuel element "cold end" region is composed of a pure Mo-UN Cermet, while the "hot end" higher

temperature region consists of a Mo/W-UN Cermet. This change in material composition has a significant impact on the intra-element peaking shape.

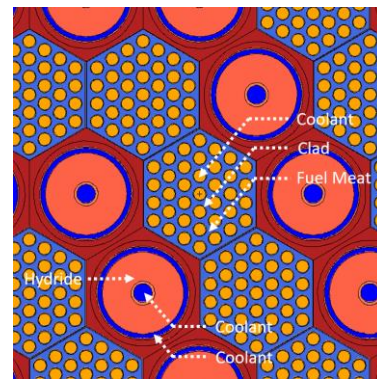


Fig. 1. Fuel Element and Moderator Radial Cross Section

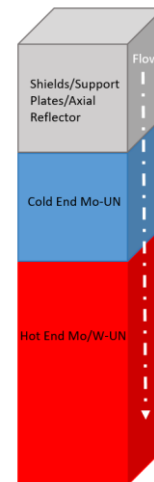
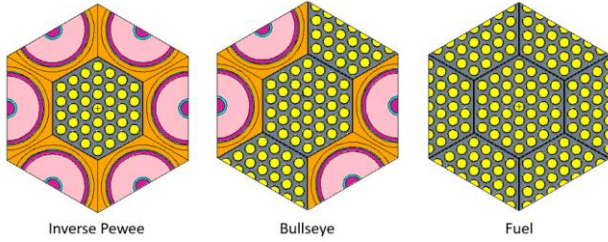


Fig. 2. Axial Core Configuration

Three unique core patterns will be evaluated in this paper. These configurations are presented in Fig. 3. Full core intra-element peaking calculations have extreme computational costs but are required in order to accurately model the critical spectrum in each fuel element. The calculation time using a full core solution is on the order of several days, even when executed in parallel to sufficiently converge the energy deposition mesh. In order to increase the computational efficiency while preserving

the relevant physics and similar neutron spectrum, a simple unit cell model was constructed where the center fuel element is the element of interest. This approach allows for a well converged mesh to be calculated in a matter of hours instead of several days.



**Fig. 3.** Core Element Configurations

### LB Examination of Material Cross Sections

Light water reactors operate in the thermal energy range in order to improve the neutron economy of the system. The fission cross section of Uranium-235 is the highest in the thermal energy range, as demonstrated in Fig. 4. It should be noted that the fission cross sections become very similar at energies greater than 1 MeV.

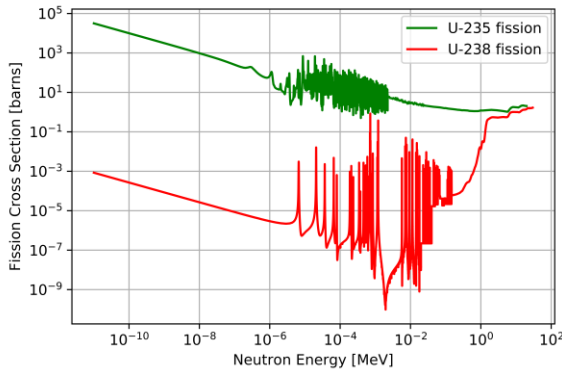


**Fig. 4.** Uranium-235 and Uranium-238 Fission Cross Sections

In the thermal energy range, the ratio of the total absorption (capture) cross section to the fission cross section is very low. Lower capture to fission ratios (C:F) allow for neutrons to be more efficiently utilized and, as a result, allow for critical cores with reduced uranium enrichment. The Cermet matrix materials Molybdenum and Tungsten both have strong epi-thermal resonances and are both strong thermal neutron absorbers. Therefore, these materials have a significantly higher C:F ratio than the moderator element, coolant and structural component materials. This trend is presented in Fig. 5. Ideal neutronic performance is achieved when the C:F ratio is at a minimum. It is also important to note that nitrogen does not contain any high energy scattering resonances which

are present in oxygen. These scattering resonances are important in oxide fuel, as they have a significant effect on the slowing high energy fission neutrons. However, this study only considers a uranium nitride fuel form.

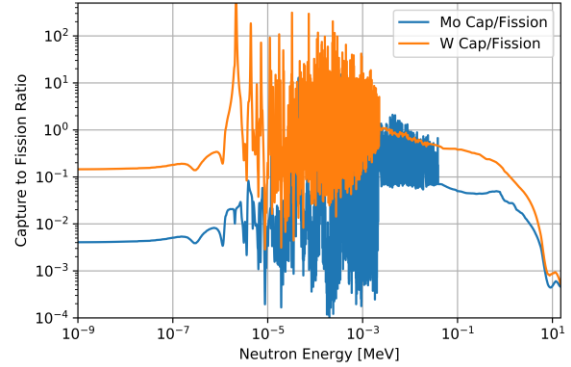


**Fig. 5.** Molybdenum and Tungsten Capture to Fission Cross Section Ratio

### II. Computational Tools

MCNP6.1 was the neutron transport code<sup>5</sup> used in the analysis presented. In order to accurately evaluate the spatial energy deposition, a type 3 TMESH was used which accounts for both neutron and gamma heating. The focus of this paper is evaluating the intra-element peaking in the meat fuel. However, this approach is equally valid for any region in the moderator element. A custom built software package was developed to handle input generation and post-processing. Additionally, the package includes the capability to export power peaking maps which were used in ANSYS calculations and other internally developed multi-physics solvers to support NASA's GCD NTP program.

In order to better understand the root cause of the intra-element peaking, the fission (MT=18) reaction rate and absorption (MT=102) reaction rate will be tracked throughout the fuel element. With this information, the local effective fuel utilization factor,  $f$ , can be calculated using the following equation:

$$f(j) = \frac{\sum_i \sum_j \sigma_{f,i,j} * \Phi_j}{\sum_i \sum_j \sigma_{a,i,j} * \Phi_j}$$

The fuel utilization factor is calculated by summing the fission reaction rate of all isotopes,  $i$ , in node  $j$  of the fuel and dividing by the total absorption reaction rate, including fission of all the isotopes in the node. This is accomplished using a mesh tally to discretize the fuel element.

### III. Analysis

The intra-element peaking factors are calculated based on filtering out non-fuel material from the TMESH and then normalizing the energy deposition to the average value. The mesh used across the problem contained 500 bins in the x and y axis direction and two z-axis bins. The average relative uncertainty in each bin was less than one percent. Table I summarizes the peaking factors for each configuration. Fuel is the best performing configuration, with an almost flat power distribution in the cold end. The worst performing configuration is Bullseye, with a maximum peaking factor of 1.90.

**Table I.** Intra-Element Peaking Factors

Configuration	Inverse		Fuel
	Pewee	Bullseye	
Cold End Max PF	1.71	1.85	1.11
Hot End Max PF	1.78	1.90	1.02
Max % $\Delta$	9.75	11.90	3.43
Avg. % $\Delta$	-0.41	-0.21	0.003

The intra-element peaking factors for the Inverse Pewee, Bullseye and Fuel patterns are presented in Figures 5, 6 and 7, respectively. The power peaking color scale was fixed with a maximum value of 2.0 and a minimum value of 0.6. This was done to ensure a fair visual comparison between the three different configurations and to encompass the full range of peaking factors present in the problem. No interpolation methods were applied to the results. Each figure contains three sub figures; the left sub figure displays the power peaking in cold-end region; the middle figure displays the power peaking in the hot-end region; the right hand side figure displays the percent difference between the cold and hot end power peaking. It is important to note that, based on visual inspection, the cold end and hot end peaking factors look very similar. However, when compared analytically, there are significant differences between the hot and cold end intra-element peaking patterns. The percent difference color scale has not been normalized and is independent for each figure. Positive percent difference values show where the hot end peaking factors are larger than the cold end peaking factors, and vice versa for negative percent difference values. The larger value shows where the intra-element peaking is worse in the hot end of the fuel. For both Bullseye and Inverse Pewee configurations, the edge heating is greater in the hot end than the cold end of the fuel elements. This result is expected due to the C:F ratio being larger in Tungsten than Molybdenum.

The increased power peaking is occurring in the fuel meat regions adjacent to the moderator elements due to the proximity to the transport of the thermal neutrons back into the fuel meat region. Additionally, the

configurations with just fuel show a nearly uniform power distribution. This is due to the fact that, in the all fuel configuration, the neutron spectrum is extremely hard and there is no migration of the worthier thermal neutrons back into the fuel meat. This results in a significant increase in the average mean free path. Therefore, the neutrons can penetrate much deeper into the fuel element and cause fissions throughout the element. Additionally, the fast energy range has an equally and potentially more favorable C:F ratio. The inverse Pewee and Bullseye configurations have significant moderation and result in thermal to epi-thermal neutron spectrums. As such, some of the neutron population resides with a very high C:F ratio energy range.

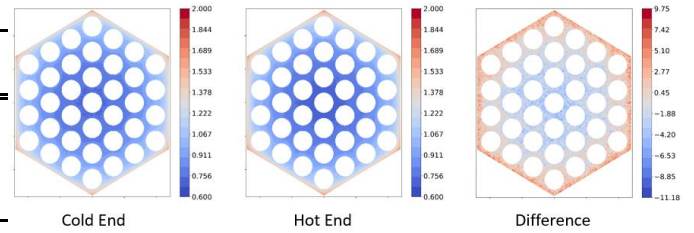


**Fig. 5.** Inverse Pewee Intra-Element Peaking

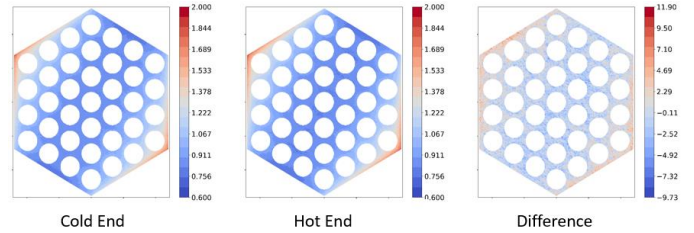


**Fig. 6.** Bullseye Intra-Element Peaking

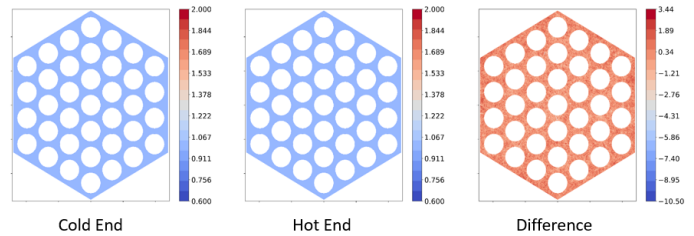


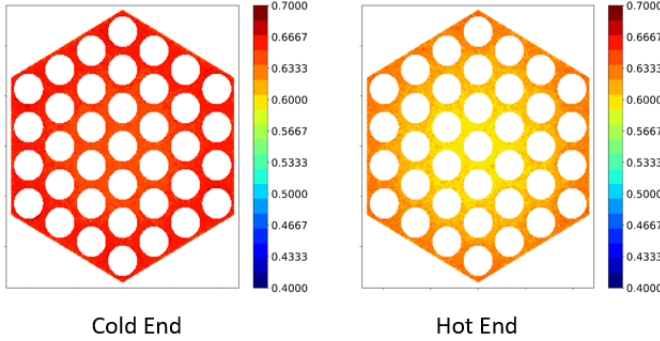
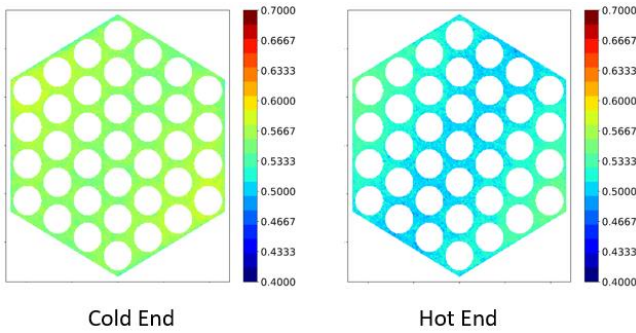
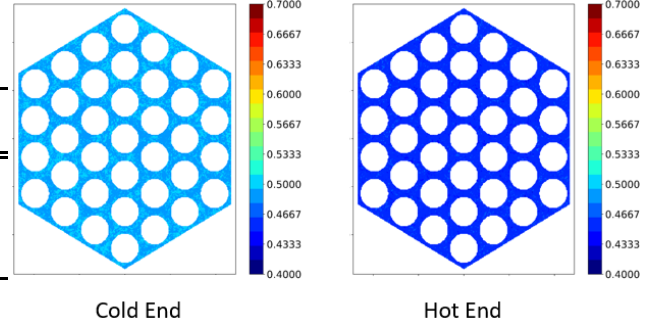
**Fig. 7.** Fuel Intra-Element Peaking

The fuel utilization factors for the Inverse Pewee, Bullseye and Fuel patterns are presented in Figures 8, 9 and 10, respectively. Table II summarizes the fuel utilization factor results. The fuel utilization factor increases as the number of surrounding moderator element increases, which increases the uranium to hydrogen ratio and results in an increase in the resonance escape probability. This allows the configurations with a higher number of moderator elements to achieve a more thermal spectrum. The worst fuel utilization factor, 0.456, is present in the hot end all fuel configuration. While the best fuel utilization factor, 0.682, is present in the cold end Inverse Pewee configuration.

**Table II.** Fuel Utilization Factors

Configuration	Inverse Pewee		Fuel
	Pewee	Bullseye	
Cold End Max f	0.682	0.599	0.498
Cold End Avg f	0.654	0.559	0.494
Hot End Max f	0.655	0.566	0.487
Hot End Avg f	0.616	0.514	0.456

The figures below display an almost identical distribution to the power peaking distributions. Again, a fixed color scale is used in Figs. 8, 9 and 10 to provide a fair visual comparison. Higher fuel utilization factors represent regions where the fission reaction is more dominant than a capture reaction. The average energy released by a fission event is much greater than that of a capture ( $n,\gamma$ ) reaction. This explains why higher fuel utilization regions coincide with higher intra-element peaking regions. The cold end regions have a more uniform fuel utilization distribution than the hot end fuel regions. This is due to the absence of Tungsten in the cold end fuel section. In the hot end fuel section, the spectrum becomes harder and the C:F ratio increases much more significantly, which results in a more pronounced distribution.

**Fig. 8.** Inverse Pewee Pattern Fuel Utilization Factor**Fig. 9.** Bullseye Pattern Fuel Utilization Factor**Fig. 10.** Fuel Pattern Fuel Utilization Factor

#### IV. Conclusions

The intra-element peaking is a result of the discrete moderator element and fuel element arrangement and the use of highly absorbing material as the fuel matrix material. The fuel utilization factor distribution shows that fission events are more likely to occur at the fuel element and moderator element interface. The maximum intra-element peaking of 1.90 is present in the Bullseye configuration, while the minimum intra-element peaking of 1.02 is present in the all fuel configuration. The highest fuel utilization factor of 0.682 is achieved in the Inverse Pewee configuration, while the lowest fuel utilization factor of 0.456 is present in the all fuel configuration.

Future studies will include the evaluation of the energy deposition inside the moderator element hydride material and an evaluation of the resonance escape probabilities throughout the fuel element. Use of delta tracking Monte Carlo code would be advantageous if fast spectrum cores will be considered in the future. The all fuel configuration required significantly more computing time than the other cases due to the ray-tracing algorithm having to update material parameters at each surface interface. Work on developing an intra-element calculation methodology to reduce computational time, while precisely preserving specific problem conditions, have shown promising initial results but are premature to publish at present.

#### V. Acknowledgements

This work was authored under Contract No. 80MSFC17C0006 with the National Aeronautics and Space Administration and Department of Energy Contract and Department of Energy subcontract through Idaho National Laboratory in Battelle Energy Alliance, LLC Contract No. BEA 00212687. The United States Government retains and the publisher, by accepting the article for publication, acknowledges that the United States Government retains a non-exclusive, paid-up, irrevocable, worldwide license to reproduce, prepare derivative works, distribute copies to the public, and

perform publicly and display publicly, or allow others to do so, for United States Government purposes. All other rights are reserved by the copyright owner. The authors would like to thank Jeremy Gustafson for the support to complete this paper.

## REFERENCES

1. NASA, “Space Technology Game Changing Development Nuclear Thermal Propulsion” [https://gameon.nasa.gov/gcd/files/2018/02/FS\\_NTP\\_180213.pdf](https://gameon.nasa.gov/gcd/files/2018/02/FS_NTP_180213.pdf) (2018).
2. M. HOUTS, S. MITCHELL, K. ASCHENBRENER, M. V. DYKE, “NASA’s Nuclear Thermal Propulsion (NTP) Project” <https://ntrs.nasa.gov/archive/nasa/casi.ntrs.nasa.gov/20170003378.pdf> (2019)
3. M. Stewart. “Thermal, Fluid and Neutronic Analysis of an LEU Nuclear Thermal Propulsion Core” *AIAA Propulsion and Energy Forum*, Indianapolis, IN; United States, August 19 - 22, (2019).
4. S. Mitchell “Game Changing Development Program – Nuclear Thermal Propulsion Annual Review” <https://ntrs.nasa.gov/archive/nasa/casi.ntrs.nasa.gov/20190031810.pdf> (2019).
5. “MCNP6 User’s Manual Version 1.0” LA-CP-13-00634 Los Alamos National Lab (2013).

## DESIGN AND ANALYSIS OF A 250 MW PLATE-FUEL REACTOR FOR NUCLEAR THERMAL PROPULSION

Ching-Sheng Lin and Gilles Youinou

Idaho National Laboratory: 2525 Fremont Ave., Idaho Falls, ID, 83402, 208-526-4704, [chingsheng.lin@inl.gov](mailto:chingsheng.lin@inl.gov)

*Nuclear thermal propulsion (NTP) is a viable option for deep space missions due to its high thrust and lightweight system. Promising fuel options considered for the high operating temperature of NTP include graphite composite fuel and tungsten cermet fuel. As there remain uncertainties in the fabrication and performance of these two fuel elements, alternative designs using fuel plates and more typical fuels based on proven nuclear technologies are also being considered. This paper provides a summary of thermal hydraulic and neutronic analyses of the straight-plate fuel assembly design used for a 250 MW NTP core. The summary of technical findings from a series of scoping studies might be useful for future NTP engine designs.*

### I. INTRODUCTION

Nuclear thermal propulsion (NTP) engines use a nuclear reactor to heat up hydrogen to high temperatures. Thrust is generated when the hydrogen is ejected at high velocity through a nozzle. This technology was first studied and tested during the Space Age, but NTP research programs were cancelled by Congress over cost concerns in the early 1970s. Since then, NTP has been revisited on occasion, with a focus on conceptual mission studies and technology feasibility studies. Due to renewed interest in a human mission to Mars, NASA began new studies of NTP, recognizing its potential for reducing travel times in deep space missions.

### II. PLATE-FUEL REACTOR CORE DESIGN

#### II.A. Design Objectives

Since there remain uncertainties associated with the fabrication and performance of historical graphite composite fuel and W/VO<sub>2</sub> cermet fuel, alternative designs using plate geometry with ceramics fuels (UN, UC, and UO<sub>2</sub>) and refractory metal cladding (W or Mo) are being studied at Idaho National Laboratory. The objective of this study<sup>1</sup> is to analyze preliminary conceptual designs for nuclear reactor cores that use fuel plates and could serve as a heat source for NTP engines. Unlike the engines considered during the Rover/NERVA Program, the <sup>235</sup>U content in these fuels should be less than 19.75 wt% (i.e. low enriched uranium [LEU] fuel). To meet the operational requirement of generating ~12,500 lbf of thrust with a specific impulse of 900 seconds, the reactor core should be able to produce ~250 MW of thermal power, and the

propellant (H<sub>2</sub>) outlet temperature should be as high as 2750 K.

#### II.B. Material Selections and Design Constraints

##### II.B.1. Fuel Assembly Geometry

Fig. 1 shows the radial and axial layouts of the straight-plate fuel assembly (FA). The square fuel assembly was arbitrarily designed with a duct dimension of 8 cm and an active core height of 80 cm. The impact of several geometric parameters on fuel, coolant (H<sub>2</sub>), and structure volume fractions, as well as surface-to-volume ratios, were examined because they directly impact core neutronic and thermal hydraulic performances. The range of geometric parameters investigated is shown below.

- cladding thickness (0.25 mm to 0.5 mm)
- fuel meat thickness (0.5 mm to 10 mm)
- H<sub>2</sub> flow gap between fuel plates (0.5 mm to 1 mm)
- number of fuel plates per assembly (7 to 49)

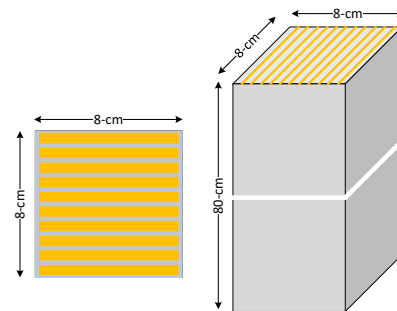


**Fig. 1.** Schematic of a square fuel plate assembly.

##### II.B.2. Fuel Assembly Materials

The three fuel types considered are UN, UC, and UO<sub>2</sub>. The maximum allowable UN, UC, and UO<sub>2</sub> centerline temperatures assumed in the analyses are, respectively, 3100 K, 2700 K, and 3100 K—corresponding to the melting temperature of each. The three high-temperature compatible structural materials considered are natural molybdenum (Mo), natural W, and enriched W. The isotopic compositions of natural and enriched W used in this study are adopted from Reference 2. Table I shows the isotopic compositions of W and these data are interpolated for the criticality calculations. An LANL Subject Matter Expert recommended that cladding thickness be at least 0.2 mm for W and 0.4 mm for Mo. Analyses were performed

assuming 0.25 mm and 0.50 mm. Maximum allowable Mo and W temperatures assumed in the analyses are, respectively, 2320 K and 3000 K—corresponding to 80% of their melting temperatures.

**TABLE I.** Isotopic composition of Tungsten (atom %)<sup>2</sup>.

	Natural		Enriched Tungsten	
W-180	0.1	10 <sup>-3</sup>	10 <sup>-4</sup>	10 <sup>-7</sup>
W-182	26.5	12	3.4	0.5
W-183	14.4	19	17.1	5.5
W-184	30.6	60	78.4	95.0
W-186	28.4	9	1.1	1.6

### II.B.3. Moderator Material

The use of zirconium hydride (ZrH<sub>1.6</sub>) blocks in the core is thought to increase core reactivity and, consequently, minimize core size and mass. These blocks must be thermally insulated and cooled separately from the fuel to ensure that their temperatures do not exceed about 800 K. For the current design, it is assumed that the ZrH<sub>1.6</sub> is insulated by a 0.5-cm ZrC40 (60% porous) insulator inside the 8x8 cm block and cooled by four cooling channels with a diameter of 1.7 cm.

### II.B.4. Core Layout

Fig. 2 shows the radial layouts of the core, both with and without moderator blocks. Each core is made up of 8x8-cm fuel assemblies surrounded by a 20-cm beryllium reflector containing 12 rotatable reactivity control drums and a 20-cm top beryllium axial reflector.

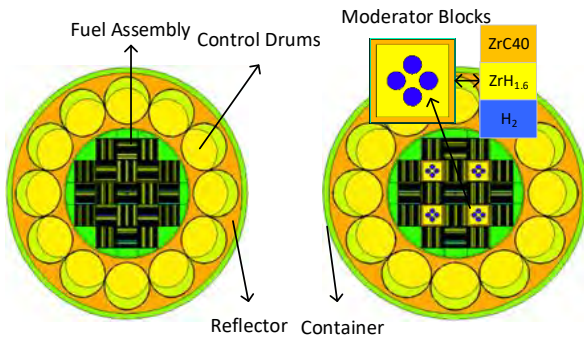


**Fig. 2.** Examples of core radial configurations without (left) and with (right) moderator blocks.

### II.C. Calculation Method and Model

The design of a nuclear reactor core is affected by interrelated parameters. For example, the degree of fuel subdivision, i.e. plate thickness, has a strong effect on the core power density obtainable, since it determines the ratio of fuel volume to fuel-element surface area available for heat removal. Similarly, the hydrogen cross-sectional area

through the core has a marked effect on the heat-removal-system circulation specifications. Consideration must also be given to the core pressure drop, heat-transfer coefficient, etc. These are, of course, sensitive to hydrogen velocity and, in turn, the cross-sectional area. For these reasons, numerous fuel assembly geometries and materials were considered in order to cover a wide range of design spaces.

For the initial parametric studies to develop assembly designs, heat removal scoping analyses were performed to estimate the maximum acceptable fuel assembly/plate power given the assumed design constraints and overall core dimensions and masses for a 250 MW output. These analyses were performed with an assumed inlet temperature of 350 K, a chopped cosine shape for axial power distribution, and a peak-to-average fuel assembly power ratio of 1.35.

Using results that were obtained from the heat removal scoping analysis and correspond with the various assembly designs, MCNP6<sup>3</sup> calculations were performed to determine whether these designs fulfill the criticality requirement. The MCNP calculations were performed using 0.5 M histories per cycle and 100 inactive and 400 active cycles. For this scoping study, the criticality requirement is k-effective = 1.02, where the control drums are in the full-out position.

## III. RESULTS

The results shown in subsection III.A were obtained purely from a heat removal perspective that assumes the criticality requirement can be achieved via proper adjustments. The criticality of these assembly designs would then be confirmed by the neutronics calculations discussed in subsection III.B.

### III.A. Heat Removal Scoping Analysis

The fuel assembly design with 0.5-mm cladding and a 0.75-mm H<sub>2</sub> flow gap was selected to show general trends in thermal performance in relation to changing assembly design parameters. Table II presents the selected fuel assembly's geometrical descriptions.

**TABLE II.** Geometrical descriptions of selected FA.

FA identifier	A	B	C	D
Duct outer, cm	8.00	8.00	8.00	8.00
Thickness of duct, cm	0.10	0.10	0.10	0.10
Number of plates	16	19	22	31
Thickness of fuel, mm	3.125	2.355	1.795	0.766
Thickness of clad, mm	0.5	0.5	0.5	0.5
Thickness of H <sub>2</sub> , mm	0.75	0.75	0.75	0.75
Vol. frac. of fuel, %	60.16	53.84	47.52	28.57
Vol. frac. of struc., %	25.22	28.79	32.37	43.09
H <sub>2</sub> flow area, cm <sup>2</sup>	9.36	11.12	12.87	18.14
Fuel S/V, cm <sup>-1</sup>	3.90	4.63	5.36	7.56

### III.A.1. Impact of Plate Numbers and Outlet Temperature

Using this assembly design with W cladding and UN fuel, the impact the number of plates and the outlet temperature had on core characteristics were investigated. The results are shown in Table III. Increasing the number of fuel plates per assembly from 16 to 31 allows increased core power density by a factor of two and, consequently, decreases core size and mass by about a half. Lowering the outlet temperature by 200 K (from 2750 K to 2550 K) allows an increase of almost 60% in core power density while decreasing specific impulse by only about 4%.

**TABLE III.** Impact of plate number on W structured FA.

Outlet temp., K	2550		2750	
# of plates per FA	16	31	16	31
P_max Plate/FA, MW	0.7/11	0.8/25	0.4/7	0.5/16
Avg. power density, W/cm <sup>3</sup>	1587	3662	1009	2333
# of FAs for 250 MW	31	13	48	21
Dia. of system*, cm	96	81	110	87
Total mass, mT	2.7	1.4	4.0	1.9

\* includes a 20-cm thick Be radial reflector

### III.A.2. Impact of Fuel and Cladding Materials

Based on the 16-plate assembly design with W cladding, the core characteristics of UO<sub>2</sub> and UC fuels are compared in Table IV. Contrasted with the data in Table III for the same plate thickness and outlet temperature, core power densities obtainable with UO<sub>2</sub> are significantly lower than those obtainable with UN thanks to lower thermal conductivity. The higher the outlet temperature, the larger the difference between the two fuels. The use of UC fuel requires lowering the H<sub>2</sub> outlet temperature to no more than ~2350 K in order to maintain a reasonable core size. At this temperature, the power density obtainable with UC is less than that obtainable with UN by a factor of about two, due to its lower melting temperature.

**TABLE IV.** Impact of fuel material for W structured FA.

Fuel Material	UO <sub>2</sub>		UC		UN
Outlet temp., K	2550	2750	2350	2550	2350
P_max Plate/FA, MW	0.2/4	0.1/2	0.5/8	0.2/3	0.9/15
Avg. power density, W/cm <sup>3</sup>	558	329	1116	478	2109
# of FAs for 250 MW	87	148	44	102	23
Dia. of system, cm	133	164	107	142	91
Total mass, mT	5.9	9.5	3.5	7.4	2.2

Based on the assembly design with Mo cladding, the core characteristics of UN, UC, and UO<sub>2</sub> fuels are compared in Table V. The use of Mo as cladding limits the H<sub>2</sub> outlet temperature to no more than about 2100K for maintaining reasonable core sizes. In this case, the Mo temperature is the limiting factor, and the UN/UC cores can

reach the same power density. The same is true for UO<sub>2</sub> if the UO<sub>2</sub> fuel meat thickness is less than 2 mm.

**TABLE V.** Core characteristics for Mo structured FA.

Fuel Material	UN/UC/UO <sub>2</sub>	UO <sub>2</sub>	UN/UC
Outlet temp., K	2200	2100	2100
P_max Plate/FA, MW	0.3/6	0.5/12	0.5/9
Thickness of fuel, mm	2.3	1.8	2.3
Avg. power density, W/cm <sup>3</sup>	822	1738	1293
# of FAs for 250 MW	59	28	38
Dia. of system, cm	117	94	102
Total mass, mT	4.8	2.5	3.2

### III.B. Neutronic Scoping Analysis

Using the given assembly designs composed of different combinations regarding the number of fuel plates, type of fuel and structure materials, etc., and the associated number of FAs required for 250 MW output, neutronic calculations were performed to find the limitations of using LEU fuel to meet the criticality requirement of k-effective = 1.02. In other words, the designs presented below satisfy both the criticality and heat removal requirements.

#### III.B.1. Impact of Enrichment and Outlet Temperature

Using 0.25-mm W-FAs and UN fuel, the impact of enrichment and outlet temperature on core characteristics were estimated. The results are shown in Table VI. To estimate the impact of enrichment on core performance, the sensitivity to criticality regarding both U and W vectors were investigated. The use of highly enriched uranium fuel can reduce the total reactor mass by ~70% in comparison to cores using LEU fuel. A 20% difference in total reactor mass is achieved when using enriched W, which is higher in <sup>184</sup>W content than the 30.6 wt% of natural W, as structure material. Total reactor mass increases more than 15% when increasing the outlet temperature from 2550 K to 2750 K.

**TABLE VI.** Impact of enrichment for W structured FA.

Outlet temp., K	2550		2750			
<sup>235</sup> U enrich., wt%	18.3	85.2	19.8	18.8	71.7	19.6
<sup>184</sup> W enrich., wt%	30.6	30.6	66.0	30.6	30.6	93.0
# of plates per FA	13	43	16	16	43	19
# of FAs	42	9	32	50	15	40
U mass, kg	2078	183	1477	2322	288	1737
Dia. of system, cm	106	74	97	111	82	104
Total mass, mT	3.5	1.0	2.7	4.0	1.3	3.2

#### III.B.2. Assessment of Different Fuel Materials

Using the 0.5-mm Mo-FAs, the impact of fuel materials and outlet temperature on core characteristics were estimated. The results are presented in Table VII. Total reactor mass obtainable with UN and UC fuel are significantly lower than those obtainable with UO<sub>2</sub> fuel,

and a marginal benefit in  $^{235}\text{U}$  mass is observed when using UC fuel as opposed to UN fuel. Total reactor mass is very sensitive to outlet temperature, which increases by 10% for  $\text{UO}_2$  fuel and 40% for UN and UC fuels when the outlet temperature increases from 2100 K to 2200 K.

**TABLE VII.** Core characteristics with Mo structured FA.

Outlet temp., K	2100			2200		
Fuel material	UN	UC	$\text{UO}_2$	UN	UC	$\text{UO}_2$
# of plates per FA	13	13	13	16	16	13
# of FAs	48	48	85	71	71	93
$^{235}\text{U}$ enrich., wt%	18.1	17.3	19.0	19.2	17.7	18.7
U mass, kg	2103	2103	3750	2823	2823	4110
Dia. of system, cm	110	110	133	124	124	142
Total mass, mT	4.0	4.0	6.7	5.6	5.6	7.4

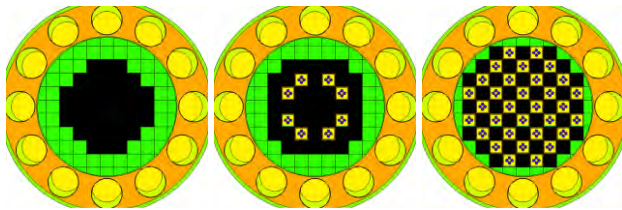
### III.B.3. Impact of Moderation

Table VIII presents the moderation effect on the performance of a core with 37 16-plate W-UN-FAs. As can be seen from the calculated k-effective, the impact of moderation on reactivity is limited when natural W is used as the structure material, because moderation enhances not only the absorption in fuel but also the absorption in W. When using enriched W, the reactivity increases significantly with moderation due to the reduced absorption in W. Fig. 3 shows the radial layouts of these three cases, where a layer of Be was placed in between the active core and the 20-cm Be radial reflector for small-diameter cores to make the radial reflector outer diameter of below cases identical. On the other hand, Table IX shows that, for Mo (natural) structured FAs, use of a moderator significantly increases the reactivity. The total reactor mass obtainable with a moderator is significantly lower than those obtainable in non-moderated cases.

**TABLE VIII.** Impact of moderation for W structured FA.

$^{184}\text{W}$ enrich., wt%	30.6 (natural)			93.0		
# of Mod. blocks	0	8	32	0	8	32
Dia. of core, cm	61.0	68.8	82.4	61.0	68.8	82.4
Be layer*, cm	10.7	6.8	0	10.7	6.8	0
Dia. of system, cm	122.4	122.4	122.4	122.4	122.4	122.4
k-effective	1.052	1.040	1.008	1.097	1.151	1.195

\* additional layer of Be between the core and 20-cm Be radial reflector



**Fig. 3.** Radial core layouts (120x120 cm) of 37 FAs with 0, 8, and 32 moderator blocks.

**TABLE IX.** Impact of moderation for Mo structured FA.

Outlet temp., K	2100		2200	
# of FA/Mod. blocks	48/0	22/23	71/0	36/21
# of plates per FA	13	28	16	31
$^{235}\text{U}$ enrich., wt%	18.1	18.9	19.2	19.5
U mass, kg	2103	512	2823	692
Dia. of system, cm	110	108	124	116
Total mass, mT	4.0	2.6	5.6	3.3

### III.B.4. Reactor Dynamics and Control Parameters

The reactor dynamics and control parameters were investigated using the core model with 41 13-plate W-UN-FAs. Fig. 4 shows the radial layout of this core. Two 40x0.5x28 cm  $\text{B}_4\text{C}$  (90% enriched  $^{10}\text{B}$ ) control blades are loaded between fuel assemblies to ensure the core is subcritical when flooded. As seen in Table X, k-effectives for the normal and flooded cases are 1.02 and 0.97, respectively. The hydrogen worth is -9 pcm, which is the difference in k-effective between the no-hydrogen (void) operating state versus the full steady-state inventory. The temperature defect via cross sections is -805 pcm. The worth shown is the difference between hot (1200 K for  $\text{H}_2$  and fuel, 900/600 K for structures in core/reflector) and cold (all 300 K) conditions. In general, the low hydrogen reactivity worth and small temperature defect would be beneficial in reactor startup. The power distribution of this core is also estimated by using the F7 tally function of MCNP. The assembly power peaking factor is 1.2, and the peak plate power is 0.9 MW. By employing the enrichment zoning strategy, the peak plate power is reduced to 0.60 MW, which is below the design limit of 0.62 MW.

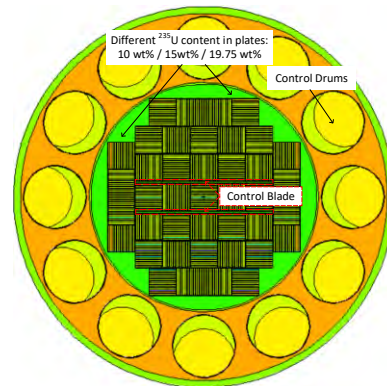


**Fig. 4.** Radial core layout of 41 FAs with control blades.

**TABLE X.** Core characteristics of 41 W structured FAs.

Base k-eff	$\text{H}_2$ worth	Temp. def.	Flood k-eff*
1.021	-9 pcm	-805 pcm	0.972

\* flooded with water, control drums turned inward, and control blades inserted

## IV. CONCLUSIONS

The preliminary conceptual designs for plate-fuel nuclear reactor cores for NTP have been analyzed. The results obtained from thermal hydraulic and neutronic analyses confirm the potential performance of this design; but more detailed analyses are necessary to confirm the level of performance and of practicality of the ceramic plate-fuel concept. A summary of how core performance is impacted by several key design parameters for fuel assemblies is given below.

- Uranium enrichment is a major factor affecting engine performance.
- The total reactor core mass is highly sensitive to core outlet temperature.
- Core reactivity increases with moderation only when molybdenum or enriched tungsten is used as structure material.
- Unlike with LEU-cermet fuel, plate-fuel LEU core configurations with a fast neutron spectrum appear feasible, i.e. there is no need for  $ZrH_x$ .

## ACKNOWLEDGMENTS

The research is being performed using funding received from the DOE's NTP project.

## REFERENCES

1. G. YOUINOU, C. S. LIN, A. ABOU-JAOUDE, and C. JESSE, "Scoping Analysis of Nuclear Rocket Reactor Cores Using Ceramic Fuel Plates," INL/EXT-19-57004, Idaho National Laboratory (2020).
2. S. A. LEVIN, D. E. HATCH, and E. VON HALLE, "THE SEPARATION OF TUNGSTEN-184," The Space-Nuclear Conference, Gatlinburg, Tenn., May 1961
3. C. J. WERNER (editor), "MCNP USER'S MANUAL, Code Version 6.2," LA-UR-17-29981, Rev. 0, Los Alamos National Laboratory (2017).

## Combined Cycle Nuclear Power and Propulsion: Reduction in Engineering Complexity to Enable Human Mars Mission Architectures in the 2020s

Jack Maydan<sup>1</sup> James Nabity<sup>2</sup>

<sup>1,2</sup>University of Colorado at Boulder, Boulder, CO, 80309

Primary Contact: (303) 492-3243 [james.nabity@colorado.edu](mailto:james.nabity@colorado.edu)

*Crewed Mars missions face a multitude of challenges and as a result current proposed architectures rely on chunky mass budgets and very slow transit times. This increases complexity by drawing out runtime requirements and constraining propulsive and power provisions. This paper highlights historical problems, describes how nuclear propulsion could relieve those issues, and then presents an architecture which reduces space based nuclear system complexity while providing substantial benefits to the architecture via the combination of the power and propulsion subsystems into a single nuclear core.*

### I. Introduction to Human Mars Missions and Combined Cycle Nuclear Systems

In the context of a space system architecture capable of transporting several astronauts from Earth to a semi-permanent habitat on Mars, there are several obstacles which current technologies struggle to accommodate. Primarily, the thrust performance metrics (specific impulse, thrust-to-weight, and endurance) of flight proven systems are not at a level which can produce significant delta-v without substantial propellant mass and volumes, excessive orbit maneuvering durations, or infeasible propulsion subsystem masses. This imposes a bottleneck on space transport architectures to have either extremely large mass budgets, or durations which push biological astronaut constraints. The canonical solution to such a problem has been nuclear thermal propulsion (Ref. 7); a propulsion system which offers moderate specific impulse while still being capable of producing kilonewton to meganewton levels of thrust. Nuclear thermal propulsion systems have been demonstrated on the ground in the past with NASA's NERVA or the Soviet's RD-0410 programs, but were not without their own complications in terms of mass, support systems, and overarching complexity. As the technology exists today, the additional complexities associated with implementation of a nuclear thermal propulsion subsystem do not trade positively when compared against more traditional architectures. In other words, when keeping all else the same, swapping a chemical propulsion system out for a nuclear thermal engine does not bring sufficient benefits to surmount its additional complexities. This paper will describe a nuclear propulsion solution for a human Mars mission which augments the propulsion subsystem with a power production plant: the Combined Cycle Nuclear Thermal Rocket (CCNTR). The CCNTR's intent is to circumvent historical problems by using a nuclear core to produce highly efficient thrust, as well as to generate large

quantities of electricity. Fig. 1 below represents the flow of propellant or working fluid through the core. The CCNTR will demonstrate that a single integrated package can accomplish the responsibility of two spacecraft subsystems while alleviating mass budget exceedances, considerably reducing complexities of nuclear space systems, and also substantially increasing available power and delta-V. This paper will outline an architecture for a CCNTR solution for human space transport systems based on modern innovations to the concept, a strong heritage base, and several major design choices specifically driven to alleviate the historical complexities, mass constraints, and support limitations found in traditional architectures. Moreover, the architecture described will also be based on near-term available technologies, within the 2020s, to complete a system that can be realistically adopted in the near future.

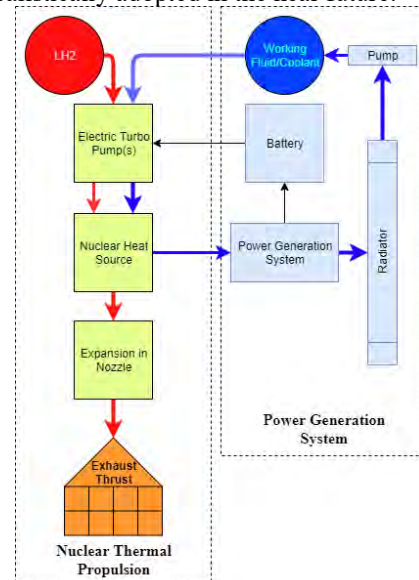


**Fig. 1. CCNTR Functional Block Diagram**

### II. Background: Human Mars Mission Complications

There are a numerosity of complications associated with Human Mars Missions. A mission of such caliber typically requires the extension of current space-fairing capabilities far beyond their current levels, however a few specific performance characteristics have been longstanding obstacles which have not seen substantial improvement. In the context of this paper these characteristics can essentially be accounted for in three different categories: biological constraints associated with mission duration, hardware performance associated with

mission duration/environment, and overarching system mass constraints. Key questions include:

1. How can transit time be reduced to limit crew exposure to space radiation?
2. How can hardware be designed to be functional and robust for the duration?
3. How can overall system mass be minimized while not imposing major limitations to capabilities?

Under the domain of each of these questions are well based research fields which, while there is active contribution to resolution, have yet to produce acceptable results. In addition to these characteristics, this paper is rooted in a solution which is achievable within the 2020 decade. As such, it is also necessary to consider how technologies selected for the architecture can be realistically achieved soon.

**II.A. How Nuclear Propulsion Resolves Crewed Mars Mission Complications**

The first two questions described above are essential to multi-year crewed Mars missions; the crew must be kept safe and healthy, and hardware must be reliable and robust during continuous operation in the deep space environment. There is a large research effort associated with this, however it is very difficult to provide high confidence results due to the lack of deep space crewed operations. This is compounded by the lack of access to deep space as well as the lack of crew time spent in it. NASA’s Design Reference Architecture (DRA) (Ref 1) concludes that with chemical propulsion architectures can achieve two-way transport times of 360-621 days. The DRA also demonstrates that, while feasible, these missions approach the limit for human radiation dosage which is 1 sievert for the lifetime of the astronaut. Moreover, there are extremely few modern examples of human space habitats which sustain durations of over 360 days – because the only crewed habitat to visit deep space was Apollo, the best example is the aging ISS. The contribution to this problem which nuclear propulsion brings is a massive reduction in mission duration. This can be derived in multiple ways, however, the simplest approach is to study specific impulse and the ideal rocket equation:  $\Delta V = I_{sp} * g * \ln(MR)$  where MR is the wet/dry mass ratio of the system. For this example assume 300mT of propellant to 100mT dry mass (MR=3).

**TABLE I.** Performance metrics for propulsion systems.

Propulsion Type	Specific Impulse	Delta-V for MR of 3
Chemical	~381 seconds (Ref. 5,6)	4.11 km/s
Nuclear Thermal	1000 seconds (Ref. 7)	10.77km/s

*II.A.1. Nuclear Propulsion Transit Time*

When compiling these results into an impulsive Fast Hohmann transfer, the relationship between transfer time

becomes clear. Nuclear propulsion reduces one-way transfer time from over 215 days to below 160 days with a mass ratio of. In this paper, electric propulsion was not considered due to the lack of feasibility in power systems which could enable electric propulsion to generate substantial thrust. Enticingly, a mass ratio of about 7 brings transit times down to approximately 100 days. As a result of nuclear thermal propulsion’s specific impulse being 2-3x that of chemical, deep space two way transfer times can potentially be realistically reduced from over 1 year to below 300 days. This substantially reduces bioastronautical constraints associated with radiation and the micro-g environment, and also reduces hardware performance constraints associated with continuous runtime, contributing significantly to the improved feasibility of a human Mars mission.

*II.A.2. Nuclear Propulsion Mass Benefits*

In order to answer the 3<sup>rd</sup> question posited above, it is necessary to elaborate on how the increase in specific impulse associated with nuclear propulsion can also be employed to benefit system mass. There are two improvements which can come from this: possibility of ‘all-up’ deployment, and reduction of overall cost based on reduced mass to orbit.

First, various architectures recommend pre-deployment of assets including the ascent system, surface habitats, and various crew consumables like water and food. While there are risk tradeoffs to doing this, nuclear propulsion’s increase in specific impulse enables much larger payloads to depart earth orbit at one time. While monolithic structures are a technology which may exceed the 2020 decade technology constraint, it is feasible to ‘daisy chain’ various modules and transport them to Mars together. The benefit to flying ‘all-up’ is that astronauts always have access to all mission elements and consumables. This can enable monitoring and maintenance which improves confidence by knowing that everything brought along for the journey is operational. Moreover, it will reduce the total critical events of a successful mission by requiring less propulsive maneuvers for things like orbital departure and injection.

The second benefit associated with nuclear propulsion is the homogeneity in its propellant as well as the reduction in total propellant required. It is likely that on-orbit fueling will be necessary for any deep space crewed mission, and the simple fact that nuclear propulsion only requires a single propellant type is a small benefit. The real benefit is that, regardless of dry payload mass and desired transit time, the mass of propellant which must be delivered to orbit (and therefore the number of launches required) is substantially less. The fact that a single large tank can be used reduces tank dry mass compared to bipropellant systems.

## II. Nuclear Propulsion Complications and the Advent of the CCNTR

There are major obstacles associated with nuclear space-based architectures. Three will be discussed and their resolution in the CCNTR context will be described.

1. How is the mass of the nuclear system reduced?
2. How is overarching complexity for nuclear space systems affected by 2020-decade ready architecture?
3. How is the reactor's health maintained over long duration missions?

### III.A. Reducing Uncertainty in Nuclear System Mass

The 1st question posited above stems from development issues during the NERVA era of nuclear propulsion. Difficulty was found in the miniaturization of the propulsion unit during the testing phases which limited tested units to laboratory-sized orchestrations of machinery necessary for operation. Due to the lack of development in nuclear thermal propulsion since the NERVA era there is a lack of confidence that a system mass is achievable which fits within some reasonably allotted mass budget. In order to reduce this uncertainty, the direct method would be to construct a real flight-like system – a doubtlessly costly and time consuming endeavor which may be infeasible within the 2020 decade. An alternative method would be to increase the mass budget allotted. This can best be done by increasing the capability of the nuclear system. Consider that if the core can perform the functionality of multiple subsystems, it can consume the mass budget of those subsystems. This is the where the advent of the Combined Cycle Nuclear Thermal Rocket (CCNTR) stems from. On the ISS, the power subsystem consists of sixteen very large solar arrays. These arrays take up substantial volume and mass; they are estimated at over 50mT (Ref 2). In addition, it can be assumed that a deep space mission with insolation dropping at  $1/r^2$  that this mass may grow, or its capability reduced. If the CCNTR can produce electrical power continuously, and be used for propulsive maneuvers occasionally, then its allotted mass budget can be increased substantially and thus its feasibility as a usable technology in this architecture is vastly improved.

### III.B. CCNTR Reactor Health & Complexity

While the CCNTR was envisioned to help alleviate concerns in the 1<sup>st</sup> question, it conveniently addresses 2<sup>nd</sup> and 3<sup>rd</sup> questions posited as well.

The 3<sup>rd</sup> question regarding reactor health must be considered as it is a major limitation to the employment of nuclear thermal propulsion. In short, nuclear reactors are well behaved when placed under constant conditions. Abrupt spikes in power demand, thermal output, and moderator control can cause problems such as thermal stress, inconsistent consumption of nuclear fuel, and

poison build up generated during transient processes. This constraint is placed on a nuclear thermal propulsion system because it is required to be started and stopped during any impulsive maneuver, trajectory correction, or orbital insertion. These events require it to transition from a fully shut down reactor to peak thermal output very rapidly, and also may occur at unexpected times such as in an abort scenario or collision avoidance. These events may also be time sensitive such as during orbital injection at Mars where the reactor must perform its duty at a specific time with no margin for start up delays without missing orbital capture. As such, there is interest in keeping the nuclear reaction going at all times, even if at a low output. The benefits include the enabling of 'warm' starts, rather than 'cold' starts, as the reactor will always be generating some heat even if throttled down. Warm starts are also quicker to respond to demand as neutron absorbers (control rods) will already be retracted. The fact that the reaction is constant also prevents poison build up by providing a base of heat to burn off Xenon when ramping. In addition, because the reactor is not allowed to cool from peak temperature to space background temperature (approximately 3K), thermal stress and odds of fuel cracking are reduced. Finally, continuous reactor operation is beneficial because it allows for continuous monitoring of functionality. The reactor is always active, monitored, and controlled – any changes in operation should be detectable in advance via trending. This allows the architecture to predict and prevent issues before they arise, rather than having a spontaneous problem surface at the onset of a vital propulsion maneuver.

The CCNTR also addresses the 2<sup>nd</sup> question in various ways. Nuclear thermal propulsion has no heritage in flight, nuclear fission reactors have no heritage either outside terrestrial applications; thus, it is vital to include justification for how this combined cycle architecture is achievable in the 2020 decade. The major complexities associated with space based nuclear systems include thermal waste rejection, reactor health, mass constraints, cost of development and testing, and lack of heritage. The architecture resolves health and mass as discussed, but also addresses thermal waste heat rejection for the reactor. Consider that a 100MW peak thermal output reactor operated continuously at even 1-5% of peak output can be cooled with reasonably sized radiators. This is equivalent to a 1MW thermal load which can be radiated at 500K with an emissivity of 0.9 requiring radiator surface area of about  $333m^2$  (or  $1500m^2$  at 5%). (Ref. 3, 4) Development costs can be reduced by simultaneous development of a single nuclear core which serves two purposes, contrasted by the independent development of separate power and propulsion elements. Moreover, cost can be reduced by heavy reliance on previous nuclear thermal propulsion and space-based fusion reactors. Some heritage base does actually exist in the technology

designed in NASA funded efforts throughout the 1900s including the NERVA program which is presently being adapted by NASA in conjunction with BWXT, as well as the SNAP and SP programs which included limited flight heritage as well as flight ready designs for MW level reactors.

### III.C. Unrealized Benefits of the CCNTR

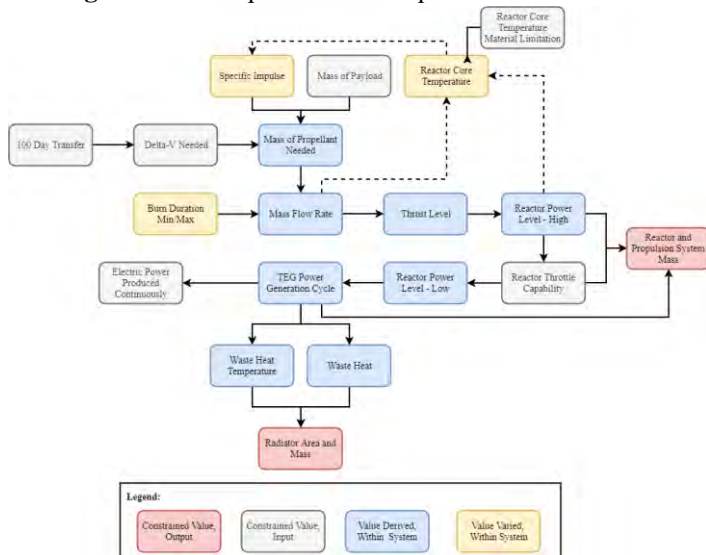
In addition to the technological benefits, a CCNTR system provides architectural benefits. These architectural benefits add additional categories to the trade space which make nuclear systems trade positively against more traditional architectures.

A reduction in complexity to the architecture is seen by the removal of solar arrays for power generation. The lack of insolation at Mars, in combination with the high-power demands of human missions, would require a very large array with constant pointing to deliver safe power. In addition, solar systems are susceptible to the seasons, eclipses, and degradation over time. A nuclear power generation system can have a useful constant performance lifespan measured in decades, and is impervious to those fallacies. An additional benefit to the nuclear system over traditional architectures is the provision of power which is high in magnitude and constant, enabling the habitat used to be a laboratory stocked with high power equipment and capabilities like the ISS. This also enables technologies such as cryogenic coolers for propellant or cold storage of consumables for the crew. The final benefit worth mentioning is the flexibility in propulsion performance that a system like this would be capable of. Due to its throttle-ability there should be no fixed thrust level nor mass flow rate, a CCNTR system will be capable of any ‘sized’ maneuver without sacrifice in specific impulse.

### IV. Architecture Specifications and Recommendations

An in-depth analysis of system requirements for a CCNTR power and propulsion system was conducted in order to determine specifications and technology selections. This flowchart represents the interdependency.

Fig. 2. CCNTR Specification/Requirement Derivation.



between mission constraints from the NASA DRA, governing equations, and performance metrics to enable derivation of values for a baseline design of the CCNTR system’s performance, mass, and sizing. Table II below tabulates baseline design values for reference.

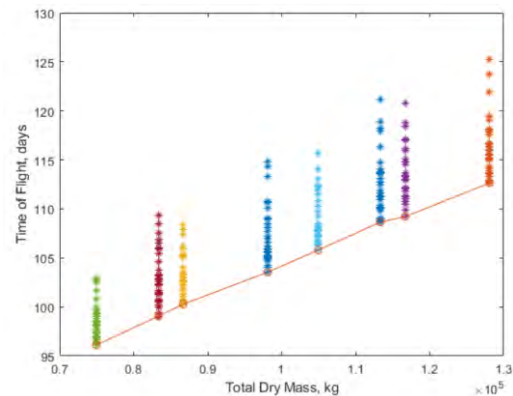
TABLE II. CCNTR Derived Baseline Specifications.

Propulsion Spec.	Quantity	Power Spec.	Quantity
Thermal Output	100 MWt	Conversion Eff	10% (Ref. 8)
Specific Impulse	1000 seconds	Thermal Output	1 MWt
Chamber Temp	2650 K	Power Generated	100 kW <sub>e</sub>
Mass Flow	1.5 kg/s	Radiator Temp	500 – 800 K
Thrust	25 kN	Radiator Size	< 333m <sup>2</sup>

Note that a thermoelectric power generation (TEG) system is used here, despite its low conversion efficiency, to heritage in space, scalability, and robustness to failure. Moreover, even at its low efficiency TEGs easily match that of the ISS at 100 kW<sub>e</sub>, so this penalty is acceptable.

The requirement flow derived in figure 2 was compiled to a genetic optimization algorithm which models trajectories to build the following performance map for Mars missions with a payload mass of 70-100 mT and an additional CCNTR mass of 5,000-28,000 kg.

Fig. 3. CCNTR Performance Map: Mass & Time of Flight



### V. Conclusions

This paper presents background on crewed Mars missions and elaborates on how many associated complexities are alleviated via use of nuclear propulsion. Moreover, historical problems with nuclear space systems described as well as how their resolution brought forth the CCNTR system. Complementarily, the added benefits to employment of a CCNTR system were highlighted in order to better the trade space in favor of nuclear systems for crewed Mars missions. Finally, the derivation of requirements and specifications for a CCNTR system were presented and a baseline design was outlined. This system was compiled into an optimization algorithm which derived performance specifications enabling 100 day transits to Mars. This represents a strong argument for a CCNTR enabled human Mars mission which is founded in feasibly achievable metrics within the 2020 decade.

## REFERENCES

1. Mars Architecture Steering Group, *Human Exploration of Mars Design Reference Architecture 5.0*, Bret G. Drake, editor, NASA (2009)
2. SpacecraftEarth, *ISS Integrated Truss Structure*, Eugen Dobric and Drazen Vukovic (2007)
3. NASA Ames Space Settlement Homepage, *Thermal Management in Space*, Abe Hertzman [space.nss.org/settlement/nasa/spaceresvol2/thermalmanagement.html](http://space.nss.org/settlement/nasa/spaceresvol2/thermalmanagement.html).
4. Los Alamos National Laboratory, *SP100 Space Reactor Design*, Scott F Demuth (1970)
5. Aerojet Rocketdyne, *RL10 Data Sheet*, [https://www.rocket.com/sites/default/files/documents/Capabilities/PDFs/RL10\\_data\\_sheet.pdf](https://www.rocket.com/sites/default/files/documents/Capabilities/PDFs/RL10_data_sheet.pdf) (2019)
6. NASA, *Launch Vehicle Report Falcon 9 Data Sheet*, <https://sma.nasa.gov/LaunchVehicle/assets/space-launch-report-falcon-9-data-sheet.pdf> (2017)
7. NASA Lewis Research Center - NASA Technical Memorandum, *The Rationale/Benefits of Nuclear Thermal Rocket Propulsion for NASA's Lunar Space Transportation System*, Stanley K. Borowski (1991)
8. China University of Geosciences, *A 1 kW Thermoelectric Generator for Low-Temperature Geothermal Resources*, Changwei Liu, Pingyun Chen, and Kewen Li (2014)

## A LABORATORY TEST TO EVALUATE SEEDED HYDROGEN IN A NUCLEAR THERMAL ROCKET ENGINE

Dennis Nikitaev<sup>1</sup>, Dr. L. Dale Thomas<sup>2</sup>, and Dr. Jason Cassibry<sup>3</sup>

<sup>1</sup>301 Sparkman Dr., Huntsville, AL, 35899

Primary Author Contact Information: 702-287-6852 [dn0038@uah.edu](mailto:dn0038@uah.edu)

*Seeding hydrogen is the process of adding a heavy noble gas (the seed) such as argon, krypton, or xenon to the hydrogen propellant. This is done to reduce pressure losses, improve convective heat transfer, and densify the propellant at the expense of specific impulse and wetted vehicle mass. A numerical study was conducted which predicted and examined the effects of varying the seed concentrations within the hydrogen propellant. The numerical model for pure hydrogen propellant was validated against the power balance model of an actual nuclear thermal propulsion engine currently under development and also the PEWEE-1 engine developed and tested by NASA in the 1960s. To examine the predicted effects of the seeded propellant, the next step is to design and conduct an experiment which would analyze the predicted effects and enable conclusions concerning whether seeded hydrogen will indeed provide the predicted benefits in a nuclear thermal rocket engine. This paper describes the planning for this test series.*

### I. INTRODUCTION/BACKGROUND

Pure hydrogen in nuclear thermal propulsion engines is the typical propellant of choice due to its low molecular weight yielding high specific impulse and excellent energy storage properties yielding functionality as an excellent reactor coolant. On the other hand, this propellant has extremely low density resulting in large propellant storage tanks which must keep the propellant liquid at around 20K – a large challenge on its own. Several studies examined the densification of hydrogen by decreasing its temperature further. However, these studies were mostly relevant to launch vehicles that did not require long term hydrogen storage.

Due to hydrogen's excellent energy storage properties, a very powerful reactor is required in order to raise the hydrogen's temperature in order to maximize the high specific impulse potential of this propellant. Due to its low density, the high flow velocity through the ducts of the engine will result in large pressure losses yielding additional strain on the turbomachinery.

Prior analytical work<sup>1</sup> examined the effects of adding a heavy noble gas impurity to hydrogen based on the theory of nanofluids and the approach of the nuclear lightbulb project. Nanofluids involve adding nanosized particles to a base fluid in order to tune the base fluid's properties and

are widely used in heat transfer applications. The nuclear lightbulb involved seeding the hydrogen propellant with either tungsten particles or titanium vapor to maximize the radiative heat transfer.<sup>2</sup> This analytical work<sup>1</sup> examined the effects on the fluid properties of hydrogen in NTP applications by seeding hydrogen with a gaseous impurity instead of solid nanoparticles. The approach was to model an existing NTP engine model in Simulink with high fidelity and outfit it with seeding capabilities. The numerical results showed that by adding small molar amounts of heavy noble gas seeds, the hydrogen properties could be tuned to result in lower required turbopump discharge pressures or higher thrust, lower reactor power, increased convective heat transfer, and higher change in velocity ( $\Delta V$ ) given the same propellant tank volume and vehicle dry mass. However, these properties were able to be tuned only at the expense of the specific impulse, and in turn, increased vehicle wetted mass.

The model used in predicting this results was constructed in Simulink and validated against a power balance model of an NTP engine currently under development as well as the PEWEE-1 engine developed by NASA in the 1960s. Both validations resulted in less than 1% error for most states and parameters. Figure 1 shows the decrease in specific impulse as a function molar concentration of one of the considered seeds - argon.

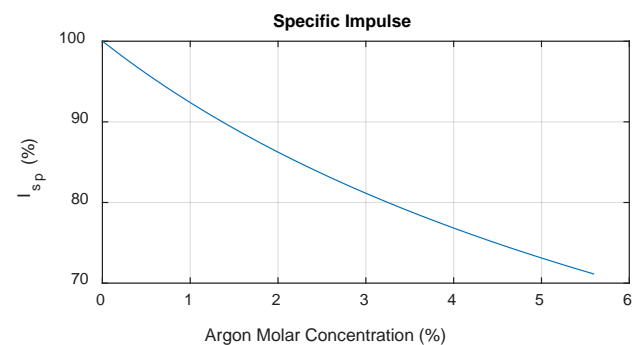


**Fig. 1. Specific Impulse Decrease<sup>1</sup>**

Despite the decrease in the specific impulse, the vehicle  $\Delta V$  increased given the same propellant volume and vehicle dry mass. However, due to the uncertainty in the resulting mass of the reactive control system (RCS) and orbital maneuvering system (OMS) thrusters, best and worst case scenarios were proposed. The worst case scenario allowed the RCS and OMS propellant masses to

grow in order to keep the same  $\Delta V$  for the more massive vehicle provided by these systems; the best case scenario kept the propellant masses allocated to these systems the same while redistributing the lost  $\Delta V$  to the main NTP propulsion system. Figure 2 shows both the best and worst case scenarios. The grey area between these two curves is representative of the design space for the vehicle. These curves are valid for all considered seeds: argon, krypton, and xenon with argon being the most economical.

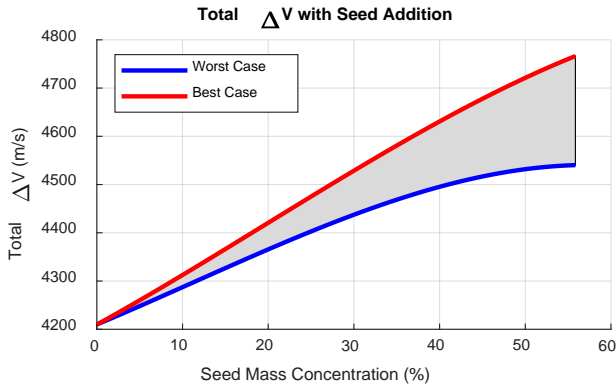


**Fig. 2.** Increase in  $\Delta V$ <sup>1</sup>

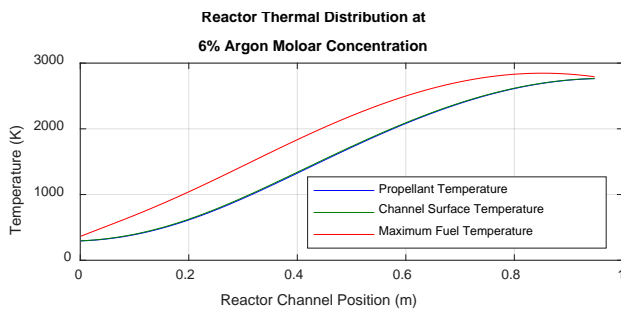
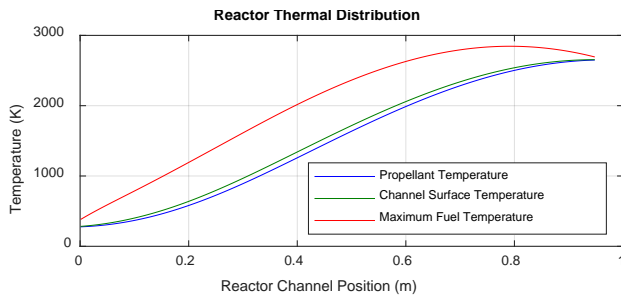


**Fig. 3.** Reactor Thermal Distribution<sup>1</sup>

The prior analytical work<sup>1</sup> also examined the heat transfer properties of seeded hydrogen. The top graph of Figure 3 shows the fuel, channel surface, and bulk hydrogen temperature at 0% seed concentration. The gap between the channel surface and propellant bulk temperatures, although small, is still significant. The bottom graph of Figure 3 shows the same curves but at 6% argon molar concentration. The maximum fuel temperature in both graphs stayed the same, however, the propellant exit temperature in the seeded case increased while the gap

between the channel surface temperature and bulk propellant temperature decreased.

Furthermore, since the specific heat capacity of a mixture is dependent on the mass concentration of each species and the heavy noble gases have extremely low specific heat capacities, the reactor power also decreased despite the increased reactor exit temperature. This is shown in Figure 4. The total power decrease at the maximum seed concentration was found to be 23.48%.

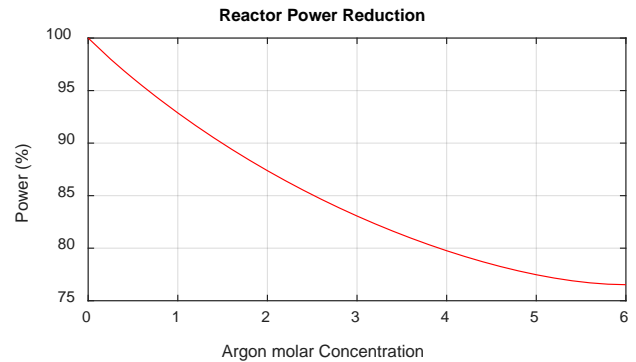


**Fig. 4.** Reactor Power Reduction<sup>1</sup>

One of the limitations of this model is the fact that the neutron flux was not modeled. This neutron flux is responsible for the reactor power and consists of two types of neutrons: fast and thermal. The fast neutrons are those that are released shortly after a uranium atom fissions. These fast neutrons are too energetic to be captured by the uranium atoms inside the LEU thermal reactor considered for NTP and need to be slowed down. The slowing down process of neutrons is called moderation and is achieved by moderator substances. In the NTP reactor, there are two moderators: the solid moderator elements and the hydrogen. By adding an impurity to the hydrogen, its moderation properties will change proportionally to the molar concentration of that impurity. Argon will not impact the reactivity (change in the neutron population inside the core) since its neutron absorption cross section differs from the hydrogen molecule by only 0.1% but may slightly lower the moderation of neutrons at the considered low molar concentrations (up to 6%). However, the density increases and balances out the lost moderation. Therefore, although the moderation capabilities of hydrogen will be impacted by argon, this impact, when coupled with the moderator elements, is less than 1% which should be well within the tolerance and/or control band of the LEU NTP reactor.

Although these results have been based on fluid properties and the engine architecture and functionality has been validated for pure hydrogen, experimental support evidence is lacking. There has never been a study done on a hydrogen-argon mixture flowing through a thermal rocket engine. Furthermore, the hydrogen-argon mixture properties made available by the CoolProp library<sup>3</sup> were

also based on mostly analytical functions. Therefore, in order to truly validate these results, an experiment must examine the trends outlined by the prior analytical work<sup>1</sup>.

## II. TEST APPARATUS

This paper will continue the previous study and examine a laboratory apparatus and test in order to validate the numerical results with physical data. The purpose of this test is to ensure that the predictions provided by the analytical work<sup>1</sup> based on a homogenous mixture are adequate. It is possible that due to the large difference in molecular masses of hydrogen and the seed that the mixture will not necessarily behave homogeneously in the pressure and temperature regimes representative of a NTP engine. The purpose of this test will be to show if the predicted fluid behavior is accurate.

This experiment will involve using the Nuclear Thermal Rocket Element Environmental Simulator (NTREES) at NASA's Marshall Space Flight Center to examine the thermal properties of the fluid. A detailed experimentation plan using this apparatus will be developed in the early months of 2020. Further, a small rocket nozzle will be constructed and tested in a vacuum chamber to examine the thrust and specific impulse effects from seeding hydrogen. Detailed analysis on this experiment will also be conducted in the early months of 2020. Seeded hydrogen will have mixing accomplished externally from the apparatuses. The heat will be provided by an induction coil in NTREES and transferred into the seeded hydrogen propellant by convection along the fuel element channels.

## III. NUMERICAL SIMULINK MODEL 2.0

Once the laboratory test has been outlined, the geometry will be put into a Simulink model which will incorporate heat transfer and flow equations that match the analytical work<sup>1</sup> to examine the theoretical outputs. The goal of this model is to match the approach of the analytical work<sup>1</sup> and compare this approach to the experimental data. In order to validate the effects of seeding hydrogen in a thermal engine, the general trends must be found to match:

1. Chamber pressure rise with constant inlet pressure as the seed concentration increases. (Direct measurement, must be fine precision)
2. Chamber temperature rise with constant inlet temperature and constant heat or a heating power drop to yield the same chamber temperature as the seed concentration increases. (Direct measurement)
3. A significant decrease in specific impulse as the seed concentration increases. (Calculated from the direct measurement of the thrust and mass flow rate)

4. Increased change in velocity for a given arbitrary propellant volume. (Calculated from the specific impulse and bulk seeded hydrogen density)

If these trends occur, further validation of the numerical model will involve comparing the experimental data to the predicted results. The degree to which the results must match the predictions are yet to be determined. However, if these results match the analytical results within the to be determined error margin, the analytical work's<sup>1</sup> approaches and predictions will be experimentally validated.

A second test series will focus specifically on the diffusion process of supercritical argon at turbulent flow conditions into supercritical hydrogen also at turbulent flow conditions. This will require higher pressures of around 70 atm and ambient temperatures (~300 K). The analytical work<sup>1</sup> assumed with expert advice<sup>4</sup> that since supercritical fluids are completely miscible, the added turbulent flow conditions will result in rather instantaneous and complete diffusion. Should this test confirm complete and relatively instantaneous diffusion, then it may be confirmed that these two species, when introduced to each other at supercritical states and turbulent flow conditions, do not require any assistance in diffusing with each other. Future work may use this same apparatus for testing other species combinations at turbulent flow conditions and their diffusion rates. Furthermore, since the exhaust from this mixture will be at high pressures (70 atm), it will then flow through a rather long tube and the pressure losses along this flow will be measured. Details for this test are still being developed.

## IV. OUTLINE OF THE LABORATORY TEST

The laboratory tests will consist of running hydrogen at molar seed concentrations between 0% and 16% of argon through the apparatus. The 16% molar seed concentration is substantially higher than that of the analytical work, which capped at 6% due to pump and turbine performance, in order to capture the entire range of seed benefit. It was found by the analytical work<sup>1</sup> that the seeding benefit for the vehicle extends to 14.67%. 16% was chosen to go somewhat past this arc to capture it.

This apparatus will be inductively heated by an inductive heater with the propellant flowing through the fuel element channels and thus cooling this element. An expected challenge for this test is the ability to measure the seed concentration of the propellant. A proposed option is to measure the flow rate, temperature, and pressure of each species as mixing occurs and then use a look up table, such as CoolProp<sup>3</sup>, to determine the density of each species as well as the mixture. This will yield the mass flow rate of each species from which the seed concentration may be obtained. If sensors are available at the NTREES facility

that are able to accomplish this task, then they will be used instead.

During the testing procedure of the nozzle, the produced thrust will need to be measured in order to obtain the specific impulse of the apparatus. A standard fine precision force measurement may be utilized as the expected thrust levels are to be between 2 and 4 newtons. This will be coupled with fine precision pressure sensors at both the inlet and chamber of the apparatus which will yield the pressure drop through the propellant channels. Further, the temperature at both the inlet and chamber must also be measured to determine the change in temperature given the heat produced by the inductive heater.

Unfortunately, there is no plausible way to measure the surface temperature and bulk propellant temperature inside the propellant channels due to the extremely small scale of the apparatus. This will result in lack of data to confirm that the temperature gap between the channel surface temperature and bulk propellant temperature decreased. However, based on the amount of heat inputted into the propellant and the inlet and outlet temperatures, the surface temperature and bulk propellant temperature along the channels can be extrapolated mathematically.

## V. EXPECTED RESULTS

The expected results of this study are to confirm the trends and predictions of the prior analytical work<sup>1</sup>. A rough MATLAB code was written to estimate the results of this test. The heat input into the seeded hydrogen was held constant at an arbitrary value of 1000 W and the argon molar concentration was varied up to 10%, the general trends were observed which match those of the analytical work<sup>1</sup>. Both the chamber pressure and chamber temperature were observed to rise as indicated by Figure 5. However, the magnitude by which the chamber pressure rises is extremely small due to the relatively short length of the propellant channels.

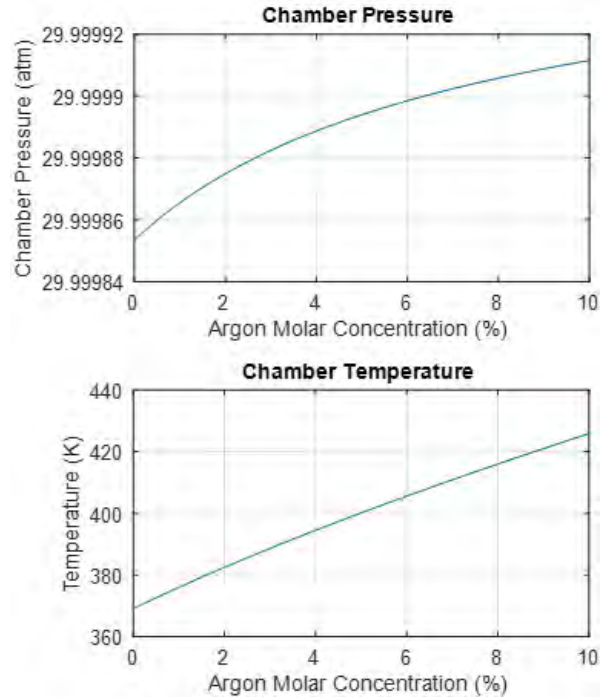


**Fig. 5.** Chamber Pressure and Temperature Versus Argon Molar Concentration

Due to the increase in chamber pressure, the thrust was observed to increase marginally, however, as the analytical work<sup>1</sup> predicted, the specific impulse decreased significantly as shown in Figure 6. The throat and exit diameters of the nozzle were set to be small: 0.001 mm and 0.003 mm respectively.

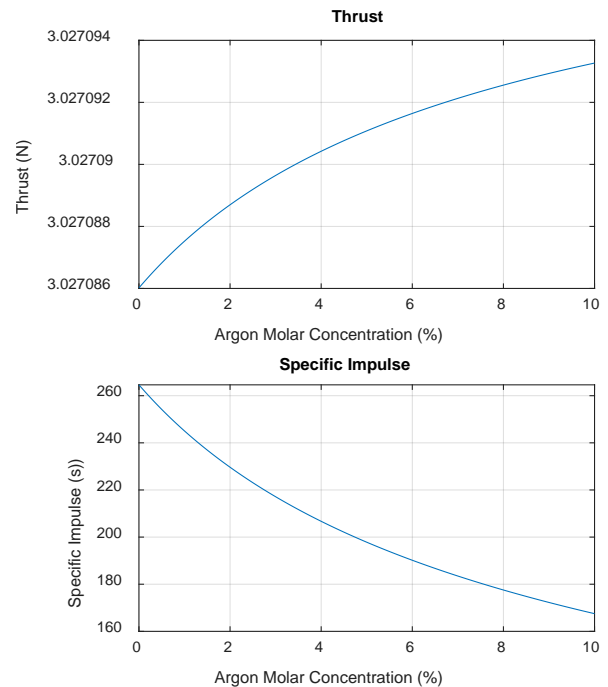


**Fig. 6.** Thrust and Specific Impulse Versus Argon Molar Concentration

A propellant volume of an arbitrary amount of 10 liters was chosen to find the change in velocity given a seed concentration. The dry mass was arbitrarily chosen to be 5 kg. The calculations involved finding the bulk density of the propellant using the densities of each species in their respective liquid storage conditions. Using the specific impulse, the calculated density, and the arbitrary constant values, the delta V in vacuum was found to increase as the seed concentration increased, just like the analytical work<sup>1</sup> predicted. The predicted delta V for this test is shown in Figure 7.

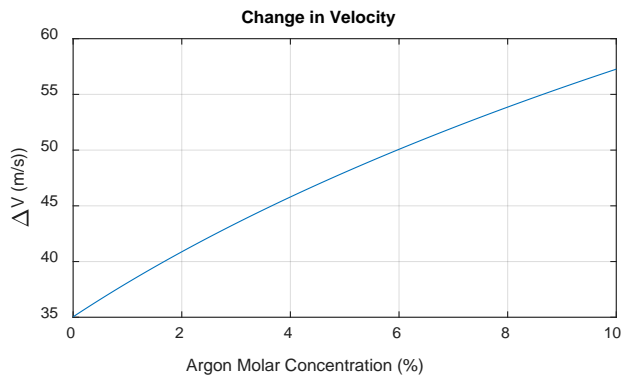


**Fig. 7.** Change in Velocity Versus Argon Molar Concentration

## VI. CONCLUSIONS

Seeded hydrogen could help solve some volume limitations incurred by pure non-densified hydrogen. Prior analytical work<sup>1</sup> examined hydrogen mixed with heavy noble gases and made some conclusions about the expected trends that could occur in a nuclear thermal propulsion engine as their concentrations increased. Furthermore, due to the ability to cater the propellant properties such as the specific heat capacity, seeded hydrogen could prove to be very beneficial in engine transients when the reactor is building up power. However, in order to validate these predictions, an experiment must be conducted to observe if these predicted trends really do occur. Such an experimental apparatus and laboratory test were outlined in this paper.

## ACKNOWLEDGMENTS

NASA

## REFERENCES

1. Nikitaev, D. (2019). *Seeding Hydrogen Propellant in Nuclear Thermal Propulsion Engines* (Unpublished

Masters' Thesis). University of Alabama in Huntsville.

2. McLafferty, George H. (1970). "Gas-Core Nuclear Rocket Engine Technology Status," *Journal of Spacecraft and Rockets*, vol. 7, no. 12, pp. 1391-1396.
3. Bell, I. H., Wronski, J., Quoilin, S., and Lemort, V. (2014). "Pure and Pseudo-pure Fluid Thermophysical Property Evaluation and the Open-Source Thermophysical Property Library CoolProp," *Industrial & Engineering Chemistry Research*, vol. 53, pp. 2498-2508.
4. Poliakoff, M. (June 27, 2019). "Supercritical Fluid Miscibility".
5. Stradi, B. A., Brennecke, J. F., Kohn, J. P., and Stadtherr, M. A. (2000). "Reliable Computation of Mixture Critical Points," University of Notre Dame, Notre Dame, IN.
6. Kreglewski, A. (1968) "Critical and Pseudocritical Pressure of Binary Mixtures," *Journal of Physical Chemistry*, vol. 72, no. 6, pp. 2280-2281.

## THE SIRIUS-1 NUCLEAR THERMAL PROPULSION FUELS TRANSIENT TEST SERIES IN THE IDAHO NATIONAL LABORATORY TREAT REACTOR

Robert C. O'Brien<sup>1</sup>, Douglas E. Burns<sup>1</sup>, Nicolas E. Woolstenhulme<sup>1</sup>, Douglas Dempsey<sup>1</sup>, Connie M. Hill<sup>1</sup>, and Cody Hale<sup>1</sup>

<sup>1</sup>Idaho National Laboratory, Idaho Falls, Idaho, 83415, +1-208-526-0111, Robert.Obrien@inl.gov

*Nuclear Thermal Propulsion (NTP) fuels and component materials are subjected to extreme temperature transients through nuclear heating to NTP system from space cold to operational temperatures. Methodology for transient testing conceptual NTP fuels is presented in addition to the capsule design for static testing under the SIRIUS-1 series at the Idaho National Laboratory Transient Reactor Test (TREAT) reactor. Preliminary results from the SIRIUS-1 Test series will be presented.*

### I. INTRODUCTION

Nuclear Thermal Propulsion (NTP) fuels when brought to a targeted operational temperature from a cold zero-power condition may be subjected to thermo-mechanical stresses. Understanding the limitations to any fuel system must be determined in order to facilitate operational system performance, specifications and service ratings. Modern modeling and simulation tools such as the Department of Energy's Nuclear Energy Advanced Modeling and Simulation tools (e.g. MOOSE framework, Ref. 1) can couple nuclear physics with materials properties to estimate performance. However, for qualification and licensing (e.g. in compliance with Nuclear Regulatory Commission NUREG Guide 0800 (Ref. 2) for performance under severe accident conditions) and operations purposes, several energy thresholds and power ramp rates must be empirically measured (Ref. 3). Similarly, launch safety and approval processes will likely require determination and demonstration of materials performance under the conditions that are prescribed for nominal operations and postulated accidents. These measured values include:

- 1) Fuel fragmentation threshold enthalpy rise and ramp rate.
- 2) Coolable / functional reactor geometry maximum enthalpy rise.
- 3) Energy deposited during fuel-coolant interactions.
- 4) Fuel and fission product loss rate as a function of temperature and time.
- 5) Submersion criticality environment fuel behavior.

The Idaho National Laboratory's Transient Reactor Test (TREAT) reactor is a digitally controlled test reactor which can be pulsed to a peak power of the order 19 GW or ramped to a prescribed power through the maneuvering of banks of control and transient drive control rods. The complexity of the power profile that can be derived within a test specimen is limited fundamentally only by the tolerance of the specimen, the capsule or specimen holder, and the maximum permissible enthalpy rise of the TREAT driver core of ~2500 MJ at or under which, no damage to the fuel/cladding system can occur. The driver core is composed of a 19x19 array of fuel-reflector assemblies, Ref. 4. Each fuel assembly is approximately 9 feet long and has a cross section of approximately 4 inches by 4 inches and has an active fuel length of approximately 4 feet. The active fuel region of an assembly is a UO<sub>2</sub>-graphite dispersion fuel within a zircaloy cladding. Unfueled graphite reflectors, approximately 2 feet in length above and below the active fuel region are housed within the cladding of a fuel assembly. Fuel or other test specimens are encapsulated within an irradiation test vehicle that offers either static or flowing environments inside doubly encapsulated containment. These irradiation test vehicles can be installed within any of the 19x19 grid positions by displacing one or more fuel assemblies. Typically, experiments are placed, but not limited to the center of the reactor, Ref. 4.



**Fig. 1.** The Idaho National Laboratory's Transient Reactor Test (TREAT) Reactor. (Left) View of 19x19 array of driver fuel assemblies. An irradiation test vehicle is visible at the center position of the core. (Right) Ariel view of the TREAT facility at the Idaho National Laboratory Materials and Fuels Complex.

As shown in Figure 2, a combination of transient shaping and clipping can be used to derive an aggressive heating rate within a specimen, e.g. a ramp to full temperature, followed by a sharp decrease in driver core power to sustain specimen temperature for a period of time. Such transient shaping may be executed for static capsule

testing of NTP specimens, although the magnitude of the reactor power will differ to the historical transients illustrated in Figure 2.

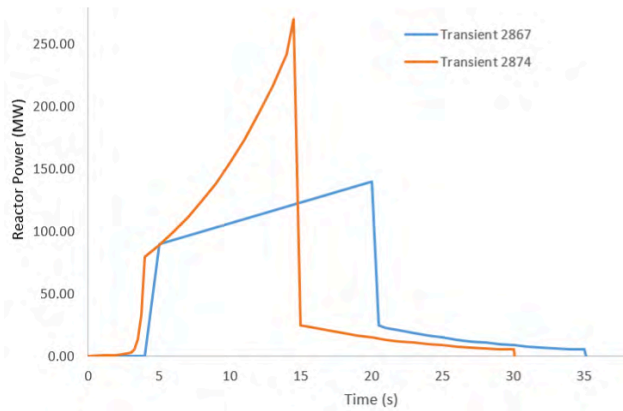


**Fig. 2.** Example power transients that can be prescribed, demonstrating the shaping complexity that can be achieved through TREAT digital control while restricting total enthalpy rise for the core to under 2500 MJ.

Historically, the TREAT reactor has performed thousands of transient tests on fuel and reactor components, emulating the nuclear test environment of thermal reactor systems, epithermal and fast reactors. Sample temperature ramp rates have been prescribed and demonstrated in TREAT at up to 16,000 K/s (Ref. 5). Various chemical environments have been successfully tested within irradiation vehicles from light water, inert gas to hydrogen. The natural, unfiltered spectrum of the TREAT reactor central test position is highly analogous to the spectral environment of heavily moderated, low enriched uranium systems, such as those being explored under the current NASA programmatic efforts. Filtering and shaping of the neutron spectrum to which a TREAT capsule / specimen is subjected can be applied through the application of a collar (e.g. dysprosium foil) to the external surfaces of a capsule.

## II. THE SIRIUS TEST SERIES

The United States Department of Energy and NASA have funded the initial development of the SIRIUS-1 transient test series at the Idaho National Laboratory, Ref. 6. This work is focused on the development of a static capsule design, validation and verification of capsule and in-pile instrumentation for the transient testing of concept NTP fuels. Following demonstration of the capsule design with a dummy or baseline NTP fuel specimen fabricated via Spark Plasma Sintering at INL, the capsule(s) will be used to evaluate the performance of concept NTP fuels from NASA and Industry.

Static capsule testing within a safe gas atmosphere (3% H<sub>2</sub> in 97% Ar) allows for incipient chemical interactions between hydrogen and fuels/claddings to be examined while preventing complete reaction and thus avoiding significant fuel disruption that would cause uncertainty in post-irradiation examination analysis. Since the SIRIUS-1 series of tests will be static capsule tests, the specimens will be ramped to their peak design temperature (approximately 2600-2850 K) at a rate of 95 K/s or otherwise prescribed rate (higher or lower). No coolant flow is possible in a static capsule, therefore the volumetric power density prescribed in a SIRIUS-1 test will be lower than prototypical operation, however, once at peak temperature, the specimen can be sustained through an isothermal hold for a prescribed period of time, seconds to minutes. This will allow prototypical thermal gradients to be established within the specimen and for chemical interactions, if any, to onset between the fuel system and the H<sub>2</sub> species within static environment. Five or six transient tests / thermal cycles will be performed on each of the concept specimens tested under the SIRIUS-1 series to allow for restart behavior to be observed. A combination of in-pile instrumentation (TREAT Fast Neutron Hodoscope) and the TREAT neutron radiography station will be at intervals in transient tests to determine the location and integrity of the specimen. In the event that a specimen is severely disrupted, or fragmentation is observed during radiography, a test will be concluded on that specimen.

Following transient testing at the TREAT reactor, the capsule will be transported to the INL's Hot Fuel's Examination Facility (HFEF) by the HFEF-15 cask for detailed Post Irradiation Examination (PIE), including: high resolution neutron radiography and tomography, burnup distribution, fission gas retention within fuel systems, metrology, microstructural evolution and thermophysical properties.

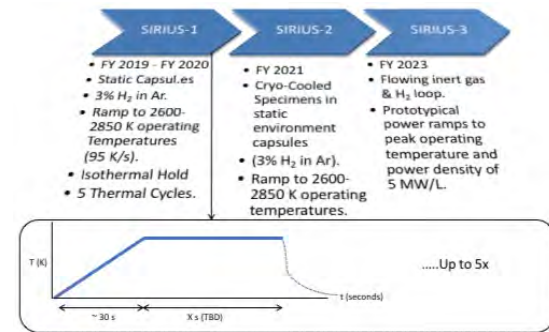


**Fig. 3.** The Sirius 1 Test Series objectives as currently funded. Notional objectives of potential follow-on experimental series beyond 2021 (currently unfunded).

Expansion of the SIRIUS test series will be possible through future funding opportunities to include flowing

loops and refrigerated specimen holders for pre- test conditioning and full power testing.

### III. SIRIUS-1 STATIC CAPSULE DESIGN.

The capsule that will be used in the SIRIUS-1 test series will be manufactured in Grade 5 titanium alloy, produced by powder bed additive manufacturing. The capsule will be lined with a high purity, low density multi-layer crucible, inside which a specimen will be suspended on a refractory alloy pedestal and mirror hanger. Highly polished molybdenum mirrors will minimize thermal losses from the specimen and minimize heating of and hence protect the capsule integrity during the test. A combination of in-pile instrumentation will be used to gather safety and programmatic data during each test. Optical pyrometry will be used to measure specimen temperature. High temperature thermocouples will be attached to the surface of the specimen for low power, low temperature calorimetric calibration for transient prescription confirmation tests and during the full power transient to full prototypical temperatures. It is understood that during the first ramp to full temperature, the thermocouple junction will be lost, but a correlation and confirmation of pyrometer performance will be obtained during this first transient. The pyrometer will perform measurement of the fuel specimen surface temperature via an optical assembly located a stand-off distance to minimize radiant heat damage of the optic. Light gathered through the optical assembly will be transmitted via a fiber optic cable to the out-of-pile spectrometer and data acquisition system.

The SIRIUS-1 capsule design is evolved from the TREAT Static Experiment Test Holder (SETH) capsule that was originally designed to support the Department of Energy’s Accident Tolerant Fuels Program. A Computer Aided Design (CAD) rendering of the SIRIUS-1 capsule is provided in Figure 4. A combination of MCNP, STARCCM+ and ABAQUS codes have been used to perform preliminary design of the SIRIUS-1 Capsule. MCNP is used to estimate the heat generation rate per gram of specimen, and the effective energy coupling factor (ECF) between the TREAT driver core and the specimen for transient prescription purposes. The MCNP model is used to provide heat generation data for the specimen and neutron/gamma heating of the capsule components under a given transient prescription. This is used to model heat transfer and temperature distribution within a specimen. Example results of this transient analysis is provided in Figures 5 and 6.

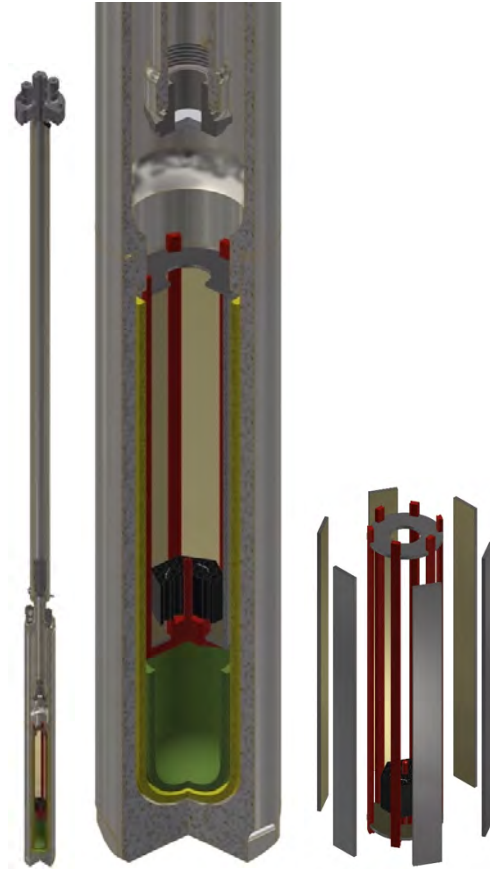


**Fig. 4.** Preliminary design of the SIRIUS-1 Capsule. (Left) Overall Capsule Assembly. (Middle) detailed view of the specimen test section of the capsule showing standoff for the pyrometer optic assembly. (Right) Explosion view of the Mo mirror assembly.

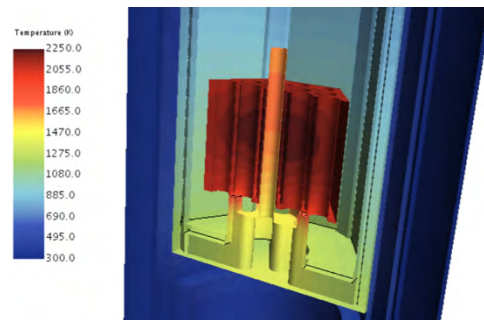


**Fig. 5.** Example predictive analytical results of specimen holder designs and specimen held at constant heat generation rate. The analytical modeling techniques are used to optimize capsule and fixture design while informing mechanical behaviors under transient testing. Here, a cross section of specimen and support pedestal nested inside a crucible is shown during the ramp to peak temperature. (Top) during ramp to temperature, (Bottom)

during isothermal hold – See Figure 6 for temperature ramp profile.

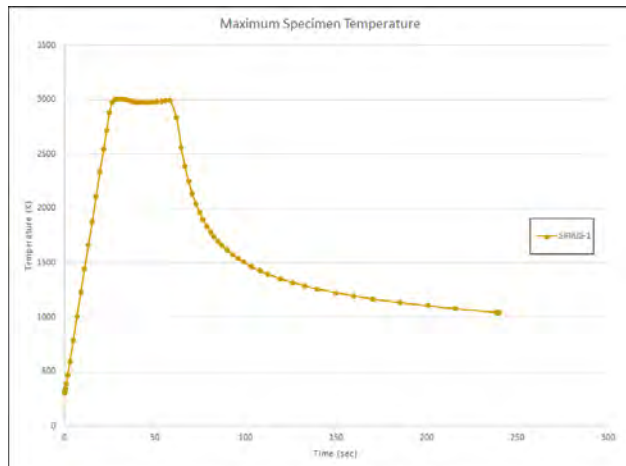


**Fig. 6.** Predicted temperature-time response curve for the preliminary SIRIUS-1 baseline capsule test.

#### IV. BEYOND STATIC CAPSULE TESTING

While static capsule testing offers an affordable approach to testing of NTP fuels, the nature of capsule testing limits the volume of propellant that can be exposed to a specimen. For incipient performance phenomenological studies, capsule testing is therefore relevant and attractive in many cases, especially where unpredicted adverse chemical reactions with propellant species are limited by the initial number of moles present within the capsule upon closure. However, in the absence of flowing propellant, it is not possible to sustain both the full volumetric power density and the peak operational temperature of fuels in typical prototypical fuel specimens, unless the cross-sectional area of a fuel specimen is very small. Therefore, in order to perform testing with both prototypical heat generation while maintaining NTP operational temperatures, flowing loop testing is required in order to target a specific heat removal rate.

The extreme stresses that will be experienced within space based NTP system fuels as they are ramped from space cold, as low as cryogenic temperatures (-192 C) to full operating temperatures, can be explored within transient reactor experiments at TREAT. For example, ramping at a low rate of temperature rise from space cold through the ductile to brittle transition temperature may be required to mitigate fracture behaviors in coatings, claddings and fuel meat. The development of a dedicated refrigerated specimen holder can accomplish the exploration of these needs in a static capsule design, either refrigerated via the use of a cryogenically cooled cold finger and liquid nitrogen heat exchanger, or another mechanical chiller (e.g. Stirling cryo-cooler).

Understanding fuel performance under submersion criticality accidents may be required to satisfy a launch

safety review process and/or civil regulatory licensing. The development of static capsule steam and/or sea water environmental loops may be of importance, especially where fission product release and fuel system corrosion behavior must be characterized. Such testing will be possible through future extension of a SIRIUS1 capsule or SIRIUS-3 loop.

#### V. CONCLUSIONS

The TREAT reactor offers great flexibility and versatility for the testing of NTP fuels which can be used to accelerate the screening and technology readiness level (TRL) of a concept fuel system or design. Similarly, the TREAT reactor can be used to prescribe beyond nominal operating conditions to determine fuel fragmentation thresholds and performance phenomena that may be exhibited under postulated accident conditions, e.g. submersion criticality. Overall, TREAT testing of fuels is an economical approach towards escalating TRL of a fuel system prior to full NTP system design, development and demonstration testing.

#### ACKNOWLEDGMENTS

The Authors would like to acknowledge both the Department of Energy and NASA for funding this research and the SIRIUS-1 transient test series at TREAT.

#### REFERENCES

1. R.L. Williamson, et al “Multidimensional Multiphysics simulation of nuclear fuel behavior,” *Journal of Nuclear Materials*, **423**(1), pp. 149-163, (2012).
2. U.S. Nuclear Regulatory Commission, Regulatory Guide NUREG0800
3. U.S. Atomic Energy Commission, “Assumptions Used for Evaluating a Control Rod Ejection Accident for Pressurized Water Reactors,” Regulatory Guide 1.77, (1974).
4. N.E. Woolstenhulme, J.D. Bess, C.B. Davis, G.K. Housley, C.B. Jensen, R.C. O’Brien, and D.M. Wachs, “TREAT Irradiation Vehicle Designs, Capabilities, and Future Plans”, Proceedings of the PHYSOR-2016 Conference, Sun Valley Idaho, May 1-5, 2016.
5. C.R. Simmons, W.R. Yario and R.O. Ivins “FINAL REPORT ON THE TESTING OF GRAPHITE-TYPE NUCLEAR ROCKET (ROVER) FUEL IN A PULSED REACTOR (TREAT)” Argonne National Laboratory Report ANL-6783 (1964).
5. R.C. O’Brien, “The SIRIUS-1 NTP Fuel Tests In The TREAT Reactor” Idaho National Laboratory Transient Test Plan PLN-5768 (2019).

## DYNAMIC NUCLEAR THERMAL ROCKET AND ENGINE MODELING

J. D. Rader<sup>1</sup> and M. B. R. Smith<sup>1</sup>

<sup>1</sup>Oak Ridge National Laboratory, Oak Ridge, TN 37831

[raderjd@ornl.gov](mailto:raderjd@ornl.gov)

*Oak Ridge National Laboratory (ORNL) is part of multiagency team investigating nuclear thermal propulsion technology. As part of this work, ORNL is developing a dynamic engine and reactor model to inform all aspects of engine instrumentation and controls (I&C). This paper describes updates made to the dynamic model in the past year and showcases some of the visualizations created to facilitate system integration.*

*The updates include new, more detailed component models for the fuel and moderator elements and generally focus on improvements to the details of simulations presented previously. The visualizations provide spatial and temporal context to increase understanding of simulation results.*

### I. INTRODUCTION

As part of a multiagency, interdisciplinary team established to develop nuclear thermal propulsion (NTP) technology led by the National Aeronautics and Space Administration (NASA) Marshall Space Flight Center (MSFC), researchers at Oak Ridge National Laboratory (ORNL) are developing dynamic system models to support the engine's instrumentation and controls (I&C) effort. The models are constructed in the Modelica language using the Dymola environment. This setup allows for flexibility and customization in model development as required for advanced applications of nuclear systems and I&C modeling like NTP. The many different types of processes and phenomena to be captured simultaneously by a dynamic NTP model necessitate an accommodating code system such as Modelica.

When modeling with Modelica, it is commonplace to use customized libraries tailored to specific problems. Over the past few years, ORNL has developed the Transient Simulation Framework of Reconfigurable Models (TRANSFORM) library of Modelica components for modeling advanced nuclear systems.

Using components and models from TRANSFORM, the Modelica standard library (MSL), and other open-source libraries, NTP-specific models have been created and assembled into a system model<sup>1</sup>. The system model includes turbomachinery, fuel and moderator elements, and nuclear reactor kinetics, among other elements. The system

model also includes basic I&C for performing transients. Inputs to the model like fuel and moderator element geometry, turbomachinery performance parameters, and nuclear data are provided by external partners. The model is fully parameterized to accept these inputs and is thus amenable to rapid updates in design specifications.

As this is an ongoing project that considers the design and operation of a nuclear reactor for space applications, many design details are withheld from public dissemination for export-control reasons. Therefore, this paper describes the current dynamic modeling effort in as much qualitative detail as allowed.

### II. COMPONENT MODEL DEVELOPMENT

The current NTP reactor configuration under consideration is a hexagonal array of fuel and moderator elements. Component models for the moderator element and the fuel element were created from TRANSFORM components, as described below.

#### II.A. Moderator Element Component

The moderator element is a two-pass design composed of concentric cylinders/annuli of coolant channels and moderating material with an outer thermal insulator (Fig. 1). The thermal insulator protects the solid moderating material from the high temperatures of neighboring fuel elements.

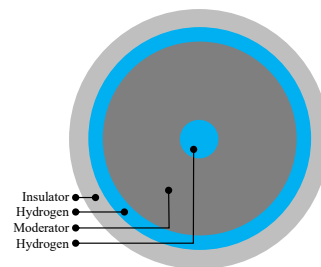


**Fig. 1.** Moderator element component design.

The moderator element component (MEC) is composed of pipe and thermal resistor TRANSFORM components (Fig. 2). The pipe walls are used to model the annular solid regions. The thermal insulator is approximated as an annulus, with a volume equivalent to

<sup>1</sup>This manuscript has been authored by UT-Battelle, LLC, under contract DE-AC05-00OR22725 with the US Department of Energy (DOE). The US government retains and the publisher, by accepting the article for publication, acknowledges that the US government retains a nonexclusive, paid-up, irrevocable, worldwide license to publish or reproduce the published form of this manuscript, or allow others to do so, for US government purposes. DOE will provide public access to these results of federally sponsored research in accordance with the DOE Public Access Plan (<http://energy.gov/downloads/doe-public-access-plan>).

the hexagonal design. The thin claddings are approximated as thermal resistors to conserve computational resources.

Thus, the MEC includes a one-dimensional (1D) fluid solution and a two-dimensional (2D) (r-z) solid solution. The geometry is parameterized according to the radii of the various regions. The spatial power distribution from neutronics calculations can provide input with separate r-z power shapes for each of the regions.

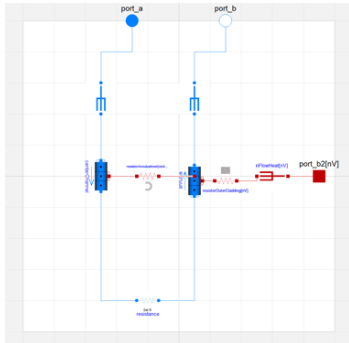


**Fig. 2.** Modelica model of MEC using TRANSFORM components.

### II.B. Fuel Element Component

The fuel element is a single-pass design with an array of cooling channels in a hexagon of fuel material (Fig. 3). The coolant channels are clad, and the outer fuel hex may or may not be clad, depending on the design. The number and size of the cooling holes also depend on the design.

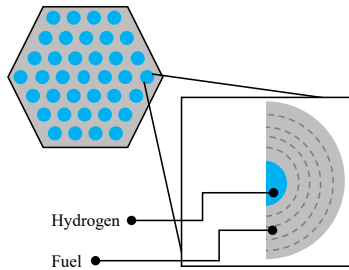


**Fig. 3.** Fuel element design.

Like the MEC, the fuel element component (FEC) is composed of pipe and thermal resistor TRANSFORM components (Fig. 4). Currently, a single average cooling channel is modeled, and claddings are approximated as thermal resistors. The fuel is approximated as an annulus surrounding the cylindrical coolant channel, and the volume of the fuel material is conserved to match the physical design. Currently, two axial zones are supported to allow for different materials in the hot and cold ends of the core. As with the MEC, spatial power distributions for the fluid and solid zones can be included.

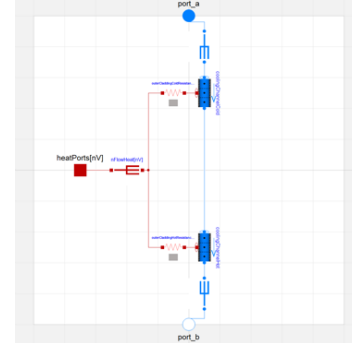


**Fig. 4.** Modelica model of FEC using TRANSFORM components.

For both the MEC and FEC, the number of axial and radial (for solid zones only) nodes of each zone is a parameter.

### III. CONTROL LOGIC

Basic I&C is included in the system model to test at-power control schemes. Proportional-integral (PI) controllers were included that use the core outlet conditions to control power and flow. The core outlet temperature is used to control the control drum position (power), and the core outlet pressure is used to control the turbine bypass valve position (flow).

Control drum worth curves (reactivity vs. angle) are provided by neutronic analysts at BWXT and are supplied as a parameter to the system model. Turbomachine parameters are supplied by Aerojet Rocketdyne (AJRD) and are used to inform turbopump models.

A sample thrust-up transient was chosen to demonstrate the model's capabilities and the visualizations. An initialization hold is performed for the first few minutes to allow the model to reach steady-state at low power. This is denoted as time 0s. Then, a 60s thrust-up followed by a 120s hold and 120s controlled thrust-down is commanded. The thrusting maneuvers have two different p/T trajectories to demonstrate the system's time-dynamics in the intermediate thrust range. The controllers used in this study were not optimized and represent basic controllers for demonstration purposes only.

### IV. SYSTEM INTEGRATION

This section describes some aspects of the integration of various components into a single system model.

#### IV.A. Reactor Integration

Since the fuel and moderator elements are in close physical contact, a significant amount of heat transfer is expected from the hot fuel elements to the cold moderator elements (approximately 5% of thermal power at 100% conditions). This heat transfer was studied using finite-element and computational fluid dynamics models of fuel

and moderator elements at NASA Glenn Research Center. The results of those models were used to inform the selection of a heat transfer coefficient placed between the outsides of the FEC and MEC in the Modelica model. This provides a temperature-dependent calculation of the inter-element heat transfer with some physical basis at all conditions, not just at 100% power.

Perhaps the most important aspect of the dynamic model is nuclear kinetics. Temperature- or density-dependent reactivity coefficients for each of the zones in the reactor are provided by BWXT. An effective temperature or density is calculated using a flux-squared weighting. The weighted temperature or density is used in a lookup table to obtain the reactivity for each zone. These amounts are then summed, along with the current worth of the control drums, and the totals are fed into the point kinetics calculation. The TRANSFORM point kinetics model also allows for decay heat and xenon poison calculation.

#### IV.B. Power Balance Integration

Performance maps for pumps and turbines are provided by AJRD. The performance maps are used to provide nominal values to the TRANSFORM turbine and pump components used in the system model. AJRD is also providing pressure, temperatures, and flow rates at various locations in the *power balance model* (PBM). PBM data are used to calibrate the transient model at 100% conditions.

### V. RESULTS VISUALIZATION

The results of the thrust-up transient were used to create animations of the engine's systems and components. Static images of the animations are shown and described in the following sections.

#### V.A. Design Space Map

A design space map (DSM) was crafted by NASA MSFC engineers using details of the engine components to relate core power, core flow, core outlet temperature, and core outlet pressure so that if two of those values are known, then they can be used to calculate the other two. Limit lines for pump stall, maximum fuel temperature, and reactivity can be overlaid on the DSM so that operating margins to these limits can be visualized when pressure and temperature traces of the transient data are animated. A frame of this animation that is presented near the end of the thrust-down portion of the transient is shown in Fig. 5. The green trace shows the pressure and temperature taken from the core outlet, and the red trace is the setpoint sent to the power and flow controllers.

#### V.B. Moderator Element

The moderator element has very large temperature gradients. Maintaining the solid moderator within its acceptable temperature range is critical to the success of

the mission. Visualization of temperatures in the fluid and solid zones in the moderator element is a useful means for determining the acceptability of a particular transient to the moderator element.

Figure 6 shows a frame from the moderator element animation. The top figure is a colormap of a diametric slice of the element. From left to right, the graphs show minimum and maximum temperature in the element, hydrogen temperature in the coolant channels, and radial temperature profiles at several axial slices.

#### V.C. Control Drums and Reactivity

The movements of the control drums in response to the demand of the core outlet temperature controller are important for determining acceptability of a transient result. The most important factors are drum position, drum speed, and drum acceleration. These results determine if the drums have enough worth, and they place requirements on the drum motor. For example, if it is determined that the drums must rotate all the way in or out, then the bias of the drum can be adjusted up or down by the core designers to account for this. Once a candidate drum motor is selected, its parameters of maximum speed and acceleration can be included in the model and used to set limits on the behavior of the transient.

A frame of the control drum animation is shown in Fig. 7. The large figure on the left shows all of the drums situated at the periphery of the core and their relative rotational positions. The graph in the upper right corner is the drum reactivity vs. position; a box has been placed around the bounding values encountered during the transient. The graph on the middle right shows the controller parameters. The red line indicates the differential of the setpoint and the actual value, while the blue line indicates the same values with artificial noise included to demonstrate what an actual temperature transmitter signal might look like. The bottom right graph shows the actual temperature values and the reactivity as a function of time to give additional context to the other figures.

#### V.D. Turbine Control

A frame presenting animation of the turbine system and its control is provided in Fig. 8. The turbine system is composed of three components: the main turbine, the boost turbine, and the bypass valve. The upper left image shows the two turbines, as well as the bypass valve and their associated mass flows, pressures, and temperatures before and after each component. (The values are omitted here for export control reasons.) The upper right graph shows the controller's parameters. The gray line represents the pressure setpoint and measurement differential, the black line includes artificial noise demonstrating what an actual pressure sensor signal might look like, and the blue line shows the normalized bypass valve's position. The bottom right graph shows the mass flow rates through the three

components. The bottom left graph is a pie chart of the flows through each component displayed as a fraction of the instantaneous total engine flow.

Together these images and graphs provide context on the behavior of the turbine system and its control as a whole. Of particular importance is the normalized valve position. The valve should have margin for control at both low and high-power sections of the transient. As shown, there is a small amount of control margin at either end, but it certainly could be improved. This is one of the key elements that can be learned from analyzing a transient simulation vs. the outcome of a steady-state, full-power level calculation.

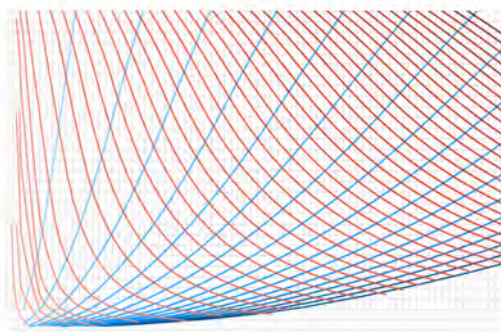


Fig. 5. Frame taken from design space map animation.

Model development will continue to increase the fidelity and capability of the NTP dynamic simulation platform at ORNL. Specific points of future development include optimized control parameters, integration of detailed regenerative nozzle cooling calculations, and introduction of actual instrument parameters (e.g., response times).

**ACKNOWLEDGMENTS**

This work was funded by NASA Marshall Space Flight Center.

The authors also wish to acknowledge their colleagues at ORNL, Idaho National Laboratory, NASA Glenn

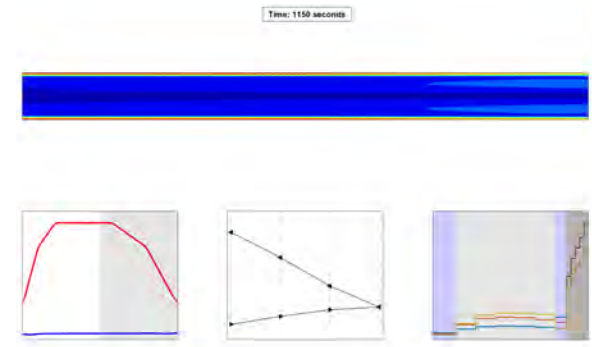


Fig. 6. Frame taken from moderator element animation.

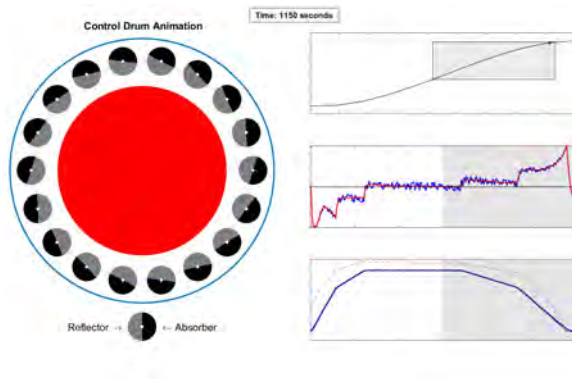


Fig. 7. Frame taken from control drum animation.

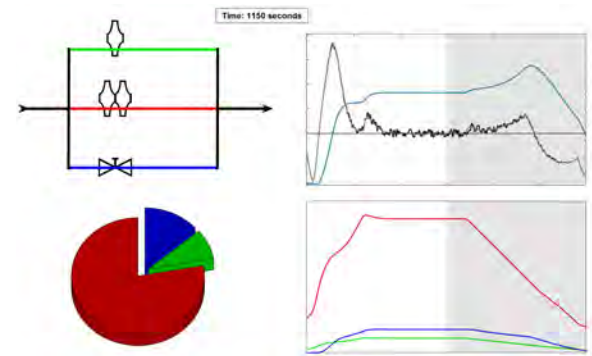


Fig. 8. Frame taken from turbine control animation.

**VI. CONCLUSIONS**

ORNL developed a basic transient model of a conceptual NTP engine to investigate I&C schemes. The model is fully parameterized using design data from external partners. Basic controllers for the power and flow through the engine were constructed. A simple thrust-up transient was used to test the controllers, and the results of the simulation were used to create animations. The animations provide contextualized information for use in the evaluation of simulation results and I&C settings.

Research Center, the University of Tennessee–Knoxville, and industry partners BWXT and Aerojet Rocketdyne for their collaboration.

**REFERENCES**

1. Rader, J. D. et al., “Nuclear Thermal Propulsion Dynamic Modeling with Modelica,” *Nuclear and Emerging Technologies for Space 2019*, Richland, WA.

## FABRICATION OF UN-MO CERMET NUCLEAR FUEL USING ADVANCED MANUFACTURING TECHNIQUES

Alicia M. Raftery<sup>1</sup>, Rachel Seibert<sup>1</sup>, Daniel Brown<sup>2</sup>, Michael Trammell<sup>1</sup>, Andrew Nelson<sup>1</sup>, and Kurt Terrani<sup>1</sup>

<sup>1</sup>Oak Ridge National Laboratory, Oak Ridge, TN, 37831

<sup>2</sup>X-Energy, Rockville, MD, 20852, 865-576-7882

Primary Author Contact Information: 865-241-0130, [rafteryam@ornl.gov](mailto:rafteryam@ornl.gov)

*This paper demonstrates the use of advanced manufacturing techniques to produce ceramic-metallic nuclear fuel pellets with uranium nitride (UN) microspheres encased in a molybdenum (Mo) matrix. Binder jetting is used to print Mo disks that are filled with UN microspheres and afterwards are sintered using spark plasma sintering. Two fuel pellets were fabricated to demonstrate success of the methodology and to provide a baseline analysis of the effects of temperature processing conditions. Characterization of the resulting fuel pellets includes microstructural analysis and thermal conductivity measurements.*

### I. INTRODUCTION

Ceramic-metallic (CERMET) nuclear fuel consists of ceramic fuel particles embedded in a metal matrix. Interest in CERMET fuels originated in the search for a fuel suitable for use in very high temperature reactors, such as those used in nuclear thermal propulsion (NTP) systems proposed for deep space exploration.<sup>1</sup> The purpose of the metallic matrix is to increase the thermal conductivity and protect the fuel from detrimental interactions with a high temperature coolant. This is especially true in NTP reactors, where hydrogen gas at temperatures up to 2600°C (2873K) is the proposed coolant.<sup>2</sup> Various CERMET fuel compositions were investigated with promising results in the 1960's, including UO<sub>2</sub>-W, UO<sub>2</sub>-Mo, UN-W, and UN-Mo.<sup>3,4</sup> In recent years, the emergence of advanced manufacturing technologies has revitalized research and development into fabrication of CERMET fuels.

Advanced manufacturing techniques, or those that use innovative technology to build parts compared to conventional methods, are aggressively being explored for a wide array of fields that utilize materials processing. Spark Plasma Sintering (SPS) is a sintering technique that uses an electrical current to provide heat while simultaneously applying a uniaxial pressure to sinter materials. SPS has been used successfully to fabricate high-density CERMET fuels with properties including enhanced thermal conductivity and controlled grain size.<sup>5,6</sup> Additive manufacturing refers to a subset of advanced manufacturing techniques that are used to build parts on a layer by layer basis. Binder jetting is one technique that uses alternating deposition of binder and powder to create a three-dimensional part and has been used to print a

number of different metallic materials.<sup>7</sup> Some type of post-processing step, such as sintering or infiltration, is typically required since the parts are printed with a green density of approximately 40-60% theoretical density (TD), depending on powder feedstock properties.<sup>8</sup> This study demonstrates a route of fabrication using binder jetting of Mo and subsequent SPS to fabricate UN-Mo fuel pellets. The microstructure and thermal conductivity of the pellets are characterized, and recommendations for improvements of fuel properties are made.

### II. EXPERIMENTAL

#### II.A. UN Feedstock

UN microspheres were fabricated via solution-gelation (sol-gel) and conversion at Oak Ridge National Laboratory (ORNL) using a processing methodology previously described in literature.<sup>9-11</sup> The resulting microspheres had an average diameter of 810 μm and a density of 13.60 g/cm<sup>3</sup> (94.89% TD). The carbon content of the UN microspheres was determined to be 9772 ppm, corresponding to a stoichiometry of UC<sub>0.2</sub>N<sub>0.8</sub>, which is generally considered high for bulk UN fuel but was acceptable for these preliminary studies. Figure 1 (a-c) shows a series of scanning electron microscope (SEM) images of the UN microspheres; energy dispersive spectroscopy (EDS) was used to analyze the material for impurities. Sulfur impurities were detected (Figure 1(c)), the presence of which is likely due to a dispersing agent that is used in the sol-gel process.

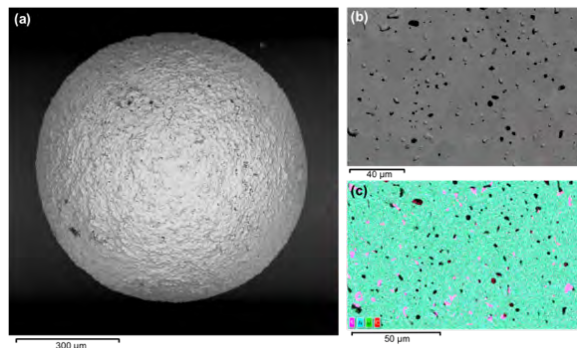


**Fig. 1.** (a) SEM image of the surface of a UN microsphere, (b) the microstructure showing grains and pores, and (c) the coupled EDS scan showing the presence of sulfur impurities (pink) in the material.

## II.B. Binder Jetting Mo

Mo disks were printed using an ExOne Innovent binder jet printer. The Mo feedstock was TEKMAT Mo-45 spherical powder with an average size of  $45\ \mu\text{m} \pm 15\ \mu\text{m}$ , an oxygen content  $< 250\ \text{ppm}$ , and a tap density of  $5\ \text{g}/\text{cm}^3$ , according to the manufacturer's specifications.

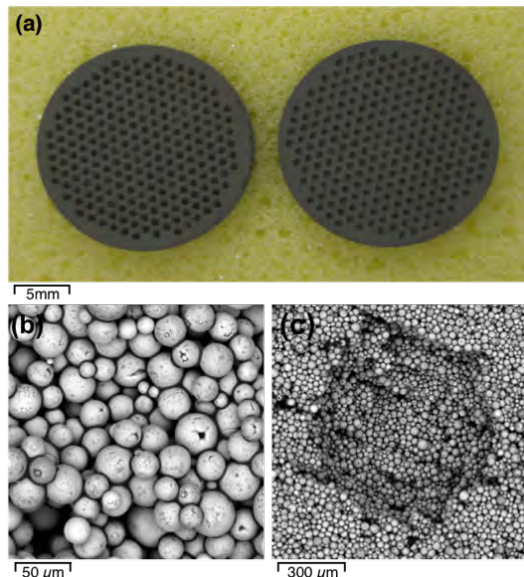


**Fig. 2.** (a) Photograph of binder jet printed Mo disks, SEM images showing (b) the binder providing particle to particle bonding, and (c) a printed hole for placement of a UN microsphere.

The Mo disks were printed to approximately 20mm in diameter and 2mm in height, with a pattern containing 225 holes located on both sides of the disk for placement of UN microspheres. The disks were printed using an aqueous binder, and immediately after printing were placed in a furnace at  $190^\circ\text{C}$  for 6 hours to cure the binder. After curing, the disks were excavated from the powder bed by removing excess powder; the resulting parts are shown in Figure 2(a). SEM images of the disks indicate good wetting of the binder between Mo particles (Figure 2(b)). In addition, the printed holes for the UN microspheres are not entirely spherical and have rough edges, as seen in Figure 2(c).

## II.C. UN-Mo Pellet Fabrication

The SPS system used for sintering was a Thermal Technology SPS 25-10. All materials were loaded into a graphite die, between two graphite punches, with graphite foil surrounding the material both axially, with 0.5mm on top and bottom, and radially, with 0.127mm around the sample. The purpose of the graphite foil is to prevent interaction of the material being sintered with the graphite die and punches at high temperatures. The bottom Mo disk was loaded in the graphite die and one layer of 225 UN microspheres were placed in the disk, with one microsphere per hole. The loaded disk is shown in Figure

3(a). The second Mo disk with the matching pattern was fit on top to hold the microspheres in place. Figure 3(b) shows the graphite die prepared with material and punches. The die was loaded into the chamber between graphite blocks, which aid in centering and provide a pathway of conduction for the current to pass through the die (Figure 3(c)). In addition, graphite felt surrounded the die axially and radially to insulate during sintering.

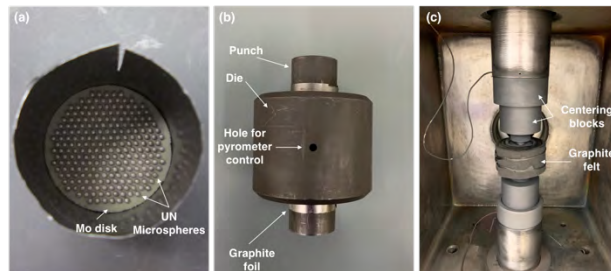


**Fig. 3.** (a) Photograph of Mo disk placed inside of graphite die and loaded with UN microspheres before sintering, (b) graphite die with punches inserted, and (c) graphite die positioned in SPS stack for sintering.

To ensure consistency between samples, many of the processing parameters were held constant. The vacuum was brought to and held at  $2.0 \times 10^{-3}$  Torr and the direct current (DC) pulse was set to 12ms on/2ms off. The temperature ramp rate for heating and cooling was  $150^\circ\text{C}/\text{min}$ , and the hold time at maximum temperature was 10 minutes. The pre- and post-pressure was 15 MPa, which ensures good electrical contact between the punches and graphite centering blocks. The sample temperature was measured during the experiments with an optical pyrometer; therefore, the recorded temperatures are representative of the surface temperature of the material being sintered. Two UN-Mo pellets were fabricated at two different temperatures and pressures, as a proof-of-concept and to obtain a baseline analysis of temperature effects.

## III. RESULTS

The processing parameters and resulting densities are shown for each pellet in Table I. After sintering, silicon carbide grit paper was used to remove the graphite foil from the fueled pellets. Some residual graphite foil remained, which can be seen on pellet UNMo-1, pictured in Figure 4(a). The pellets were mounted in conductive epoxy and cut aggressively to remove the Mo and reach mid-plane of the microspheres for imaging and analysis. Figure 4(b) shows a photograph of pellet UNMo-1 during metallographic preparation; the UN microspheres are mostly intact, but a small number have cracked, which is either a result of pressure during sintering or material pullout during sample preparation. Figure 4(c) is an x-ray radiograph of pellet UNMo-2, showing the UN microspheres distributed evenly throughout the Mo matrix.

**TABLE I.** Results for two UN-Mo pellets made, showing the SPS processing conditions and resulting densities.

Pellet ID	Temperature [°C]	Pressure [MPa]	%TD
UNMo-1	1600–1650	25–35	71.97
UNMo-2	1650–1700	55–65	92.31

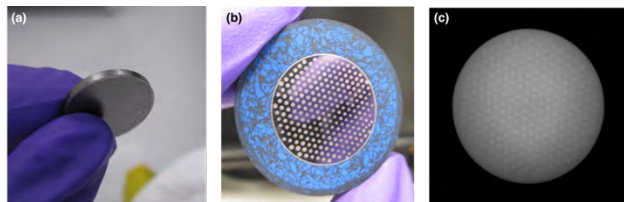


**Fig. 4.** (a) Photograph of pellet UNMo-1 after sintering, (b) during metallographic preparation, and (c) an x-ray radiograph of pellet UNMo-2, showing UN microspheres distributed throughout the Mo matrix.

### III.A. Microstructural Characterization

The pellets were polished to a finish suitable for electron backscatter diffraction (EBSD) and imaged using a TESCAN MIRA3 GHM SEM. The primary features of interest were the grain size, the thickness and composition of interaction layers, and the presence of any secondary phases or impurities. Figures 5(a,b,d,e) show optical and SEM overviews of UN microspheres located within the Mo matrix of each pellet, highlighting the varying level of densification between the two pellets. Figures 5(c,f) show a similarity in grain structure and grain size in the UN regions between the two pellets. The grain structure in the Mo regions differs between the pellets due to the different levels of densification, but on the whole the matrix Mo grains are larger than those observed in the UN.

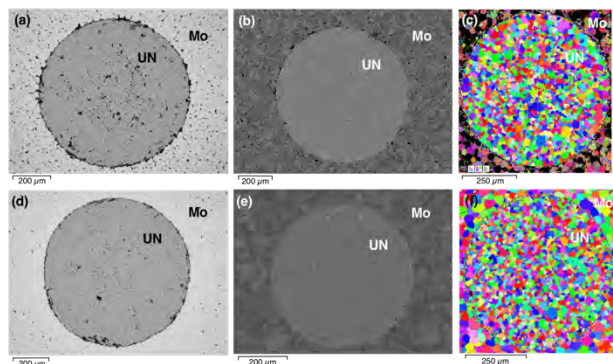


**Fig. 5.** (a) Optical image, (b) SEM image, and (c) EBSD band contrast map of the cross section of selected UN microspheres from pellet UNMo-1 and (d) optical image, (e) SEM image and (f) EBSD band contrast map of selected UN microspheres from pellet UNMo-2.

Figures 6(a-d) show the UN-Mo interface for each pellet. There is a continuous crack along the perimeter of the UN microsphere between the UN and the Mo regions in both pellets. The crack width ranges from 1–30 $\mu$ m in UNMo-1, with the large range due to the Mo particles only

necking around the microsphere, leaving gaps between particles. The crack size around the UN microspheres in UNMo-2 is consistently < 2 $\mu$ m. The cracks in both pellets are most likely explained by the higher coefficient of thermal expansion in UN compared to Mo, resulting in its shrinkage during cooldown. There was no interaction phase observed at the boundary between the UN and Mo in either pellet.

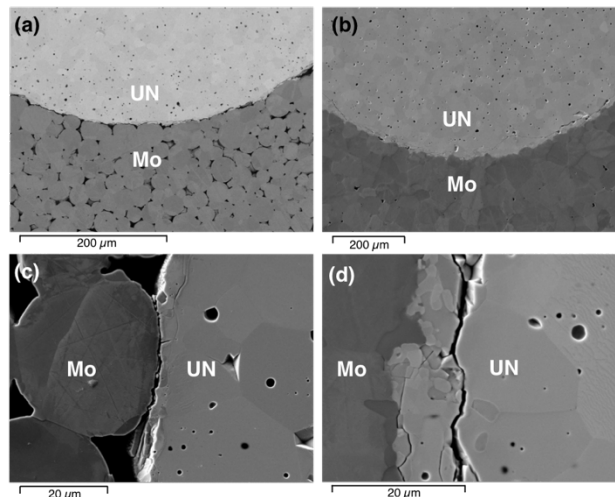


**Fig. 6.** Overview of UN-Mo interface for (a) pellet UNMo-1 and (b) pellet UNMo-2, and close-up of the interface for (c) UNMo-1 and (d) UNMo-2.

It was expected that carbon diffusion from the graphite foil surrounding the pellet during sintering would form an interaction layer along the perimeter of the pellet, since this is observed in many materials that are processed using SPS. The presence of a carbide layer was confirmed in each pellet and was characterized using EBSD to be Mo<sub>2</sub>C. Figures 7(a,b) show a comparison of the interaction layer between the two pellets; the thickness was measured to be approximately 80–100 $\mu$ m in UNMo-1 and 100–140 $\mu$ m in UNMo-2. The difference in thickness is likely due to the higher temperature used during fabrication of UNMo-2.

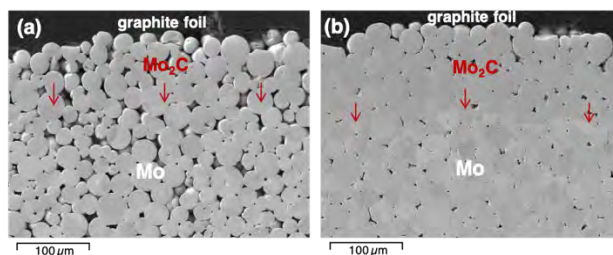


**Fig. 7.** Interface between graphite foil and Mo regions in (a) UNMo-1 and (b) UNMo-2, showing the carbide layer resulting from interaction with the graphite foil.

An EDS map scan of the UN microspheres revealed an oxide layer surrounding each sphere, which is shown for a microsphere in UNMo-1 in Figure 8. The oxide was present at the same thickness (~8 $\mu$ m) on the perimeter of

each microsphere in both pellets. The oxide formation is likely a result of the feedstock being stored in air for an extended period of time before being used in this study. No other significant impurities or secondary phases were found in the pellets.

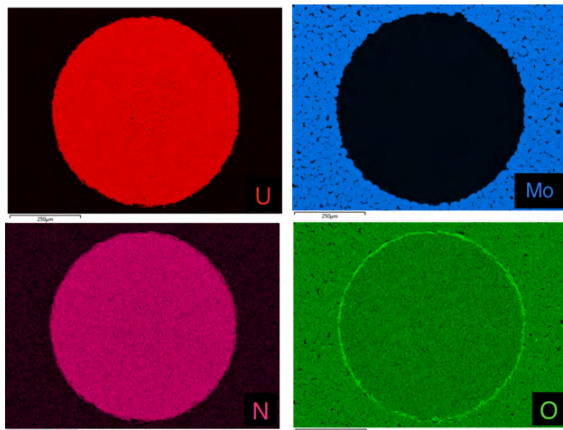


**Fig. 8.** EDS map results for UN microsphere located in UNMo-1, showing an oxide layer on the perimeter of the microsphere.

### III.B. Thermal Conductivity

Thermal diffusivity measurements were made using a Netzsch LFA 475 MicroFlash instrument. The thermal diffusivities of UNMo-1 and UNMo-2 were measured as a function of increasing temperature. Measurements were recorded every 50°C from room temperature (25°C) to 900°C. Figure 9 shows the results converted to thermal conductivity, along with reference values for Mo and UN fabricated via conventional routes.<sup>12,13</sup>

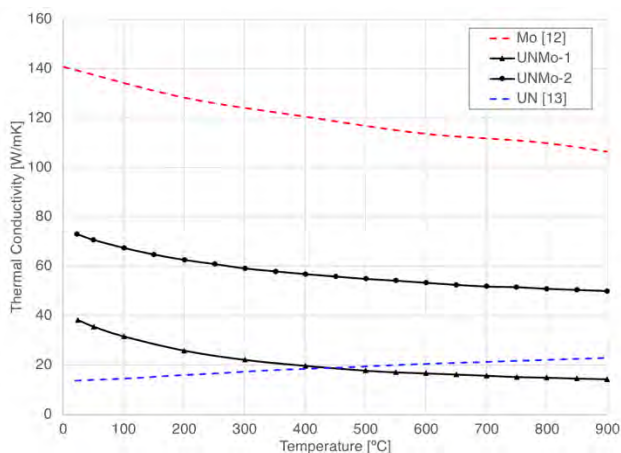


**Fig. 9.** Thermal conductivity results for UNMo-1 and UNMo-2, as well as reference values for Mo and UN fabricated via conventional routes.<sup>12,13</sup>

UNMo-2 has higher values for thermal conductivity across all temperatures when compared to UNMo-1, which is due to the higher density in the Mo region. There is an increase in the thermal conductivity of both pellets with

respect to reference values for UN, but a significant decrease compared to the reference values of Mo. The reduction is likely due to the trapped porosity within the disks, as well as the lower thermal conductivity contribution from the UN.

### IV. CONCLUSIONS

This paper describes the fabrication of UN-Mo CERMET nuclear fuel using a route that utilizes advanced manufacturing techniques. Characterization of the two pellets showed results that are consistent with those expected from the two temperature processing conditions and resulting densities. Notably, the high-density pellet showed an enhanced thermal conductivity compared to monolithic UN fuel while featuring a full encapsulation of the UN fuel microspheres within a densified Mo matrix. Both properties are advantageous when considering this fuel for use in high temperature systems.

Adverse pellet properties include cracking of some microspheres and the formation of a carbide interaction layer at the perimeter of the pellet, both of which have the potential to be mitigated by altering the processing parameters. Modifications that would improve the fuel properties of the UN-Mo fuel design specific to this work include increasing the fuel volume fraction with slight changes to the Mo disk design. For instance, the disks could be made thinner with holes printed only on one side to minimize porosity and maximize the fuel volume fraction. The ease with which these changes could be implemented using the binder jetting technique is a testament to the versatility of this processing methodology.

Perhaps most significant in this work is the demonstration of a novel fabrication methodology, which proves the ability to spatially place fuel inside of a matrix using a combination of advanced manufacturing techniques. This innovation has far-reaching implications in terms of expanding the nuclear fuel design space. It is reasonable to conclude that these techniques will provide the ability to achieve fuel geometries, compositions, and properties outside of the realm of current traditional manufacturing techniques.

### ACKNOWLEDGMENTS

The authors would like to acknowledge Rodney Hunt and Jake McMurray for their contributions in producing the UN feedstock materials and Austin Schumacher for his initial efforts in design. Desarae Godsby and Derek Siddell are recognized for producing the binder jetted Mo parts at the Manufacturing Demonstration Facility (MDF). Lastly, Jeff Pryor, Stephanie Curlin, and Hsin Wang are acknowledged for their efforts in characterization. This work was supported by the Transformational Challenge Reactor (TCR) under the auspices of the U.S. Department of Energy, Office of Nuclear Energy.

## REFERENCES

1. S.K. BOROWSKI, D.R. MCCURDY, and T.W. PACKARD, "Nuclear Thermal Propulsion (NTP): A proven growth technology for human NEO/Mars exploration missions," *IEEE Aerospace Conference Proceedings*, 1-20 (2012).
2. WALLACE, T.C. "Review of Rover element protective coating development at Los Alamos," *AIP Conference Proceedings*, 217, 1024-1036 (2008).
3. PAPROCKI, S.J., KELLER, D.L., CUNNINGHAM, G.W., KIZER, D.E., *Preparation and properties of UO<sub>2</sub> CERMET fuels*, BMI-1487, Battelle Memorial Institute: Columbus, OH (1960).
4. TAKKUNEN, P.D., *Fabrication of CERMETS of uranium nitride and tungsten or molybdenum from mixed powders and from coated particles*, NASA TN D-5136, Lewis Research Center: Cleveland, OH (1969).
5. BUCKLEY, J., TURNER, J.D, and ABRAM, T.J., "Uranium dioxide – molybdenum composite fuel pellets with enhanced thermal conductivity manufactured via spark plasma sintering," *J. Nucl. Mater.*, 433, 50-54 (2013).
6. O'BRIEN, R., and JERRED, N.D., "Spark plasma sintering of W-UO<sub>2</sub> cermets," *J. Nucl. Mater.*, 433, 50-54 (2013).
7. SACHS, E., CIMA, M. and CORNIE, J., "Three-dimensional printing: rapid tooling and prototypes directly from a CAD model." *CIRP Annals*, 39, 201-204 (1990).
8. BAI, Y., WAGNER, G., and WILLIAMS, C.B., "Effect of particle size distribution on powder packing and sintering in binder jetting additive manufacturing of metals," *J. Manuf. Sci. Eng. Trans. ASME*, 139, 1-6 (2017).
9. HUNT, R.D., and COLLINS, J.L., "Uranium kernel formation via internal gelation," *Radiochim. Acta*, 92, 909-915 (2004).
10. LINDEMER, T.B., et al., "Quantification of process variables for carbothermic synthesis of UC<sub>1-x</sub>N<sub>x</sub> fuel microspheres," *J. Nucl. Mater.*, 483, 176-191 (2017).
11. MCMURRAY, J.W., KIGGANS, J.O., HELMREICH, G.W., and TERRANI, K.A., "Production of near-full density uranium nitride microspheres with a hot isostatic press," *J. Am. Ceram. Soc.*, 101, 4492-4497 (2018).
12. ZINOV'EV, V.E., "Thermal properties of metals at high temperatures," *Metallurgiya* (1989).
13. HAYES, S.L, THOMAS, J.K., and PEDDICORD, K.L., "Material property correlations for uranium mononitride," *J. Nucl. Mater.*, 171, 289-299 (1990).

## FISSION MATRIX IMPLEMENTATION IN TRICORDER FOR NTP SYSTEM ANALYSIS

Adam J. Rau<sup>1</sup>, Vishal Patel<sup>2</sup>, and William J. Walters<sup>1</sup>

<sup>1</sup>Ken and Mary Alice Department of Nuclear Engineering, Penn State University, University Park, PA 16802

<sup>2</sup>USNC-Space, Seattle, WA 98199

Primary Author Contact Information: Phone: 814-867-4329, Email: [wjw24@psu.edu](mailto:wjw24@psu.edu)

*This paper documents the implementation of steady-state, temperature-dependent fission matrix neutronics methods into TRICORDER, a code to simulate core heat transfer, fluid flow, and transients in nuclear thermal propulsion (NTP) systems. In the present work, the fission matrix for an arbitrary temperature distribution is estimated by interpolating fission matrices tallied using the Monte Carlo code Serpent. The dominant eigenvalue and eigenvector of the fission matrix are the multiplication factor and fission source distribution (respectively), which is assumed to be proportional to the power shape. Details of the implementation are discussed, and code-to-code validation is performed against Serpent on two temperature profiles. For both temperature profiles, the normalized error in the 3-D fission source distribution is within 1.1%. The multiplication factor error for the arbitrary cosine shaped profile is -209 pcm, and the error for the profile found through iteration between neutronic and thermal-hydraulic calculations is 12 pcm.*

### GLOSSARY OF TERMS

E	Energy
r	Position
V	Volume
$\kappa$	Energy produced per fission
$\nu$	Number of neutrons produced per fission

## I. INTRODUCTION

### I.A Background

Detailed design of nuclear thermal propulsion (NTP) technologies will require transient simulations that couple neutronics, thermal-hydraulic, and thermomechanical simulations. Monte Carlo methods serve as the gold standard for neutronics calculations, but these calculations are computationally intensive, particularly if they are to be coupled with other physics. Deterministic methods can be very fast, but can suffer from spatial, angular, and energy discretization errors. Fission matrix methods incorporate some of the benefits of both, and can have a fast computation time while still being very accurate. For example, the code RAPID relies on fission matrix methods and other response function methods, and has been applied to spent fuel pools<sup>1</sup>, power reactors<sup>2,3</sup>, and research reactors<sup>4</sup>. Transient fission matrix methods have been developed for Molten Salt reactors<sup>5,6</sup> as well as the Flattop-Pu benchmark<sup>7</sup>.

The present work documents the integration of recently-developed, steady-state temperature-dependent fission matrix methods<sup>8,9</sup>, into the code TRICORDER<sup>10</sup>. TRICORDER was developed by USNC-Tech to simulate core heat transfer, fluid flow, and control transients in NTP systems. The code is based on the MOOSE framework<sup>11</sup>, and system modeling tools are built on the Modelica framework. This work is intended as a first step toward adding transient fission matrix capability to this code.

### I.B Theory

The fission matrix  $A$  results from the integration of the k-eigenvalue form of the neutron transport equation

$$k_{\text{eff}} \vec{s}(\vec{r}) = \int_V \vec{s}(\vec{r}') A(\vec{r}' \rightarrow \vec{r}) d\vec{r}' \quad (1)$$

over  $N$  spatial cells, yielding

$$\vec{s} = \frac{1}{k_{\text{eff}}} \mathbf{A} \vec{s} \quad (2)$$

where  $A$  is composed of

$$a_{ij} = \frac{\int_{V_i} d\vec{r} \int_{V_j} d\vec{r}' \cdot \vec{s}(\vec{r}') A(\vec{r}' \rightarrow \vec{r})}{\int_{V_i} d\vec{r} \int_{V_j} d\vec{r}' \cdot \vec{s}(\vec{r}')} \quad (3)$$

Physically,  $a_{ij}$  represent the expected number of neutrons created in cell  $i$  per fission neutron born in cell  $j$ .

Equation (2) shows that the multiplication factor is the dominant eigenvalue of the fission matrix and the fundamental mode fission source is the corresponding eigenvector.

## II. METHODS

The methods discussed in the present work have two phases. First, a database of fission matrices is tallied using the Monte Carlo code Serpent.<sup>12</sup> The resulting fission matrix data is processed and reformatted so it can be easily read by the tools provided in MOOSE. Then, during the coupled calculation, this fission matrix data is read and interpolated based on the fuel temperatures calculated by TRICORDER. Interpolation is performed assuming that each fission matrix element is assumed to be a function of the destination volume temperature:

$$a_{ij} = f(T_i) \quad (4)$$

Where  $T_i$  is the temperature of fuel in volume  $i$ . This interpolation assumes that the fission probability depends (or is dominated by) the fuel temperature at the fission site, as opposed to the fuel temperature at other locations.

Once the fission matrix has been estimated, the dominant eigenvalue and eigenvector are found. As shown in equation (2), the normalized eigenvector is the fission source distribution. An additional assumption is made that this is proportional to the heat generation though fission, effectively assuming that

$$\nu(E) \propto \kappa(E) \quad (5)$$

and neglecting non-local heating.

## II.A Pre-calculation

### II.A.1 Fission Matrix Tallying

Fission matrices were tallied using the Monte Carlo code Serpent. The “set fmtx” option of Serpent is used, which tallies fission matrix elements during a criticality calculation over a cartesian grid. This option is advantageous for two reasons. First, tallying fission matrix elements over a criticality calculation means that the source distribution is known, so fission matrix elements can be tallied even if the source varies within the volume (see equation 3). Second, the method is relatively simple to use. Although the mesh is cartesian, the mesh spacing was selected to overlay the hexagonal NTP core elements. A portion of this mesh is shown in Fig. 1.

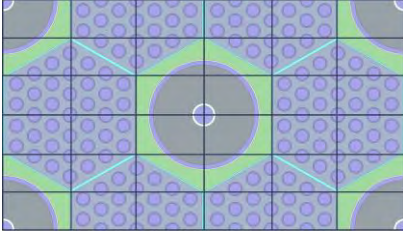


**Fig. 1** Portion of the fission matrix mesh used in the present work

### II.A.2 Mesh Modification

The fission matrix mesh must be decided before tallying the fission matrix database. However, depending on the purpose of the calculation, different dimensionality (2D or 3D) or domain (whole-core, fraction of core, unit cell) may be appropriate. Since the fission matrix database calculation is typically the most time-consuming part of the process, it is desirable to re-use this data as much as possible without repeating this calculation.

To this end, pre-processing scripts were written to combine fission matrix volumes, so an initially fine mesh can be coarsened as needed. This process preserves the dominant eigenvalue and eigenvector. Scripts were

written so a whole-core fission matrix can be collapsed to represent 1/2, 1/4, 1/3, 1/6, or 1/12 of a core. Fission matrix mesh modification is performed following the tallying step, as fission matrix data is transformed into CSV format that can be read by TRICORDER.

## II.B Calculation

Several new objects were created to add fission matrix calculations to TRICORDER. Generally, these objects fell into one of two categories; either transferring data between the thermal-hydraulic finite-element mesh and the fission matrix finite volume mesh, or storing, interpolating, and solving fission matrices. An overview of the objects and calculation scheme is shown in Fig. 2.

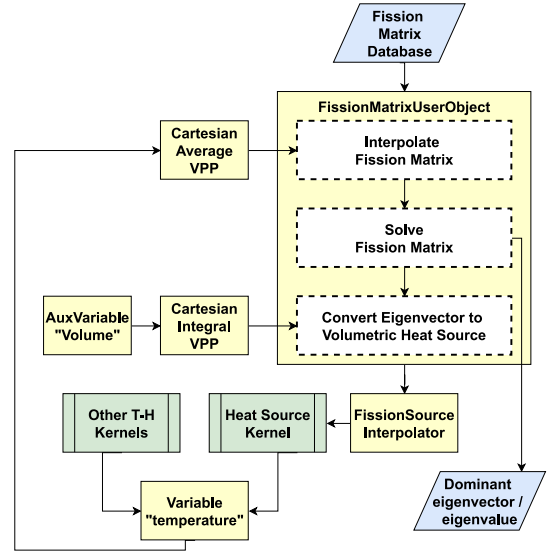


**Fig. 2** Flowchart for fission matrix calculation

### II.B.1 Cartesian Integrator

TRICORDER requires a volumetric heat source, but the fission matrix provides the integral of the fission source over each fission matrix volume. To convert from one to the other, the fuel volume within a cartesian cell must be known. To calculate this quantity, a cartesian integrator object was created, which integrates a quantity within a specified material and  $x$ ,  $y$ , and  $z$  boundaries. Integrating unity gives the volume of the fuel within the fission matrix cell.

### II.B.2 Cartesian Averages

When estimating the fission matrix, fission matrix elements are interpolated based on the fuel temperature at the destination cell. The cartesian averager inherits from the cartesian integrator and is used to calculate the volume-averaged fuel temperature for this interpolation.

### II.B.3 Heat Source Sampler

Since the finite element calculation is performed on a different grid than the fission matrix calculation, an

additional object was created to project the volumetric heat source back to the finite element mesh. The current object just takes the fission source from the nearest fission matrix mesh cell.

#### II.B.4 Fission matrix object

The fission matrix object reads in fission matrix data in the initialization phase, and interpolates and solves fission matrices during the calculation phase.

Initially, fission matrix equations were represented by a set of kernels, which are objects used to represent equations in the MOOSE framework. However, the memory overhead from storing a kernel for every entry in the fission matrix ( $N^2$  entries for  $N$  volumes) proved to be prohibitive, so instead lower-level (LibMesh denseMatrix) object is created to represent the entire matrix.

Fission matrix elements are interpolated based on local temperature given by the CartesianIntegrator object. Interpolation is performed by fitting a cubic spline to each fission matrix element.

### III. CODE-TO-CODE VALIDATION

Since the fission matrix method serves as a proxy for Monte Carlo, code-to-code validation is performed by comparing Serpent and TRICORDER output on the same temperature profile. To conduct this validation, temperature profiles are entered into Serpent using the Multiphysics interface, and the resulting fission source distribution and multiplication factor calculated by each code is compared.

Validation is performed on two temperature distributions; the first is a steady-state achieved through Picard iteration between TRICORDER thermal-hydraulics and the fission matrix method, assuming a constant heat transfer coefficient and sink temperature at the coolant channels. Since there was relatively little variation in this temperature profile, the process was repeated using an artificial cosine-shaped temperature profile, with a value of 600K at the center of the core moving down to 300K at the periphery. Both temperature profiles are shown in Fig. 3. Fission matrices were calculated at 294, 600, 900, 1200, and 2500 K.

#### III.A. Verification Case

Verification was performed on a conceptual nuclear thermal propulsion core. It is a NERVA-derived design with a UN particle fuel in a natural W matrix moderated by  $ZrH_{1.89}$ . The core utilizes low-enriched uranium and provides high specific impulse ( $\sim 900s$ ) with low mass ( $\sim 3500$  kg).

Monte Carlo models of this core were generated using the in-house code CURSOR. CURSOR creates full-core 3D models. A 2D 1/12-core TRICORDER

model was used for the coupled thermal-hydraulic calculation.

### III.B. Results

Normalized errors for the power shape are shown in Fig. 4. Root-mean-square average and maximum power shape error are shown in Table I and multiplication factor errors are shown in Table II.

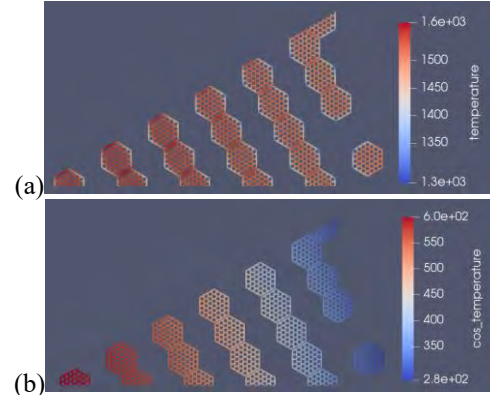


**Fig. 3** Steady-state (a) and cosine (b) fuel temperature profiles for code-to-code validation cases

Different shapes of the error can be seen in the different cases. In particular, the cosine temperature profile seems to underestimate the fission source near the center of the core and overestimate the fission source near the core periphery. This is likely due to the artificially large temperature gradient, and relatively small number of database temperature points.

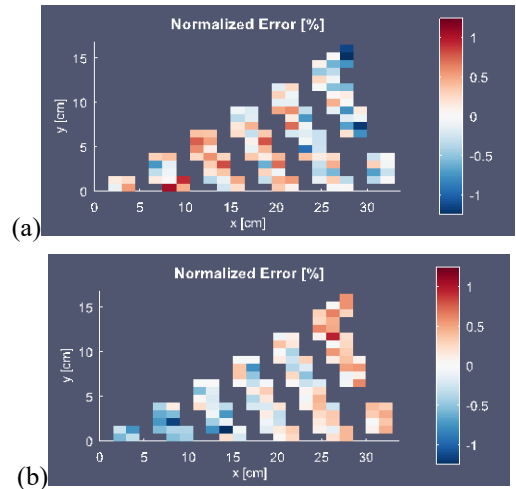


**Fig. 4** Normalized error in power shape for (a) steady-state and (b) cosine-shaped temperature profile

The multiplication factor has been predicted within statistical accuracy for the steady-state temperature profile. Error is higher than expected for the cosine-shaped temperature profile, and may result from the

destination temperature assumption. Underestimation of the multiplication factor is consistent with the error observed in the power shape, where higher importance regions are underestimated in this model.

**TABLE I.** Norm. error of TRICORDER power shape (rel. to Serpent) and uncertainty of Serpent power shape

Temp. Profile	Error		Uncertainty	
	RMS	Max.	RMS	Max.
Steady-state	0.5	1.0	0.2	0.3
Cosine	0.4	0.9	0.3	0.3

**TABLE II.** Multiplication factors calculated by TRICORDER and by Serpent. Uncertainty on multiplication factors provided by Serpent is 5 pcm.

Temp. Profile	Tricorder	Serpent	Error [pcm]
Steady-state	1.01955	1.01973	12
Cosine	1.03601	1.03392	-209

#### IV. SUMMARY AND CONCLUSIONS

This paper documents implementation of fission matrix methods in TRICORDER. Code-to-code validation indicates that the method is implemented correctly, although results from the artificial temperature profile bear further investigation. The solution could be as simple as using more reference temperature points, or it could involve implementing a ratio-correction method.<sup>3</sup>

To help be useful for detailed design work, the method should be extended in several ways. Adding in methods to account for control drum movement is straightforward<sup>9</sup> and can help account for the effect of control drum position on power shape. Since the intention of this method is to replace Monte Carlo in transient calculations, transient fission matrix methods should be implemented. Finally, since non-local heating is important to the problem, response function methods for this should be investigated.

#### REFERENCES

1. W. WALTERS et al., “Calculation of Sub-critical Multiplication Using a Simplified Fission Matrix Method,” *Trans. Am. Nuc. Soc.* **101** 1, 447 (2009).
2. W. J. WALTERS, N. J. ROSKOFF, and A. HAGHIGHAT, “The RAPID Fission Matrix Approach to Reactor Core Criticality Calculations,” *Nucl. Sci. Eng.* **192** 1, 21, Taylor & Francis (2018); <https://doi.org/10.1080/00295639.2018.1497395>.
3. D. HE and W. J. WALTERS, “A local fission matrix correction method for heterogeneous whole core transport with RAPID,” *Ann. Nucl. Energy* **134**, 263, Elsevier Ltd (2019); <https://doi.org/10.1016/j.anucene.2019.06.008>.
4. V. MASCOLINO et al., “EXPERIMENTAL AND COMPUTATIONAL BENCHMARKING OF RAPID USING THE JSI TRIGA MARK-II REACTOR,” in *International Conference on Mathematics and Computational Methods applied to Nuclear Science and Engineering*, pp. 1328–1337 (2019).
5. A. LAUREAU, L. BUIRON, and B. FONTAINE, “Towards spatial kinetics in a low void effect sodium fast reactor: core analysis and validation of the TFM neutronic approach,” *EPJ Nucl. Sci. Technol.* **3**, 17 (2017); <https://doi.org/10.1051/epjn/2017008>.
6. A. LAUREAU et al., “Transient coupled calculations of the Molten Salt Fast Reactor using the Transient Fission Matrix approach,” *Nucl. Eng. Des.* **316**, 112, Elsevier B.V. (2017); <https://doi.org/10.1016/j.nucengdes.2017.02.022>.
7. V. MASCOLINO and A. HAGHIGHAT, “VALIDATION OF THE TRANSIENT FISSION MATRIX CODE TRAPID AGAINST THE FLATTOP-PU BENCHMARK,” in *International Conference on Mathematics and Computational Methods applied to Nuclear Science and Engineering*, pp. 1338–1347, Portland, Oregon (2019).
8. T. J. TOPHAM, A. RAU, and W. J. WALTERS, “An Iterative Fission Matrix Scheme for Calculating Steady-State Power and Critical Control Rod Position in a TRIGA Reactor,” *Ann. Nucl. Energy*.
9. A. RAU and W. J. WALTERS, “Fission Matrix Methods for Nuclear Thermal Propulsion Applications,” in *International Conference on Mathematics and Computational Methods*, American Nuclear Society, Portland, Oregon (2019).
10. L. B. CARASIK, M. EADES, and V. PATEL, “DECAY HEAT STUDIES TO REDUCE ACTIVE COOLING TIME OF A NUCLEAR THERMAL PROPULSION SYSTEM,” in *Nuclear and Emerging Technologies for Space*, American Nuclear Society Topical Meeting, Richland, WA (2019).
11. D. GASTON et al., “MOOSE: A parallel computational framework for coupled systems of nonlinear equations,” *Nucl. Eng. Des.* **239** 10, 1768 (2009); <https://doi.org/10.1016/j.nucengdes.2009.05.021>.
12. J. LEPPÄNEN et al., “The Serpent Monte Carlo code: Status, development and applications in 2013,” *Ann. Nucl. Energy* **82**, 142 (2015); <https://doi.org/10.1016/j.anucene.2014.08.024>.

## HYDROGEN ABSORPTION BEHAVIOR OF Y-10Ce

A.P. Shivprasad<sup>1</sup>, T.A. Saleh<sup>1</sup>, E.P. Luther<sup>2</sup>, H.R. Trellue<sup>3</sup>

<sup>1</sup>Materials Science and Technology, Los Alamos National Laboratory, Los Alamos, NM, 87545, [aps@lanl.gov](mailto:aps@lanl.gov)

<sup>2</sup>Sigma Division, Los Alamos National Laboratory, Los Alamos, NM, 87545

<sup>3</sup>Nuclear Engineering and Nonproliferation, Los Alamos National Laboratory, Los Alamos, NM, 87545

Yttrium dihydride is an attractive high-temperature moderator material that can be used in small reactors to reduce the required fuel mass. Additionally, hydrided yttrium-cerium alloys are of interest for nuclear reactor moderator applications due to the ability to retain hydrogen at high temperatures with a lower thermal neutron absorption cross-section than pure yttrium dihydride. An yttrium alloy containing 0.1 weight fraction cerium was fabricated by arc-melting and was hydrided between 600 and 1000 °C in a hydrogen/argon gas mixture. Hydriding was performed using thermogravimetry to a final stoichiometry of 2.0 H/M units. Thermogravimetric results were compared with those of pure yttrium metal to show that the onset temperature for rapid hydrogen absorption was delayed for the alloy, as compared with pure yttrium. X-ray diffraction of the hydrided material showed that cerium remained in solid-solution in the yttrium sublattice during fabrication and upon hydriding. These results indicate that yttrium-cerium alloys show great promise for moderator applications.

## I. INTRODUCTION

### I.A. Background

Moderators, which thermalize neutrons to more efficiently participate in the nuclear fission reaction of uranium-235, could be fabricated to meet the needs of surface power generation and nuclear thermal propulsion<sup>1</sup>. Zirconium hydrides (ZrH<sub>2-x</sub>) have traditionally been considered for this application. However, yttrium dihydride (YH<sub>2-x</sub>) is able to retain hydrogen to much higher temperatures than are zirconium hydrides<sup>2-4</sup>. This ability to retain hydrogen to higher temperatures would result in improved thermal efficiencies and reduction in mass of the power conversion and heat rejection systems<sup>1</sup>.

One drawback to the use of yttrium dihydride is that its production requires the use of high-purity yttrium metal, which is expensive compared to zirconium and other rare earths considered for moderator applications<sup>5</sup>. Another drawback is that yttrium, which is mono-isotopic as yttrium-89, has a thermal neutron absorption cross-section of 1.28-b, which is approximately two orders of magnitude higher than of natural zirconium<sup>6</sup>. To mitigate these drawbacks, the production of metal alloy hydrides has been proposed<sup>7</sup>. This could be achieved by alloying yttrium with other metals that have similar abilities to retain hydrogen

to high temperatures and maintain small thermal neutron absorption cross-sections.

### I.B. Yttrium-cerium composite hydrides

To assess which hydrides would make good candidates for compositing with yttrium dihydride, the partial pressures required to hydride various metals were examined as a function of temperature. This is plotted in Fig. 1.

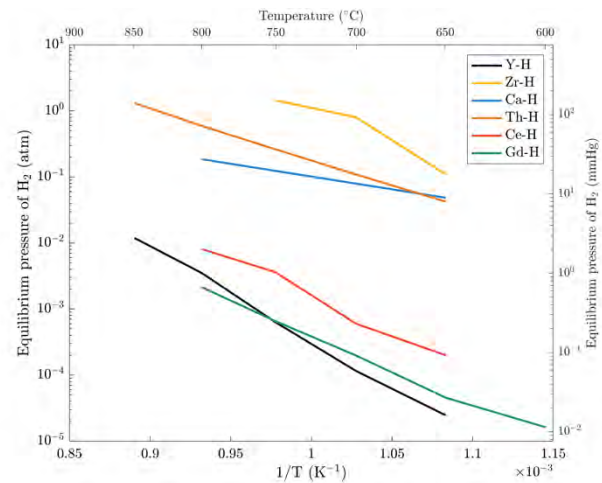


**Fig. 1:** Equilibrium pressure of H<sub>2</sub> required to form metal hydrides as a function of 1/T (K<sup>-1</sup>). Plots shown for the Y-H, Zr-H, Ca-H, Th-H, Ce-H, and Gd-H systems. Data taken from literature<sup>2,4,8-11</sup>.

Fig. 1 shows the equilibrium pressure of hydrogen required to hydride selected pure metals to a stoichiometry of approximately 1.7 H/M units. This result shows that the partial pressures required to hydride yttrium, gadolinium, and cerium are two to four orders of magnitude lower than for calcium, thorium, and zirconium. Gadolinium has a high thermal neutron absorption cross-section and is conventionally used as a burnable poison<sup>12</sup>. However, cerium, which has a radiative capture cross-section that is approximately one order of magnitude lower than that of yttrium, could potentially be alloyed with yttrium to produce composite hydrides<sup>6</sup>. One additional advantage of the use of cerium is the reduced cost for fabricating the pure metal with respect to yttrium<sup>5</sup>.

In evaluating the Y-Ce system, it was found that the two elements have significant solubility with each other<sup>7</sup>.

The Ce-H system is also interesting, as cerium can hydride to high hydrogen contents, up to H/Ce of 3 without changing structure, and has the ability to retain hydrogen above the melting point of the base metal; that is, cerium hydride remains solid at temperatures where cerium metal is liquid in the presence of 1-atm of hydrogen<sup>10</sup>. Coupled with the reduced thermal neutron absorption cross-section and the reduced cost of cerium metal, hydrided alloys of yttrium and cerium for nuclear reactor moderators are of particular interest.

In this study, we show initial results towards the development of yttrium-cerium alloy hydrides, particularly an alloy containing 10 weight percent cerium, Y-10Ce. The hydriding behavior of this alloy was examined using thermogravimetry, while the phases present upon hydriding were also examined using X-ray diffraction (XRD). Thermogravimetry results were compared with those of pure yttrium, while XRD patterns were compared against literature for phase identification.

## II. EXPERIMENTAL METHODS

### II.A. Alloy preparation

Yttrium and cerium metals were obtained from the Sigma Division of Los Alamos National Laboratory. Yttrium castings and rolled cerium were 99.99% and 99.95% pure on a rare earth metals basis. These metals were combined in a 9:1 yttrium-to-cerium mass ratio.

Buttons of alloyed material were prepared in an inert, argon glovebox with oxygen and moisture levels maintained below 0.1 ppm. Attention was paid to ensure that the cerium content of the material did not exceed approximately 10 wt% to reduce the formation of the  $Y_{0.5}Ce_{0.5}$  intermetallic phase, which forms over the range of 40 to 70% in cerium content on a mass basis<sup>13</sup>. Samples of Y-10Ce were prepared by arc-melting the high-purity Y and Ce metals together to produce buttons of an approximate mass of 1.8-g each.

Fabrication was performed in an arc-melter (5TA Reed Tri-Arc, Centorr Vacuum Industries, USA) constant current welder connected to a water-cooled 2% thoriated tungsten electrode and a water-cooled copper hearth with small hemispherical cavities to contain the Y and Ce feedstocks. A gettered argon gas stream was flowed through the arc-melter with a composition of less than  $10^{-13}$  ppm oxygen. A molten Ti getter was also used as an internal getter to capture any remaining free oxygen within the copper hearth. A total of six melts were performed with pinwheeling (mixing of elements) for five minutes per melt.

### II.B. Hydrogen absorption measurements using thermogravimetry

Hydrogen absorption measurements were performed using a tungsten (W) metal furnace Simultaneous Thermal

Analyzer (STA 449 F3, Netzsch Instruments, Germany) to measure sample mass *in situ* as a function of temperature and exposure time for each testing condition. Temperature was measured using a Type-S thermocouple, while samples were held using an aluminum oxide pan wrapped in molybdenum foil. The foil was used to prevent any potential reactions between yttrium or yttrium dihydride and the alumina pan. A titanium foil was used as an oxygen getter to reduce the effects of potential leaks within the system. Based on literature data on titanium oxidation and hydriding, it was determined that titanium would not appreciably absorb hydrogen in the temperature range of interest<sup>14</sup>. An image of the experimental setup is shown in Fig. 2.

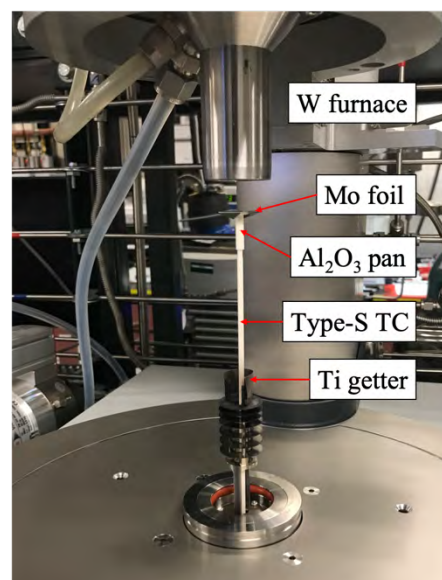


**Fig. 2:** Experimental setup for thermogravimetry experiments. Highlighted are the W furnace, the type-S thermocouple, and the  $Al_2O_3$  pan. Also highlighted are the molybdenum foil to prevent chemical interaction between samples and the  $Al_2O_3$  pan, as well as the titanium getter to reduce sample oxidation within the setup.

The mass of hydrogen absorbed was measured by exposing sectioned alloys to a gas mixture containing 6% hydrogen (balance argon) at temperatures up to 1000 °C. Measurements were performed as temperature ramps. Samples were heated to temperatures of interest under gettered argon with oxygen levels maintained below  $10^{-15}$  ppm using a copper oxygen getter.

### II.C. Phase identification

Phases present in the directly-hydrided yttrium and the sintered monoliths were investigated with a Bruker D2 X-ray diffractometer (XRD, Bruker, Wisconsin, USA). Samples were prepared into approximately 100-mg of powder in an inert, argon glovebox line. Samples were loaded onto a silicon-crystal zero-background plate with a

thin layer of vacuum grease as an adhesive and sealed in a polymer dome with an air-scatter shield to reduce X-ray background at low angles. XRD scans were performed using a copper  $K_{\alpha}$  X-ray in Bragg-Brentano focusing geometry from  $25^{\circ}$  to  $40^{\circ}$   $2\theta$  with a scan resolution of  $0.02^{\circ}$   $2\theta$  and a live time of 5 s per  $2\theta$ -step, as was done in previous work<sup>15</sup>.

### III. RESULTS AND DISCUSSION

#### III.A. Hydriding behavior of Y-10Ce

Thermograms of pure yttrium and Y-10Ce in 6%  $H_2/Ar$  during temperature ramps from 600 to 1000  $^{\circ}C$  are shown in **Fig. 3**. Results for pure yttrium are shown in the solid, black line, while those for Y-10Ce are shown in the dashed, black line. Yttrium and Y-10Ce gained 1% mass, which corresponds to an approximate composition of 0.9 in H/M units, which is consistent with previous studies examining the thermodynamics of the hydriding of yttrium<sup>2</sup>. As expected, for both materials, the hydrogen absorption rate increased with temperature. However, preliminary results showed that the onset of fast hydrogen absorption was delayed for Y-10Ce, as compared with pure yttrium. Both thermograms appeared to converge at approximately 950  $^{\circ}C$ , indicating that both materials exhibit similar H/M ratio at temperatures above this value. The analysis to determine this onset temperature is also shown in **Fig. 3**.

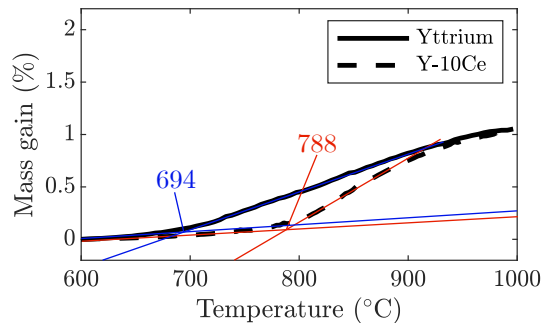


**Fig. 3:** Thermograms of pure yttrium and Y-10Ce during temperature ramps between 600 and 1000  $^{\circ}C$  in 6%  $H_2/Ar$ . Figure is annotated to show the temperatures where the hydrogen absorption reaction becomes faster.

From the analysis of preliminary results, as shown in **Fig. 3**, it was observed that hydrogen absorption significantly increased at approximately 694  $^{\circ}C$  for pure yttrium, but was delayed to approximately 788  $^{\circ}C$  for the Y-10Ce alloy.

Previous hydriding studies showed that below such an onset temperature, the mass gain due to gas-solid interactions was characterized by film-like growth, though hydride films tended to crack and spall<sup>16</sup>. For Y-10Ce, no hydride spallation was noted. In previous work studying the cerium-hydrogen reaction, it was noted that a change in

hydride growth rate was characterized by a self-ignition of material; i.e. the heat produced during the metal-hydrogen reaction resulted in a positive feedback loop of temperature and reaction kinetics increases. Above such transition temperatures, the gas-solid interaction is characterized by linear kinetics, which indicates surface-limited reactions because of fast diffusion of hydrogen. These could be either the metal-hydrogen reaction at the metal/hydride interface to further ingress the hydride or at the gas/hydride interface to intercalate hydrogen into the hydride lattice.

Based on previous work studying the kinetics of hydrogen absorption to form metal hydrides, the shift of the onset temperature to a higher value upon alloying with cerium could indicate that the transition between slow and fast hydrogen absorption kinetics required a higher temperature, which could imply that the barrier for hydrogen diffusion in the metal hydride is higher for Y-10Ce than it is for pure yttrium. This could positively affect moderator performance, as a higher barrier for hydrogen diffusion through the hydride would impact hydrogen redistribution rates within the moderator during operation.

#### III.B. Phase identification

The Y-10Ce sample was further hydrided to compositions of 1.3 and 2.0 H/M units.

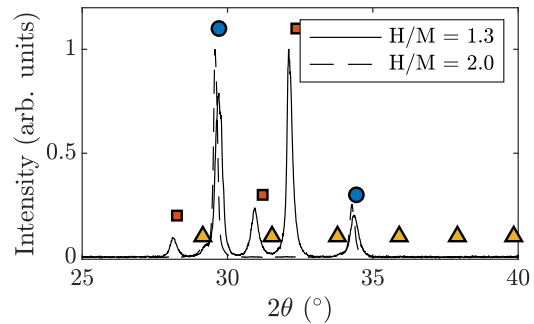


**Fig. 4:** XRD patterns for Y-10Ce hydrided to 1.3 (solid line) and 2.0 (dashed line) H/M units. Phases and patterns were indexed against literature data for pure  $YH_{1.98}$  (blue circles), Y metal (orange squares), and  $Y_2O_3$  (yellow triangles)<sup>17-19</sup>.

**Fig. 4** plots diffracted intensity as a function of  $2\theta$  for Y-10Ce hydrided to both compositions mentioned above. Diffraction patterns were indexed against literature results for pure  $YH_{1.98}$ , Y metal, and  $Y_2O_3$ <sup>17-19</sup>. As expected, the partially-hydrided Y-10Ce exhibited significant amounts of yttrium metal and yttrium dihydride. It was observed that the  $2\theta$ -positions of the yttrium-metal peaks in the XRD pattern were slightly lower (higher d-spacing) than the literature values for pure yttrium<sup>18</sup>. This phenomenon makes sense, as cerium is a much larger atom and accommodation of cerium will expand the yttrium

sublattice. Increasing the composition of the alloy to 2.0 H/Y units yielded nearly pure yttrium dihydride with a small amount of yttrium(III) oxide (Y<sub>2</sub>O<sub>3</sub>). It is interesting to note that powders of the hydrided material exhibited no contribution from cerium hydride, indicating that cerium remained in solid-solution upon hydriding. This was also observed by the shift in peak position for the fully-hydrided material to lower 2θ, as compared with the literature value<sup>17</sup>. No peaks associated with other cerium-containing compounds were observed, which highlights the high quality of the arc-melted material and the propensity for cerium to remain in the yttrium sublattice of yttrium dihydride.

#### IV. CONCLUSIONS AND FUTURE WORK

Yttrium-cerium alloys are of interest for nuclear reactor moderator applications due to the low thermal neutron absorption cross-section of natural cerium as compared with yttrium and the improved thermal stability and ability to retain hydrogen at high temperatures of cerium hydride, as compared with zirconium hydride. In this study, Y-10Ce was fabricated by arc-melting and then subjected to hydrogen absorption measurements.

Preliminary thermogravimetric results showed that the hydrogen absorption rate of Y-10Ce significantly increased at approximately 788 °C. However, the onset temperature for rapid hydrogen absorption appeared to be increased by the addition of cerium; this result has significant implications for the diffusion of hydrogen through the hydride and, thus, for hydrogen redistribution during reactor operation. Partially- and fully-hydrided Y-10Ce were examined for phase content using XRD. The presence of other cerium-bearing phases was not observed in either pattern, indicating the purity of the starting material and the ability for cerium to remain in the yttrium sublattice upon hydriding. Additionally, the measured d-spacings of Y-10Ce and the fully-hydrided Y-10Ce were slightly larger than literature values for yttrium metal and YH<sub>1.98</sub>, which is consistent with the accommodation of cerium in the yttrium sublattice.

These results imply that yttrium-cerium alloys show great promise for nuclear reactor moderator applications, particularly with regard to the mitigation of hydrogen migration during reactor operation. To that end, more work is needed to confirm these results and future work will examine the effect of higher cerium content on hydrogen absorption. Additionally, hydrogen desorption is of interest to study, due to its effect on reactivity.

#### V. ACKNOWLEDGMENTS

This work was funded by the U.S. Department of Energy, Office of Nuclear Energy (NE) Fuel Cycle Technology (NE-5) Micro-Reactor RD&D Program. The authors thank John Dunwoody and Chris Grote for operational support. The authors would also like to thank

Jason Cooley for support with materials and fabrication techniques.

#### VI. REFERENCES

1. D. I. POSTON and P. MCCLURE, "White paper - Use of LEU for a space reactor," LA-UR-17-27226, Los Alamos National Laboratory (2017).
2. L. N. YANNOPOULOS, R. K. EDWARDS, and P. G. WAHLBECK, "The Thermodynamics of the Yttrium-Hydrogen System," *J. Phys. Chem.* **69** 8, 2510 (1965); <https://doi.org/10.1021/j100892a004>.
3. C. E. LUNDIN and J. P. BLACKLEDGE, "Pressure-Temperature-Composition Relationships of the Yttrium-Hydrogen System," *J. Electrochem. Soc.* **109** 9, 838 (1962); <https://doi.org/10.1149/1.2425565>.
4. E. ZUZEK et al., "The H-Zr (hydrogen-zirconium) system," *Bulletin of Alloy Phase Diagrams* **11** 4, 385 (1990); <https://doi.org/10.1007/BF02843318>.
5. J. A. OBER, "Mineral commodity summaries 2019," Report, Reston, VA, p. 204 (2019); <https://doi.org/10.3133/70202434>.
6. J. CHANG, "Table of Nuclides, KAERI (Korea Atomic Energy Research Institute)."
7. C. E. LUNDIN and D. T. KLODT, "FUNDAMENTAL ALLOY DEVELOPMENT. Quarterly Progress Report, August 1, 1959- October 31, 1959," TID-6728; XDC-60-9-72, Denver. Univ. Denver Research Inst. (1959).
8. R. W. CURTIS and P. CHIOTTI, "THERMODYNAMIC PROPERTIES OF CALCIUM HYDRIDE1," *J. Phys. Chem.* **67** 5, 1061 (1963); <https://doi.org/10.1021/j100799a027>.
9. M. W. MALLETT and I. E. CAMPBELL, "The Dissociation Pressures of Thorium Dihydride in the Thorium-Thorium Dihydride System1a," *J. Am. Chem. Soc.* **73** 10, 4850 (1951); <https://doi.org/10.1021/ja01154a112>.
10. F. D. MANCHESTER and J. M. PITRE, "The Ce-H (Cerium-Hydrogen) system," *JPE* **18** 1, 63 (1997); <https://doi.org/10.1007/BF02646759>.
11. G. E. STURDY and R. N. R. MULFORD, "The Gadolinium-Hydrogen System1," *J. Am. Chem. Soc.* **78** 6, 1083 (1956); <https://doi.org/10.1021/ja01587a003>.
12. D. BERNARD and A. SANTAMARINA, "Qualification of gadolinium burnable poison: Interpretation of MELUSINE/GEDEON-II spent fuel analysis," *Annals of Nuclear Energy* **87**, 21 (2016); <https://doi.org/10.1016/j.anucene.2015.02.034>.
13. R. W. CAHN, "Binary Alloy Phase Diagrams—Second edition. T. B. Massalski, Editor-in-Chief; H. Okamoto, P. R. Subramanian, L. Kacprzak, Editors. ASM International, Materials Park, Ohio, USA. December 1990. xxii, 3589 pp., 3 vol., hard- back. \$995.00 the set," *Advanced Materials* **3** 12, 628 (1991); <https://doi.org/10.1002/adma.19910031215>.

14. A. SAN-MARTIN and F. D. MANCHESTER, "The H-Ti (Hydrogen-Titanium) system," *Bulletin of Alloy Phase Diagrams* **8** 1, 30 (1987);  
<https://doi.org/10.1007/BF02868888>.
15. A. P. SHIVPRASAD et al., "Elastic moduli of high-density, sintered monoliths of yttrium dihydride," Accepted by *Journal of Alloys and Compounds* (2020).
16. D. SARUSSI et al., "The kinetics and mechanism of cerium hydride formation," *Journal of Alloys and Compounds* **191** 1, 91 (1993);  
[https://doi.org/10.1016/0925-8388\(93\)90277-T](https://doi.org/10.1016/0925-8388(93)90277-T).
17. D. KHATAMIAN et al., "Crystal structure of YD1.96 and YH1.98 by neutron diffraction," *Phys. Rev. B* **21** 6, 2622 (1980);  
<https://doi.org/10.1103/PhysRevB.21.2622>.
18. I. R. HARRIS and G. V. RAYNOR, "The constitution of yttrium-cerium and yttrium-lanthanum alloys, with special reference to lattice spacings," *Journal of the Less Common Metals* **7** 1, 1 (1964);  
[https://doi.org/10.1016/0022-5088\(64\)90011-6](https://doi.org/10.1016/0022-5088(64)90011-6).
19. K. MARTIN and G. MCCARTHY, "PDF No. 41-1105," ICDD Grant-in-Aid, North Dakota State University, Fargo, North Dakota, USA (1989).

## REDUCED ORDER NUCLEAR THERMAL ROCKET ENGINE MODEL

David Sikorski<sup>1</sup>, Dan Floyd<sup>1</sup>, and Richard Wood<sup>1</sup>

<sup>1</sup>University of Tennessee Department of Nuclear Engineering, Knoxville, Tennessee, 37966

Primary Author Contact Information: [dsikorsk@vols.utk.edu](mailto:dsikorsk@vols.utk.edu)

*This paper describes the current effort focused on recapturing previous work to enable further development of nuclear thermal rocket engine control systems. The paper discusses the state of the art in nuclear thermal rocket engine control experience and describes historical engine configurations of interest. Next, the value of investigating through simulation the dynamic behavior of nuclear thermal rocket engines is introduced. Capturing the dynamics of a nuclear thermal rocket engine generally requires complex models unsuitable for rapid control design studies. Thus, work to digitally recapture a prior simplified dynamic model as a tool for nuclear thermal rocket engine control development and rapid prototyping is presented.*

### I. INTRODUCTION

Recent interest in manned missions beyond cislunar space has prompted the revival of nuclear thermal rocket (NTR) engine technology as an advanced propulsion option for deep space missions.<sup>1</sup> Nuclear thermal propulsion (NTP) has the potential to offer significant benefits over chemical propulsion. Perhaps most notably, NTR engines promise higher efficiency and shorter trip times than chemical rocket engines.<sup>2</sup> Historically, these anticipated benefits were the drivers for NTP research and development, which resulted in the experimental space reactor and nuclear rocket engine programs known as Rover, and the Nuclear Engine for Rocket Vehicle Application (NERVA).<sup>3</sup> These seminal programs were dedicated to the research and development of highly advanced nuclear rocket engines for space propulsion. They were successful in building several test reactors, and ultimately built and tested experimental reactors in two engine configurations. The culmination of the experimental systems produced through the Rover and NERVA programs was the XE-Prime engine, the only flight style NTR engine ever built. Further information on NTP development and the Rover and NERVA programs can be found as historical background presented in a prior publication that describes initial investigation under the current research activities supporting further development of NTR technology.<sup>4</sup>

Review of the historical record from the NTR experimental programs substantiates the long-standing consensus that instrumentation and control of NTR engines are essential enabling technologies and a high

priority development need. In this regard, XE-Prime is identified as the state of the art for NTR engine control experience. Thus, the engine control philosophy and methodology for XE-Prime can serve as a basis for further development of NTR engine control. Based on the evolution of technology over the past 50 years, there is significant opportunity for improvement of NTR engine control systems.

While XE-Prime is considered to be the apex of NTR engine control experience, further control development continued, employing mathematical models until the end of the NERVA program.<sup>5</sup> These mathematical models are crucial to control development and dynamical study of highly nonlinear cross-coupled systems such as NTR engines. Various engine model iterations are in development today for the same purposes.<sup>6</sup> While the majority of these models are relatively complex, consisting of at least 50 differential equations, a relatively simple model with minimal computational requirements is desirable for conceptual controls development purposes. This paper presents current efforts to recapture a reduced order model of an NTR engine, and digitally implement it using MATLAB/Simulink as a testbed for controls development.

### II. ENGINE CONFIGURATION AND CONTROL

A nuclear rocket engine functions, as shown in Figure 1, by pumping hydrogen through a reactor core to be heated and subsequently accelerated through a nozzle to generate thrust. The amount of thrust generated by the engine is determined by the temperature and pressure of the hydrogen before being exhausted through the nozzle. Therefore, the nozzle chamber temperature and pressure define the engine's operating point and are the primary control parameters of interest. Various engine configurations and control methods were devised during the Rover and NERVA programs to accomplish these control objectives. As noted, the most recent experience arises from the XE-Prime experimental engine. Further developments occurred after XE-Prime, but were never physically realized. However, iterations of the NERVA E-1 designs resulted in more advanced engine control approaches for more complicated engine configurations.<sup>7</sup>



Thus, revision 6.1 had 4 control inputs for two primary control parameters. Recognizing the highly cross-coupled nature of the engines, engineers developed multivariable controllers as an improvement over previous single-input, single-output control approaches. Linear quadratic optimal controllers with two region gain scheduling were designed for thrust buildup, and supervisory startup logic modules were under development as a prototype. Some as-yet undetermined level of supervisory adaptation logic for expected component degradation was included, and diagnosis and adaption to single turbopump failure was implemented.<sup>10</sup>

The engine dynamics were further complicated by the new closed loop engine cycle. This cycle directs all of the propellant used to power the turbopump back into the engine to be further heated and used for thrust. The benefit of this engine cycle is increased efficiency, at the cost of greater complexity.

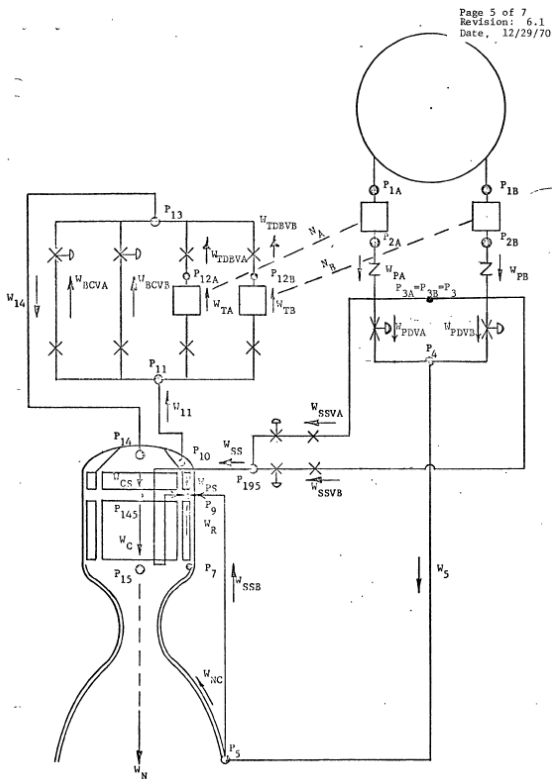


Figure 4. NERVA E-1 revision 6.1 diagram.<sup>11</sup>

### III. ENGINE MODELING

The dynamic behavior of these new engine designs was assessed by performing transient analysis using simulation capabilities of the time. Throughout the Rover and NERVA programs, engineers built dynamic models to perform transient analysis of the various engine and reactor configurations. The common analog model (CAM)

was developed as an evolution of the various analog models used for previous engine studies. This model pedigree meant that although the NERVA E-1 engine series was not physically realized, it remained “anchored” in test data from previous experiments due to the iterative process of model development and correction with test data.<sup>9</sup>

#### III.A. Common Analog Model

The CAM was a time dependent mathematical description of the various components of a given NTR engine configuration, implemented on state of the art analog and hybrid computers that were available at the time.<sup>11</sup> The various CAM iterations were relatively complex models based on conservation of mass, momentum, energy, and neutron density as described by reactor point kinetics. In addition, the ideal gas law was employed as the equation of state for hydrogen. The latest model consisted of 52 differential equations, at least as many algebraic equations, and empirical functions from experimental data.

As of the early 1970’s, the CAM was considered too complex for rapid controller development given limited computational resources, resulting in the development of the simplified nonlinear model (SNM).<sup>12</sup>

#### III.B. Reduced Order Model

The SNM was derived from the NERVA E-1 Revision 6.1 CAM by selecting dynamic variables which were considered essential for representing the predominant dynamic behavior of the system. This simplification was achieved through a three-part process. First, an initial variable selection based on engineering judgement was performed. Then, those equations were linearized, and time constants were obtained for comparison with the CAM behavior. The differential equations with time constants less than one tenth of the dominant system time constant were reduced to algebraic equations. Subsequently, some of the algebraic equations were replaced with curve fits of E-1 revision 6.1 CAM data.

The result of this process was a lower order model that primarily reflects the low frequency response of the system. Two of the most significant reductions to this model were the removal of the pump discharge valves, and one of the turbopumps. For the purpose of the SNM, the additional turbopump was considered redundant. This major simplification is likely not possible for a modern NTR engine design, because current designs incorporate a boost pump that is required for normal engine operation.

The SNM, illustrated in Figure 5, consisted of 11 differential equations and 13 algebraic equations.



8. DANIEL R. KOENIG, "Experience Gained from the Space Nuclear Rocket Program (Rover)," Los Alamos National Laboratory, Los Alamos NM, 1986
9. "E-1 Common Analog Model Revision 1," Aerojet Nuclear Systems Company NERVA program report to AEC-NASA Space Nuclear Propulsion Office, Sacramento Ca, 1969
10. E. A. PARZIALE, R. F. SCHENZ JR., "Thrust Buildup State Variable Feedback Control System for the E-1 CAM (Revision 6.1)," Aerojet Nuclear Systems Company, Sacramento Ca, 1971
11. "E-1 Common Analog Model Revision 6.1," Aerojet Nuclear Systems Company NERVA program report to AEC-NASA Space Nuclear Propulsion Office, Sacramento Ca, 1970
12. LARRY E. KENDRICK, "On-Line Digital Computer Control of The NERVA Nuclear Rocket Engine," Doctoral Dissertation, University of Arizona, 1972

## PROCESSING TRISO-BEARING ULTRAHIGH TEMPERATURE CARBIDE FUELS FOR NUCLEAR THERMAL PROPULSION

Lance Snead<sup>1</sup>, Jason Trelewicz<sup>1</sup>, David Sprouster<sup>1</sup>, Caen Ang<sup>2</sup>, and Yutai Katoh<sup>2</sup>

<sup>1</sup>Engineering Drive, Stony Brook University, Stony Brook, NY 11794

<sup>2</sup>1412 Circle Drive, University of Tennessee, TN, 37996

Primary Author Contact Information: Lance Snead, 631-632-4174

*The use of microencapsulated TRISO fuel conveys a number of advantages to the performance, safety, and road to qualification of a nuclear thermal propulsion reactor. One primary advantage is the ability for these fuels to retain their fission products under relatively harsh conditions of temperature and fissile burnup. However, both operating temperature and the corrosive hydrogen coolant/exhaust provide challenges to the TRISO fuel and the compacting matrix that binds them into a fuel element. This paper will discuss the potential application and processing of Ultra-High-Temperature Carbide TRISO bearing fuels.*

### I. FIRST-LEVEL HEADING

The technology for microencapsulated fuel was born as a result of nuclear reactor Project Rover that ran between 1955 and 1972. For that application uncoated or pyrolytic graphite (PyC) coated, highly enriched UC<sub>2</sub> fuel was used. While these graphite elements were coated with niobium carbide to mitigate the hot hydrogen attack of the coolant/exhaust, operation of this reactor inevitably led to release of fission products to the exhaust. This microencapsulated fuel form became the seed-technology for an international program aimed at progressively increasing the outlet temperature and plant efficiency of gas-cooled reactors. In comparison with the metallic fuel slugs that fueled the early gas-cooled reactors, a transition in fuel forms became necessary. For this reason fully ceramic microencapsulations, starting with the bistructural-isotropic (BISO) fuel, a layering of low and high-density PyC on the fissile kernel, were developed. An improvement over this semi-permeable microencapsulation was the addition of the SiC fission product barrier coating onto the BISO. For this layer chemically vapor deposited (CVD) SiC, serving as a primary pressure vessel, was applied using a fluidized bed technology over the layers of porous carbon and pyrolytic carbon surrounding the fuel kernel of the BISO, thereby containing the fission products produced. This structure, which also included an additional external pyrolytic carbon layer, became known as the Tri Structural ISotropic (TRISO-see Figure 1) fuel, simultaneously developed for the UK Dragon Reactor during its experimental High Temperature Gas-Cooled Reactor's (HTGR) operating run (1965-1976) and for an

experimental fuel campaign in the US Peach Bottom Unit 1 experimental HTGR. The Peach Bottom test fuel was a directed program for the eventual fueling of the US Fort St. Vrain Prototype power reactor that operated from 1976-1989, exclusively utilizing TRISO fuel.

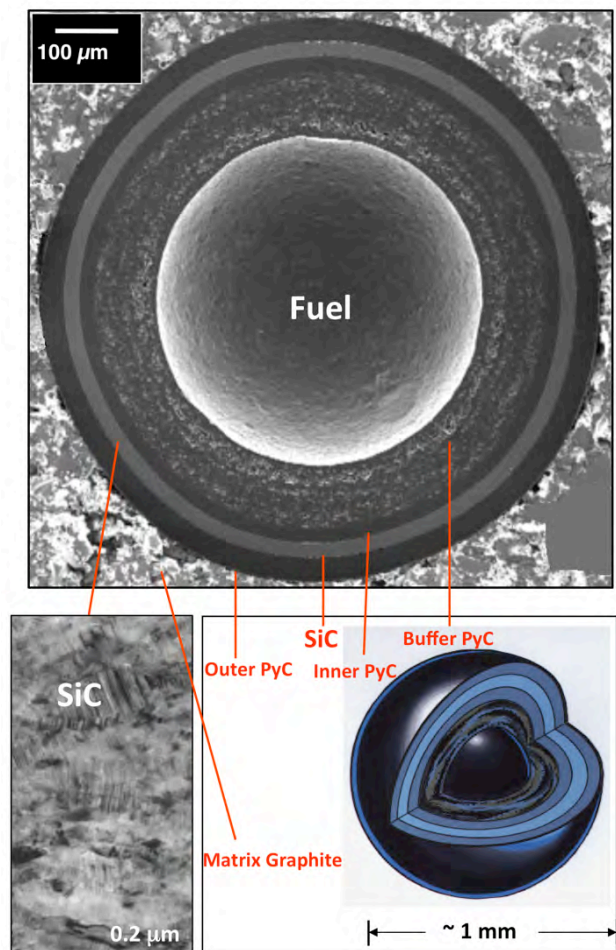


Fig. 1. Schematic describing a typical TRISO microencapsulate graphite matrix fuel.

Since these beginnings, and given a vigorous international program to understand the processing and behavior of all the constituents of TRISO fuel under irradiation, TRISO fuel with a nominally 35 micron thick CVD SiC shell has become the standard fuel for HTGR's. This application of SiC was the early and primary driver for the study of

irradiation effects in SiC in the 1970's and 1980's, which was reinvigorated by the Department of Energy Advanced Gas Cooled reactor program starting in 2002 and resulting in very high quality fuels in terms of fission product release. A summary of the historic testing and performance of TRISO fuels is provided in Figure 2a,b (per Kania [1] and Terrani [2]) with a presentation/review of the fabrication and US capabilities provided by Demkowicz. [3, 4]

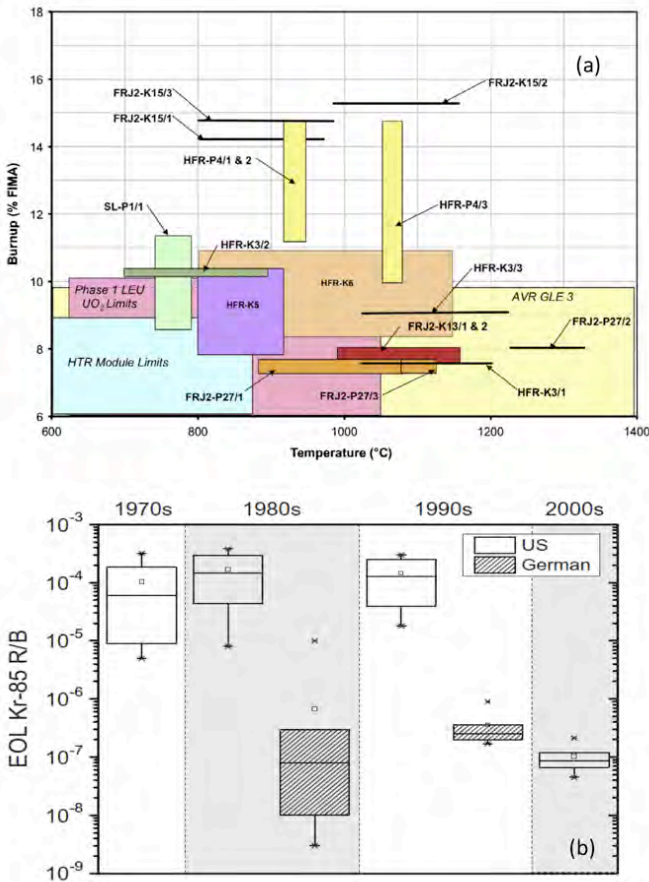


Fig. 2. (a) Summary of programs and test conditions for TRISO, (b) Comparison of fission product release of historic and modern TRISO fuel.

Two takeaways can be gained from Figure 2a. Firstly, TRISO-technology has been widely studied as a function of temperature and burnup, though the temperature range will only cover the lower range of an NTP application, which calls for a very low fuel temperature driven by the hydrogen into the core (nominal 300K) and desired temperature in excess well in excess of 2000°C near the reactor exhaust. Secondly, the fissile burnup reported for the major fuel campaigns is well in excess of that likely to be experienced by TRISO in an NTP application.

This paper addresses the potential for use of TRISO for

NTP and in particular the potential for ultra-high-temperature carbides as a replacement for the standard graphite matrix coated by NbC (or other coating).

### I.A. Fabrication of UHTC Microencapsulated Fuel

For the extreme operating temperature sought for NTP, incorporation of TRISO within an UHTC, while technically challenging, appears an obvious fuel solution. A range of UHTC materials can be considered, as outlined in Table 1 below, though some are either unattractive due to the lackluster temperature performance or their high neutron absorption.

Table 1: Potential UHTC Materials

Material	Crystal	Density (g/cm <sup>3</sup> )	Melt or Decomp. Temperature (°C)
NbN	Cubic	8.470	2573
TaN	Cubic	14.30	2700
VC	Cubic	5.77	2810
SiC	Cubic	3.21	2820
ZrN	FCC	7.29	2950
TiN	FCC	5.39	2950
TaB <sub>2</sub>	HCP	12.54	3040
TiC	Cubic	4.94	3100
TiB <sub>2</sub>	HCP	4.52	3225
ZrB <sub>2</sub>	HCP	6.10	3245
HfB <sub>2</sub>	HCP	11.19	3380
HfN	FCC	13.9	3385
ZrC	FCC	6.56	3400
NbC	Cubic	7.820	3490
TaC	Cubic	14.50	3768
HfC	FCC	12.76	3958

Table 1. Ultra-High-Temperature Carbide Materials

Of these, the most attractive materials are SiC and ZrC. The fabrication of fully-dense SiC-matrix microencapsulated fuel is an established technology [2, 5-7] and will not be discussed here other than to say that its hydrogen corrosion may be unacceptable and its potential temperature limit is not ideal for the high specific impulse desired by NTP.

A study was carried out into the potential for direct current sintering (DCS) of ZrC-matrix TRISO fuels. Zirconia surrogate TRISO were obtained in collaboration with Triso-X and a study of the sintering kinetics of a series of potential powder routes and additives was conducted. As shown in Figure 3 compacts have been successfully demonstrated by processing at a temperature in the range of 1600-1800°C at 10 MPa, a combination assumed not compromise the layered shells of the TRISO. Of note is that greater than 98% matrix density is as

measured through gas pycnometry and inferred by X-ray lattice spacing. No visible porosity is observed under X-ray tomography. Figure 4 provides an x-ray analysis of the as-processed ZrC ceramic. From this figure we can confirm the purity of the ZrC and that a slight reduction in stoichiometry, though the product remained in the desirable FCC phase. While this series of studies has identified more than one attractive consolidation method for ZrC and the preliminary results on TRISO incorporation are encouraging, the work on incorporating TRISO should be considered preliminary.

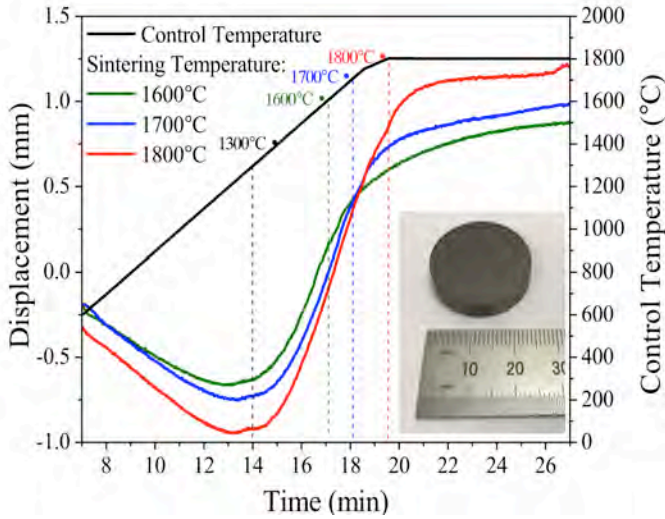


Fig. 3. Displacement and temperature ramps for by direct current sintering ZrC-matrix TRISO compacts.

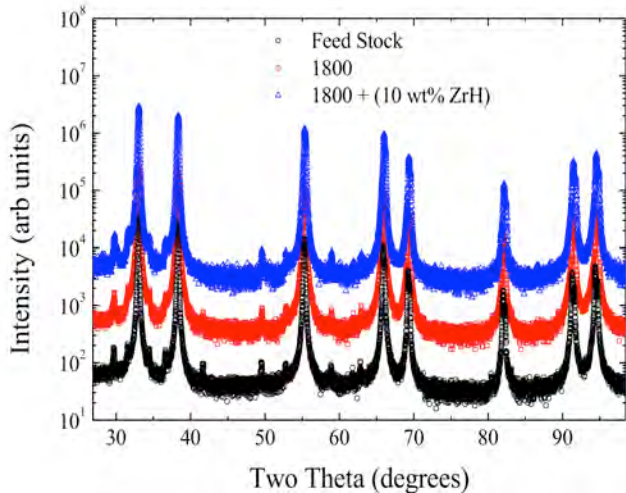


Fig 4. X-ray of monolithic ZrC.

### I.B. TRISO for Use at Very High Temperatures

For the application of TRISO in commercial high-temperature gas-cooled reactors the community, as communicated through a number of technical documents such as IAEA-TECDOC-CD-1614, April 2009, suggest

an upper operating temperature range of ~1600°C. Above 1600°C and dependent on time-at-temperature, reaction of the SiC microcapsule vessel can lead to microencapsulation failure. For this reason some advocated the replacement of SiC with ZrC, the so-called TRIZO microencapsulation. [8-10] However, as the NTP application is both of short duration and essentially insignificant burn-up (thus limited oxygen liberation by the kernel) the potential for extending the useful life of the TRISO prior to vessel failure is expected to be above the 1600°C guidance and bounded by SiC decomposition at ~2830°C. Supporting, though limited evidence for this can be found in the literature of Kania [1](see figure 3) and others[11].

As evidenced by the lower burnup curves of Figure 5 (2-3% FIMA) in these post-irradiation furnace ramp-and-hold tests significant release of <sup>85</sup>Kr does not occur until well above 2100°C. It is further noted that the suggestion of incorporation of TRISO within an UHTC as compared to the graphite (i.e. Fig 5 materials) should only serve to limit the release of fission products.

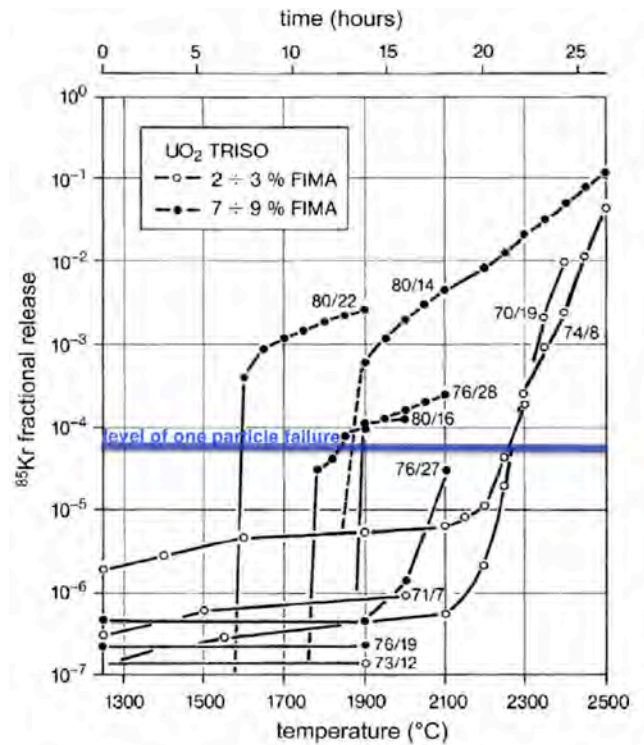


Fig. 5. Post-irradiation annealing of irradiated TRISO.[1]

As a preliminary test of the stability of standard TRISO within a ZrC matrix wafers were fabricated through DCS and reintroduced into the DCS and packed in a graphite bed and heated to 2000°C and 2250°C. Samples were held for 30 minutes, on par with an NTP fuel lifetime at power. Following annealing a number of TRISOs were inspected for signs of SiC shell degradation using X-ray tomography. Figure 6 provides a macro-image of the

ZrC-matrix TRISO fuel (upper) and a high-resolution image of a single TRISO (lower). No apparent reaction or difference in the layer structure or SiC was observed for the 2000°C and 2250°C soaks for a large number of TRISO microencapsulations visualized.

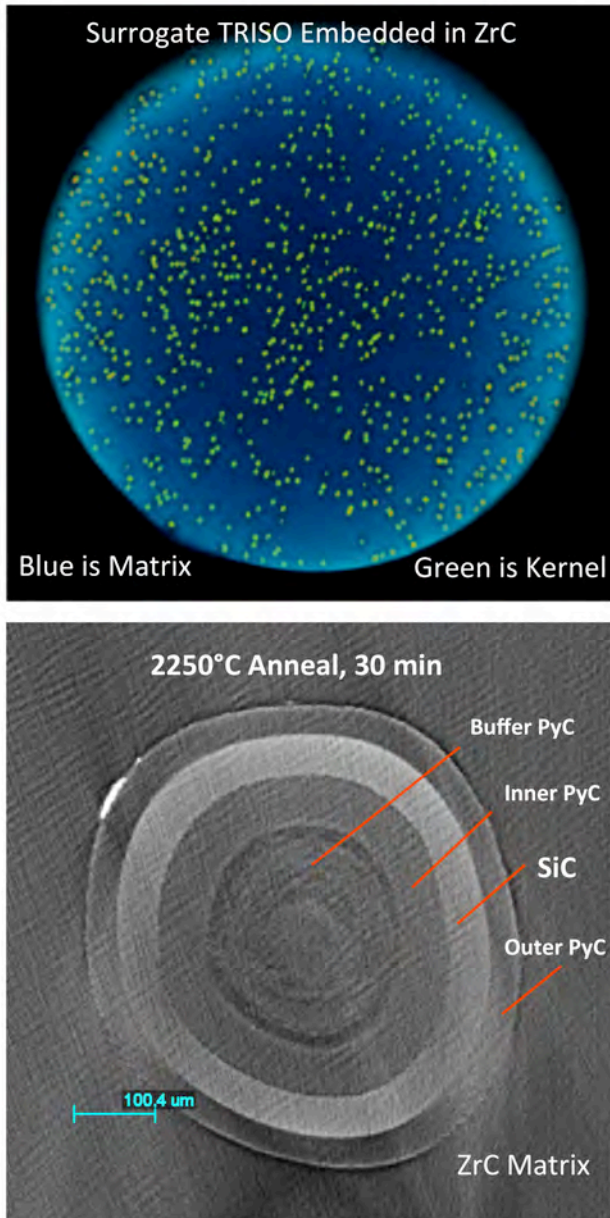


Figure 6: X-ray tomography imaging an entire ZrC-matrix TRISO compact and individual TRISO soaked at 2250°C.

## II. CONCLUSIONS

This work suggests a potential route to the processing of current, standard TRISO particles in the ultra-high-temperature carbide ZrC. Fully dense ZrC has been fabricated through direct current sintering at <1800°C and 10 MPa, consistent with processing conditions assumed

necessary for TRISO compaction. Using these processing conditions TRISO-bearing ZrC matrix samples were fabricated. These materials were then utilized for a high-temperature anneal to 2000 and 2250°C for 30 minutes. Interrogation of those SiC micropressure vessels did not reveal TRISO layer compromise.

## ACKNOWLEDGMENTS

Work pertaining ZrC densification and ZrC/TRISO processing were funded by USNC-Tech through a NASA-funded initiative. The authors would like to thank Paolo Venneri, Jason Trelewicz, and Pete Pappano for fruitful discussions and assistance.

## REFERENCES

1. Kania, M.J., et al., *Testing of HTR UO<sub>2</sub> TRISO Fuels in AVR and in Materials Test Reactors*. Journal of Nuclear Materials, 2013. **441**: p. 545-562.
2. Terrani, K.A., L.L. Snead, and J.C. Gehin, *Microencapsulated Fuel Technology for Commercial Light Water and Advanced Reactor Application*. Journal of Nuclear Materials, 2012. **427**: p. 209-224.
3. Demkowicz, P., et al., *TRISO Fuel Experience and Capabilities in the DOE Advanced Gas Reactor Program*. March 5-6, 2019: GAIN-EPRI-NEI Advanced Fuels Workshop.
4. Demkowicz, P.A., et al., *Irradiation Performance of AGR-1 High Temperature Reactor Fuel*. Nuclear Engineering and Design, 2016. **306**: p. 2-13.
5. Snead, L.L., et al., *Fully Ceramic Microencapsulated Fuels: A Transformational Technology for Present and Next Generation Reactors – Properties and Fabrication of FCM fuel*. Transaction American Nuclear Society, 2011. **104**: p. 688.
6. Snead, L., Y. Katoh, and F. Venneri, *Fully Ceramic Nuclear Fuel and Related Methods*. United States Patent No. 9,299,464 B2. March 29, 2016, UT-Battelle LLC, LOGOS Technologies LLC.
7. Snead, L.L., *Method for Fabrication of Fully Ceramic Microencapsulated Nuclear Fuel*. U.S. Patent Number 2017/0025192 A1. 2017.
8. Minato, K., T. Ogawa, and K. Fukuda, *Review of experimental studies of zirconium carbide coated fuel particles for high temperature gas cooled reactors*. JAERI-Review 95-004. 1995.
9. Minato, K., et al., *Fission Product Release from ZrC-Coated Fuel Particles During Postirradiation Heating at 1600°C*. Journal of Nuclear Materials, 1995. **224**(85).
11. Goodin, D.T., *Accident Condition Performance of Fuels for High-Temperature Gas-Cooled Reactors*. J. Am. Cer. Soc. **65**(5): p. 238-242.

**MAGNESIUM OXIDE FOR COMPOSITE MODERATORS AND TRISO FUEL MATRICES**

D. J. Sprouster<sup>1</sup>, L. L. Snead<sup>1</sup>, C. Ang<sup>2</sup>, N. Brown<sup>2</sup>, E. Duchnowski<sup>2</sup>, and J. R. Trelewicz<sup>1</sup>

<sup>1</sup>Engineering Drive, Stony Brook University, Stony Brook, NY 11794  
<sup>2</sup>1412 Circle Drive, University of Tennessee, TN, 37996

Primary Author Contact Information: David Sprouster, 631-2948983

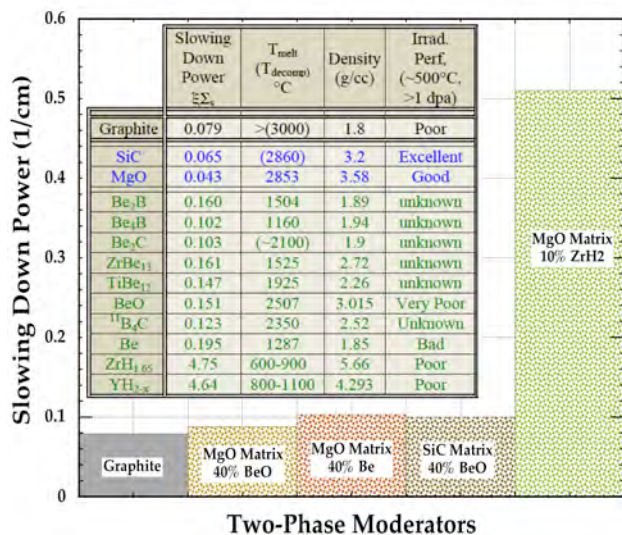
*In this work, we describe the advanced processing and fabrication of monolithic MgO through direct current sintering. Through a unique combination of sintering aid and the Direct Current Sintering technique a significant beneficial shift in processing windows has occurred, allowing combinations of new composite materials. In particular highly moderating MgO-based composites and MgO-TRISO fuels have been demonstrated.*

**I. Introduction**

Following its initial development as a moderator for the Chicago Pile, graphite became the first and arguably most studied nuclear material[1]. Today, a number of gas-cooled systems (prismatic or pebble-bed) and salt-cooled systems assume large graphite core loadings. We have recently proposed a simple two-phase composite design as an enhanced-moderating replacement to graphite, MgO as the primary (host) phase, and Be, ZrH or BeO as the second entrained phase. The motivation for such a moderator is found in inspection of Figure 1, which provides the matrix neutron slowing down power of matrix (blue) and entrained phases (green), which are combined to make the composite moderator. The combined slowing down power for candidate composite moderators are also shown in Figure 1, all being somewhat superior to graphite.

These material combinations, in addition to being exceptional moderators for high temperature gas reactors, have been used historically in the Aircraft Reactor Experiment (ARE) and the Heat Transfer Reactor Experiment No. 3 (HTRE-3). Moreover, they have potential applications as moderators for space power due to their excellent irradiation tolerance, chemical stability [2-3] and ease of processing. At a high level, the impact of these materials on miniaturization of thermal systems is provided in Figure 2, providing the critical radius of a gas-cooled prismatic block system for varied moderator to fuel ratio calculated from critical buckling which is a metric of minimum reactor size that incorporates neutron leakage and their cycle performance and natural resource requirements shown in Table 1 for a 3-batch loading scheme. The optimal moderator to fuel ratio is at the minimum critical radius for each case shown. It is shown that systems employing hydride and beryllium based moderators have very substantial radius reductions and have the potential for an increased reactor cycle length as compared to the graphite case. In addition, through application of the same MgO processing technology, further improvement may be realized by incorporation of TRISO into an MgO-TRISO fuel form.

**Table. 1:** Calculated discharge burnup and natural resource utilization 3-batch loading scheme.



	Graph.	MgO 0.4BeO	MgO 0.4 Be	MgO 0.2 ZrH
3-Batch Discharge Burnup [MW-d/kgU]	123.5	126.2	144.1	149.5
3-Batch Natural Resource Utilization [t/GWe-y]	195.5	191.4	167.6	161.5

**Fig. 1:** Slowing down power of composite constituents and composite moderators.

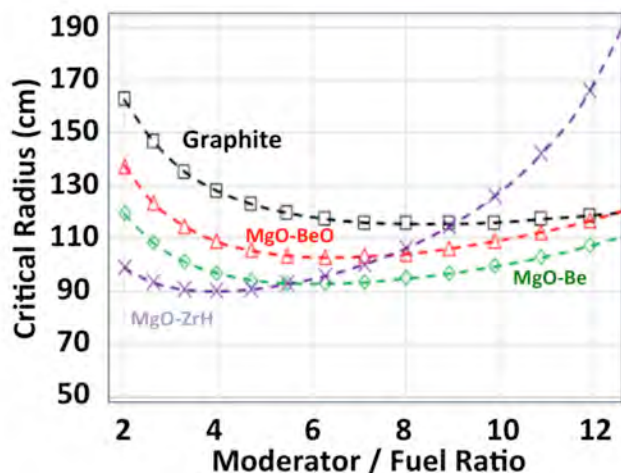


Fig. 2: Critical core radius of prismatic block gas reactor.

The development of these advanced MgO composites for nuclear and space applications begins with an in-depth understanding of the sintering and processing behavior of MgO powder. MgO can be effectively processed via rapid sintering techniques (direct current sintering (DCS), otherwise known as spark plasma sintering) to very high densities (over 99% theoretical density) though at relatively high temperatures:  $\sim 1400^{\circ}\text{C}$  for undoped MgO and  $\sim 1100^{\circ}\text{C}$  for doped powders. DCS is an advanced material sintering technique, which uses a direct electric current pulse to heat a powder filled graphite die under a uniaxial compressive loading. Due to the Joule heating and constant external pressure, the powder materials can be sintered to a full density within a short time period. The DCS technique is a highly efficient ceramic sintering method, which has many advantages over traditional sintering technique, such as fast heating rates, short sintering time and energy-efficient processes, and potential industrial scalability. However, from a mass production standpoint more conventional techniques such as hot-pressing or isostatic press-and-sinter would be equally effective at achieving matrix densification.

Here we report on recent progress showing that efficient sintering to above 99% theoretical density is possible in MgO with Li-based sintering dopants. Additionally, and more importantly, we have shown that we can effectively suppress the processing temperature of MgO by over  $300^{\circ}\text{C}$ , allowing fabrication of a range of moderator and fuel forms. We speculate that the Li dopants form a eutectic phase with the MgO, which in turn enhances surface diffusion and sintering [4,5]. Representative moderator and fuel forms are presented.

## II. Experimental Description

The DCS machines used in this work was a LABOX systems manufactured by Sinter Land®. Inc. (housed at Stony Brook University and UT-Knoxville). The MgO

and MgO+LiF powders (1 wt% LiF) were cold pressed into graphite dies. The cold-pressed green bodies had densities  $\sim 54\%$  theoretical density of MgO ( $3.58\text{g}/\text{cm}^3$ ). Each graphite die assembly was then loaded into the DCS chamber. To ensure the conductivity, the assemblies were placed under low pressures during the sintering. Powder mixtures were subject to a heating cycle of  $100^{\circ}\text{C}/\text{min}$ . The whole sintering process including heating, peak temperature holding/cooling, took  $\sim 1$  hr. Composite materials containing  $\text{ZrH}_2$  were DCS-processed in an H environment.

The density of sintered compacts prepared in this work were quantified using the Archimedes method. X-ray diffraction (XRD) was used to identify the crystallographic phase evolution with processing parameters. The internal microstructure was visualized and quantified with x-ray computed tomography with a Zeiss Xradia microscope.

## III. Results and Discussion

The in situ displacement curves during sintering of pure MgO and LiF doped MgO are shown in the Figure 3. The densification process (the increase in displacement) of pure MgO powder starts at  $<1000^{\circ}\text{C}$  and is complete at  $\sim 1300^{\circ}\text{C}$ . The ultimate displacement of the pure MgO powder was  $\sim 2.5$  mm. The MgO+LiF powder started sintering at  $700^{\circ}\text{C}$ ,  $300^{\circ}\text{C}$  lower than the pure MgO powder and densification was complete at  $1000^{\circ}\text{C}$ . The peak displacement of the MgO+LiF was  $\sim 2.75$  mm.

After this initial demonstration of the enhanced sintering of MgO with LiF, a systematic study of the effects of sintering temperature (ranging from  $800^{\circ}\text{C}$  to  $1000^{\circ}\text{C}$ ) and pressure (10, 15 and 20 MPa) on the resulting density were examined for the MgO+LiF and other Li-bearing salt powder mixtures. Figure 4 shows the effects of sintering temperature and pressure on the monolithic compact density from this systematic study. The specimens sintered at 10 MPa and 15 MPa have similar densities while specimens sintered at 20 MPa have slightly higher densities. Interestingly, for all applied pressures, sintering of the monolith to  $\sim 99\%$  density (theoretical density) is achievable at  $850^{\circ}\text{C}$ .

XRD patterns for the monolithic MgO specimens fabricated at  $900^{\circ}\text{C}$ ,  $1000^{\circ}\text{C}$ , and  $1100^{\circ}\text{C}$  with 10MPa pressure are shown in Figure 5 (with reference LiF feedstock). In addition to the MgO phase, there are multiple phases from trace impurities. The green diamond makers label the impurities peaks from the MgO feedstock powder. These peaks do not appear to change with increasing sintering temperature. The blue squares in Figure 5 highlight that after sintering LiF does not completely evaporate from the specimens. For increasing sintering temperature, however, the LiF peaks do appear to slightly decrease in intensity (LiF peaks have almost completely disappeared at  $1100^{\circ}\text{C}$ ) suggestive that the LiF

requires higher temperatures or longer times to completely be removed from the monoliths (SEM/EDS also confirm the lower LiF contents with higher sintering temperatures). This was confirmed with a 2 hr anneal at 1000°C.

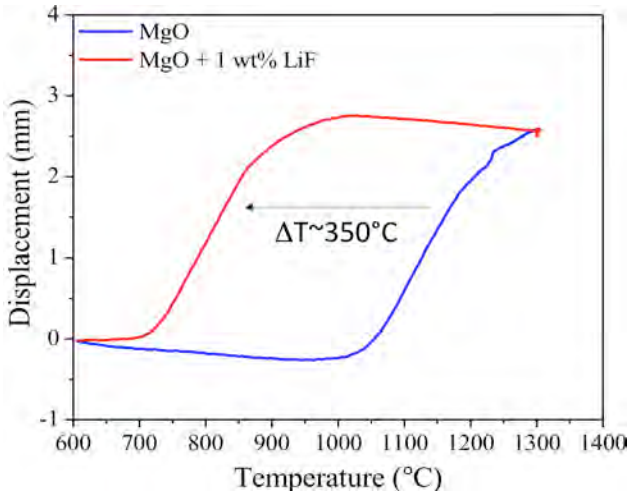


**Figure 3. Displacement curves of pure MgO powder (blue) and MgO powder with 1 wt% LiF additive (red) as a function of temperature recorded during the DCS sintering at 1300 °C under 30 MPa pressure.**

The reduction in sintering temperature, low impurity content and low porosity is highly beneficial for MgO particularly for space and nuclear applications and entraining the second phases of Be, BeO and ZrH. Reducing the sintering temperature below the melting and phase transformation temperatures can improve the successful encapsulation and limit the formation of toxic vapors and unwanted crystal phases during processing. The physical mechanism for this impressive shift in the sintering temperature window is, at the present time unknown. We speculate that the Lithium dopants form a eutectic phase with the MgO which enhances surface diffusion and sintering. The object of future work is to directly uncover the phase evolution of Li-doped MgO, in situ, using synchrotron-based XRD experiments to capture the atomic evolution while sintering MgO powder mixtures and shed light on the crystallographic phase evolution with Lithium dopants.

With the depressed sintering temperature for MgO (Fig 3) the potential for incorporating a wide range of beryllium-containing materials, including metallic beryllium, was made possible. A program of MgO-BeX development was undertaken with focus on Be-metal and BeO. Additional work is ongoing with respect to Be<sub>2</sub>C. Boride containing beryllides, while assumed similar in processing behavior to BeO, were not pursued. Additionally, through the introduction of hydrogen into the DCS cover gas an approximate 250°C increase in the

effective ZrH<sub>2</sub> processing temperature was achieved (through retardation of the dehydriding.)

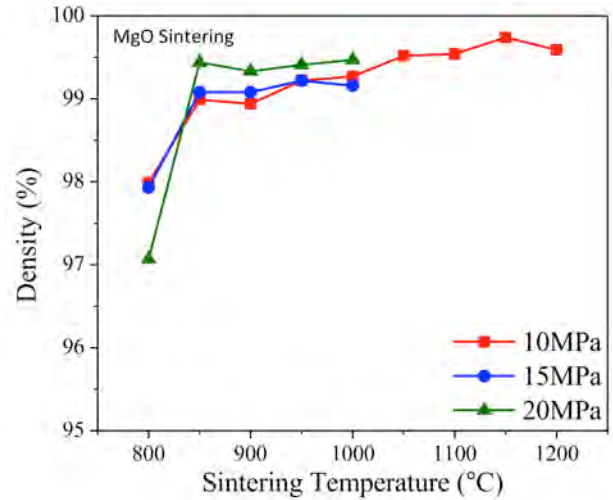


**Figure 4. The density as a function of sintering temperature for the MgO sintered using 10 MPa, 15 MPa and 20 MPa sintering pressure.**

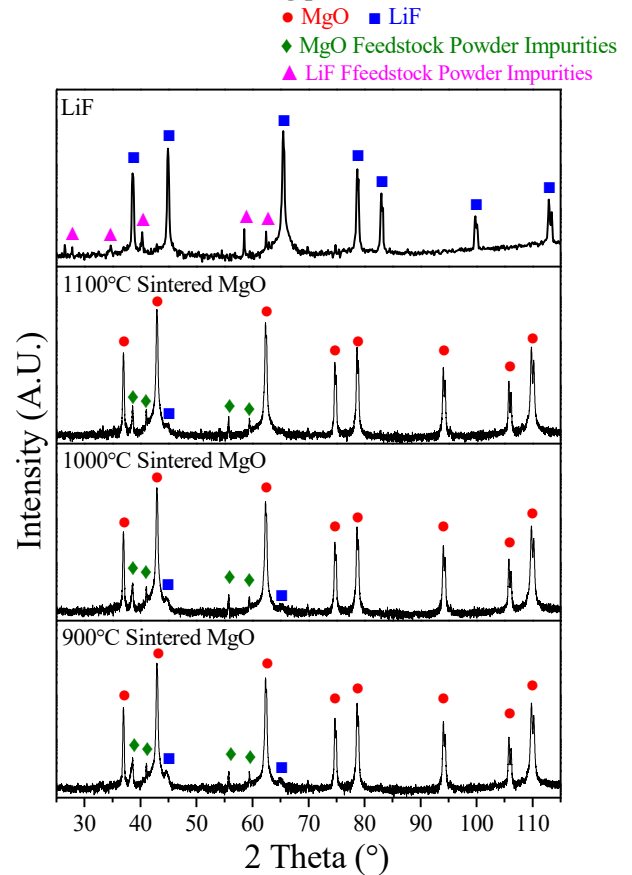


**Figure 5. X-ray diffraction patterns of the LiF powder, 900°C, 1000°C and 1100°C sintered MgO samples. The intensity is displayed on a log-scale.**

Figure 6 provides tomography images taken in the center of as-sintered composites of the MgO-beryllium materials and MgO-ZrH<sub>2</sub> materials processed. Of note is that these microstructures indicate a relatively homogeneous distribution of entrained phase within the MgO and only limited flattening of the entrained phase. Moreover, x-ray analysis indicate that an acceptable loss of hydrogen occurs during processing, resulting in the desirable  $\delta$ -Phase ZrH<sub>-1.6</sub>.

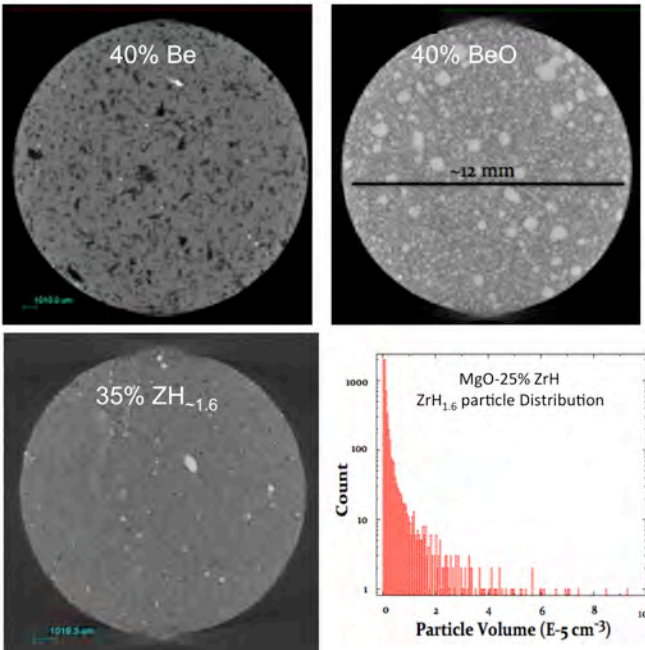


Fig. 6: Tomography Images of two-phase moderators with particle distribution of entrained hydride.

In addition to the beryllide and hydride MgO composite moderators, the same technology for MgO sintering was used for the compaction of MgO-TRISO and MgO-BISO (surrogate) compacts. Surrogate microencapsulations were provided by TRISO-X. Figure 7 provides a tomography image of these “fuels”. The left figure provides the a cross section of the sample with the light green/orange dots being the contrast images of the zirconia kernel of the BISO fuel. On the right is a higher magnification image of the MgO/BISO compact. Below that image is an even higher magnification image of the surrogate TRISO with the individual layers distinct. Of note in this figure is that full density matrix was achieved during the 10 MPa compaction without disruption of the SiC shell of the TRISO.

#### IV Conclusion

This work suggests a potential route to significantly reduce the processing window of MgO for advanced nuclear reactor technology. Low-temperature processing for MgO has been effectively demonstrated using a dilute amount of LiF dopant. That MgO is both full density and

of good strength. The massive reduction in sintering temperature, uniform morphology, lack of porosity and minute traces of impurity phases opens up potential opportunities for MgO in space and nuclear applications.

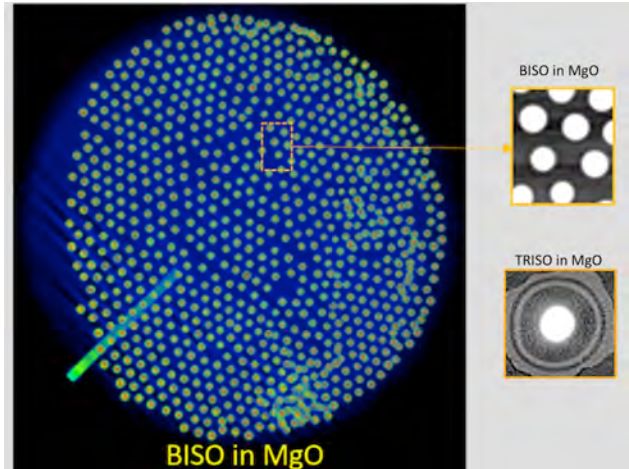


Figure 7: BISO and TRISO compacted within MgO

#### ACKNOWLEDGMENTS

We acknowledge the excellent work of Dr. B. Cheng supporting the processing and characterization. Additionally we would like to thank Dr. Pete Pappano of TRISO-X/X-energy for providing the microencapsulations. This work was funded by the Advanced Research Projects Agency-Energy (ARPA-E) program: Modeling-Enhanced Innovations Trailblazing Nuclear Energy Reinvigoration (MEITNER) under contract DE-AR0000977

#### REFERENCES

1. B. J. Marsden, “Irradiation damage in graphite due to fast neutrons in fission and fusion systems”, Report No. IAEATECDCDOC-1154, 2000
2. M.C.R. Heijna, et al. “Material Property Changes to HTR Graphite Grades Irradiated Between 650°C and 950°C, International Nuclear Graphite Specialists Meeting”, INGS-13. Meitingen Germany. (2012).
3. F.W. Clinard, et al. Journal of Nuclear Materials 108&109, 655, (1982).
4. N. Jiang, et al. “Fabrication of sub-micrometer MgO transparent ceramics by spark plasma sintering”, Journal of the European Ceramic Society 37 (2017) 4947-4953.
5. S. Meir, S. Kalabukhov, N. Froumin, M.P. Dariel, N. Frage. “Synthesis and Densification of Transparent Magnesium Aluminate Spinel by SPS Processing”, Journal of the American Ceramic Society 92 (2009) 358-364.

## NUCLEAR THERMAL PROPULSION SUBSCALE EXPERIMENTAL TESTBED FOR MATERIAL INVESTIGATIONS USING THE OHIO STATE UNIVERSITY RESEARCH REACTOR

Tyler R. Steiner<sup>1,2</sup>, Richard H. Howard<sup>1,2</sup>, N. Dianne Bull Ezell<sup>2</sup>, Emily N. Hutchins<sup>1,2</sup>, and C. Miller McSwain<sup>1</sup>

<sup>1</sup>University of Tennessee, Knoxville, Department of Nuclear Engineering, TN, 37996

<sup>2</sup>Reactor and Nuclear Systems Division, Oak Ridge National Laboratory, Oak Ridge, TN, 37830

Primary Author Contact Information: [tsteine1@vols.utk.edu](mailto:tsteine1@vols.utk.edu)

Nuclear thermal propulsion (NTP) has demonstrated a technology readiness level of 5 during the work performed in the 1950s-1970s under the Rover program. This level of capability was achieved through the design, construction, and use of 22 experimental rocket reactors. These experiments served as testbeds for designs, materials, and instrumentation at prototypical NTP conditions. It is of the opinion of the author that there are three primary challenges pertaining to the NTP environment: temperature, neutron and gamma fluence, and hydrogen (propellant) flow. To continue the investigation into NTP system materials, components and fuels, a modern experimental testbed has been designed and implemented. Using the In-Pile Experiment Set Apparatus, developed by Oak Ridge National Laboratory, in conjunction with the Ohio State University Research Reactor, candidate subscale fuel samples have been tested under two of the three NTP prototypical environmental factors: temperature and fluence. The experiment is presented here.

### I. INTRODUCTION & BACKGROUND

Nuclear thermal propulsion utilizes the thermal energy produced by a nuclear reactor to superheat a working propellant – usually hydrogen. The superheated propellant leaving the reactor core is expanded through a supersonic nozzle to generate thrust.<sup>2</sup> Using hydrogen as the working fluid enables the NTP system to reach specific impulse values nearly twice that of conventional chemical rockets used for crewed space flight.<sup>2</sup> Solid core NTP specific impulse values of 900 seconds can correspond to a crewed Mars mission duration of around 500 days. Whereas chemical rocket specific impulse values of 450 seconds delay a crewed Mars mission duration to around 900 days (Ref. 2). A longer flight time will expose the crew onboard to more space radiation, which will put them at a higher risk of radiation induced health effects.

The extreme environment that enables NTP systems to achieve a high specific impulse is one that has been challenging scientists and engineers for decades. The superheated propellant can reach exhaust temperatures up to 3000 K (Ref. 2). During a proposed 500 day mission to Mars, the reactor core will produce a neutron fluence of

roughly  $10^{17}$  neutrons/cm<sup>2</sup> (Ref. 3). Additionally, the propellant of interest is hydrogen, which can react with system components at such high temperatures. The high temperature, fluence, and use of hydrogen in nuclear thermal rockets (NTRs) poses a challenge when selecting fuel candidates and instrumentation meant to withstand the NTP environment.

One approach to addressing the aforementioned challenges is the implementation of experimental testing under prototypical conditions. The Rover program ran from 1955 until 1972 and ground tested over twenty nuclear rocket reactors at various conditions to simulate NTRs.<sup>4</sup> A chronology of these tests is shown in Figure 1.

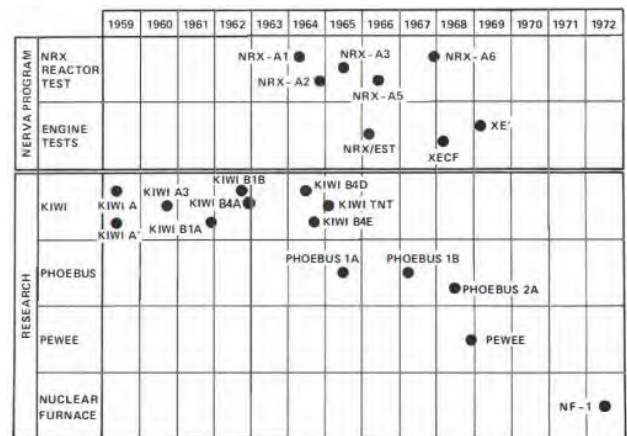


**Fig. 1.** Chronology of Rover rocket reactor tests.<sup>5</sup>

The Rover program tests demonstrated a thrust level of 930 kN (PHOEBUS-2A), a hydrogen flow rate of 120 kg/s (PHOEBUS-2A), an equivalent specific impulse of 845 seconds (PEWEE), a peak fuel temperature of 2750 K (PEWEE), among several other accolades.<sup>5</sup>

Following the termination of the Rover program, the Space Nuclear Thermal Propulsion (SNTTP) program ran from 1987 until 1992. The SNTTP program partially sought to continue the NTP testing from the Rover program, albeit with a new particle bed reactor design. However, the nuclear surface testing infrastructure from the Rover program was deemed unsuitable for use due to environmental health and safety concerns.<sup>6</sup>

Modern NTP testing is supported by several experimental apparatus under NASA's Advanced

Exploration Systems (AES) NTP project.<sup>7</sup> Two well established testing facilities under this project are the Nuclear Thermal Rocket Element Environmental Simulator (NTREES) and the Compact Fuel Element Environmental Test (CFEET). NTREES can simulate the thermal hydraulic conditions within an NTR fuel element, but it cannot demonstrate NTP fluence levels. NTREES can reach temperatures of 3000 K, flowing hydrogen pressures of 7 MPa, and near-prototypical reactor channel power densities.<sup>7</sup> CFEET is used for subscale, non-nuclear fuel element testing in stagnant hydrogen at prototypical temperatures. NTREES and CFEET both use radio frequency induction heating.

The current established capabilities under the AES NTP project do not satisfy the three primary challenges posed by the NTP environment – temperature, fluence, and hydrogen flow. CFEET and NTREES only simulate the temperature and hydrogen flow. To complement the existing capabilities, an experimental testbed has been developed to achieve subscale NTP temperature and fluence.

## II. EXPERIMENTAL SETUP

The Oak Ridge National Laboratory (ORNL) has developed the In-Pile Experiment Set Apparatus (INSET) to reach prototypical NTP temperatures in a vessel suitable for introduction to a nuclear reactor.

The Ohio State University Research Reactor (OSURR) was selected as the first reactor to irradiate INSET due to its flux levels and accessibility. The cooperation between ORNL and OSURR has enabled the experimental testing of candidate NTP material samples at desired temperatures and prototypical NTP fluence levels.

The first specimens that were tested using INSET and OSURR were developed by graduate researchers with the University of Tennessee, Knoxville. The material specimens consisted of molybdenum formed by three different production methods in addition to a molybdenum-zirconium cermet. The specimens were cylindrical with a diameter of 3 mm and a thickness of 1 mm. This work specifically intends to investigate irradiation damage of cermet fuel candidates for use in NTP systems. To minimize the annealing in the specimens, the experiment maintained a temperature below 1070 K (Ref. 8).

INSET provides the experimental capability to test candidate fuel materials as well as instrumentation under prototypical NTP conditions.

### II.A. In-Pile Experiment Set Apparatus

INSET is cylindrical, roughly 60 cm tall, and 25 cm in diameter. Figure 2 shows INSET instrumented prior to its irradiation at OSURR. An introduction to INSET is presented here, but a detailed account can also be found in the NETS 2020 conference proceedings, titled: DESIGN OF THE IN-PILE EXPERIMENT SET (INSET) APPARATUS TO SUPPORT NUCLEAR THERMAL PROPULSION FUEL AND COMPONENT TESTING.



Fig. 2. INSET at OSURR.

The structural components of INSET are made from 6061 aluminum. Aluminum was chosen over traditional stainless steel to limit the apparatus's activation. Although aluminum presents manufacturing challenges, it produces fewer and less intense radioactive isotopes following irradiation from a reactor than stainless steel.

INSET is designed to reach prototypical NTP temperatures while permitting for the apparatus's introduction to a reactor environment. INSET uses electrical resistive heating to generate temperatures reaching 2500 K in a vacuum environment.

The first irradiation using INSET and the OSURR implemented two C-type thermocouples and one K-type thermocouple. The two C-type thermocouples were both placed within the heater to redundantly measure the generated temperature. The K-type thermocouple was

used to monitor the external surface temperature of INSET to ensure the heat generated would not influence reactor operation (i.e. moderator boiling). INSET offers the freedom to be instrumented with up to six thermocouples. Each thermocouple mounts to a 3.38 cm ConFlat® thermocouple vacuum passthrough. Each of the three passthroughs may be alternately instrumented if thermocouples are not the desired instrumentation.

A detailed thermal model of INSET has been developed to provide additional confidence to the redundancy provided by the thermocouples. The computational model was produced using the ANSYS thermal radiation environment. The ANSYS model and the INSET experiment have shown strong agreement.

### II.B. The Ohio State University Research Reactor

The Ohio State University Research Reactor was chosen to provide the prototypical NTP fluence due to its flux and ease of access.

Prior to the irradiation, a detailed neutron activation analysis was conducted to predict the earliest safe shipping date. This analysis can also be found in the NETS 2020 conference proceedings by the University of Tennessee, Knoxville’s Emily Hutchins, titled: ACTIVATION ANALYSIS OF SUBSCALE EXPERIMENTAL TESTBED: TOWARDS SIMULATING NUCLEAR THERMAL PROPULSION PROTOTYPIC CONDITIONS FOR MATERIAL TESTING.

At 450 kW the OSURR can generate a total neutron flux up to roughly  $1.3 \times 10^{12}$  n/cm<sup>2</sup>/s at the ex-core 9.5 in. vertical dry tube. At this location, the maximum thermal neutron flux is  $8.7 \times 10^{11}$  n/cm<sup>2</sup>/s. This is the dry tube that was used in the experiment to house INSET. During the experiment, the reactor was operated at roughly 250 kW (Ref. 9).

The reactor was operated for 5 hours to achieve a prototypical NTP fluence of roughly  $10^{17}$  n/cm<sup>2</sup>. The reactor power sequence can be seen in Figure 3 in addition to the reactor’s influence on heating the thermocouples.

### III. RESULTS & CONCLUSIONS

The performed experiment sought to test NTP candidate materials at relevant NTP temperature and fluence levels. The results from the experiment, as produced from data using two redundant C-type thermocouples in the heater and one external K-type thermocouple can be seen in Figure 3. The OSURR is a well understood and instrumented facility, enabling high confidence that prototypical fluence levels were achieved.

Figure 3 shows the temperature of three thermocouples during the irradiation of INSET. The blue curve (“Surface TC” or top curve) corresponds to the

vertical axis on the right and the external K-type thermocouple. The red curve (“Crucible TC2”) corresponds to left vertical axis and one of the C-type thermocouples in the heater. The black curve (“Crucible TC1”) also corresponds to left vertical axis and the other C-type thermocouple in the heater. The horizontal axis shows the time formatted as “hour:minute:second.” The shaded region around 12:14 shows the electrical heating of INSET (12:02 – 12:18). For this experiment, the supplied electrical power was increased to around 40 W over roughly 5 minutes and held at 40 W for about 10 minutes. This generated the temperature values shown in Figure 3. The reactor was powered on at 8:07 and powered off at 13:07, resulting in a 5 hour irradiation.

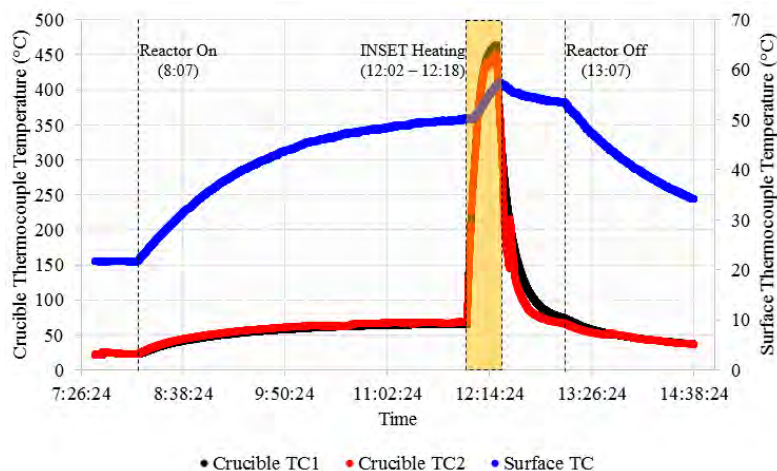


Fig. 3. INSET November 2019 thermocouple data.

The redundant thermocouples show a maximum temperature achieved around 730 K (455 °C). These thermocouples are located a few millimeters from the centerline. The ANSYS model and benchtop testing show that there is a roughly 250 K difference between the centerline and the thermocouple location. Accounting for this difference, the peak temperature achieved by INSET during this experiment is around 980 K, which is safely below the noted annealing limit of 1070 K mentioned earlier.

The K-type thermocouple was implemented to ensure minimal temperature-related impacts on the reactor. The maximum temperature recorded by the external K-type thermocouple was around 330 K (57 °C), which is well below the boiling point of the moderator.

It is suspected that the thermocouple-recorded temperatures began to rise with the reactor’s startup because of radiation induced heating effects. The neutron and gamma heating of the thermocouples will need to be further explored to be well-quantified. Benchtop testing, thermal models, and the distinct change in the shape of the curves when the electrical heating is applied offer

evidence that the electrical heating is still generating heater temperatures around 980 K.

It is also suspected that the discontinuity seen in Crucible TC2 around 12:28 is the result of thermal expansion effects. This jump discontinuity is an immediate 70 K spike followed by 4 minutes of continually declining temperature readings until the trend is resumed at 419 K (146 °C). During this cooling period, it is likely that components shift under thermally induced stresses and deformations. It is possible that the thermocouple came into contact with the internal wall of the crucible during the cooling period. This discontinuity does not warrant substantial concern as it is not seen in Crucible TC1 and since the cooling trend resumes after a short time.

#### IV. FUTURE WORK

At the time of this writing, no post irradiation examination (PIE) has been performed on the material samples or the experimental apparatus. Once the apparatus reaches safe levels of radioactivity, it will be removed and shipped to ORNL for post irradiation examination. The PIE results will be made public upon their acquisition and processing.

Relevant future work includes the ongoing development of INSET. This development will focus on reliably and more efficiently generating the maximum temperatures seen in an NTP system (3000 K). More robust instrumentation will also be explored to provide data at more locations within the apparatus. Long-term INSET development work may include the ability to introduce flowing hydrogen into the heater region.

In addition to continuing to improve INSET, the thermal model will also be improved. Various thermal modelling programs and methods will be implemented to provide a robust computational testing environment and predictive tool.

INSET will continue to serve as a testbed for NTP related interests. It is planned that INSET will be irradiated quarterly, providing ample testing opportunities.

#### ACKNOWLEDGEMENTS

The authors would like to acknowledge the National Aeronautics and Space Administration, who funded this work.

We would like to acknowledge Dr. Thomas J. Harrison of the Oak Ridge National Laboratory for securing the funding for this work as well as for his relevant insight.

We would like to acknowledge the support of The Ohio State University Nuclear Reactor Laboratory and the assistance of the reactor staff members Andrew Kauffman, Kevin Herminghuysen, and Ohio

State University doctoral candidate Neil Taylor for the irradiation services provided.

We would like to acknowledge Neal Gaffin, a doctoral student at the University of Tennessee, Knoxville, for providing the material samples that were tested during the experiment.

Tyler Steiner would like to acknowledge Dr. Lawrence Heilbronn of the University of Tennessee, Knoxville for his mentoring and experimental insight.

#### REFERENCES

- [1] H. Gerrish Jr., *Nuclear Thermal Propulsion Ground Test History: The Rover/NERVA Program*, NASA Marshall Space Flight Center, 2014.
- [2] S. Borowki, D. McCurdy and T. Packard, "Nuclear Thermal Propulsion (NTP): A Proven Growth Technology for Human NEO / Mars Exploration Missions," *IEEE Aerospace Conference*, pp. 1-20, 2012.
- [3] M. King and M. Houts, "Sensor Needs for Nuclear Thermal Propulsion," in *IEEE Wireless for Space and Extreme Environments*, 2018.
- [4] J. Finseth, "Overview of Rover Engine Test," NASA Marshall Space Flight Center, 1991.
- [5] D. Koenig, "Experience Gained from the Space Nuclear Rocket Program (ROVER)," Los Alamos National Laboratory, 1986.
- [6] R. Haslett, "Space Nuclear Thermal Propulsion Program Final Report," Grumman Aerospace Corporation, 1995.
- [7] M. Houts, D. Mitchell, T. Kim, W. Emrich, R. Hickman, H. Gerrish, G. Doughty, A. Belvin, S. Clement, S. Borowski, J. Scott and K. Power, "The NASA Advanced Exploration Systems Nuclear Thermal Propulsion Project," in *51st AIAA/SAE/ASEE Joint Propulsion Conference*, 2015.
- [8] N. Gaffin, S. Zinkle and K. Benensky, "REVIEW OF IRRADIATION HARDENING AND EMBRITTLEMENT EFFECTS IN REFRACTORY METALS RELEVANT TO NUCLEAR THERMAL PROPULSION APPLICATIONS," in *Nuclear and Emerging Technologies for Space*, 2019.
- [9] "Nuclear Reactor Laboratory," Ohio State University College of Engineering, 2019. [Online]. Available: <https://reactor.osu.edu/>.

## DESIGN OF A RADIATION SHIELD FOR A LOW-ENRICHED URANIUM SPACE NUCLEAR REACTOR

Aaron Unger<sup>1</sup>, Ian Wilkinson<sup>1</sup>, Jessica Berry<sup>1</sup>, Haley Eley<sup>1</sup>, and Jeffrey King<sup>1</sup>

<sup>1</sup> Colorado School of Mines, 1500 Illinois St, Golden, CO 80401

[aunger@mines.edu](mailto:aunger@mines.edu)

### I. INTRODUCTION

The growing interest in high power-consumption space technologies with long operating lifetimes has motivated a burgeoning interest in space nuclear fission power systems. These power sources have historically been designed to use highly enriched uranium (HEU) to create high power density energy for long term operations.<sup>1,3</sup> However, there is a growing desire in the non-proliferation community to use low-enriched uranium for new space fission reactor designs. Thus, it is of interest to both the space fission power and non-proliferation communities to study the feasibility of a space fission system fueled by low enriched uranium (LEU). The Colorado School of Mines Nuclear Reactor Design team is conducting a study of the efficacy of an LEU fueled space nuclear power system compared to a like-designed HEU system, as part of the 2019-2020 reactor design class.

The proposed design consists of an HT-9 clad uranium nitride fuel matrix, zirconium hydride moderator, and metallic beryllium reflector. The core is designed to produce 250 kW<sub>e</sub> of power over a 10-15 year lifespan by Stirling energy conversion and is cooled by NaK eutectic. A radiation shield has been developed to minimize radiation damage to critical electronic components and the payload. The shield, located between the reactor core and payload, attenuates impinging neutrons and gamma rays to provide a “shadow” of radiation protection behind the core.

Appropriate radiation shielding for the payload is crucial to the success of a space nuclear fission power system, as ionizing radiation poses a significant threat to critical payload components.<sup>4,5</sup> The shielding challenge is unique to space fission power compared to other methods of space power production because the reactor core generates a high flux of neutrons and gamma rays that are capable of penetrating deeply through materials and damaging sensitive electronics. Telecommunications devices and semiconductor crystals consisting of silicon are particularly sensitive, as they contain materials that are prone to radiation damage by introduction of defects in their crystal lattices.<sup>1</sup> Thus, it is necessary to shield the payload components from the reactor core’s neutron and photon flux to levels at which the ionizing radiation no longer imposes a significant threat.

### II. BACKGROUND

Galactic cosmic rays in near-Earth space can impose dose rates of approximately 30 mrad per day on small silicon sphere and slab detectors. However, over a 10-year

lifespan, these values result in total doses of approximately 100 krad which is significantly less than the thousands of Mrad that may be imposed by an unshielded reactor.<sup>6</sup> As a result, the dose requirements and results presented in this report will be related only to the dose imposed by the nuclear reactor itself and cosmic background radiation will be neglected. Furthermore, a shadow shield geometry will be employed to minimize mass by shielding the payload in a “shadow” region behind the reactor’s core.<sup>1</sup>

Neutron attenuation can be maximized through one of two routes. The first is through the use of neutron absorbing materials such as boron that reduce the overall neutron population.<sup>1,7</sup> However, this results in heating effects in the shield, which may cause further complications.<sup>5</sup> The second, and more commonly used, route incurs low atomic number materials to maximize neutron scattering. Light elements such as hydrogen are able to maximize momentum transfer from the impinging neutron and scatter the neutron. Historically, lithium hydride has been used for neutron shielding as it offers high hydrogen density, low weight, known fabrication ability, and is relatively inexpensive.<sup>3,7</sup> Lithium hydride has been extensively studied and fits many of the material requirements for a space reactor neutron shield. Its high melting point and excellent moderating power align well with the design scope, and as such, it has been selected as the material to be evaluated in this design.

Gamma attenuation, in contrast to neutron attenuation, is maximized through interaction with high atomic number and high density elements.<sup>8</sup> This is namely due to the three ways in which gamma rays interact with matter: the photoelectric effect, Compton scattering, and pair production. These processes involve the interaction of the gamma-ray with atomic electrons; consequently, elements with a higher atomic number will result in better gamma attenuation.<sup>5,8</sup>

Tungsten has been used for gamma shielding in space nuclear reactors, ranging from the early SNAP-8 reactor to the modern Kilopower design.<sup>3,9</sup> Tungsten has a high density of 19.30 g/cm<sup>3</sup>, has a high atomic number of 82, is relatively inexpensive, and is readily fabricated.<sup>4</sup> There has also been some interest in the use of depleted uranium (DU) as a gamma shield material due to its even higher atomic number and comparable density to tungsten (19.10 g/cm<sup>3</sup>).<sup>4,5</sup> However, DU may present issues with internal heat generation due to uranium-235 fission.<sup>5</sup> Thus,

this project uses tungsten as the primary gamma shield material, with some comparisons to DU in terms of reduced shield mass.

The design dose limit criteria are based on historical information and the anticipated radiation resilience of the electronic components. The maximum allowable neutron dose for neutrons with energy greater than 0.1 MeV at 10 cm behind the shadow shield is  $10^{14}$  n/cm<sup>2</sup> over a 10-year lifespan at full power operation. This value is consistent with the neutron dose thresholds used in the Prometheus and Kilopower projects.<sup>9,10</sup> The gamma dose limit in silicon at 10 cm behind the shadow shield is 1 Mrad over a 10 year lifespan at full power, also based on values from the Prometheus and Kilopower projects. Finally, a human dose limit at 20 m from the shadow shield of less than 50  $\mu$ Sv/hr will ensure that astronauts will not be exposed to a radiation area by the reactor.

### III. MODEL DESCRIPTION

The Optimized Gamma REducer design and the Dose-Optimized Neutron-shield for Kilowatt Electric Energies design, or OGRE and DONKEE, are optimized shadow shield designs for the 250 kW<sub>e</sub> LEU-fueled reactor. The designs feature truncated cone sections consisting of a tungsten or depleted uranium layer for the OGRE region and lithium hydride layers for the DONKEE regions (Figure 1). The shield is coaxial with the core, 10 cm from the core. The parameters *b*, *c*, *d*, *R1*, *R2*, and *R3* in Fig. 1 varied over several runs to compare the resulting attenuation. Parameter *a* was held constant at 10 cm, as this is the distance that the shield will sit from the reactor core. Monte Carlo N-Particle Transport Code 6.2 (MCNP6.2) simulated the particle transport through the shield to determine attenuation values.

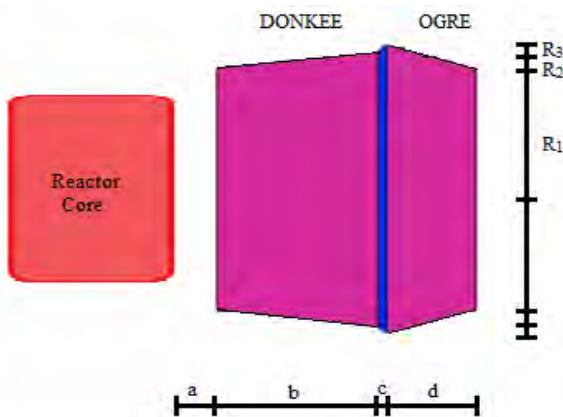


**Fig. 1:** Layout of the radiation shadow shield.

All of the MCNP neutron calculations used ENDF71x libraries, which employ cross-section data from ENDF/B-VII.1 at 293 K. Similarly, the photon calculations used the MCPLIB84 libraries which employ ENDF/B-VI.8 cross-section data. Thus, temperature effects on the shield were

not considered. The models used neutron and photon disk sources with radii equal to the top radius of the reactor core and followed energy and angular distributions received from the LEU core given in Tables I and II. The particles were distributed across the source by a power law. The neutron calculations ran  $1.1 \times 10^9$  particles and the photon calculations ran  $7.5 \times 10^9$  particles. A ratio of the current (F1) tallies at the front and back of the shield determined the percentage of the particles attenuated by the shield. These ratios were then multiplied by the denormalized flux from the LEU core to produce flux and fluence values.

Shielding problems are inherently challenging for Monte Carlo methods and require effective variance reduction to produce efficient answers. Importance weighting increased the number of particles reaching the tally through the shield. The sections were weighted by allotting region *b* of Fig. 1 importance 1, region *c* importance 2, and region *d* importance 4. All reported values were produced with variances below 0.5% at the 95% confidence level.

**Table I:** Source particle energy distributions.

Particle Energy (MeV)	Neutron Energy Probability	Photon Energy Probability
$1 \times 10^{-8}$	0	0
$1 \times 10^{-7}$	$3.08 \times 10^{-2}$	0
$1 \times 10^{-6}$	$3.93 \times 10^{-2}$	0
$1 \times 10^{-5}$	$4.29 \times 10^{-2}$	0
$1 \times 10^{-4}$	$5.69 \times 10^{-2}$	0
$1 \times 10^{-3}$	$6.90 \times 10^{-2}$	0
$1 \times 10^{-2}$	$8.84 \times 10^{-2}$	$2.16 \times 10^{-4}$
$1 \times 10^{-1}$	$1.35 \times 10^{-1}$	$1.10 \times 10^{-1}$
1	$3.00 \times 10^{-1}$	$5.94 \times 10^{-1}$
2.5	$1.71 \times 10^{-1}$	$2.16 \times 10^{-1}$
5	$5.02 \times 10^{-2}$	$6.51 \times 10^{-2}$
7.5	$1.35 \times 10^{-2}$	$1.11 \times 10^{-2}$
10	$2.43 \times 10^{-3}$	$4.06 \times 10^{-3}$
12.5	$3.15 \times 10^{-4}$	0
15	$1.02 \times 10^{-4}$	0
17.5	$1.55 \times 10^{-5}$	0
20	0	0

**Table II:** Source particle angular distributions.

Particle angle from z-axis (degrees)	Neutron Angular Probability	Photon Angular Probability
15	$9.43 \times 10^{-2}$	$1.42 \times 10^{-1}$
30	$2.42 \times 10^{-1}$	$3.68 \times 10^{-1}$
45	$2.88 \times 10^{-1}$	$4.25 \times 10^{-1}$
60	$2.35 \times 10^{-1}$	$3.04 \times 10^{-1}$
75	$1.24 \times 10^{-1}$	$1.23 \times 10^{-1}$
90	$1.56 \times 10^{-2}$	$1.03 \times 10^{-2}$

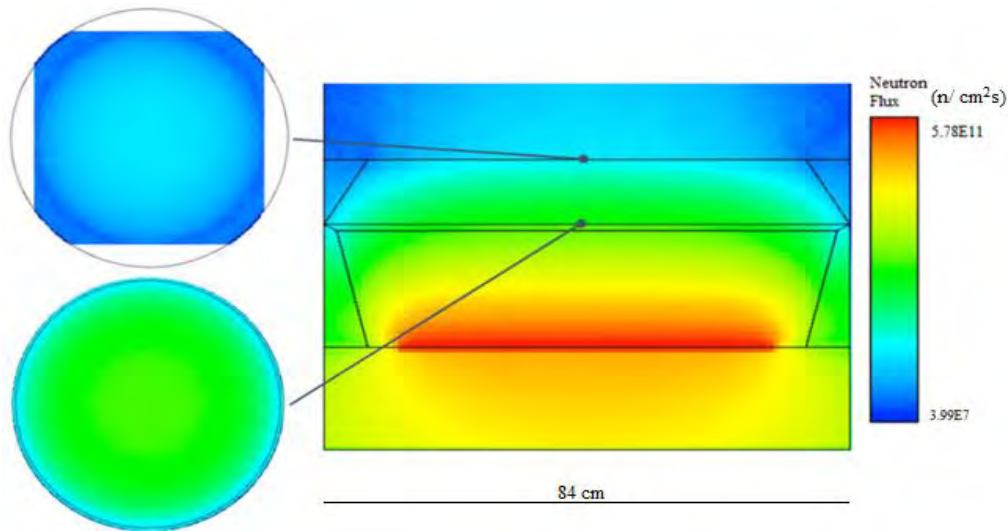


**Fig. 2:** Axial and radial cross sections of the neutron flux through the shield based on the LEU core.

#### IV. RESULTS

The MCNP simulations indicate the feasibility of the designed shadow shield through the shield’s ability to attenuate radiation. The mass and attenuation percentage were optimized by changing the radii and thicknesses of the various sections and observing the resultant attenuation percentages. Tables III and IV present the final dimensions of the DONKEE and OGRE sections and Table V presents the results of the attenuation calculations. The present design exhibits 99.94% neutron attenuation, effectively reducing total neutron population. Gamma reduction is slightly lower at 93.87% due to the high energy photons emitted by the core. The dose in silicon has not yet been determined for the current photon fluence.

**Table III:** Dimensions of the DONKEE shield.

b	d	R <sub>1</sub>	R <sub>3</sub>	Mass
20 cm	10 cm	35 cm	42 cm	109.08 kg

**Table IV:** Dimensions of OGRE shield.

c	R <sub>2</sub>	R <sub>3</sub>	Mass
1 cm	40 cm	42 cm	101.94 kg

**Table V:** Attenuation capabilities of the OGRE and DONKEE shields for photon and neutrons. Only neutron energies greater than 0.1 MeV are considered.

Pre-shield Flux	Post-shield Flux	Attenuation Percent	10 Year Fluence at 10 cm

	(particles .cm <sup>2</sup> s <sup>-1</sup> )	(particles .cm <sup>2</sup> s <sup>-1</sup> )		(particles/cm <sup>2</sup> )
Neutron Attenuation	3.42 x 10 <sup>11</sup>	2.05 x 10 <sup>8</sup>	99.96%	6.46 * 10 <sup>14</sup>
Photon Attenuation	6.23 x 10 <sup>11</sup>	3.82 x 10 <sup>10</sup>	93.87%	1.20 x 10 <sup>17</sup>

Figures 2 and 3 present axial and radial mesh tally results of the radiation shield for neutrons and photons, respectively. Figure 2 demonstrates that the neutron flux is significantly reduced by 99.74% before reaching the central OGRE section. The flux is then reduced by an additional 0.22% by the time the neutrons reach the far end of the shield for a total attenuation of 99.96%. Likewise, Figure 3 shows that the photons are effectively shielded by the tungsten shield section resulting in 93.87% total attenuation. They interact very little with the lithium hydride until they reach the tungsten, where the field is seen to drop to near its final levels.

#### V. SUMMARY AND CONCLUSION

An LEU configuration of a space nuclear fission power system is being analyzed for its potential use in long operating lifetime missions. In order to protect electronics and the payload from radiation damage and significant dose, a radiation shield has been designed to attenuate both neutron and gamma ray fields. The results herein suggest

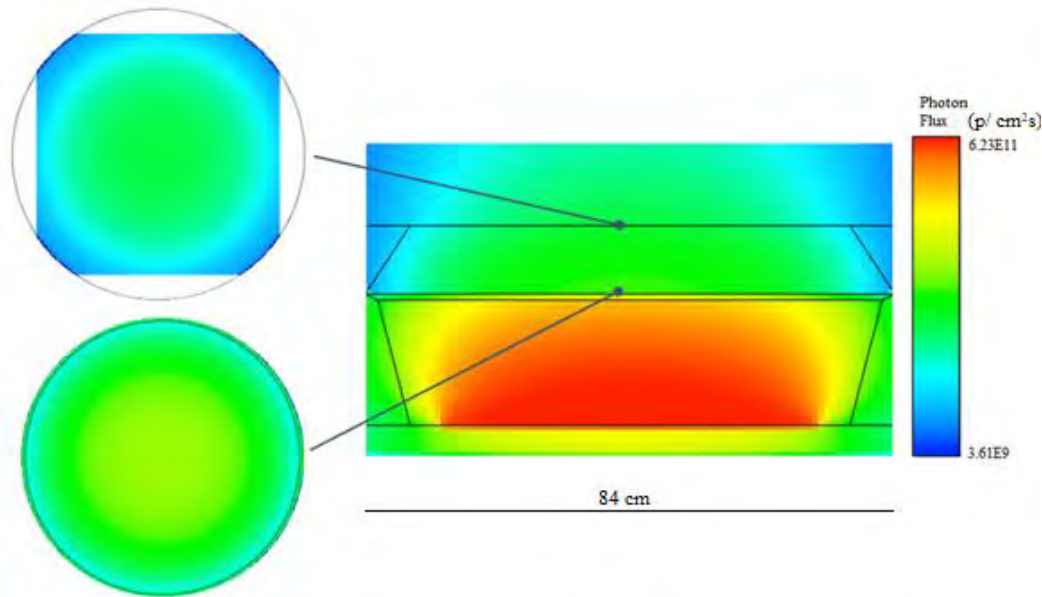


**Fig. 3:** Axial and radial cross sections of the photon flux through the shield based on the LEU core.

the efficacy of a shadow shield configuration consisting of lithium hydride and tungsten for neutron and gamma attenuation, respectively.

The OGRE and DONKEE shields significantly reduce the radiation dose to the payload in the shadow that they cast. Overall, they are able to reduce the neutron fluence to  $6.5 \times 10^{14}$  n/cm<sup>2</sup> at 10 cm and 10 years at full reactor power. This is slightly above the design requirement and suggests needing to increase the lithium hydride regions slightly to accommodate longer neutron path lengths. The required attenuation percentage to meet the  $10^{14}$  n/cm<sup>2</sup> limit is thus 99.991%, or approximately 2 cm increase in shield thickness according to linear attenuation calculations.<sup>7</sup> Additionally the gamma field is attenuated to produce a fluence of  $1.20 \times 10^{17}$  p/cm<sup>2</sup> at 10 cm and 10 years at full reactor power.

Future work will convert the photon fluence to dose in silicon to determine if the dose rate is acceptable and if the tungsten needs to be thickened. There is further room for mass optimization, as well, in slight reductions of the shield radii. The tungsten layer may, however, need to increase in thickness to accommodate more photon shielding, resulting in uncertainty in the final system mass. Furthermore, the ideal position of tungsten layer within the LiH to minimize photon dose as a result of secondary photon production still needs to be determined. Finally, the heating effects in the shield need to be quantified.

## REFERENCES

1. D. BUDEN, *Space Nuclear Fission Electric Power Systems Book 3: Space Nuclear Propulsion and Power*, First, Polaris Books, Lakewood, CO (2011).
2. E. F. DE ARAÚJO and L. N. F. GUIMARÃES, “American Space Nuclear Electric Systems,” in *Journal of Aerospace Technology and Management*, **10**, (2018). DOI:10.5028/jatm.v10.976
3. D. J. COCKERAM, “SNAP 2, 8, and 10A Reactor Programs Progress Report,” in *Space Power Systems Engineering*, Vol. 16, p. 393, Academic Press Inc., New York, New York (1966). DOI:10.1016/B978-1-4832-3056-6.50021-9
4. V. BANJAC and A. S. HEGER, “Mass Optimization Studies of Gamma Shield Materials for Space Nuclear Reactors,” *Nuclear Technologies*, **108**, 1, 126 (1994). DOI:10.13182/nt94-a35048
5. W. J. BARATTINO, “Coupled Radiation Transport/Thermal Analysis of the Radiation Shield for a Space Nuclear Reactor,” Ph.D. Thesis, The University of New Mexico, Chemical and Nuclear Engineering (July 1985).
6. S. BANJAC et al., “Galactic Cosmic Ray Induced Absorbed Dose Rate in Deep Space – Accounting for Detector Size, Shape, Material, as well as for the Solar Modulation,” *Journal of Space Weather and Space Climate*, **9**, A14 (2019). DOI:doi.org/10.1051/swsc/2019014.
7. F. H. WELCH, “Lithium Hydride: A Space Age Shielding Material,” *Nuclear Engineering Design*,

- 26**, 3, 444 (1974). DOI:10.1016/0029-5493(74)90082-X
8. D. R. MCALISTER, “Gamma Ray Attenuation Properties of Common Shielding Materials,” Rev. 3, PG Research Foundation Inc. (Jan. 2013).
  9. M. A. GIBSON et al., “Development of NASA’s Small Fission Power System for Science and Human Exploration,” *Proceedings of 12th International Energy Conversion Engineering Conference*, May 2014. DOI:10.2514/6.2014-3458
  10. J. ASHCROFT and C. ESHELMAN, “Summary of NR program Prometheus efforts,” *AIP Conference Proceedings*, **880**, 497, February 2007. DOI:10.1063/1.2437490

## INITIAL COMPARISON OF REDUCED AND HIGHER ORDER THERMAL HYDRAULIC SOLVERS FOR NUCLEAR THERMAL PROPULSION FUEL ELEMENT DESIGN

Jim Wang, Matt Krecicki, and Dan Kotlyar

Georgia Institute of Technology, Atlanta, GA, 30318

Primary Author Contact Information: [jimwang312@gatech.edu](mailto:jimwang312@gatech.edu)

*This paper compares reduced order engineering tools against computational fluid dynamics in order to explore potential computational gaps within reduced order solvers and legacy thermal hydraulic correlations. Legacy heat transfer correlations, were developed for limited flow regimes, and are particularly sensitive to the inlet conditions and axial power shapes in certain engine core designs. These sensitivities can have significant effects on the predicted maximum fuel temperature, and therefore the maximum power a particular fuel element can withstand. This could potentially lead to an over-estimation of the maximum achievable exit gas temperature and the specific impulse ( $I_{sp}$ ) performance of a nuclear thermal propulsion system.*

### I. Introduction

The goal of Nuclear Thermal Propulsion (NTP) engines is to provide an  $I_{sp}$  greater than or equal to 875 seconds<sup>1</sup>. This requires the exit bulk hydrogen temperature to be greater than or equal to 2500 degrees kelvin. Therefore, extreme focus is placed on the design of the fuel element (FE) to maximize the outlet gas temperature while remaining within the FE's material thermal constraints. This task is often performed using an iterative solution scheme which accounts for neutronic and thermal hydraulic feedbacks to determine the maximum allowable power within the fuel for a single case. In order to optimize fuel element performance various input parameters are perturbed such as geometry, fuel material composition, and inlet thermal hydraulic conditions. These perturbations can require hundreds or even thousand unique cases to be calculated, therefore reduced order thermal hydraulic solvers have been utilized to perform these calculations. Such computational analyses are not possible with high-fidelity tools such as CFD as their computational time becomes prohibitive. A more efficient alternative relies on the use of engineering-based tools. However, these typically adopt various correlations, such as Petukhov, Wolf-McCarthy, or Taylor<sup>2</sup>. By definition these correlations have limited ranges of applicability. Modern NTP designs may no longer be inside the range of applicability for these correlations, which could reduce the accuracy of reduced order engineering tools.

#### I.A. Problem Description

The problem considers a standard KIWI-B4E fuel element design<sup>1</sup>. Table I presents the fuel element and dimensions and Fig. 1 presents the FE cross section. The fuel type considered in this paper is a refractory cermet. The fuel kernel is uranium nitride (UN) with a molybdenum (Mo)-tungsten (W) alloy (Mo/W) matrix, similar to the fuel utilized in previously published BWXT and NASA studies<sup>3,4,5,6</sup>. The cermet fuel loading is fixed at 60 vol% UN, porosity of 3%.

TABLE I. Fuel element dimensions.

Parameter	Value
Coolant Channel Radius	0.1727 cm
Hexagonal Flat to Flat	1.9050 cm
Element Length	100 cm
Number of Channels	19

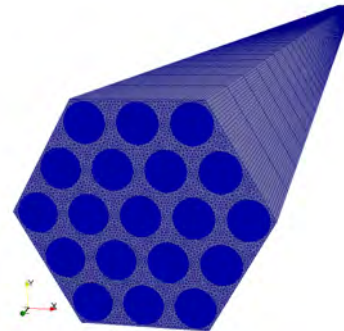


Fig. 1. Fuel element cross section

Table II documents the thermal hydraulic inlet conditions, and material temperature limitations of the fuel element used in this study. These inlet conditions have been calculated based on an internally developed NTP system code POWER, which is similar to other published NTP systems<sup>7</sup>.

Two different fuel element configurations are considered in this paper, both use the KIWI-B4E geometry, and the same inlet conditions presented in Table II, however their axial split ratio is different. The active core region is split into an upper and lower region in this study similar to the ANL-200 design<sup>8</sup>, where the

upper region of the core will utilize a Mo matrix material and the lower region of the core will utilize a dispersion strengthened Mo/W alloy.

**TABLE II.** FE inlet conditions and material constraints

Parameter	Value
Mass flow rate per fuel element	0.040172 kg/s
Inlet temperature	190 Kelvin
Inlet pressure	7.1 MPa
Maximum Allowable Temperature in Mo-UN	2400 Kelvin
Maximum Allowable Temperature in Mo/W-UN	2600 Kelvin

The split ratio is defined as the fraction of total element height that contains the Mo/W matrix. Higher split ratios mean that more Mo/W will be loaded into the core. Case 1 has a split ratio of 0.4 and case 2 has a split ratio of 0.7, these cases are presented in Fig. 2.

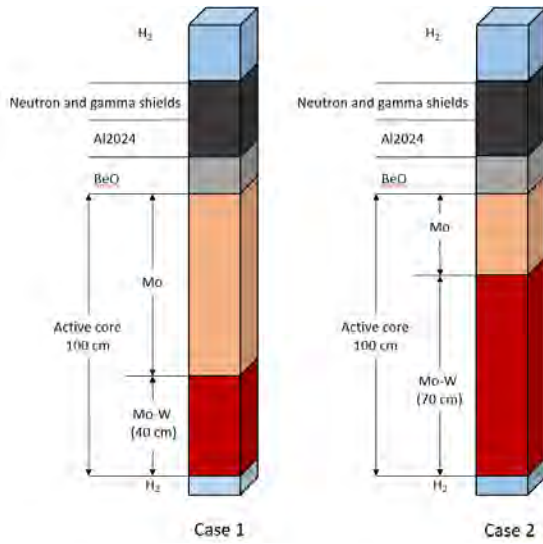


**Fig. 2.** Fuel element axial configurations

Changing the split ratio has a significant effect on the axial power profile of the core, this effect is demonstrated in Fig. 3. Case 2 has a significantly increased peaking factor, and the peak is drawn towards the top of the core. The axial power profiles for each case, were calculated using the Monte-Carlo based SERPENT code with coupled neutron and gamma transport enabled<sup>9</sup>. The serpent code has been extensively verified, and is well suited for multi-physics calculations<sup>10</sup>. In this paper the ENDF/B-VII.0 evaluated data library was used.

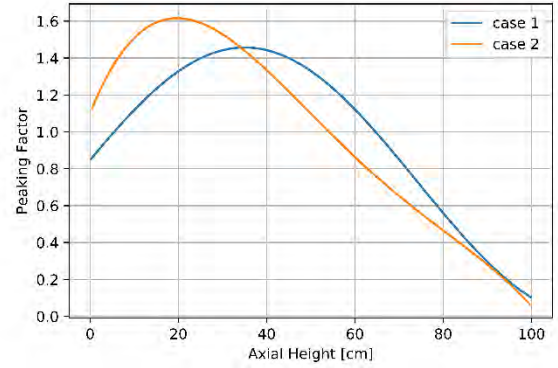


**Fig. 3.** Fuel element axial power profiles

## II. CODES AND METHODS

### II.A. NTP-THERMO

The THERMO code module was originally developed for light water reactor thermal hydraulic analysis. However a specifically adapted version of THERMO has been developed for NTP analysis (NTP-THERMO). One of the major upgrades implemented in NTP-THERMO was a mesh-based resistance network and the implementation of a numerical solution to the radial conduction problem. This approach was implemented due to hydrogen's general heat transfer coefficient correlation's dependence on the fuel surface temperature ( $T_w$ ) and bulk coolant temperature ( $T_b$ ).

The heat transfer coefficients are typically correlated using the Nusselt number as a way to measure the convective heat transfer at the wall. The NASA Glenn research center developed a general Nusselt number correlation formula for gas flowing through a heated pipe, presented by Eq. 1, which included a correction term that accounted for the ratio of the surface wall temperature to bulk hydrogen temperature<sup>2</sup>. Taylor's Nusselt number correlation was used to calculate the heat transfer coefficient in the fuel element flow path. Taylor's correlation has been printed in several different publications, some of which are inconsistent. Eq. 2 presents the correct correlation

$$Nu = C_1 \times Re_b^{C_2} Pr_b^{C_3} \times (T_w/T_b)^{C_4} * (C_5 + C_6 * (X/D)^{C_7})^{C_8} \quad (1)$$

$$Nu = 0.023 \times Re_b^{0.8} Pr_b^{0.4} \times (T_w/T_b)^{-0.57-1.59*x/D} \quad (2)$$

The problem was discretized into 250 axial nodes in order to ignore axial conduction in the solid regions. Only radial conduction from the fuel to the hydrogen coolant was considered using Eq. 3. Where  $\dot{m}$  is the mass flow rate of hydrogen,  $q'''$  is the power density in the volume  $V$ ,  $C_p$  is the heat capacity of the hydrogen, and  $T_\infty$  is the bulk hydrogen temperature.

$$T_{\infty(out)} = T_{\infty(in)} + \frac{V}{\dot{m}C_p} q''' \quad (3)$$

Friction, and acceleration pressure losses are all accounted while gravity was neglected in the analysis.

The thermal conductivities the fuel and matrix materials are present in Eq. 4-6. The effective thermal conductivity of the matrix was calculated using the parallel geometric mean model.

$$k_w \left[ \frac{W}{m K} \right] = \begin{cases} 165.54 - 85.57 \times \left( \frac{T}{10^3} \right) + 33.51 \times \left( \frac{T}{10^3} \right)^2 & T < 890 \\ 133.82 - 15.57 \times \left( \frac{T}{10^3} \right) & T \geq 890 \end{cases}$$

$$k_{Mo} \left[ \frac{W}{m K} \right] = \begin{cases} 16.186T - 0.00298T^3 - 0.0605T^2 - 4.545 & T < 50 \\ 0.02T^2 - 5.4776T + 522.44 & 50 \leq T < 150 \\ 9 \times 10^{-6}T^2 - 0.0513T + 153.29 & T \geq 150 \end{cases}$$

$$k_{UN} \left[ \frac{W}{m K} \right] = \begin{cases} 1.43T^{0.39} & T < 1910 \\ 27 & T \geq 1910 \end{cases}$$

The effective matrix-fuel thermal conductivity was then calculated using the Bruggeman's method<sup>11</sup>. This method was applied in NTP-THERMO code resulting in the average fuel thermal conductivities presented in Fig. 4. The initial sharp increase in thermal conductivity is due the fact that UN's thermal conductivity increases with temperature and comprises 60 vol% of the fuel material. The jump discontinuity occurs exactly where the fuel element matrix material transitions from a Mo-UN cermet to a Mo/W-UN cermet. Tungsten has a higher thermal conductivity and thus causes an increased average fuel thermal conductivity.

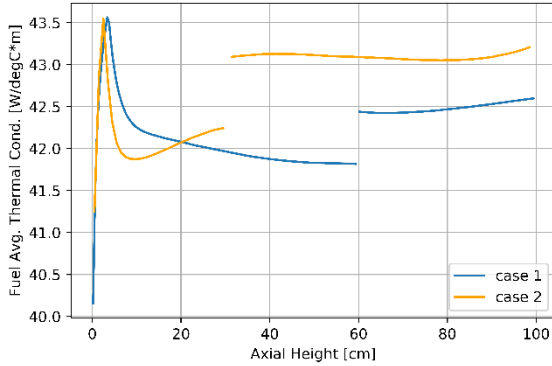


Fig. 4. Fuel element average thermal conductivity

The thermal and transport hydrogen data material properties, which are a function of both temperature and pressure were utilized in the analysis<sup>12</sup>.

### II.A.I Equivalent Model

NTP-THERMO is a 1.5-D sub-channel code designed to generate thermal output in a robust manner.

The code adopts an analytically well-established model known as equivalent model. The concept of the equivalent model for FE takes 1/19 of the original hex model while preserving flow channel diameter, wetting area, and solid fuel volume. The model also assumes axis-symmetry with insulated boundary on the outer boundary. Fig. 5 shows a comparison between the hexagonal FE model and the equivalent model.

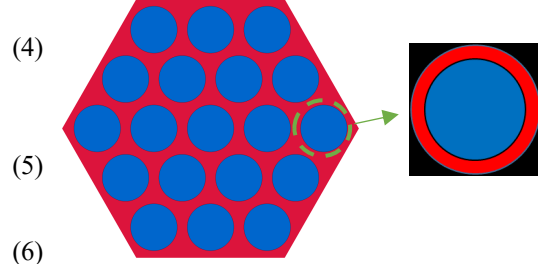


Fig. 5. Comparison between the original FE model (left) and equivalent model (right).

### II.A.II. Fuel element design iteration loop

Both cases maximum allowable power were determined using an iterative scheme which is detailed in Fig. 6. The procedure starts with specifying the inlet conditions to the fuel element and maximum allowable temperature in each material region, detailed in Table II.

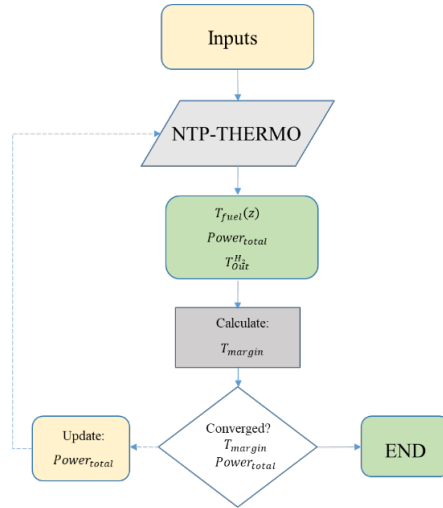


Fig. 6. FE design iteration scheme

The procedure then executes NTP-THERMO, which returns the centerline fuel temperatures as a function of axial height. This profile is then used to determine the location of the most limiting node and then calculates limiting node's margin to the specified limit. This margin is then used inside a Newton-Raphson iterative scheme to update the total element power. The axial power profiles

remain constant through each iteration. The loop continues until the margin to the limit is within 1 degree of the target and the total element power has converged within 10 watts. This procedure typically requires 8 iterations and approximately 140 seconds of computational time on a single processor.

## II.B. OpenFOAM

OpenFOAM is a C++ based open source finite volume code designed to solve the continuum problem. OpenFOAM has been widely used for various nuclear application such as sub-channel CFD analysis, neutron diffusion problem, and full core multi-physics modeling. This paper uses OpenFOAM to perform high resolution thermal hydraulic analysis for the proposed FE design. The objective is to generate a high fidelity result that can be treated as reference solution for the reduce-order model.

### II.B.I. Conjugate Heat Transfer (CHT) Solver

Reduced-order solvers, like THEMRO-NTP, depend on legacy correlations when solving the convective heat transfer problem; and these legacy correlations are bounded by flow conditions and flow channel geometry. The adopted OpenFOAM solver implements a Conjugate Heat Transfer (CHT) method that does not rely on empirical correlation but rather assumes continuity of heat flux between solid and fluid interface. The method refers to two thermally connected subdomains, in which the heat transfer governed by differential equation is solved<sup>13</sup>. Eq. 7 describes the balance of heat flux between two neighboring solid and fluid cells, where  $\lambda$  represents thermal conductivity,  $T$  represents cell temperature.

$$\lambda_{solid} \nabla_{solid} T = \lambda_{fluid} \nabla_{fluid} T \quad (7)$$

Eq. 8 estimates the continuous heat flux based on the linearly interpolated interface boundary temperature  $T_b$  and the temperature  $T$  of its two subdomains.

$$q'' \approx \lambda(T_b) \frac{T_b - T}{\Delta} \quad (8)$$

### II.B.II. Iterative Scheme, Mesh Scheme, and Boundary Conditions

The adopted OpenFOAM CHT solver iterates between conservation equations and Reynolds Average Navier-Stokes (RANS) turbulence model for fluid domain and heat diffusion equation for solid domain. The simulation uses Semi-Implicit Methods for Pressure Linked Equations (SIMPLE) algorithm to generate steady-state solution in three dimensions. The solver setting is given in Table III. OpenFOAM obtains its temperature dependent thermal physical properties using high order polynomial fit from property data library with minor regression.

**TABLE III.** OpenFOAM solver settings

Description	Settings
Solver	Modified 'chtMultiregionSimpleFoam'
Algorithm	SIMPLE
Turbulence model	K-OmegaSST
Simulation Type	Steady-State
Gradient Scheme	Gauss linear
Laplacian Scheme	Gauss limited linear
Diversion Scheme	Gauss linear orthogonal
Residual criteria	1.00E-7

The numerical mesh is generated using Gmsh-4.0. Fig. 7 shows the mesh configuration for the FE model where the hybrid mesh structure is adopted. The mesh structure in Fig. 7 consists a mixture of structured grid in fluid domain and unstructured grid in solid domain. The mesh model is also sub-divided into three different layers: (a) freestream layer where fluid can be modeled without near wall treatments, (b) fluid near-wall layer where near wall treatment is significant and the CHT boundary condition requires finer mesh grid to approximate heat flux continuity, and (c) solid layer where Laplacian heat transfer dominates. The mesh convergence work for this specific model has been detailed in previous research publication<sup>14</sup>.

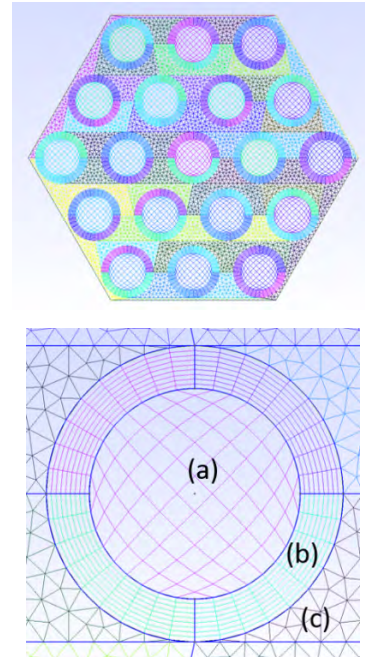


**Fig. 7.** Cross-section view of fuel element with structural grid (top), and zoom-in of FE near flow channel (bottom)

Table IV presents the boundary conditions for FE. The boundary condition describes a steady-state pressure-

linked CFD problem with internal flow. The velocity and temperature profile are fixed at the inlet and the pressure is fixed at the outlet. The gravitational force has been set to zero to mimic operation conditions.

**TABLE IV.** OpenFOAM Model Boundary Conditions

Velocity (Axial direction), m/s		
Inlet	Fixed Value	190.15
Coolant wall	No slip	
Outlet	Zero-gradient	
Temperature, K		
Inlet	Fixed Value	25.88
Coolant wall	CHT	
Outlet	Zero-gradient	
Pressure, MPa		
Inlet	Zero-gradient	
Coolant wall	Fixed Value	6.8
Outlet	Zero-gradient	

### III. ANALYSIS AND RESULTS

A code-to-code benchmark study was performed using the 1.5D NTP-THERMO and 3D OpenFOAM CHT model. Both models share the same boundary conditions on temperature, velocity, and pressure as well as their usage of thermal physical properties.

The outlet hydrogen temperature is plotted as a function of axial height in Fig. 8. It can be observed that the exit gas temperature shows good agreement between OpenFOAM and NTP-THERMO. This confirms the ability of reduced order codes to accurately predict the exit gas temperature of the fuel element, and therefore the  $I_{sp}$  of a specific design.

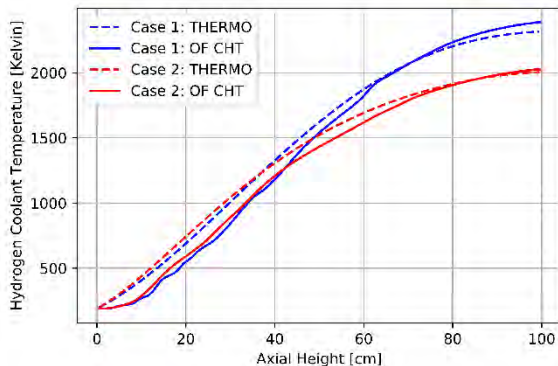


**Fig. 8.** Hydrogen coolant temperature vs axial height

However, there is a considerable disagreement between the maximum fuel temperature predicted by NTP-THERMO and OpenFOAM. Some differences are to be expected as the NTP-THERMO model only considers a

single channel problem, while the OpenFOAM model considers a 19 channel problem with radial and axial heat conduction between the 19 channels. It can be noted that the initial temperature peak is under predicted by NTP-THERMO. The predicted OpenFOAM maximum temperature significantly exceeds the maximum allowable temperature in the cold end fuel material for both cases. This poses a serious concern that reduced order TH methods under predict the maximum fuel temperature.

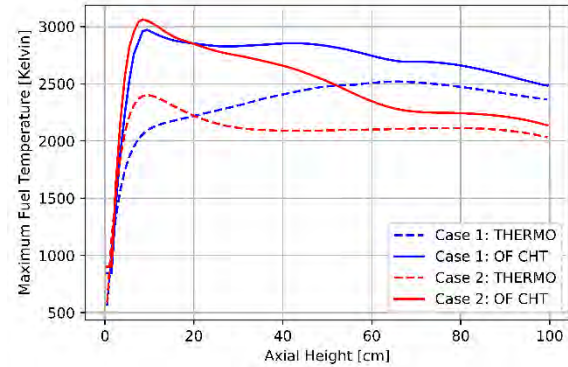


**Fig. 9.** Maximum fuel temperature vs axial height

This disagreement is partially caused due the heat transfer correlation implemented in THERMO. While OpenFOAM does not use a heat transfer coefficient to calculate an average convective heat transfer, an effective coefficient can be calculated using Newton’s law of cooling. Fig. 10 presents the heat transfer coefficient as a function of axial height for each case. It can be observed that the OpenFOAM predicts a lower minimum of the heat transfer coefficient, than Taylor’s correlation. It is also worthwhile noting that in OpenFoam an explicit 3D fuel element was modeled rather than the approximated 1.5d equivalent heated channel. Therefore, in the axial layers near the exit, the coolant temperature for some radial T/H channels might be higher than certain adjacent solid regions; which will cause a “negative” heat transfer. The latter description partially explains the behavior shown in Fig. 10.

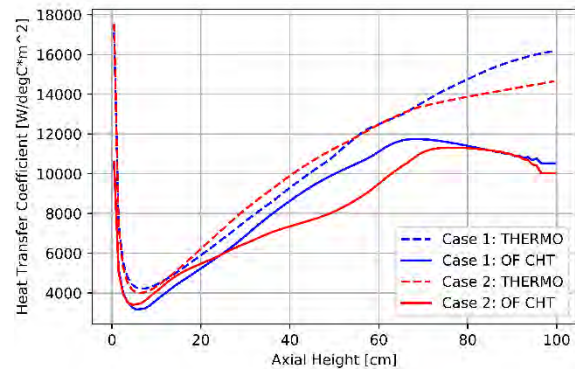


**Fig. 10.** Heat transfer coefficient vs axial height

Additionally, there is a disagreement in the Reynolds number between OpenFOAM and NTP-THERMO near the fuel element inlet. After approximately 60 centimeters the two codes agree well. OpenFOAM is predicting a rapid reduction in the Reynolds number in the initial 20 centimeters of the FE. As the Reynolds number decreases the effective heat transfer, which will result in higher maximum fuel temperatures.

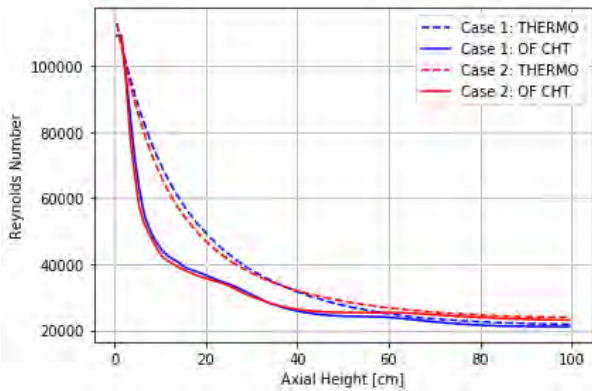


Fig. 11. Reynolds number vs axial height

The discrepancy between two models' maximum fuel temperature may also be explained by observing the temperature distribution heat map obtained using OpenFOAM's 3D model. Fig. 12 and 13 display slices of OpenFOAM generated temperature footprint for the FE (Case 1) solid domain taken at the axial height of 30 cm and 70 cm. Under the insulated boundary condition, it can be seen that the most heated regions where peak temperature occurs has shifted from the edge to the center of the fuel element along with the height. Such phenomena cannot be observed by the reduced-order tool since NTP-THERMO assumes maximum temperature always occurs near the insulated boundary. Given the axis-symmetry nature of 1.5D Equivalent model, it will be difficult for the reduced-order model like NTP-THERMO to estimate an accurate peak fuel temperature.

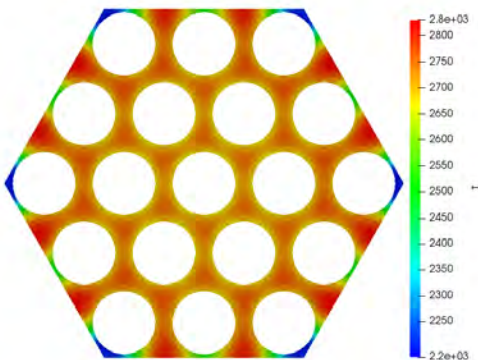


Fig. 12. FE (Case 1) temperature distribution at an axial height of 30 cm

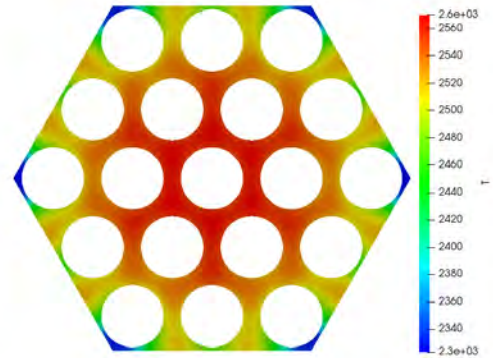


Fig. 13. FE (Case 1) temperature distribution at an axial height of 70 cm

#### IV. CONCLUSIONS

The CFD code OpenFOAM was compared against the reduced order code NTP-THERMO for NTP thermal hydraulic analysis. The results of this paper show that reduced order methods accurately predict the exit hydrogen gas temperature and therefore can provide accurate predictions of an engine's  $I_{sp}$  performance. However, reduced order single channel models do not compare well against higher-order CFD solvers when calculating maximum fuel temperatures. Reduced order codes which employ legacy heat transfer correlations have been shown to under predict maximum fuel temperature by more than 500 degrees kelvin. It is extremely important to investigate the source of these discrepancies as reduced order codes can be modified to capture the relevant physics. Upgrading reduced order solvers is critical due to their utilization in design space searches and optimization schemes to maximize NTP thermal performance and to achieve NASA future goals for manned space flight to Mars.

#### REFERENCES

1. Finseth J. L., 1991. Rover Nuclear Rocket Engine Program: Overview of Rover Engine Tests: Final Report. Tech. Rep. NASA-CR-184270
2. Walton T., 1992. Program ELM: A Tool for Rapid Analysis of Solid-Core Nuclear Rocket Fuel Elements. Lewis Research Center. NASA-TM-105867.
3. Krecicki M., et Al. Quantification of Intra Element Peaking in Low Enriched Nuclear Thermal Propulsion Cores, BWX Technologies, NETS, 2020.
4. Stewart M., 2019. Thermal, Fluid, and Neutronic Analysis of an LEU Nuclear Thermal Propulsion Core. VPL at NASA Glenn Research Center. AIAA Propulsion and Energy 2019 Forum

5. Houts et al., 2019. NASA's Nuclear Thermal Propulsion Project. <https://ntrs.nasa.gov/archive/nasa/casi.ntrs.nasa.gov/20170003378.pdf>
6. NASA, Space Technology Mission Directorate Game Changing Development Program, FY19 Annual Review
7. Belair M. et al., 2013. Nuclear Thermal Rocket Simulation in NPSS. NASA Glenn Research Center.
8. Argonne National Lab, 1966. *Nuclear Rocket Program Terminal Report, ANL-7236*.
9. Leppänen, J., Pusa, M., Viitanen, T., Valtavirta, V., Kaltiaisenaho, T., 2015. The Serpent Monte Carlo code: Status, development and applications in 2013. *Ann. Nucl. Energy* 82, 142–150.
10. Leppänen, J., Mattila, R., Pusa, M., 2014. Validation of the Serpent-ARES code sequence using the MIT BEAVRS benchmark – initial core at HZP conditions. *Ann. Nucl. Energy* 69, 212–225.
11. Bruggeman, D.A.G., 1935. Berechnung Verschiedener Physikalischer Konstanten von Heterogenen Substanzen. *Annalen der Physik (Leipzig)* 24, 636–679.
12. Computer Program for Thermal and Transport Properties of Parahydrogen from 20 to 10000 K, NASA Lewis Research Center, Tech. Rep., 1993.
13. Tuominen, R., 2015. Coupling Serpent and OpenFOAM for neutronics - CFD multi-physics calculations, Aalto University School of Science, Espoo, Finland.
14. Wang, J. C., Kotlyar, D., 2019. OpenFOAM Thermal Analysis of Nuclear Thermal Propulsion Fuel and Moderating Elements. Top Fuel Conference 2019.

## ALTERNATIVES FOR ELECTRICAL POWER PRODUCTION FROM A NUCLEAR THERMAL PROPULSION ENGINE

Emily Wood<sup>1</sup> and Dr. L. Dale Thomas<sup>2</sup>

<sup>1</sup>Department of Mechanical and Aerospace Engineering, The University of Alabama in Huntsville, 301 Sparkman Drive, Huntsville, AL, 35899

<sup>2</sup>Department of Industrial and Systems Engineering and Engineering Management, The University of Alabama in Huntsville, 301 Sparkman Drive, 35899

256-824-8100 [egw0015@uah.edu](mailto:egw0015@uah.edu)

*This paper discusses the concept of a Minimally Intrusive Power generation System (MIPS) for use with a Nuclear Thermal Propulsion (NTP) engine for a crewed Mars Transfer Vehicle (MTV). In order to keep the fuel elements in the nuclear reactor above their ductile-to-brittle transition temperature (DBTT), the reactor will not be turned off after each burn, but instead will idle in a low power mode. The goal of the MIPS is to remove enough of the idle heat so that the reactor core will not be damaged, and convert this thermal energy into an adequate amount of electricity to power the vehicle, without compromising the reactor design. Three alternatives will be considered; thermoelectric generators, a closed-loop Brayton cycle, and a Stirling cycle. This paper describes the candidate systems and the design requirements of the MIPS, then goes on to outline how the systems will be modeled and what attributes will be considered when deciding which system is best for this intended use.*

### I. INTRODUCTION

In 2015, the Nuclear Thermal Propulsion Project was established as part of NASA's Space Technology Mission Directorate with the intention to "determine the feasibility and affordability of a low-enriched uranium-based Nuclear Thermal Propulsion (NTP) engine with solid cost and schedule confidence. "NTP offers very high energy density and specific impulse roughly double that of the highest performing traditional chemical propulsion systems. NTP may offer the only viable option for human exploration missions to Mars and beyond, where solar arrays can no longer provide sufficient energy and chemical propulsion would require prohibitively high mass of propellant and/or long mission durations.

Although the NTP project was not established until 2015, NASA's interest in NTP dates back to the 1960s with the Nuclear Engine for Rocket Vehicle Applications (NERVA). Testing on NERVA engines was conducted through the 1960s and early 1970s until the program was terminated due to shifting focuses and budget cuts. During the NERVA tests, thrust levels up to 75,000 pounds were observed along with specific impulse of nearly 900 seconds<sup>2</sup>. In the context of a human

exploration mission to Mars, NTP also provides the ability to abort the mission and return to Earth at any time within three months of Earth departure and also includes the ability to return immediately upon arrival at Mars, whereas other propulsion architectures do not allow for this<sup>3</sup>.

In most exploration mission scenarios, multiple burns of the propulsion system are needed at different points in the trajectory, primarily to exit or enter orbits of planets or moons. After the nuclear reactor is used to provide thrust for the first burn, it cannot be completely shut down or else the fuel elements will cool past their ductile-to-brittle transition temperature (DBTT)<sup>1</sup>. Past this temperature, the fuel elements will experience embrittlement issues<sup>1</sup>. This issue is unique to the tungsten cermet fuel elements, as carbide-based cores do not experience this. Following a burn, instead of shutting the reactor completely down, the power output will be reduced to idle in which the reactor will continue to generate sufficient heat to keep the fuel elements above the DBTT of 373 K. When in its idle mode, the reactor is estimated to generate 10 MW<sup>4</sup>. While the fuel elements located nearest the exterior of the reactor can effectively radiate this heat, the fuel elements located more interior must have heat actively removed in order to prevent damage to the reactor. Bimodal Nuclear Thermal Propulsion attempts to convert all of this idle mode heat into electricity for the vehicle. The ESCORT bimodal design gained much attention in 2005 for its proposed capability to provide 50 kWe of power and its potential for substantial mass savings, but it was ultimately cancelled because it required intrusive changes to the reactor design<sup>1</sup>. This paper proposes the concept of a Minimally-Intrusive Power generation System (MIPS) which can remove some of the heat generated by the reactor in idle mode and convert it to usable power to the vehicle without any changes to the reactor core and minimal changes to the engine.

If feasible, a MIPS will be able to convert the idle heat into usable electricity to power the vehicle and the hydrogen cooling system. The specific application mission for this MIPS study is for a crewed Mars Transport Vehicle (MTV) for a round-trip mission to Mars.

## II. DESIGN REQUIREMENTS

For this study, it is assumed that the MTV requires 25 kWe; twice that of the Orion Spacecraft. In order to achieve enough electricity to power the vehicle, the nuclear reactor idle heat must be converted through a power conversion cycle. There are several alternative technologies for this power conversion. Candidate technologies include:

- Thermoelectric generators
- Closed-loop Brayton cycle, and
- Stirling cycle

The first candidate for power conversion is thermoelectric generators. A schematic of a thermoelectric generator is shown below in Figure 1. Thermoelectric generators convert heat energy directly into electrical energy without any moving parts such as turbines. Thermoelectric generators work by exploiting a temperature gradient between two sides of a generator to produce a voltage potential. Thermoelectric generators with a radioisotope as a heat source were used on Voyager 1, Voyager 2, Cassini, and New Horizons spacecraft<sup>6</sup>. Therefore, thermoelectric generators have already been proven to be reliable in a deep-space environment. Candidates two and three consist of two dynamic power conversion systems: a closed-loop Brayton cycle and a Stirling cycle. The cooling system for the Near Infrared Camera and Multi-Object Spectrometer (NICMOS) on the Hubble Space Telescope used a closed-loop Brayton cycle to power the cryocoolers from 2002 to 2008. This technology was chosen because of its long-life operation and minimal vibration effects<sup>7</sup>.

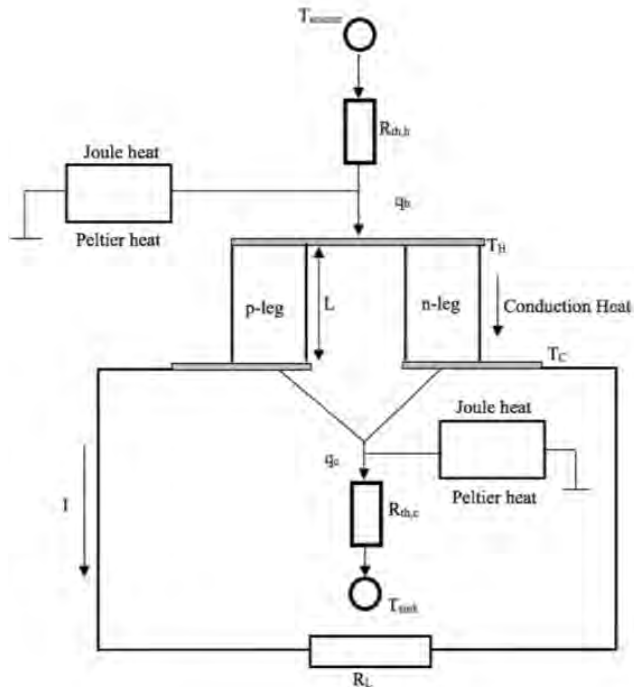


Fig. 1 Thermoelectric Generator Schematic<sup>2</sup>

Glenn Research Center successfully demonstrated the power capabilities of a Stirling converter with their Technology Demonstration Converters (TDCs) which generated about 100 watts of electrical power each, while weighing just over 18 kg<sup>8,9</sup>. TDC #13 holds the record for longest-running heat engine as of 2018 and it still shows no sign of wear<sup>9</sup>. Initially, this study included a Rankine cycle as an alternative, but it was eliminated because Rankine conversion cycles have never been used in a space environment. Therefore, the trade space for this study was confined to systems which have previously been used in space applications.

Mass is always a consideration in spacecraft and space transportation vehicle design. In order to make a MIPS worthwhile, the mass of the system needs to be minimized. Specifically, it needs to be less massive than the solar arrays that the spacecraft would be forced to carry otherwise. The MIPS only needs to generate enough power for the vehicle, any more power would be wasted. Therefore, instead of being efficiency driven, like for most terrestrial systems, this study will be mass driven. In other words, as long as the candidate systems are capable of generating the target 25 kWe, initially, the mass of each system will be the primary consideration when deciding the best system for a round-trip mission to Mars. Future studies will include reliability and cost analysis.

Once the nuclear reactor is turned off, it will continue to generate decay heat due to the continued reactive decay of the fission products. Post-operational heat is a function of the power level at which the reactor operated before shutdown and the length of time in which it operated at this power level. As stated before, this heat must be removed in order to prevent damage to the reactor<sup>1</sup>. The baseline approach for decay heat removal is the blowdown procedure which requires up to 4,000 kg of additional hydrogen to be pulsed through each core after each burn<sup>1</sup> until the reactor reaches idle conditions. The heat generated in the idle state differs from the decay heat of the cooldown transients. The decay heat occurs due to the continued radioactive decay of fission product in the core after the control drums have been rotated to make the fission process subcritical. The reactor in cooldown mode will continue to generate thermal power at a decaying rate until the power level is increased again<sup>10</sup>. In idle mode, the reactor intentionally generates enough heat to stay above the DBTT of 373 Kelvin<sup>11</sup>. The MIPS will not only remove this idle heat without the use of additional propellant, but it will also generate power to the vehicle while the engine is at an idle state. For a nominal four-burn mission profile, there will be three idle periods in which the reactor is not needed for propulsion. The first idle period will last 159 days between burns I and II, the second will last 622 days between burns II and III, and the final will last 159 days between burns III and IV<sup>13</sup>. This totals to 940 days in which the reactor will be operating at idle conditions. The mission profile is shown below in

Figure 2. Furthermore, the MIPS will need shielding from the reactor just like the other parts of the vehicle. Therefore, the geometry of the MIPS is to be considered so that it may be easily integrated with the heat shield. For the two considered dynamic power conversion systems, the radiator is the largest component. A large radiator leads to a large overall system and this system needs to be shielded from radiation, thus the need for a larger radiation shield<sup>12</sup>. For this reason, the mass penalty associated with the larger shield is a factor to be considered in this study.

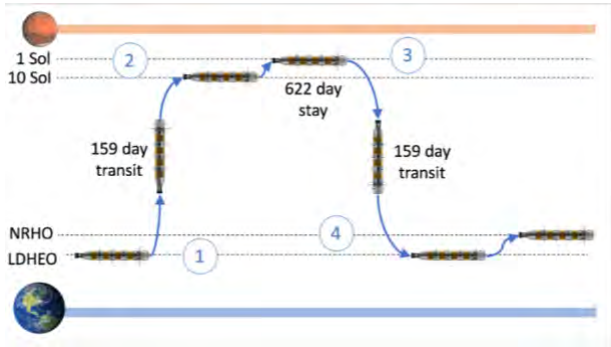


Fig. 2. Mars NTP Mission Bat Chart<sup>13</sup>

### III. MODELING AND ANALYSIS

The mathematical modeling for this study will be done using MATLAB and SysML. As stated previously, the MTV is assumed to require two times the power of the Orion spacecraft. Therefore, a value of 25 kW will serve as the target power output for the candidate power conversion systems. For the sake of simplicity, the input heat from the reactor at idle will be treated as a constant 10 MWt.

The first power conversion system to be modeled will be the thermoelectric generators and the subsequent dynamic power conversion cycles will be compared to the thermoelectric generators. The power output for the thermoelectric generators depends greatly on the material properties. The material for this study will be selected as Silicon-germanium (SiGe), which was the material used for the radioisotope thermoelectric generators (RTGs) on the Voyager 1, Voyager 2, Cassini, and New Horizons<sup>14</sup>. The use of this material also allows for the Thompson effect to be neglected, which simplifies the equation for power output<sup>15</sup>. The mathematical model is shown below in Eq. 1.

$$P = \eta \dot{Q}_{in} \quad (\text{Eq. 1})$$

The power output of the closed-loop Brayton cycle, shown in Figure 3, is limited to the maximum temperature in which the turbine blades can withstand, and by the working fluid properties. Nitrogen was chosen

as the working fluid because in the study included in Reference 15, it was proven to produce the highest efficiencies for a Brayton cycle for space applications<sup>16, 17, 18</sup>. The mathematical model for the Brayton cycle is shown below in Eqs. 2 and 3.

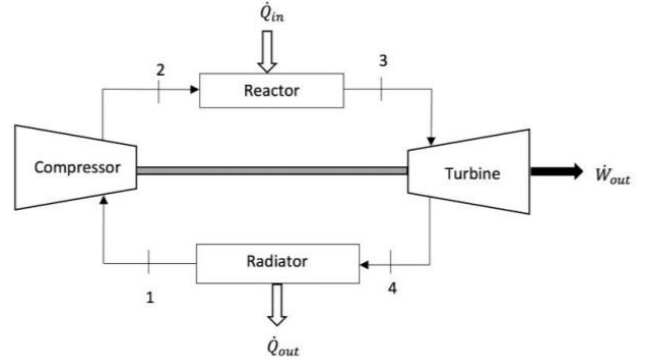


Fig. 3 Closed-loop Brayton Cycle<sup>19</sup>

$$\dot{W}_{cycle} = \dot{m}[(h_3 - h_4) - (h_2 - h_1)] \quad (\text{Eq. 2})$$

$$P = G \dot{W}_{cycle} \quad (\text{Eq. 3})$$

As for the Stirling cycle, a beta configuration was chosen for this study with helium as the working fluid because of its high gas constant<sup>20</sup>. The equations for the Stirling cycle are shown below along with a Pressure vs Volume diagram in Figure 5 and a Temperature vs Entropy diagram in Figure 6.

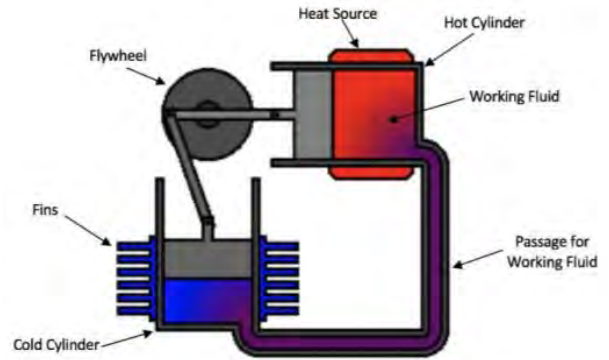
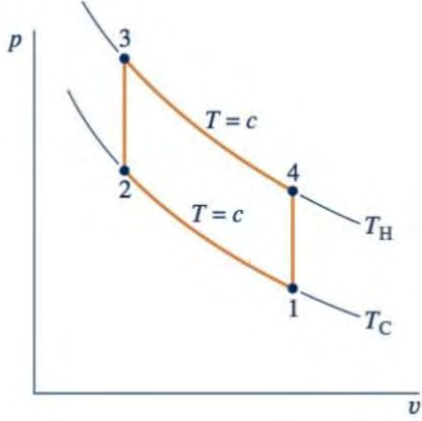
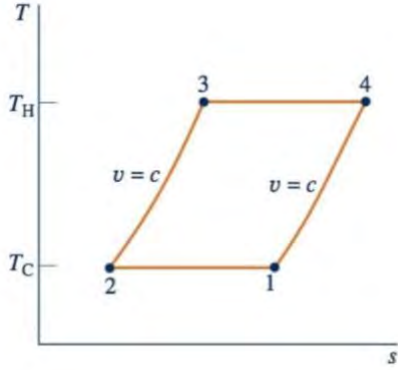


Fig. 4. Stirling Cycle Beta Configuration<sup>19</sup>



**Fig. 5.** Stirling Cycle Pressure vs Volume



**Fig. 6.** Stirling Cycle Temperature vs Entropy

The equations for calculating the power output by the Stirling cycle are shown below in Eqs 4 through 8. First, the ideal compression ratio is calculated using Eq. 4.

$$CR = \frac{T_H}{T_C} \quad (\text{Eq. 4})$$

Here,  $T_H$  is the hot temperature of the working fluid and  $T_C$  is the cold temperature of the working fluid. The mass of the working fluid in the system is found by Eq. 5.

$$m = \frac{Q_{in}}{c_v(T_H - T_C) + c_v T_C \ln(CR)} \quad (\text{Eq. 5})$$

Here,  $c_v$  is the specific heat capacity of the working fluid and  $Q_{in}$  is the heat input coming from the reactor. The next step is to calculate the efficiency,  $\eta$ , of the Stirling engine using Eq. 6.

$$\eta = \frac{m c_v T_C \ln(CR)}{m c_v (T_H - T_C) + m c_v T_C \ln(CR)} \quad (\text{Eq. 6})$$

The work out,  $\dot{W}_{out}$ , is calculated using Eq. 7, below.

$$\dot{W}_{out} = \eta Q_{in} \quad (\text{Eq. 7})$$

Finally, the generator efficiency is taken into account in Eq. 8.

$$P = G \dot{W}_{out} \quad (\text{Eq. 8})$$

For all of these models, the results of most interest are power output, mass of the power conversion system, and volume of the power conversion system. Creo Parametric will be used to model the components of the power conversion cycles to estimate the mass and volume of these proposed systems.

#### IV. RESULTS

Assuming the thermoelectric generator for this study will have the same efficiency as that of the GPHS-RTG used on the Cassini and New Horizons missions, at 6.3%, the power output of the thermoelectric generators with a heat input of 10 MWt was calculated to be 630 kWe.

For the Brayton cycle, the turbine inlet temperature,  $T_1$ , is limited by the moderator's melting temperature. Assuming the moderators are made of LiH, like in Reference 21, the turbine inlet temperature should be about 500 K. Furthermore, a common Brayton cycle pressure ratio of 13 was assumed, since the normal range is between 11 and 20, according to Reference 22. The radiator sink temperature,  $T_3$ , was assumed to be 278 K<sup>23</sup>. With a heat input of 10 MWt and a common generator efficiency of 30%, the power output of the Brayton cycle for this study was calculated to be 1187 kWe. The specific enthalpies at each state were determined using CoolProp and then the power generated by the system was calculated using equations 2 and 3.

Many assumptions had to be made to calculate the power output of the Stirling cycle. The temperatures of the working fluid and the size of the Stirling engine mirrored those from a study performed in 2016 at Glenn Research Center, which can be found in Reference 24. The hot temperature of the working fluid,  $T_H$ , was assumed to be 500 K, as it was with the Brayton cycle, and the cold temperature of the working fluid,  $T_C$ , was assumed to be 323 K<sup>24</sup>. Additionally, the length the piston travels was taken as 6 mm. This length was the same as the length the piston traveled in the study mentioned above. The generator efficiency was considered to be 30%, the same as it was for the Brayton cycle calculations. The heat input was assumed to be 10 MWt. With these input parameters, the power output of the Stirling cycle for this study was calculated to be 1331 kWe.

It can be seen that all three alternative systems and capable of generating values far above the target power of 25 kWe. Thus, the next step to determining the

recommended alternative system is to find the mass and volume of each system using Creo Parametric.

## V. CONCLUSIONS

NTP is a viable option for missions to Mars and beyond, but in its idle state, excess heat is an immediate issue for the reactor. The bimodal nuclear thermal propulsion concept has previously been favored for its ability to take all of this idle heat and convert it to usable power for the vehicle, but it would require substantial changes to the reactor design. Conceptually, a MIPS could remove enough of the idle heat so that the reactor core is not damaged, and convert this thermal energy into an adequate amount of electricity to power the vehicle, without compromising the reactor design. A comprehensive trade study will be performed considering the possible power conversion cycles for use in the MIPS, in order to determine the best option that meets the power requirements from a vehicle perspective. Beyond that, failure analysis would need to be conducted to see if backup power sources would be necessary.

## VI. FUTURE WORK

The immediate next steps for this study include modeling the mass and volume of the proposed systems using Creo Parametric. The following step is to determine which of these systems can generate power for the MTV and of those that can generate power, their respective masses. It is likely that the idle temperature of the reactor will change, therefore sensitivity analysis will be conducted on the effects of this parameter and of other selected parameters. Furthermore, reliability of the systems and cost analysis will be considered in addition to the systems power output capabilities and masses in order to better influence a well-rounded suggestion of which system would be best for use in the MTV.

## ACKNOWLEDGMENTS

Thank you to Samantha Rawlins for her contributions to this research and to Dr. Jason Cassibry for his guidance and encouragement. This work was supported by the National Aeronautics and Space Administration under contract number MTS\_UAH\_021717.

## REFERENCES

1. RAWLINS, S., "A Proposed Solution to Address Nuclear Thermal Propulsion Fuel Embrittlement and Cryogenic Hydrogen Requirements," *Nuclear and Emerging Technologies for Space*, Richland, WA, February 25 – February 28, American Nuclear Society Topical Meeting (2019).
2. FINSEITH, J.L., "Overview of Rover Engine Tests: FINAL REPORT," NASA CR – 184270, *George C. Marshall Space Flight Center Science and Engineering Contract*, February 1991 from <https://ntrs.nasa.gov/archive/nasa/casi.ntrs.nasa.gov/19920005899.pdf>
3. HALL, L., "Nuclear Thermal Propulsion: Technology for Deep Space Exploration," NASA, August 2019, from [https://www.nasa.gov/directorates/spacetech/game\\_changing\\_development/Nuclear\\_Thermal\\_Propulsion\\_Deep\\_Space\\_Exploration](https://www.nasa.gov/directorates/spacetech/game_changing_development/Nuclear_Thermal_Propulsion_Deep_Space_Exploration)
4. JENNINGS, T., "Space Technology Mission Directorate Game Changing Development Program Nuclear Thermal Propulsion Project," *Aerojet Rocketdyne*, September 2019
5. FENSTERMACHER, C. and OAKLEY, D. T., "Cooldown Requirements for Nuclear Rocket Missions," *Journal of Spacecraft and Rockets*, Vol. 4, No. 1, January 1967
6. CHENG, F., "Calculation Methods for Thermoelectric Generator Performance", *IntechOpen*, December 2016, from <http://dx.doi.org/10.5772/65596>
7. "NICMOS – Restoring Sight to the Hubble Space Telescope," Create, Hanover, New Hampshire, 2016.
8. WOLVERTON, M., "Stirling in Deep Space," *Scientific American*, March 2008.
9. COLE, M., "It Keeps Going and Going: Stirling Engine Test Sets Long-Duration Record at NASA Glenn," *Space Flight Insider*, July 2018
10. BUDEN, D., "Nuclear Thermal Propulsion Systems," Polaris Books, Lakewood, CO, 2011
11. WRONSKI, A., AND FOUKDEUX, A., "The Ductile-Brittle in Polycrystalline Tungsten," *Journal of the Less Common Metals*, Vol 8, Issue 3, March 1965
12. TORO, C., LIOR, N., "Analysis and Comparison of Solar-Heat Driven Stirling, Brayton, and Rankine Cycles for Space Power Generation," *Science Direct*, November 2016
13. RAWLINS, S., "A Proposed Solution to Address Nuclear Thermal Propulsion Fuel Embrittlement and Cryogenic Hydrogen Requirements," *Nuclear and Emerging Technologies for Space Conference*, February 27, 2019
14. MISRA, B., and ALTSEIMER, J. H., "In flight coolant Management Considerations for the NERVA Reactor Cooldown," *Nuclear Technology*, 12:3, 298-306, DOI: 10.13182/NT71-A31010 (1971)
15. MITCHELL, R., "Powering the Voyager Spacecraft with Radiation: The RTG (Radioisotope Thermoelectric Generator)", *All About Circuits*, June 2017, from <https://www.allaboutcircuits.com/news/voyager->

mission-anniversary-rtg-radioisotope-thermoelectric-generator/ s1

16. TARLECKI, J., LIOR N., and ZHANG, N., “Analysis of Thermal Cycles and Working Fluids for Power Generation in Space,” *Energy Conversion and Management*, August 2007, from [http://www.jaytarlecki.com/files/ECM\\_NOV\\_2007.pdf](http://www.jaytarlecki.com/files/ECM_NOV_2007.pdf)
17. ADAMS, R., “Nitrogen or Air Versus Helium for Nuclear Closed Cycle Gas Turbines,” *Atomic Insights*, from <https://archive.ph/20130117083141/http://atomicinsights.com/2009/04/nitrogen-or-air-versus-helium-for-nuclear-closed-cycle-gas-turbines.html>, April 2009
18. CONKLIN, J. C., COURVILLE, G. E., and SCOTT, J. H., “Evaluation of Working Fluids for Brayton Cycles in Space Applications,” AIP Conference Proceedings 699, 463 (2004); <https://doi.org/10.1063/1.1649607>
19. EMRICH, W., “Nuclear Rocket Engine Cycles,” *Principles of Nuclear Rocket Propulsion*, 1st ed, Butterworth-Heinemann, 2016, pp. 21 – 30
20. ASNAGHI, A., LADJEVARDI, S. M., SALEH IZADKAST, P., and KASHANI, A. H., “Thermodynamics Performance Analysis of Solar Stirling Engines,” *Niroo Research Institute*, Volume 2012, Article ID 321923, <http://dx.doi.org/10.5402/2012/321923>, April 2012
21. NAM, S. H., VENNERI, P., KIM, Y., LEE, J. I., CHANG, S. H., JEONG, Y. H., “Innovative Concept for an Ultra-Small Nuclear Thermal Rocket Utilizing a New Moderated Reactor,” *Nuclear Engineering and Technology*, Vol. 47, Issue 6, October 2015
22. Cengel, Y. A., and Boles, M. A., *Thermodynamics: An Engineering Approach*, 7th Ed. New York, McGraw Hill, 2011, p. 508 – 509
23. PIETSCH, A., “Space Power Systems Engineering,” *Progress in Astronautics and Rocketry*, 1966
24. BRIGGS, M. H., Prahl, J. M., and Loparo, K. M., “Improving Power Density of Free-Piston Stirling Engines,” AIAA – 2016 – 5016